**The Dissertation Committee for Yu Lu certifies that this is the approved version of the following dissertation:**

# A Bright Source of Cold Atoms

**Committee:**

**Mark G. Raizen, Supervisor**

**Qian Niu**

**Bjorn Hegelich**

**Elena Caceres**

**Chandrajit L. Bajaj**

**A Bright Source of Cold Atoms**

by

**Yu Lu**

**Dissertation**
Presented to the Faculty of the Graduate School of
The University of Texas at Austin
in Partial Fulfillment
of the Requirements
for the degree of
**Doctor of Philosophy**

The University of Texas at Austin
May, 2019

*To my parents*

*Bin Guo and Guangwen Lu,*

*and my girlfriend,*

*Wenqian He.*

# Acknowledgements

First, I would like to express my great appreciation to my advisor, Prof. Mark Raizen, for his valuable guidance, constructive suggestions, continuous support of my Ph.D. study and related research. Mark is a great physicist with a long-range vision in research. I highly respect his dedication not only to research, but also to his student, his family, and the physics community. I still remember the day in 2014 when I decided to join the Raizen group. That day I was sitting next to Mark in his office and he sketched on a paper the research plan for the next a few years. Since then, this piece of paper was kept on the first page of my notebook, and the rest of it was gradually filled with calculations and data as progresses were made. The advice and support from him is what made this work possible.

I wish to thank various people I teamed with on this project. Kevin Melin was leading the project when I first joined the group. He is brilliant in experiment and is very enthusiastic in building and controlling devices, his engineering background made the experiment much easier than I could ever imagine. Kevin is the one from whom I learned quite a lot useful experiment skills. He is more of a friend than just a colleague to me during my time of graduate study. Alina Blinova and Karl Burkhardt were also working on the project at the early phase. Alina is a great teammate to work with. She is very efficient and is always keeping everything nicely documented. She helped me a lot in ordering the parts for the magnetic decelerator. Karl is a very passinate person whose chemistry background benefited the project a lot. There were so many pleasant memories and discussions between us on chemistry and physics during his stay. Dr. Rodrigo Castillo Garza is the first postdoc I worked with in the group. He is the person who has the magic to cheer people up and make the experiment easy. Lukas Gradl joined about a year after and worked on the entrainment and heatpipe for improving the atom number in our experiment. He is very kind and always willing to help people around. We share the common enthusiasm in linux system and open source software. Dr. Jianyong Mo is a life-long friend and was leading us for a shot period during his postdoc. Jianyong is great in solving various problems in both research and life, he is a great scientist and group

leader. I appreciate his countless suggestions during my study. Logan Hillberry, Yi Xu, and Jordan Zesch joined in the summer of 2017 and brought the group fresh ideas. Jordan worked with me on constructing and testing the decelerator during the summer. He is a person full of curiosities and always asks challenging questions. I improved myself a lot through disscussions with him. Logan and Yi switched to the project after some changes in group personel and worked with me since then. Logan is always enthusiastic and optimastic about the research, his joining made the disscussions and exchange of ideas in our project more efficient. We had a lot of interesting conversations on physics, programming, and algorithms, which made the life in the underground more enjoyable. Yi is very good at bringing us new ideas from her solid theory background and contributed a lot on the optics of this project. She is also a person everyone liked to stay with and brings fun moments to our office. During the last three years of my research,the joining of two postdocs, Dr. Pavel Nagornykh and Dr. Harry Lichung Ha, has speed up the progress on this project a lot. Harry is a person with strong willingness to get things done. His strong background in the experimental atomic physics benefited us a lot. He always planed everything ahead and made the group work more efficiently. Pavel impressed me a lot with his wide range of knowledge and mathematic skills. He brought throughful thoughts and critical suggestions to the project. I appreciate those moments when we were sitting in the dark taking data while lisening his favorite music from the 19th centery. I'm also impressed by the research passion of undergraduate students Sebastian Miki and Julia Orenstein.

I would like to also express my gratefulness to my colleagues in the Raizen lab. Everyone here made my graduate study a great experience. Georgios Stratis is like a big brother in the group who takes many responsibilities and organizes activities. He cares not only research, but also other fellow graduate students in the department. Erik Anciaux worked on the atom lens project and graduated in 2018. He is very passionate in research and I learned a lot through discussions with him. Igal Bucay is in the same year as me, we talked a lot about research and career plans. His special view on things always brings new ideas to the project. Akarsh Simha is brilliant in computer science, he provided a lot help and suggestions to my career plan. Dr. Ahmed Helal worked on the field ionization project. I appreciate his helpful suggestions in both research and life. Dr. Diney Ether joined in 2018 on the optical tweezer experiment. He is very energetic and has a broad knowledge of the

frontiers in physics. It is my pleasure to work with these great people in the Raizen lab.

During the time of working on this project, I also received a lot of help from our colaborators in Weizmann Institute of Science, Israel. They are: Prof. Edvardas Narevicius, Julia Narevicius, and Dr. Nitzan Akerman.

Additionally, there are many professors who support my graduate study through their professionality. I was a teaching assistant for Prof. John Keto in his senior laboratory class during my last year. Prof. Keto was always willing to disscuss physics with student and talk with them like a friend. I gain a lot of knowledge out of my field through the disscussions with him. Prof. Varun Rai opened the door of statistical learning to me through his class, he cares student's career development even a few years after taking his class. I would like to thank Prof. Michael Downer and Mrs. Jane Downer, for their support and encouragement during my study as a Downer fellow. I also improved myself a lot through disscussions with Prof. Chandrajit Bajaj, who is my advisor on the graduate computational porfolio program. I worked with him in the Computational Visualization Center (CVC) on unsupervised image segmentation problems. There are many other professors who broadened my knowledge and guided my way towards who I am today, without listing details, they are: Prof. Linda Reichel, Prof. Todd Ditmire, Prof. Manfred Fink, Prof. Duane Dicus, Prof. Fares Fraij, and Prof. Greg Durrett.

I have to also thank my dissertation committee members for their suggestions and comments on my research, they are: Prof. Mark Raizen, Prof. Qian Niu, Prof. Bjorn Hegelich, Prof. Elena Caceres, and Prof. Chandrajit Bajaj.

The department of physics and center for nonlinear dynamics (CNLD) has offered a lot of convenience to my research. I have to specially thank Mrs. Olga Vera, the senior administration associate who took care of students‘ tuition, travel arrangement, project budget, etc. Her kindness made the CNLD a great organization. The machine shop staffs are a great team of people who trained me on machining skills as well as made many vacuum parts for our project, they are: Allan Schroeder, Jack Clifford, Ed Baez, Kenny Schneider, Robert Hasdorff, Danny Boyd, Herb Boehl, Jeff Boney, Jay Campbell, Terry Cole, Richard Goodwin, Bryan McDonald, Geroge Sandefur.

During my 5-year living in this beautiful city, my friends in Austin have offered tremendous amount of help, they are: Yucen Fang, Junho Choi, Chungeun Emily Lee, Shida Shen, Juan Trejo, Lixiang Xu, Zhaodong Chu, Xin Liu, Kurtis Evan David,

Alex Leviyev, Melina Armer, Keyur Muzumdar, Liang Dong, Hailong Zhou, Jason Derr, Ganesh Tiwari, Meng Li, Linyuan Gao, Linxiao shen, and Litian Chen.

I acknowledge that this project is supported by the W.M. Keck Foundation.

Lastly, I would give my unique thanks to my parents and my girlfriend for their unconditional love. My parents were always supporting my decisions no matter what. I appreciate everything they have done in my path towards my dream. Without their support and encouragement I cound not imagine how hard my life in graduate school could be. Words cannot express enough my gratefulness to my girlfriend, for her 8 years accompany and waiting.

Yu Lu
May, 2019
Austin, Texas

**A Bright Source of Cold Atoms**

Yu Lu, Ph.D.
The University of Texas at Austin, 2019

Supervisor: Mark G. Raizen

This dissertation describes a general approach of generating a high flux of cold atoms that can be confined in a magneto-optical trap. As an alternative to the state-of-the-art laser cooling method, this approach widens our ability to cool and control atoms without relying on a specific atomic transition and availability of laser. In this dissertation I will discuss the design, construction of the experiment and characterization of a pulsed cold atom source in detail.

This work is based on a new paradigm: entrainment of atoms in the carrier gas of a supersonic beam, followed by the magnetic deceleration and trapping. Our methodology is based on the supersonic beam created by the expansion of a dense carrier gas from a pulsed release of gas through a small aperture. Cold noble gas emerging from this pulsed high pressure supersonic nozzle acts as a carrier, into which atoms of interest are then entrained. In our studies with the lithium atoms, up to $10^{11}$ atoms per pulse could be entrained into a supersonic beam of helium at a translation temperature of below 100 mK. The supersonic valve is typically operated at a rate of below 1 Hz in the experiment. A much larger flux can be achieved at a higher repetition rate. These atoms are moving at a speed of 500 $\mathrm{m\,s^{-1}}$ and need to be decelerated almost to a complete stop, in order to be trapped and cooled to quantum degeneracy. A 2.5-meter long moving-trap magnetic decelerator with 480 coil pairs was built and characterized. Atoms moving at a speed around 500 $\mathrm{m\,s^{-1}}$ were trapped and decelerated to various final velocities ranging from 400 $\mathrm{m\,s^{-1}}$ to 50 $\mathrm{m\,s^{-1}}$, at a resulting temperature of 30 mK and a flux of $10^8 \sim 10^9$ atoms per pulse. This whole process takes place within only 10 ms, at a repetition rate of 100 Hz $10^{10} \sim 10^{11}$ atoms can be delivered per second. This approach is very general compared to the

laser cooling, since most atoms in the periodic table have a magnetic moment in their ground state or can be optically pumped to a long-lived para-magnetic metastable state.

In this dissertation, I show the working principle of each component of our experiment and characterize the atom beam at multiple stages. I describe in detail the construction and optimization of our magnetic decelerator, and demonstrate the control and monitoring system with the experiment results. Also implemented in this work is a flexible laser system that is composed of a reference diode laser and two tapered amplifiers to control and probe the internal states of atoms, as well as provide the trapping force. I also explore the optical molasses and chirped cooling techniques which help load the atoms into a magneto-optical trap. The successful demonstration of this method of creating a cold atom source leads us to believe that the magnetically decelerated supersonic atoms will play an important role in the area of cold atom physics.

# Contents

# List of Figures

# List of Tables

# Chapter One: Introduction

The field of cold atom physics is one of the fastest expanding and most interdisciplinary fields in physics. The development of cold atom physics opens doors to many exciting areas such as precision spectroscopy [36], quantum optics [71], atom laser [17], and quantum information [66]. While more and more achievements in this area have been applied to advanced topics like quantum computing [109] and cryptography [48], the fundamental study of the cold atom systems is still drawing large attention from scientists around the world, such as optical Maxwell's demon [103], cold and ultra-cold collisions [122], quantum turbulence [55], etc.

This chapter provides a brief introduction to cold atom physics, followed by a quick overview of its history. I then introduce the motivation of this research of generating a bright source of cold lithium atoms.

## 1.1 Cold atom physics

### 1.1.1 Towards absolute zero

The development of physics started with the understanding of fundamental phenomena in our environment. While there is a lof of interesting physics under normal parameter settings, exotic physics tends to exists when moving towards extreme physical conditions, such as black holes, superconducting metals, plasma, etc. Temperature, or kinetic energy, is also a parameter that provides exciting physics at its extreme ends. High energy physics, solar physics, and plasma physics have been under active studies for many decades [29, 35, 62, 127]. Moving towards the lowest limit of the thermodynamic scale, where temperature gets close to the absolute zero, we step into the amazing world of cold atom physics.

Fascinating phenomena appear in systems with dilute concentrations of atoms and molecules at temperatures near the absolute zero, where the de Broglie wavelength ($\lambda_{\mathrm{dB}}$) of characteristic thermal motions, becomes comparable to the mean interparticle separation, $r = \rho^{-1/3}$, with $\rho$ being the density. All substances begin to depart from classical physics when cooled towards this temperature, quantum mechanical

effects become dominant and new phenomena emerge. Quantum physics describes matter at absolute zero as the point of the lowest internal energy. Among other interesting phenomena, Bose Einstein Condensation (BEC), a unique state of matter that does not occur at a room temperature, has been created using neutral atoms since the 1990s.

BEC of a dilute gas, as predicted by Bose and Einstein in 1924 [19], is the macroscopic occupation of the ground-state of a system of Bosons. This system of degenerate dilute gas shows remarkable properties that contribute to understanding of various phenomena ranging from superfluidity and superconductivity [44] to the extreme density of neutron stars [104]. It has been created by numerous groups, using elements such as rubidium-87 [3], lithium-7 [20,21] and sodium [32,80]. A similar example of a new phase of matter at ultracold temperatures is the degenerate Fermi gas, which has been studied with elements such as potassium-40 [34] and lithium-6 [90].

The number density of atoms in the quantum degenerate state increases as the temperature approaches absolute zero. For a dilute gas of massive particles, the de Broglie wavelength at thermal equilibrium serves as a measure of delocalization of atoms:

$$\lambda_{\mathrm{dB}} = \frac{h}{\sqrt{2\pi m k_B T}}. \tag{1.1}$$

Here $h = 6.626 \times 10^{-34}\ \mathrm{m^2\,kg\,s^{-1}}$ is Planck's constant, $m$ is the mass of the particle, $k_B \approx 1.38 \times 10^{-23}\ \mathrm{J\,K^{-1}}$ is the Boltzmann constant, and $T$ is the temperature of the gas at equilibrium.

The de Broglie wavelength shows the wave-like nature of particles and describes the rough size of the region where atoms can be found with high probability. With total of $N$ particles occupying a space of volume $V$, the particle number density is given by $n = N/V$. From here the phase space density is defined as:

$$\rho = n\lambda_{\mathrm{db}}^3. \tag{1.2}$$

Quantum nature dominates when the de Broglie wavelength is comparable to or larger than the inter-particle spacing. For dilute condensates,

$$\lambda_{\mathrm{dB}} \gg (\frac{V}{N})^{1/3} \gg a, \tag{1.3}$$

where $a$ is the scattering length. From the aspect of the phase space density, ideal gases at thermal equilibrium follow a Maxwell-Boltzmann distribution when $\rho \ll$

1, and obey either Bose-Einstein statistics or Fermi-Dirac statistics when $\rho \sim 1$, depending on whether they are Bosons or Fermions.

The path of cold atoms towards quantum degeneracy provides a versatile platform for experiments in many-body physics. Cooling of a dilute atom gas pushed low-temperature physics into a territory orders of magnitude colder than the millikelvin regime of the helium superfluids, providing precise tests of keystone theories of many-particle quantum systems [129]. Additionally, it has lead to new physical systems such as mixed degenerate Fermi gases [34, 90, 113].

### 1.1.2 Cooling

Cooling atoms to ultracold temperatures requires techniques that slow down the atoms in their center-of-mass frame. The temperature of the atom cloud is set by the average kinetic energy of atoms relative to the center-of-mass motion:

$$T = \frac{mv^2}{k_B} \tag{1.4}$$

Here $v$ is the standard deviation of the velocity distribution that follows Maxwell-Boltzmann distribution, $m$ is the mass of an atom and $k_B$ is the Boltzmann constant.

Laser cooling and trapping are techniques used to reduce the velocity of atoms to near zero Kelvin and confine them to a particular volume in space. Laser cooling makes use of the radiation pressure of light to remove the kinetic energy of atoms, it thus slows them down and reduces their temperature to milli to micro-Kelvin range. The force used to cool and trap atoms is exerted by photons that scatter off atoms. The imbalance in momentum transfer due to absorption from one direction and re-emission in a random direction results in a net cooling mechanism. This is similar to bombarding a bowling ball by a stream of ping pong balls. However, under a high scattering rate of $10^6$ $s^{-1}$ or more photons per second, atoms can experience a deceleration as large as $10^5$ $g$, where $g$ is the standard gravity of earth. Achieving such a high deceleration requires a cycling transition in the atomic level structure as well as laser frequencies tuned to resonance. Due to its simplicity and high efficiency, laser cooling is often used as a first stage to cool atoms below milli-Kelvin [95].

The invention of the laser has played a key role in atomic physics. In 1975, Hansch and Schawlow suggested that the forces on atoms exerted from the laser light could be so substantial that cooling can be achieved using them [52]. In the same

year, Wineland and Dehmelt also suggested that laser cooling could be applied to trapped ions, with experiment reporting the cooling of $Mg^+$ ions and $Ba^+$ ions [124]. Later in 1978, Ashkin brought up the idea that lasers could also be used to trap atoms [5]. The first experimental demonstration of decelerating atoms was realized in 1982, using a Zeeman slower, by Phillips and Metcalf [96]. After advances in the laser technology, such as improved power stability, wavelength availability and tunability, laser cooling has been successfully applied to variety of atom species. By the late 1980s, researchers had achieved the lowest possible temperatures of sodium by laser cooling to its Doppler limit, 240 µK. In 1985, Steven Chu and colleagues at Bell Labs proposed a new cooling technique called optical molasses [25]. In 1988 Phillips, Metcalf and their colleagues, adopted this technique and published the first experiment on cooling the sodium atoms below the Doppler limit [74]. This violated the generally accepted theory of Doppler cooling. The unexpected cooling mechanism was then quickly explained by including more atomic states and effects of laser polarization in the theory, subsequently the recoil limit was proposed as the new lower limit of cooling. However, in the same year Claude Cohen-Tannoudji and his colleagues achieved cooling of metastable $^4He$ below its one-photon recoil limit (23 µK), by velocity-selective optical pumping [6]. As researchers gained better understanding of Doppler cooling and combined with the evaporative cooling technique [56], the first BEC was observed in rubidium atoms by Eric Cornell and colleagues in 1995 [3], and shortly thereafter in sodium by Ketterle and colleagues [32]. Since then atoms at ultracold temperatures with high phase space density have opened a new chapter for physics and led to exciting studies. Other cooling methods include buffer gas cooling [123], Sisyphus cooling [30], etc.

By applying methods like laser cooling, the temperature of atoms can be reduced to below millikelvin, usually to a few hundreds of microkelvin or even lower [6]. Another technique, evaporative cooling [69], is commonly used as the last step to reach quantum degeneracy of the atom gas. Evaporative cooling was first proposed by Harald F. Hess in 1986 [56] for spin-polarized atomic hydrogen. It is based on the removal of the most energetic atoms from the trap followed by a re-thermalization of the remaining atoms by elastic collisions. This technique was implemented on alkali atoms in 1995 to produce the first BEC [3]. The great potential of the evaporative cooling technique stems from the fact that it can increase the phase-space density by six orders of magnitude [23].

### 1.1.3 Trapping

In order to confine neutral atoms at ultracold temperatures, researchers have applied various trapping techniques. Electromagnetic fields can be configured to confine atoms. Spherical quadrupole traps [82] consisting of two coils in an anti-Helmholtz configuration were used for the first magnetic trapping of neutral atoms. Unfortunately, at low temperatures the zero magnetic field at the center of the trap causes a complete loss of atoms due to the Majorana spin flips [53, 54]. To avoid this, blue detuned laser beams were used to push atoms away from the center but with additional complexity [32]. The first stable and purely magnetic trap was the time-orbiting potential (TOP), where a rotating bias field is added to the spherical quadrupole trap [93], which was used in the first observation of a BEC [3]. The most common magnetic trap for neutral atoms is Ioffe-Pritchard (IP) trap, which consists of a radial quadrupole field and an axial parabolic field [98]. Variations of IP trap include the baseball trap [12], the cloverleaf IP trap [81] and the quadrupole Ioffe configuration (QUIC) trap [39]. The workhorse of cold neutral atom research is the magneto-optical trap (MOT), for its simplicity and depth [99]. In a MOT, the trapping force stems from radiation pressure of laser beams that converge at the center. A weak spatially inhomogeneous magnetic field is added as the tuning knob. In addition to the 3D confinement, the laser light in the MOT also provides Doppler and possibly sub-Doppler cooling of the atoms. Due to these advantages, the magneto-optical trap became the state-of-the-art trapping technique in cold atom physics for the microkelvin regime.

## 1.2 Motivation

### 1.2.1 Limitations of laser cooling

As the state-of-the-art technique, laser based cooling and trapping methods have been the workhorse for generating degenerated dilute gases. However, the laser cooling technique is not a general method.

In order to make laser cooling work, atoms or molecules mush have a cycling transition which guarantees the continuous scattering of photons. In order to achieve cycling transitons in neutral atoms, one either seeks direct two-level transitions that

cycles according to selection rules, or tries to use a combination of multiple lasers targeting different transitions. However, neutral atoms that have been cooled by laser based methods are just a very small portion of the periodical table: Li, Na, K, Rb, Cs, Be, Mg, Ca, Sr, Cr, Yb, He, Ne, Ar, Kr, Xe [1]. Additionally, the availability of stable lasers with proper power and wavelength is another limiting factor.

For molecules, due to their complex rotational and vibration energy level structures, finding a cycling transition is quite challenging. Except for a few molecular species that have been directly cooled by laser [110], many molecules were cooled by using other techniques, such as binding molecules with atoms and cool them together [84], or decelerating molecular beams from a cold source [115].

Another disadvantage of using near-resonant light for cooling and trapping is that there is a limit of the minimum achievable temperature due to a significant probability of photon recoil. In near-resonant traps with high atom number density, the collision rate between atoms is large. Due to the presence of the near resonant light, the fraction of atoms in the excited state increases and inelastic collisions between atoms with one of the atoms in the excited state occur, this results in an inelastic exchange of energy between the atoms which causes loss of atoms from the trap [23].

### 1.2.2 Our approach

We explore a new approach to cool and produce a bright source of cold atoms. With some extra engineering effort this method is generally applicable to all atoms that are paramagnetic in their ground states or metastable states, as well as molecules with a paramagnetic state. We use lithium-7 to benchmark this method.

The method is based on a supersonic beam, created from the expansion of a dense carrier helium gas from a supersonic Even-Lavie valve, which is operated in pulsed mode through controlling an actuated valve. The valve can operate at up to many times atmospheric pressure and cryogenic temperatures, providing a very directional and cold beam of atoms. This beam acts as carrier into which natural abundance lithium atoms are then entrained. The entrainment happens near the output of the supersonic valve. Through frequent collisions, the seeded lithium atoms equilibrate to the low temperature and gain the beneficial collimation properties from the super-

[1] Data from `http://chadorzel.com/principles/2013/08/19/know-your-laser-cooled-atoms/`.

sonic carrier. As the beam expands, collisions subside and the lithium atoms decouple from the carrier helium atoms, resulting in a beam with temperature below 100 mK but moving at 480 $\mathrm{m\,s^{-1}}$. We then use a series of 480 anti-Helmholtz coil traps to decelerate the lithium beam while maintaining a 3D confinement of the atoms. We constructed this decelerator from scratch based on our previous one-dimensional coil-gun [86]. Step-by-step testing and optimization has also been performed. Currently the decelerator is capable of being operated from 500 $\mathrm{m\,s^{-1}}$ to 50 $\mathrm{m\,s^{-1}}$. We also constructed the optical molasses and laser chirped cooling to help load atoms coming out from decelerator into a MOT for future experiments. In the future, modification of the circuit design and the vacuum component setup could help in reaching a lower final speed so that atoms can be captured and trapped directly by a trap without any lasers involved.

I start with introducing the related fundamentals of atomic physics in Chapter 2, followed by describing the laser system and optics in our experiment in Chapter 3. In Chapter 4, I illustrate the setup and procedures of our experiment towards a cold supersonic lithium beam. The assembling and characterization of the magnetic decelerator is discussed in Chapter 5. Experiments of optical molasses and chirped cooling on the slowed atoms are described in Chapter 6. By the end of this dissertation, in Chapter 7, a summary of this research work and its potential improvements are provided, together with a brief review of the future directions of this project.

# Chapter Two: Atomic physics and lithium-7

This chapter discusses the fundamentals of the atomic physics theory. Starting with the atom-electric field interaction with a model of two-level system. This provides us with valuable insights regarding the spontaneous emission, the scattering rates and the population distributions of the internal states of atoms. This two-level model is oversimplified in the sense that it does not take into account any spontaneous emission, which is an important process in such interaction. The distribution of internal states of two-level atoms is described via the optical Bloch equations. The interaction of atoms with external magnetic fields is discussed, where I introduce the Zeeman effect, which is a key concept that we use in many aspects of our experiment.

As we mainly used lithium-7 in our experiment, it is helpful to have an overview of its various properties, such as physical properties, hyperfine structures, optical transitions, etc. This is discussed by the end of this chapter.

## 2.1 Notation

In this dissertation, I use the generally accepted notations for atom energy state, with $L$ as the orbital angular momentum, $S$ as the spin quantum number and $J = L + S$ as the total electron angular momentum. Additionally, nuclear spin is denoted $I$. The projection of angular momentums are: $M_S$, $M_L$, $M_J$ and $M_I$, as listed in Table 2.1. An atomic state is then written in the following form:

$$^{2S+1}L_J \tag{2.1}$$

## 2.2 Atoms in an electric field

### 2.2.1 Two-level systems

The two-level system is a simple model that helps in the study of the interactions between an atom and an external field, modeled as Hamiltonian, given by

$$H = H_0 + H'(t), \tag{2.2}$$

| Notation | Meaning |
|---|---|
| n | Principle quantum number |
| L | Orbital angular momentum |
| S | Electron spin angular momentum |
| J | Total electron angular momentum |
| I | Nuclear spin |
| F | Total atomic angular momentum |
| $M_x$ | Angular momentum along projected axis, x=L,J,F,S |
| $\omega$ | Angular frequency in rad/s |
| $\tau$ | Lifetime of an excited state |
| $\Gamma$ | Atom spontaneous decay rate in rads/s, $\Gamma = 1/\tau$ |
| $\gamma$ | Nature linewidth of an atomic energy level in Hz, $\Gamma = 2\pi\gamma$ |
| $I_{\text{sat}}$ | Laser saturation intensity |

Table 2.1: Common notation used in this dissertation.

where $H_0$ describes the atom in a field-free environment and $H'(t)$ is the perturbation from a classical oscillating electric field.

The energy eigenvalues of the atom Hamiltonian $H_0$ are given by $E_n = \hbar\omega_n$ corresponding to the energy eigenstates $\phi_n(\vec{r})$. The time-evolution of the wave function is calculated by the time-dependent Schrödinger equation

$$i\hbar\frac{\partial}{\partial t}\Phi(\vec{r},t) = H\Phi(\vec{r},t), \tag{2.3}$$

where $\Phi(\vec{r},t)$ is the wave function and $\vec{r}$ is the relative position of the electron to the center of mass of the atom. For a two level system (n = 0, 1), the wave function at time $t$ is given by

$$\Phi(\vec{r},t) = c_1(t)\phi_1(\vec{r})e^{-iE_1t/\hbar} + c_2(t)\phi_2(\vec{r})e^{-iE_2t/\hbar}, \tag{2.4}$$

where $c_1(t)$ and $c_2(t)$ are constants that depend on the initial conditions, with normalization requirement of $\|c_1\|^2 + \|c_2\|^2 = 1$. One can also write Eq. 2.4 in a vector form, then the Hamiltonian $H$ becomes a 2x2 matrix. Using Dirac notation, Eq. 2.4 becomes

$$\Phi(\vec{r},t) = c_1\,|1\rangle\,e^{-i\omega_1t} + c_2\,|2\rangle\,e^{-i\omega_2t}, \tag{2.5}$$

where $\omega_1 = E_1/\hbar$, $\omega_2 = E_2/\hbar$.

To investigate the interaction of atoms with the light, consider an electric field that behaves like a monochromatic plane wave traveling in the positive z direction

$E(\vec{z},t) = \vec{E_0}\cos(kz - \omega t)$. One has to take into account the energy of the electric dipole $-e\vec{r}$. The perturbation is given by

$$H'(t) = e\vec{r}\cdot\vec{E_0}\cos(kz - \omega t). \tag{2.6}$$

If we absorb the diagonal elements of $H'(t)$ into $H_0$, and plug equation 2.4 in to 2.3, we can write the perturbation term as

$$H' = \begin{bmatrix} 0 & \langle 1|H'(t)|2\rangle \\ \langle 2|H'(t)|1\rangle & 0 \end{bmatrix}. \tag{2.7}$$

Thus, we have

$$\begin{aligned} i\hbar c_1'(t) &= c_2(t)H_{12}'(t)e^{-i\omega_0 t} \\ i\hbar c_2'(t) &= c_1(t)H_{21}'(t)e^{i\omega_0 t} \end{aligned}, \tag{2.8}$$

where $\omega_0 = \omega_2 - \omega_1$, $c_1'$ and $c_2'$ are the time dependent coefficients for the new perturbation expression.

Eq. 2.8 is effectively the time-dependent Schrödinger equation. Some approximations are needed to be able to solve these equations for $c_1(t)$ and $c_2(t)$ to obtain the state probability as a function of time.

The first is the dipole approximation, here we consider that the radiation has a wavelength $\lambda$ that is much larger than the size of the Bohr radius $a_0$ of the atom, $\lambda \gg a_0$. This means that the electric field can be treated as a uniform field over all the atoms. Thus, we can write the interaction term as

$$H_{12}' = H_{21}' = \hbar\Omega\cos(\omega t), \tag{2.9}$$

where the Rabi frequency $\Omega$ is defined as

$$\Omega = \frac{-eE_0}{\hbar}\langle 2|r|1\rangle, \tag{2.10}$$

with

$$\langle 2|\vec{r}\cdot\vec{E_0}|1\rangle = \int \phi_2^*(r)\vec{r}\cdot\vec{E_0}\phi_1(r)d^3\vec{r} = E_0\langle 2|r|1\rangle. \tag{2.11}$$

Here $E_0 = \|\vec{E_0}\|$ is constant for all space.

The second approximation is the rotating wave approximation. In this case the radiation has a frequency $\omega$ that is close to the atomic resonance $\omega_0$, such that $|\omega - \omega_0| \ll 1$ and $\omega + \omega_0 \approx 2\omega_0$. The terms of order $1/\omega$ can be neglected while

keeping terms of order $1/\delta$, where $\delta = \omega - \omega_0$ is the detuning of the electric field frequency relative to the atomic transition. The next step is to decouple the two equations in 2.8 by taking their time derivative with the initial conditions that the atoms are in the ground state $|1\rangle$, i.e. $c_1(0) = 1$, $c_2(0) = 0$. We have the solution written as

$$c_1(t) = \Big( \cos\frac{\Omega'}{2} - i\frac{\delta}{\Omega'}\sin\frac{\Omega' t}{2}\Big) e^{i\delta t/2} \tag{2.12}$$

and

$$c_2(t) = -i\frac{\Omega}{\Omega'}\sin(\frac{\Omega' t}{2}e^{-i\delta t/2}). \tag{2.13}$$

Here $\Omega' = \sqrt{\Omega^2 + \delta^2}$ is the oscillation frequency for the probability of finding an atom in the initial state $|1\rangle$ or the excited state $|2\rangle$. A special case is when $t = \pi/\Omega'$, in this case all the atoms are in the excited state, and the laser pulse that generates this distribution is called a $\pi - pulse$.

In the above discussion we assumed a monochromatic source. If we instead consider a broadband radiation source and use Einstein's treatment, we can calculate the rate of spontaneous emission of photons from the atoms, as well as the lifetime of the excited states.

Consider atoms with two levels $|1\rangle$ and $|2\rangle$, the population of the ground and excited states are given by:

$$\frac{dn_2(t)}{dt} = n_1(t)B_{12}\rho(\omega_{12}) - n_2(t)B_{21}\rho(\omega_{12}) - n_2(t)A_{21}, \tag{2.14}$$

where $\rho(\omega_{12})$ is the energy density per unit frequency interval of the radiation field. $B_{12}$, $B_{21}$ are the Einstein coefficients for photon absorption and induced emission, respectively. $A_{21}$ is the Einstein coefficient for spontaneous emission.

Additionally, when there is no laser field the population of each state at equilibrium is given by the Boltzmann equation, $n_2/g_2 = n_1/g_1 exp(-\hbar\omega/k_B T)$, we then have

$$A_{21} = \frac{\hbar\omega^3}{\pi^2 c^3}B_{21} \tag{2.15}$$

and

$$\frac{dn_1(t)}{dt} = -\frac{dn_2(t)}{dt}, \tag{2.16}$$

where $g_1$, $g_2$ account for the energy level degeneracy.

The energy density of the applied electric field in the frequency interval $\omega$ to $\omega + d\omega$ is given by $\rho(\omega)d\omega = 1/2\epsilon_0 E_0^2(\omega)$, thus the Rabi frequency has a relation

$\|\Omega\|^2 \propto 2\rho(\omega)d\omega/\epsilon$. If we integrate $\|c_2(t)\|^2$ we have the transition rate between the two levels as

$$R_{12} = \frac{\|c_2(t)\|^2}{t} = \frac{\pi e^2 \| \langle 2|r|1\rangle \|^2}{\epsilon\hbar^2}\rho(\omega_0). \tag{2.17}$$

Summarize above equations, we get

$$\begin{aligned} B_{12} &= \frac{\pi e^2 \| \langle 2|r|1\rangle \|^2}{3\epsilon_0\hbar^2} \\ A_{21} &= \frac{4\alpha}{3c^2}\omega^3 \| \langle 2|r|1\rangle \|^2, \end{aligned} \tag{2.18}$$

where $\alpha = e^2/4\pi\epsilon_0\hbar c \approx 1/137$ is the fine-structure constant. Solving equations 2.14 and 2.15 with the conditions $\rho(\omega_{21}) = 0$ and $n_1 + n_2 = N$, we find that the population in the upper level has an exponentially decaying solution $n_2(t) = n_2(0)exp(-A_{21}t)$, thus the decay rate $\Gamma$ can be derived as

$$\Gamma = A_{21} = \frac{1}{\tau}, \tag{2.19}$$

Where $\tau$ is the lifetime in seconds of the excited state. If there is more than one excited degenerate state, the Einstein A coefficients need to be summed through all possible decay channels to get the total decay rate. The decay rate $\Gamma = 2\pi f$ here has units of rad/s, while the resonant frequency $f$ for the corresponding transition is in units of Hz.

### 2.2.2 The Optical Bloch equations

Above, we have solved the two-level system for an atom coupled to an oscillating electric field. However, this simple model only takes into account the excitation and stimulated emission by an electric field with coherent evolution of the single atom state amplitudes, from its nature of using a pure state description (the ket notation). To describe a statistical mixture of several states, a mixed state using a density matrix description is needed:

$$\rho = \begin{pmatrix} \|c_1\|^2 & c_1c_2^* \\ c_2c_1^* & \|c_2\|^2 \end{pmatrix} = \begin{pmatrix} \rho_{11} & \rho_{12} \\ \rho_{21} & \rho_{22} \end{pmatrix}. \tag{2.20}$$

After plugging it into Schrödinger equation:

$$i\hbar\frac{d\rho}{dt} = [H, \rho], \tag{2.21}$$

and taking care of the commutator $[A, B] = AB - BA$, we have the optical Bloch equations:

$$\begin{aligned}
\frac{d\rho_{11}}{dt} &= \Gamma\rho_{11} + \frac{i}{2}(\Omega^*\rho_{21}e^{i\delta t} - \Omega\rho_{12}e^{-i\delta t}) \\
\frac{d\rho_{22}}{dt} &= -\Gamma\rho_{22} + \frac{i}{2}(\Omega^*\rho_{12}e^{-i\delta t} - \Omega\rho_{21}e^{i\delta t}) \\
\frac{d\rho_{12}}{dt} &= -(\frac{\Gamma}{2} + i\delta)\rho_{12}e^{-i\delta t} + \frac{i}{2}\Omega^*(\rho_{22} - \rho_{11}) \\
\frac{d\rho_{21}}{dt} &= -(\frac{\Gamma}{2} - i\delta)\rho_{21}e^{i\delta t} + \frac{i}{2}\Omega(\rho_{11} - \rho_{22}),
\end{aligned} \tag{2.22}$$

the population of excited state at steady state $d\rho_{i,j}/dt = 0\ i, j \in 1, 2$ then becomes

$$\rho_{22} = \frac{s_0/2}{1 + s_0 + (2\delta/\Gamma)^2}, \tag{2.23}$$

where the saturation parameter is given by

$$s_0 = 2\Omega^2/\Gamma^2 = I/I_{\text{sat}}, \tag{2.24}$$

with saturation intensity:

$$I_{\text{sat}} = \frac{\pi hc}{3\lambda^3\tau}. \tag{2.25}$$

In atomic physics experiments, lasers are often used to excite the atoms into the excited states. A very important equation often used is the photon scattering rate, given by the decay rate $\Gamma$ times the excited state population $\rho_{22}$,

$$R_{\text{scatter}} = \frac{s_0\Gamma/2}{1 + s_0 + (2\delta/\Gamma)^2}. \tag{2.26}$$

Note that when $s_0 \ll 1$, we have $\rho_{22} \approx 1/2$. In this case ground and excited states will be equally distributed, this happens when the laser stimulated excitation and stimulated emission rates are equal, called 'saturation'. Under this condition the scattering rate can be rewritten as

$$R_{\text{scatt}} \approx \frac{s_0}{1 + s_0}\frac{\Gamma/2}{1 + (2\delta/\Gamma')^2}, \tag{2.27}$$

where $\Gamma' = \Gamma\sqrt{1 + s_0}$ is the power-broadened linewidth of the transition. This effect of broadened linewidth at high laser power is called 'power broadening' [18], which is the result of shortening the lifetime of the upper level due to stimulated emission.

### 2.2.3 Absorption cross-section

During the interaction between atoms and laser light, absorption reduces the laser intensity while stimulated emission contributes to the light. The strength of the interaction is proportional to the intensity of the incoming light as well as the cross-section $\sigma$. The change of the laser light intensity at a small propagation distance $\Delta z$ can be calculated as

$$\Delta I(\omega) = -n_1 I(\omega)\sigma(\omega)\Delta z + n_2 I(\omega)\sigma(\omega)\Delta z, \tag{2.28}$$

where $n_1$, $n_2$ are the population of atoms in the ground and excited states, and we assume both absorption and stimulated emission have the same cross section. At the steady state, the absorbed energy must be equal to the emitted energy, which means

$$(n_1 - n_2)\sigma I = n_2 A_{21}\hbar\omega. \tag{2.29}$$

Additionally, the total number of the atoms is conserved $n = n_1 + n_2$, so

$$\sigma = \frac{\Omega^2/4}{(\omega - \omega_0)^2 + \Gamma^2/4}\frac{A_{21}\hbar\omega}{I}, \tag{2.30}$$

where $\Omega$ is Rabi frequency which can be written in terms of the laser intensity, $\omega$ is the laser frequency and $\omega_0$ is the atom energy transition frequency, in rad $\mathrm{s}^{-1}$. Thus,

$$\sigma = \frac{3\pi^2 c^2}{\omega_0} A_{21} g_L(\omega). \tag{2.31}$$

With the Lorentzian line shape function

$$g_L(\omega) = \frac{1}{2\pi}\frac{\Gamma}{(\omega - \omega_0)^2 + \Gamma^2/4}, \tag{2.32}$$

Eq. 2.28 can be written as

$$\frac{dI(\omega)}{dz} = -(n_1 - n_2)\sigma I(\omega). \tag{2.33}$$

For low laser intensity at the resonance frequency $\omega = \omega_0$, $n_1 = 1, n_2 = 0$, Eq. 2.33 can be further reduced to

$$\frac{dI}{dz} = -\sigma n I, \tag{2.34}$$

with $\sigma = 3\lambda^2/2\pi$. The transmitted light has intensity:

$$I = I_0 e^{-\sigma n z} \equiv I_0 e^{-OD}, \tag{2.35}$$

where $OD = n\sigma z$ is the optical density, or column density of the atomic cloud. This equation provides the baseline for absorption imaging. In an experiment of absorption imaging with strong laser power, one may also need to consider the saturation effects [63].

## 2.3 Atoms in a magnetic field

### 2.3.1 The magnetic dipole moment

The electron magnetic dipole moment of an atom comes from the orbital magnetic dipole moment $\vec{\mu}_L = -g_L\mu_B\vec{L}/\hbar$ which stems from the orbital motion of the electron, and the spin magnetic dipole moment $\vec{\mu}_s = -g_s\mu_B\vec{S}/\hbar$ which is intrinsic for an electron. The total magnetic dipole moment $\vec{\mu_J} = g_J\mu_B\vec{J}/\hbar$ results from both spin and orbital angular moment of the electron, which is related to the total angular momentum $J$.

The magnetic dipole moment in an externally produced magnetic field experiences a torque $\vec{\tau}$ as well as a force $\vec{F}_{\text{dipole}}$ from the magnetic potential energy $U$:

$$\begin{aligned} \vec{\tau} &= \vec{\mu} \times \vec{B} \\ U &= -\vec{\mu} \cdot \vec{B}. \end{aligned} \tag{2.36}$$

This torque leads to the precession of the angular momentum vector $\vec{J}$ about the external field axis $\vec{B}$. The precession frequency is given by the Larmor frequency

$$\omega = -\frac{eg_JB}{2m_e}. \tag{2.37}$$

In a strong magnetic field, the potential energy of a magnetic dipole becomes

$$U = M_J g_J \mu_B B. \tag{2.38}$$

Here we assume that the external magnetic field $\vec{B}$ is aligned along the z-axis of the atom such that $M_J$ takes value J, J-1, ..., 0, ..., -J+1, -J. The resulting force is then given by

$$\vec{F} = -\nabla U = -M_J g_J \mu_B \nabla B, \tag{2.39}$$

where atoms with states $M_J < 0$ are attracted to higher potential, they are called high-field-seeking (HFS) states. Atoms with $M_J > 0$ are attracted to lower potential,

and these states are called low-field-seeking (LFS) states. For the lithium-7 ground states, all the $^2S_{1/2}$ $F = 1$ magnetic hyperfine states are HFS, while the $^2S_{1/2}$ $F = 2$ state has mixed LFS ($M_J = -1, 0, 1, 2$) and HFS ($M_J = -2$) magnetic hyperfine levels. This arrangement can also be seen from the Zeeman shift in Fig. 2.1.

### 2.3.2 The Zeeman effect

The Zeeman effect is the splitting of spectral lines into several components when the atoms are subject to an external magnetic field. The resulting energy shift depends on the magnetic moment along the field axis and the field strength. Common treatment of the Zeeman effect depends on the strength of the external magnetic field as compared to the internal field which is involved in spin orbit coupling. When the external magnetic field is smaller than the internal field, the internal field dominates and the external field can be treated as a small perturbation to the Hamiltonian. Similarly, the external field dominates if it is larger than the internal field, then the internal field can be treated as a perturbation. The interaction part of the Hamiltonian is

$$H' = -(g_j \mu_B \vec{J} + g_I \mu_N \vec{I}) \cdot \vec{B}_{\text{ext}}, \tag{2.40}$$

where $g_J$ and $g_I$ are the Landé g-factors for the total orbital angular momentum and the nuclear spin, respectively.

For $B_{\text{ext}} \ll B_{\text{int}}$, the hyperfine coupling dominates and the good quantum numbers are: N, F, J and I. The energy level correction is then given by

$$\Delta E = \langle NFJI|H'|NFJI\rangle = \frac{e}{2m} B_{\text{ext}} \langle \vec{J} + \vec{I} \rangle = \mu_B g_F B_{\text{ext}} M_F, \tag{2.41}$$

where $\mu_B = \frac{e\hbar}{2m} \approx 9.274 \times 10^{-24}$ J T$^{-1}$ is the Bohr magneton, and $g_F$ is the Landé g-factor given by:

$$g_F = g_J \frac{F(F+1) + J(J+1) - I(I-1)}{2F(F+1)} - g_I \frac{m_e}{M} \frac{F(F+1) - J(J+1) + I(I-1)}{2F(F+1)}. \tag{2.42}$$

Here we assume that the external field is aligned along the z-axis such that $M_F$ takes values of F, F-1, ..., 0, ..., -F+1, -F.

For $B_{\text{ext}} \gg B_{\text{int}}$, the electron spin and the nuclear spin couple to the external field separately and F is no longer a good quantum number, and the energy shift will be

written as

$$\Delta E = \langle NJI|H'|NJI\rangle = (\mu_B g_J M_J + \mu_N g_I M_I)B_{\text{ext}}, \tag{2.43}$$

where the nuclear magneton $\mu_N \approx 5.051 \times 10^{-27}\ J \cdot T^{-1}$, which is more than 1000 times smaller than the Bohr magneton $\mu_B$, and is usually ignored in calculations. Here we also assume that the field is aligned along the z-axis where the $M_J$ takes the values of J, J-1, ..., 0, ..., -J+1, -J, and $M_I$ takes I, I-1, ..., 0, -I+1, -I. The ground state Zeeman splitting of lithium-7 is shown in Fig. 2.1.

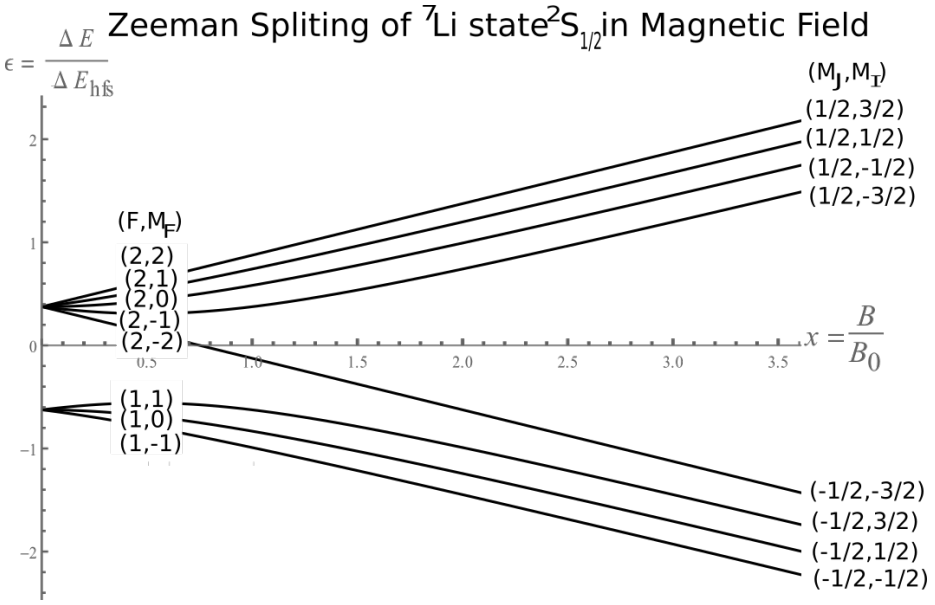


Fig. 2.1: Zeeman splitting of lithium-7 ground state. $\Delta E_{hfs}$ is the hyperfine level spliting of ground state $^2S_{1/2}$, $B_0 = \Delta E_{hfs}/(\mu_B g_J)$, given by Breit-Rabi formula.

## 2.4 Properties of lithium-7

### 2.4.1 Physical properties

Lithium is a soft silvery white alkali metal, it is the lightest metal and the lightest solid element under the standard conditions[1]. It is highly reactive with water and can easily be oxidized in air, so special care has to be taken when handling it. A list of the different physical properties are shown in Table 2.2.

[1]Defined since 1982 as: temperature of 273.15 K (0 °C) and absolute pressure $10^5$ Pa (1 bar) [78]

| Parameter | Value |
|---|---|
| Isotopes abundances | $^6Li$: 7.59%, $^7Li$: 92.41% |
| Atomic mass | $^6Li$: 6.015 u, $^7Li$: 7.016 u |
| Atomic radius | 1.82 $\mathring{A}$ |
| Melting Point | 453.65 K(180.5 °C) |
| Boiling Point | 1615 K (1342 °C) |
| Density | 0.534 g cm$^{-3}$ at 300 K |
| Electrical Resistivity | 92.8 n$\Omega$ m (20 °C) |

Table 2.2: List of lithium related physical parameters [27].

The vapor pressure of lithium [57] is given by

$$P = 10^{4.98821 - \frac{7918.984}{T - 9.52}} \quad \text{with } T \in [298.14, 1599.99]K, \tag{2.44}$$

where $P$ is the vapor pressure in bar, and $T$ is the temperature in Kelvin. Note that the melting point of lithium under standard pressure is 180 °C. Lithium has the highest vapor pressure among all alkali atoms. A plot of the vapor pressure of lithium as a function of temperature is shown in Fig. 2.2.

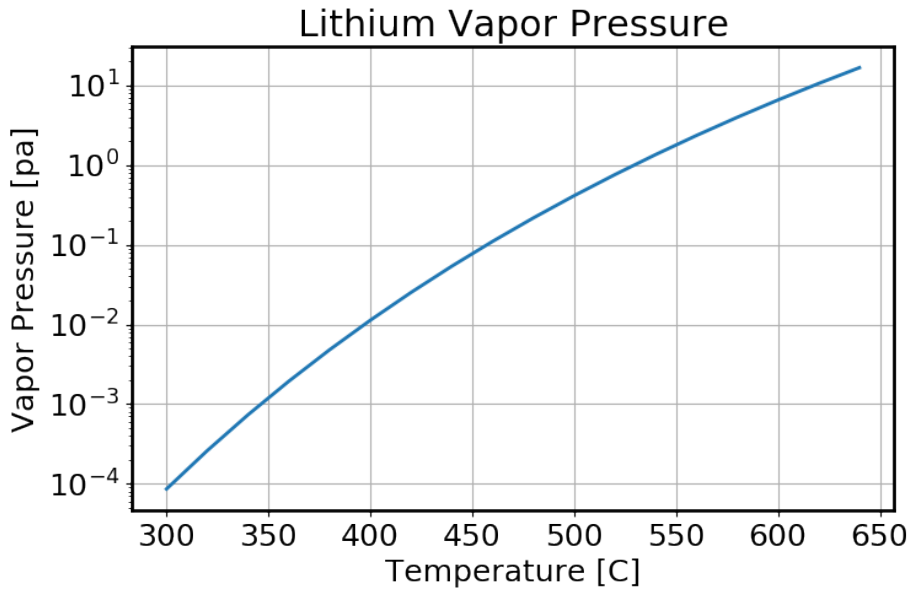


Fig. 2.2: Lithium vapor pressure at different temperatures, according to [57].

### 2.4.2 Atomic properties

The atomic properties of lithium-7 are listed in Table. 2.3. The energy levels under fine and hyperfine splitting are shown in Fig. 2.3.

| Parameter | Value |
|---|---|
| Atomic Number (Z) | 3 |
| Nucleons | 7 |
| Electron shell config. | $1s^2 2s^1$ |
| Ionization energy | 520 kJ/mol (5.4 eV) |
| Total Electron Spin (S) | 1/2 |
| Total Nuclear Spin | 3/2 |
| Electron spin g-factor ($g_s$) | 2 |
| Electron orbital g-factor ($g_L$) | 1 |
| Total spin g-factor $2^2S_{1/2}(g_J)$ | 2 [4] |
| Nuclear spin g-factor($g_I$) | -0.001182213 [4] |
| D Line Transition Wavelength | 671 nm |
| D1/D2 Line Natural linewidth | 5.87 MHz [77] |
| D1/D2 Life Time | 27.102 ns [77] |
| D1 Transition | $^2S_{1/2} \Rightarrow {}^2P_{1/2}$ |
| D2 Transition | $^2S_{1/2} \Rightarrow {}^2P_{3/2}$ |
| D1 Frequency | 446800132 MHz [31] |
| D2 Frequency | 446810184 MHz [31] |
| D1 Saturation Intensity ($I_{\text{sat}}$ D1) | 7.59 mW cm$^{-2}$ |
| D2 Saturation Intensity ($I_{\text{sat}}$ D2) | 2.54 mW cm$^{-2}$ |

Table 2.3: List of lithium-7 related atomic parameters

The lithium-7 D1, D2 lines result from the transitions between the ground state $^2S_{1/2}$ and $^2P_{1/2}$, $^2P_{3/2}$, respectively [31]. Various levels labeled by hyperfine quantum number $F$ split from the ground and excited states with their frequency shift noted. Each of these hyperfine states $F$ contains degenerate $M_F$ states with values $M_F = -F, -F+1, ..., 0, ..., F-1, F$ under the axis defined by the external magnetic field. Atoms interacting with resonant laser light experience a change in energy following the electric dipole transition selection rules, as listed in Table. 2.4.

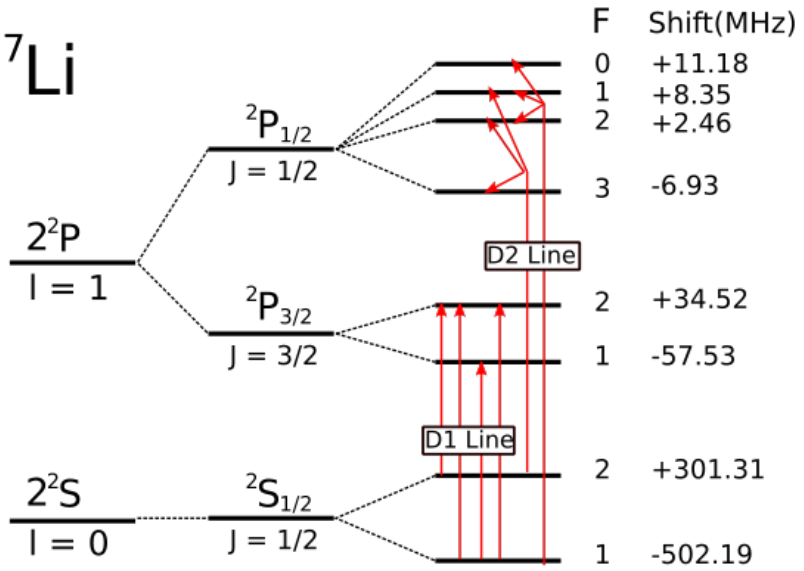


Fig. 2.3: Lithium-7 energy levels. Noted on the right are the hyperfine spliting level shifts in MHz [31].

| **Electric dipole transition selection rule** |
|---|
| Any $\Delta n$, $\Delta L = \pm 1$, $\Delta S = 0$ |
| $\Delta J = 0, \pm 1$ (exclude $J = 0 \Rightarrow J' = 0$), $\Delta M_J = 0, \pm 1$ |
| $\Delta F = 0, \pm 1$, $\Delta M_F = 0, \pm 1$, exclude $\Delta F = 0, \Delta M_F = 0$ |

Table 2.4: Electric dipole transition selection rules.

# Chapter Three: Laser system

In this experiment, we used a continuous-wave (CW) single mode diode laser for generating a reference light that was frequency stabilized to lithium-7 D line transitions, through a lithium vapor cell. In order to obtain higher laser power and frequency tunability, we used two tapered amplifier units, each of which was referenced separately to the reference laser. The output lasers of these two tapered amplifier are then used to manipulate the internal quantum states of atoms, control the atom dynamics and probe the atom distribution. For a typical atomic physics experiment, relevant physical properties pertaining to the laser include frequency, power, linewidth, tunability, and long-term stability. In this chapter, I describe the laser system we use, in particular the laser frequency stabilization, tuning and modulation. Additionally, I illustrate the optics design and setup.

## 3.1 Diode laser and tapered amplifier

### 3.1.1 External cavity diode laser

A laser light is generated by stimulated emission through a pumped gain medium with population inversion. Depend on its gain medium, there are generally four categories of lasers: solid-state laser, gas laser, liquid laser and semiconductor laser.

In our experiment, we use a commercial semiconductor laser (Toptica DL100). The free-running laser diode usually have a linewidth of almost 100 MHz, its emission frequency can be tuned by adjusting the current and temperature of the pn-junction. A commonly used approach for attaining narrow linewidth, great degrees of stability and tunability is an external cavity diode laser (ECDL) setup. A tunable ECDL is often composed of a laser diode chip with an anti-reflection (AR) coated facet, a diffraction-limited lens with a very short focal length, and a grating. The two most popular configurations of an ECDL, the 'Littrow' configuration and the 'Littman-Metcalf' configuration, are shown in Fig. 3.1.

The Littrow-ECDL of our reference laser is shown in Fig. 3.2. Light emitted from the front facet of the laser diode is collimated by the lens and then strikes

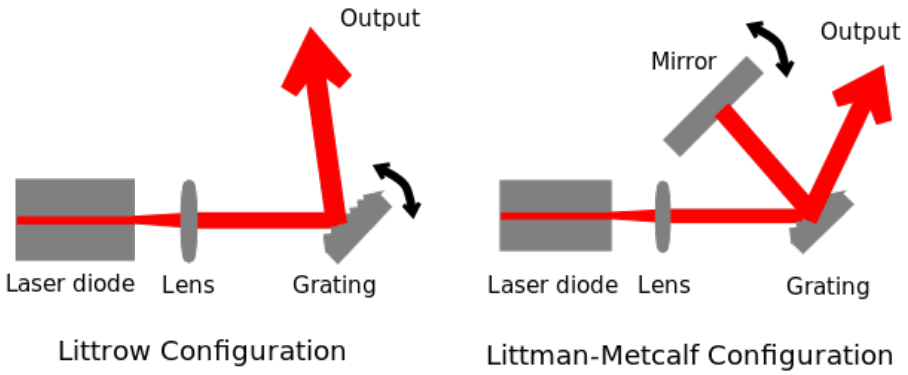


Fig. 3.1: The configurations of an ECDL.

the grating. The grating is adjusted in the 'Littrow' setup such that the first order diffraction of the grating is reflected back to the laser diode, thus adapted to the laser diode resonator mode. The resonator cavity is formed between the laser diode and the grating, this is referred to as the external cavity. This laser diode is first aligned to get a good forward optical path after reflection off the grating, then the angle of grating is coarsely adjusted close to the target frequency, followed by a fine adjustment of the grating with the piezoelectric transducer (PZT). The PZT is attached to the grating to enable the fine scanning of modulation of the laser frequency by an external voltage source, facilitating laser locking and frequency control. There are three main parameters of the laser which directly affect its frequency and stability: the laser diode current, the laser diode temperature and the grating angle.

Some advantages of the ECDL over a solitary laser diode include its narrow linewidth and wide tunability. Since the external cavity length (a few centimeters) of an ECDL is much greater than the internal cavity of a laser diode ($\approx$ 100 µm), the free spectral range (FSR) of ECDL is substantially smaller than a laser diode. Moreover, ECDL has a higher finesse. With these changes imposed by the external cavity, the linewidth can be reduced to about 100 kHz. However, after using several elements for optical manipulation, i.e. beam shaping, optical isolation and fiber coupling, the remaining optical power at our disposal is typically less than 10 mW. If one desires greater single-mode power, two choices are either a narrow-linewidth fiber laser with a low-noise fiber amplifier or a tapered amplifier. We chose the latter.

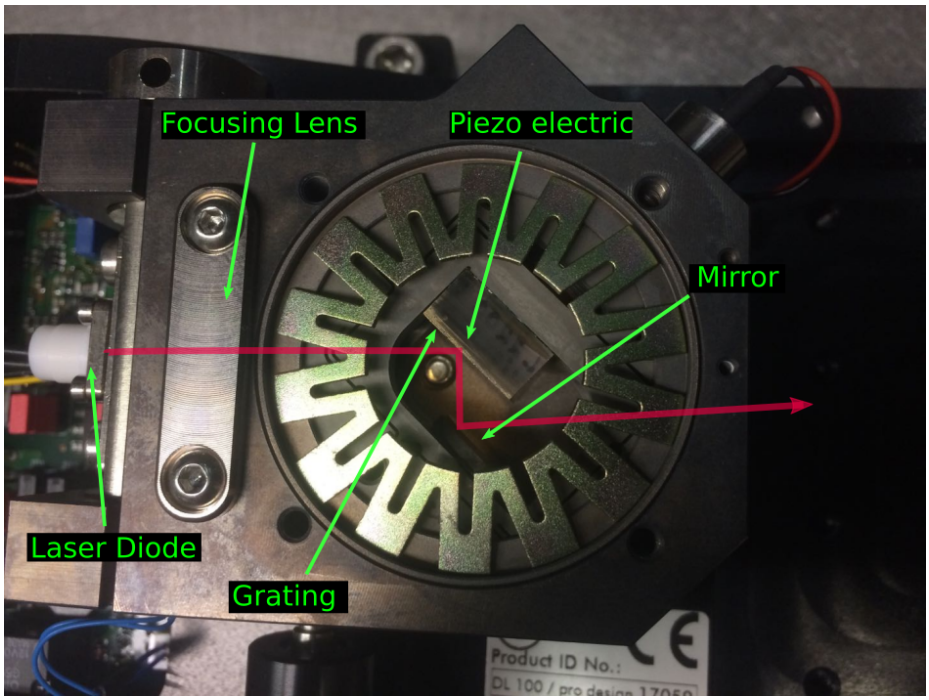


Fig. 3.2: The reference laser ECDL.

### 3.1.2 Tapered amplifier

A tapered amplifier (TA) is a unit which amplifies laser radiation to powers that would destroy the facets of normal laser diodes[1] while preserving the spectral properties of the master laser. A CW master laser is usually a diode laser with $\sim 10$ mW power that is used instead, called the 'master oscillator'. It's compact enough to have the whole amplifier units on a chip, as shown in Fig. 3.3.

In this experiment we use two TA units (Toptica TA pro) to provide laser sources with two different frequencies for different applications. It consists of a master oscillator for providing 'seed' laser and a tampered amplifier unit for amplification. The use of the TAs in our experiment benefits us in regard to two aspects: higher laser power and tunability while the laser is locked. A general schematic of our TA is shown in Fig. 3.3

[1] A typical laser diode with 5 mW output power has the emitting region of about 2 µm by 4 µm, which yields optical power density of 635 $\mathrm{W\,mm^{-2}}$. Damage to the facet usually occurs when optical energy density at the output facet exceed $10^4$ $\mathrm{W\,mm^{-2}}$

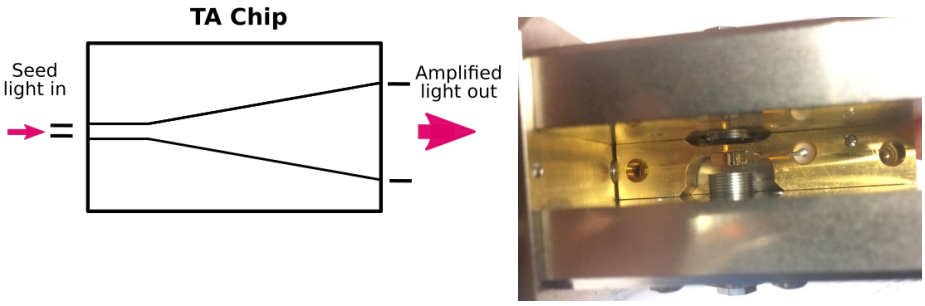


Fig. 3.3: The tapered amplifier (TA) chip.

## 3.2 Frequency stabilization

### 3.2.1 Frequency reference

In order to be used to measure and control atomic properties, a laser must be mode stabilized and have the appropriate frequency and power. Often, the aforementioned properties can be stabilized simultaneously through laser frequency locking. Generally, one refers to a known and stable frequency source, constantly compares the output laser frequency to the desired known frequency, and adjusts the parameters of the laser that control the frequency through a feedback loop. As the first step, a good frequency reference needs to be chosen. Common choices are: a resonant cavity, an atomic transition, or an already stabilized laser.

**Lock to a resonant cavity** Also called Pound-Drever-Hall (PDH) technique [16], which actively tunes the laser to match the resonance condition of a stable reference cavity. Typically, a Fabry-Perot cavity, which consists of two high-reflective mirrors separated by a spacer, is a convenient choice. Often, frequency modulation techniques are used to derive an electronic error signal that represents the deviations of the laser frequency from a given cavity reference fringe. One uses the electronic feedback to control the laser frequency and minimizes its deviations relative to the cavity fringe [85].

**Lock to an atomic transition** Naturally in atomic physics the transition of an atom is a great reference. The general idea is that if the laser frequency corresponds to that of a particular atomic transition, some fraction of the laser light will be absorbed when propagating through a gas of the atom or molecule in question. However, since

one has to heat up the atoms to generate the vapor when dealing with materials that are solid at room temperature, the absorption signal will be largely Doppler broadened due to the velocity spread of the atoms, typically from a few hundred MHz to a few GHz linewidth for dipole-allowed transitions [64, 118]. To eliminate the Doppler-induced line broadening and attain narrow linewidth, one has to apply a technique called saturated absorption spectroscopy [15], as discussed in Section 3.2.2. In this experiment, we are using this method to lock our spectroscopy laser.

**Lock to a stabilized laser** or beat-note lock [112], is a laser locking method used when referencing a laser to a different laser which is frequency stabilized by one of the above methods. This method is based on the measurement of the beat-note between lasers of the similar frequencies and of the aligned linear polarization. The advantage of this method is its simplicity, since one do not need to build a separate vapor cell or resonant cavity for each laser and only a fast photodiode and associated RF electronics are required. The disadvantage is, due to the nature of beat locking nature, the acquired frequency is shifted by some amount relative to the reference laser. Since in atomic physics there are many cases that off-resonant lasers apply, beat locking works naturally with these applications, e.g. MOT, molasses, etc. In our experiment, we use this method to lock our TA relative spectroscopy laser.

### 3.2.2 Saturated absorption spectroscopy

Saturated absorption spectroscopy, or Doppler-free spectroscopy, eliminates the Doppler broadening of observed linewidths in atomic spectra. Other broadening mechanisms, such as power broadening and collisions broadening, also contributes to a broadening of atomic transition linewidths above their natural linewidth.

Doppler broadened linewidths are typically on the order of a few hundreds of MHz to a few GHz in a vapor cell of alkali atoms, which sets a very rough limit on the resolution for optical spectroscopy. To understand how the Doppler effect influences spectroscopy, consider a single atom moving at speed $\vec{v}$ with respect to the direction of a photon with frequency of $f_0$. The atoms see a Doppler-shifted photon frequency as

$$f = f_0\left(1 \pm \frac{\vec{v}\cdot\hat{r}}{c}\right), \tag{3.1}$$

where $f_0$ is the frequency of photon, $\vec{v}$ is the velocity of atom, $\hat{r}$ is the unit vector indicating laser propagation direction and $c$ is the speed of light. For lithium 7 D

line transitions, the Doppler induced frequency shift is about 1.5 MHz for 1 $\mathrm{m\,s^{-1}}$ velocity.

If a group of vaporized atoms with Maxwellian distribution at temperature $T$ interact with a laser beam, the natural linewidth, will be Doppler-broadened to $\Delta$ as

$$\Delta = \frac{2\sqrt{2\ln 2} f_0}{c}\sqrt{\frac{k_B T}{m}}, \tag{3.2}$$

where $k_B \approx 1.38 \times 10^{-23}$ $\mathrm{J\,K^{-1}}$ is the Boltzmann constant, $T$ is the temperature of the atom cloud and $m$ is the mass of the atom. For a lithium cloud with temperature of 732 K, the D line transition is broadened to about 3.3 GHz, which is much larger than the D line natural linewidth of 5.87 MHz.

The general setup of saturated absorption spectroscopy is shown in Fig. 3.4.

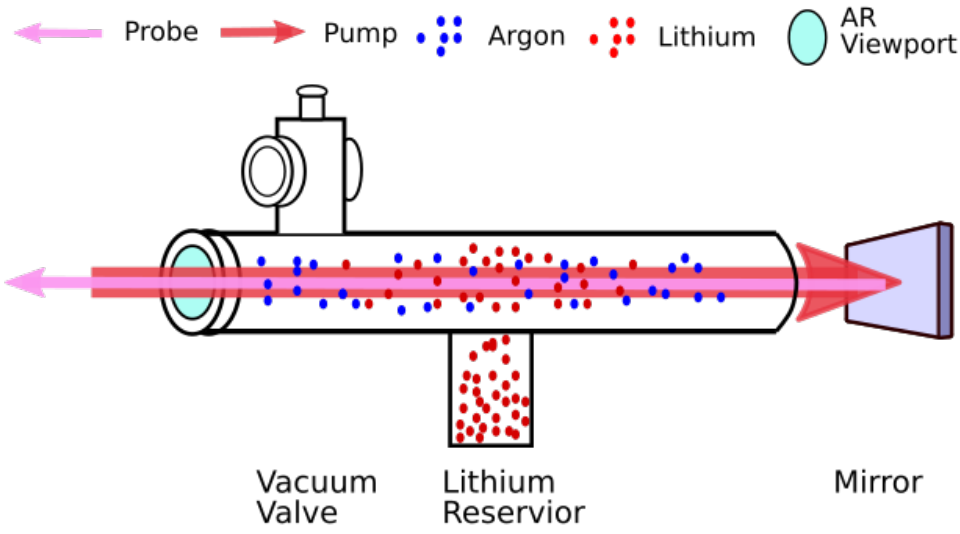


Fig. 3.4: A schematic of lithium cell for saturated absorption spectroscopy.

As seen in the figure, two counter-propagating beams from same laser were used as pump and probe beams. The frequency of laser beams is continuously scanned around the resonance frequency of the transition. A lithium cell is a "T" shaped vacuum chamber pumped down to 30 mTorr. Lithium atoms in the reservoir are heated to 450 °C (723 K) to produce a sufficiently high atom vapor density. High

purity argon is also mixed in the chamber as buffer gas to reduce the mean-free-path of the lithium atoms and thus avoid coating the viewports.

Without the pump beam, the probe beam will see the transition as broadened by the Doppler effect from the relative movement between the atoms and photons, as shown in Fig. 3.5. With the pump beam, the absorption signal from the probe beam has a narrow peak on top of the wide Doppler-broadened background which is the Doppler-free signal, called 'Lamb dip' [100].

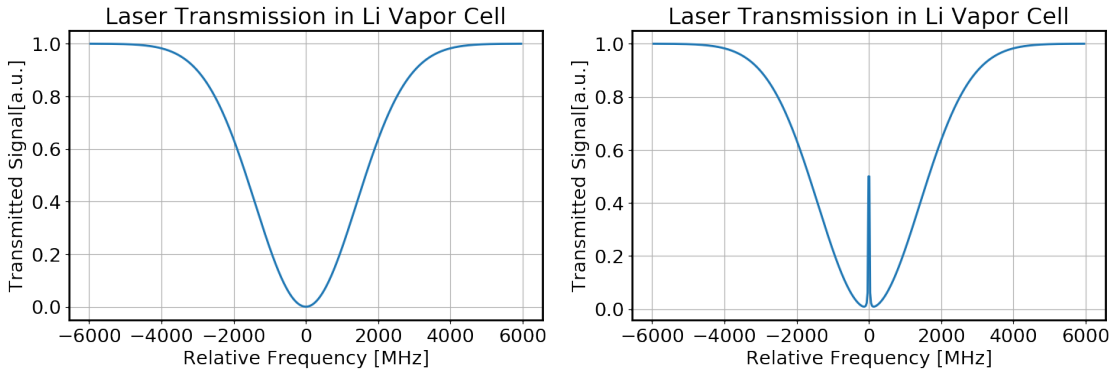


Fig. 3.5: Calculated Doppler-broadened absorption from lithium cell at 450 °C (left) and corresponding saturated absorption spectroscopy (right).

To understand the Lamb dip, let's consider following situations. First, if the laser frequency is slightly red detuned from resonance transition, atoms moving in the opposite direction of the laser with the appropriate velocity will see that red-detuned photons on resonance, due to the Doppler shift. However, for atoms moving parallel to the laser propagation direction, the light is blue shifted. Second, if the laser frequency is right exactly on resonance, only atoms with zero velocity will strongly absorb the photons of the pump beam, the transition will be saturated with laser intensity above the corresponding saturation intensity. In turn, the weaker probe beam will not get absorbed by the saturated atoms, resulting in a reduced absorption and, equivalently, a dip in the absorption signal. This dip has the width that is equal to the natural linewidth of the transition. This small Lamb dip is then detected by a photodiode and used for locking the laser. The linewidth of Lamb dip is given by power-broadened homogeneous linewidth [100]

$$\Delta f = \Gamma\sqrt{1 + I/I_{\text{sat}}}, \tag{3.3}$$

where $\Gamma$ is the linewidth, $I_{\text{sat}}$ (as in Eq. 2.24) is that saturation intensity for the same transition and $I$ is the laser intensity.

Note that if the laser frequency is scanned through a range that covers two or more resonant transitions, an extra peak or dip will appear beside the resonance lines, called cross-over, which is discussed in Section 3.2.4.

### 3.2.3 Frequency modulation spectroscopy

The saturated absorption signal detected by the photodiode provides information regarding the relative frequency between the laser and the atomic transition. This absorption signal must be converted to an error signal in order to frequency stabilize the laser with a PID controller in a feedback loop. A simplified schematic of FM spectroscopy is shown in Fig. 3.6.

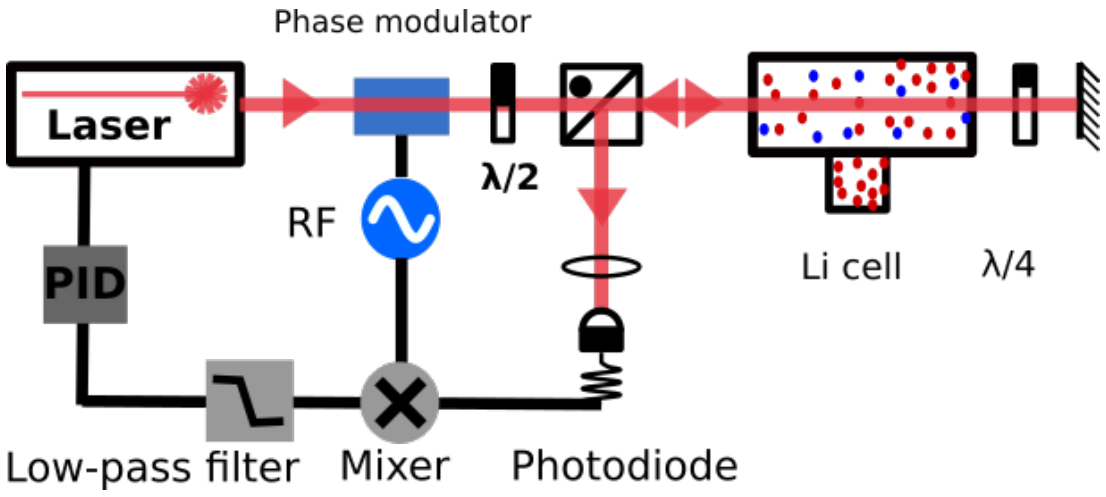


Fig. 3.6: The schematic for frequency modulated spectroscopy.

A general procedure of generating and locating the error signal for our reference laser is described below:

First, one has to tune to within a few GHz of the targeted atomic transition. This can be achieved by coarse tuning either the angle of grating from the ECDL or the current of laser diode. In the mean time, a wavemeter or a Fabry-Perot cavity should be used to monitor the laser frequency and make sure it is single mode.

Second, to determine how far off resonance the laser frequency is from the atomic transition, the PDH technique can be used to generate an additional high frequency

modulation of the phase, which is done by externally modulating the laser diode current with a low amplitude sine wave. Let $E_0 e^{-i\omega_0 t}$ describe the unmodulated original laser, where $\omega_0$ is the laser frequency. If we add phase modulation by a sine wave of $\beta \sin(\omega_m)$, with modulation frequency $\omega_m$ and modulation depth $\beta$, the modulated photon electric field can be

$$\begin{aligned} E_i &= E_0 e^{i[\omega_0 t + \beta \sin(\omega_m t)]} \\ &= E_0 e^{i\omega_0 t}[J_0(\beta) + 2iJ_1(\beta)\sin(\omega_m t)] \\ &= E_0[J_0(\beta)e^{i\omega_0 t} + J_1(\beta)e^{i(\omega_0+\omega_m)t} - J_1(\beta)e^{-i(\omega_0-\omega_m)t}]. \end{aligned} \quad . \tag{3.4}$$

Here one can see that rather than the original unperturbed laser frequency $\omega_0$, there are two more frequencies located at $\omega_0 \pm \omega_m$, called sidebands.

Now let's consider this laser light passing through the atom vapor. Two effects, absorption and phase shift, depending on the frequency, can be formulated as

$$T_{0,\,1,\,-1}(\omega) = \exp(-\kappa_{0,\,1,\,-1} - i\phi_{0,\,1,\,-1}), \tag{3.5}$$

where the indices $0, 1, -1$ denote the main frequency and sidebands, respectively. $\kappa$ is the absorption coefficient and $\phi$ denotes the phase shift. Taking this into account, Eq. 3.4 can be rewritten as

$$E = E_0[T(\omega_0)J_0(\beta)e^{i\omega_0 t} + T(\omega_0+\omega_m)J_1(\beta)e^{i(\omega_0+\omega_m)t} - T(\omega_0-\omega_m)J_1(\beta)e^{i(\omega_0-\omega_m)t}]. \tag{3.6}$$

However, the electric field is not measured directly by the photodiode. Rather, the power, or equivalently, intensity, $P = \|E\|^2$ is detected. For small modulation depth $\beta$, expanding out the power term, we have:

$$\begin{aligned} P_{\mathrm{PD}} = {} & P_c\|T(\omega_0)\|^2 + P_s(\|T(\omega_0+\omega_m)\|^2 + \|T(\omega_0-\omega_m)\|^2) && \text{[DC term]} \\ & + 2\sqrt{P_c P_s}[T(\omega_0)T^*(\omega_0+\omega_m) - T^*(\omega_0)T(\omega_0-\omega_m)]\cos(\omega_m t) && \text{[Amplitude term]} \\ & + 2\sqrt{P_c P_s}Im[T(\omega_0)T^*(\omega_0+\omega_m) - T^*(\omega_0)T(\omega_0-\omega_m)]\sin(\omega_m t) && \text{[Phase term]} \\ & + O(2\omega_m) \end{aligned} \quad , \tag{3.7}$$

where $P_c$ and $P_s$ are the power of the carrier and sideband components, respectively. As shown, the signal detected by photodiode is consists of many parts: a DC component from the carrier, two components oscillating at the modulation frequency $\omega_m$ from the sidebands, and higher order components from the interaction terms between the sidebands.

The oscillating parts of the above formula contains an amplitude term with $\cos(\omega_m t)$ and a phase term with $\sin(\omega_m t)$. Their line shape is shown in a calculation in Fig. 3.7, at a large modulation frequency of $\omega_m = 75$ MHz. The amplitude and phase plot both show three peaks: one from main transition and two sidebands. When locking the laser to a stable reference frequency, one would not want this modulation frequency to be too large. For this reason, when implementing this method, the modulation frequency is chosen to be very small ($\omega_m \ll 1$ MHz). In turn, only a tiny fraction of the main peak on Fig. 3.7 is generated and the sidebands do not show up. In order to generate the full profile of the absorption signal, we modulate the laser PZT linearly such that this tiny modulating is added on top of periodical ramp at large frequency scale.

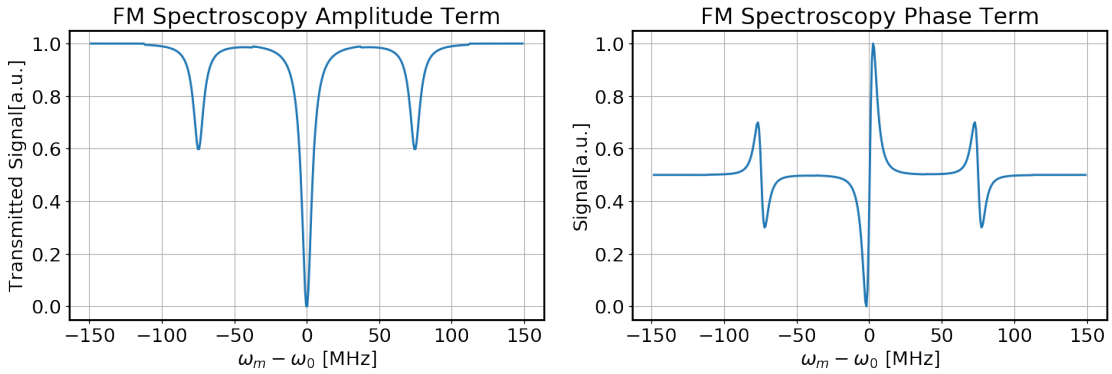


Fig. 3.7: The amplitude and phase term of frequency modulation spectroscopy signal. Three peak are from one main peak two sidebands. Calculation with large modulation frequency $\omega_m = 75$ MHz for demonstration purpose.

At this point, one unanswered question is which part of the signal should be chosen for locking the laser. To gain the ability to use the PID to lock to the resonant frequency, one can either choose the intensity term (the '$\cos(\omega_m t)$' term) or the phase term (the '$\sin(\omega_m t)$') term. Preferably, a point where the signal is most sensitive to a small deviation is beneficial, which lead us to the phase component.

Another question is how to extract the phase related signal. For this step, we have to rely on the PDH technique. For a reasonably fast modulation frequency, the imaginary component with $\sin(\omega_m t)$ will dominate, which allows us to extract the phase information. The signal from photodiode is mixed with the original modulation signal $\beta \sin(\omega_m t)$, which will result in a DC component and a frequency doubled

component. By using a low-pass filter, we can get

$$err = 2\sqrt{P_c P_s} Im[T(\omega_0)T^*(\omega_0 + \omega_m) - T^*(\omega_0)T(\omega_0 - \omega_m)]. \tag{3.8}$$

Finally, once we generated the error signal for a single frequency with a small range, expanding it to larger range is not hard. To do this, a periodic frequency ramping modulation is added to the laser. This is done through modulating the voltage of the piezo behind diffraction grating, which yields a frequency change up to hundreds of MHz. A graphical demonstration of this process the near resonant a transition is shown in Fig. 3.8

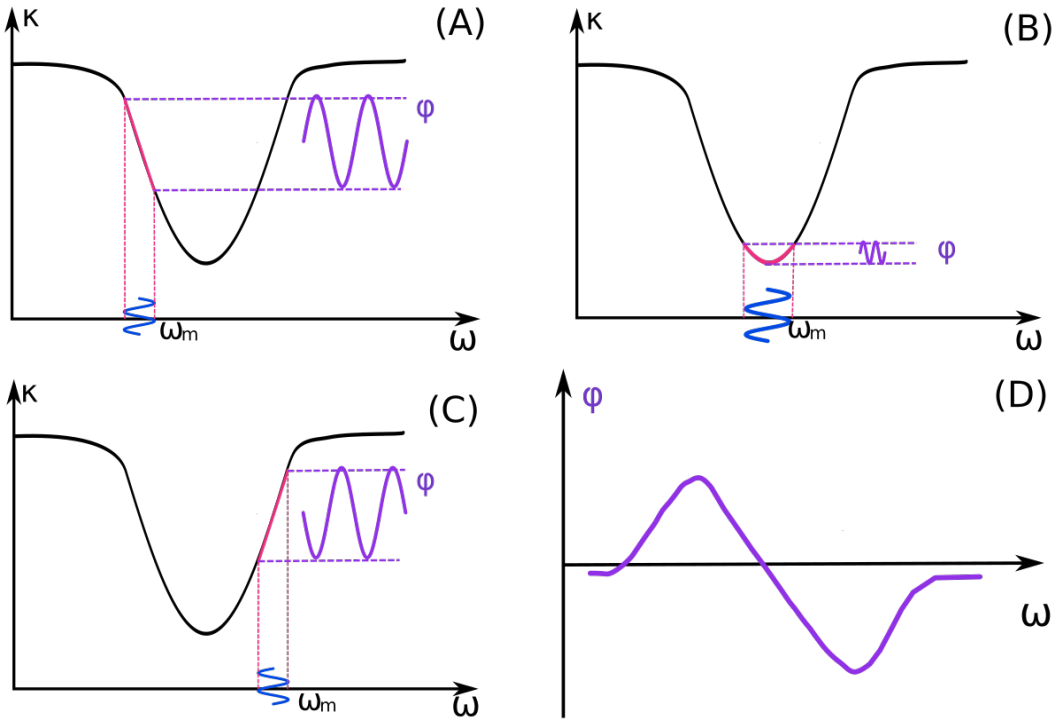


Fig. 3.8: Demonstration of frequency modulation on top of grating piezo modulation. (a) $\sim$ (c) shows small frequency modulation at different offset induced by piezo controlled grating angle. (d) shows the amplitude for different frequency offset.

To avoid skewing the error signal, a linear ramp from either a triangle or a sawtooth wave is used, as shown in Fig. 3.9

In our system, we can get about 500 MHz frequency scan range by modulating the piezo with a 1 $V_{\text{pp}}$ signal. This modulating voltage is controlled such that a

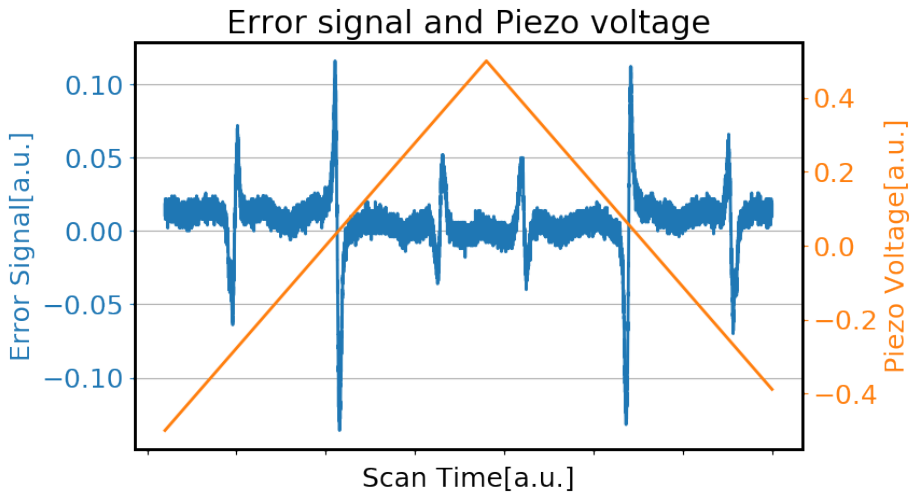


Fig. 3.9: An example of the error signal and piezo voltage for reference laser, on the lithium-7 D2 line.

wide enough range is covered to guarantee us to see both $F = 1$ and $F = 2$ ground hyperfine states of lithium 7. The repetition rate of the scan is kept low (5 Hz) so that it is within the RF circuit responding bandwidth.

After above three steps, we were able to generate the error signal for the lithium 7 D2 line, over a range of a few GHz, which results in an error signal as shown in Fig. 3.10. Note that the excited state of $^2P_{3/2}$ is not resolved.

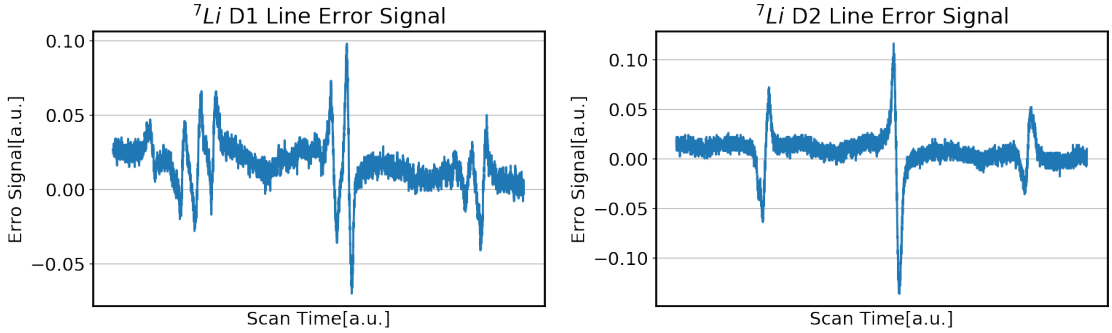


Fig. 3.10: Lithium-7 error signal for D1 (left) and D2 (right) line.

### 3.2.4 Error signal

One may notice from Fig. 3.10 that we have three phases dispersion peaks, which, from left to right, corresponding to the ${}^2S_{1/2}, F = 1 \rightarrow {}^2P_{3/2}$, crossover, ${}^2S_{1/2}, F = 2 \rightarrow {}^2P_{3/2}$ transition.

The crossover feature is a very interesting feature in saturated absorption spectroscopy, two details about the crossover feature are significant: first, the crossover signal is right at the middle of the two 'real' signals; second, it has an opposite slope compare the other two and is larger than the other two 'real' transitions.

To explain the first observation, let's consider the case where the laser frequency is exactly at the middle of the two real transitions. According to the saturated absorption spectroscopy, the atoms at zero velocity won't generate Lamb dip signal. However, atoms moving towards the pump laser with certain velocity will see it blue-shifted and become resonant through the ${}^2S_{1/2}, F = 1 \rightarrow {}^2P_{3/2}$ transition. In the mean time, the same atom will also see the probe beam as red-shifted and become resonant through the ${}^2S_{1/2}, F = 1 \rightarrow {}^2P_{3/2}$ transition. Therefore, these atoms may be resonant with both the pump and probe beams simultaneously through two different transitions. Since the crossover signal is from the atom groups with specific positive and negative velocities, it is usually larger than the normal 'real' transition.

The second observation, the opposite slope of the crossover signal, is actually only true when the cross over happens in the situation that there are two ground states and only one excited state. The slope of the crossover signal will flip sign if instead there are two excited states but only one ground states within the scanning range of laser, as shown in Fig. 3.11

In the situation that there are multiple ground and excited states within the scanning range of laser, the error signal can be more complicated and include multiple crossovers between different combinations of transitions, such as the D1 line in lithium-7, shown in Fig. 3.10.

### 3.2.5 Beat lock technique

Once a particular laser is frequency stabilized, its frequency can be used to lock other lasers through beat lock technique. The general idea is that if one can measure and stabilize a small frequency (less than or on the order of 100 MHz) differences

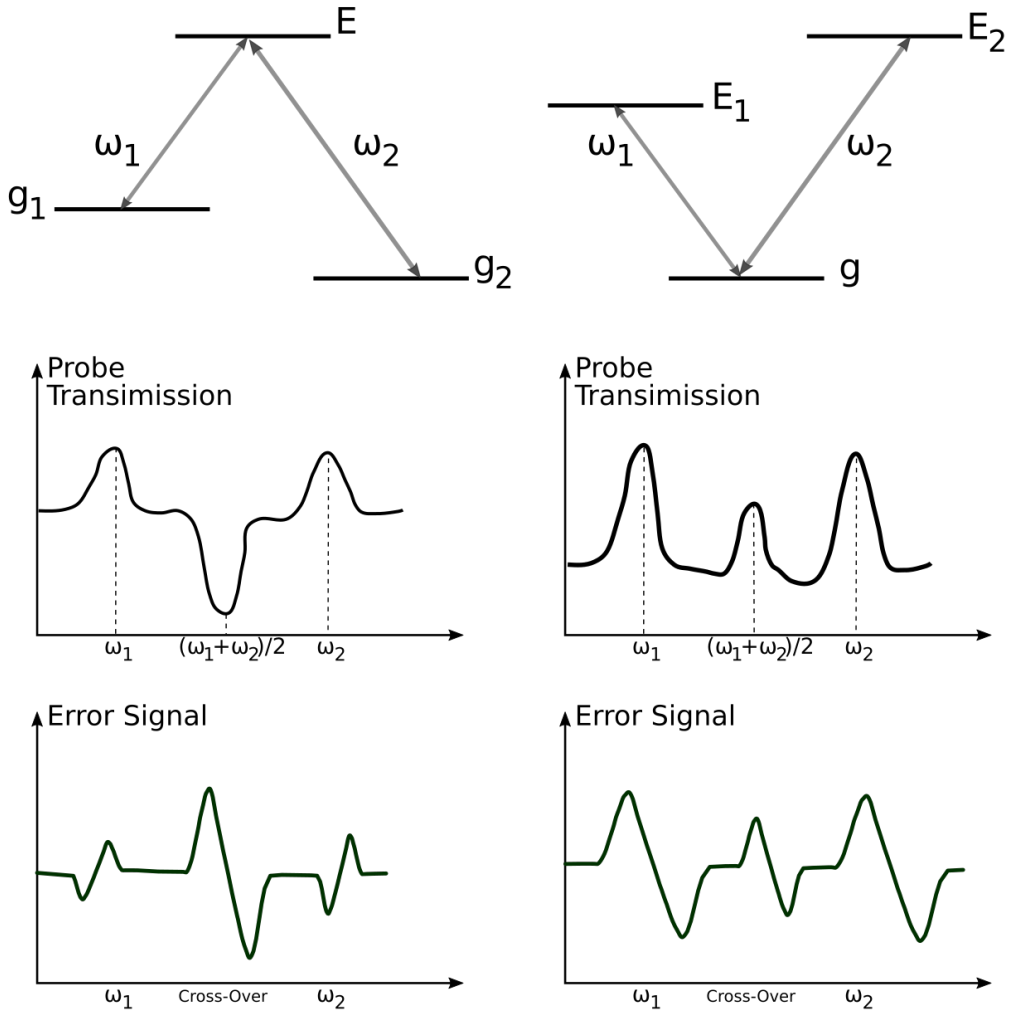


Fig. 3.11: Demonstration of error signal line shape for different energy level configurations. Top: energy level configurations. Middle: transmitted probe laser intensity from saturated absorption spectroscopy. Bottom: line shape of error signal.

between lasers, one can use if for locking. The beat note provides a useful measure of this difference.

Beats between two waves happen when the two waves are of similar frequencies, while equal polarization and comparable amplitudes. The same is true for two lasers: one has to tune the frequency of the second laser to the frequency of the reference laser, ensure that their polarization is aligned and that their intensities are of the same order. A general set up is shown in Fig. 3.12

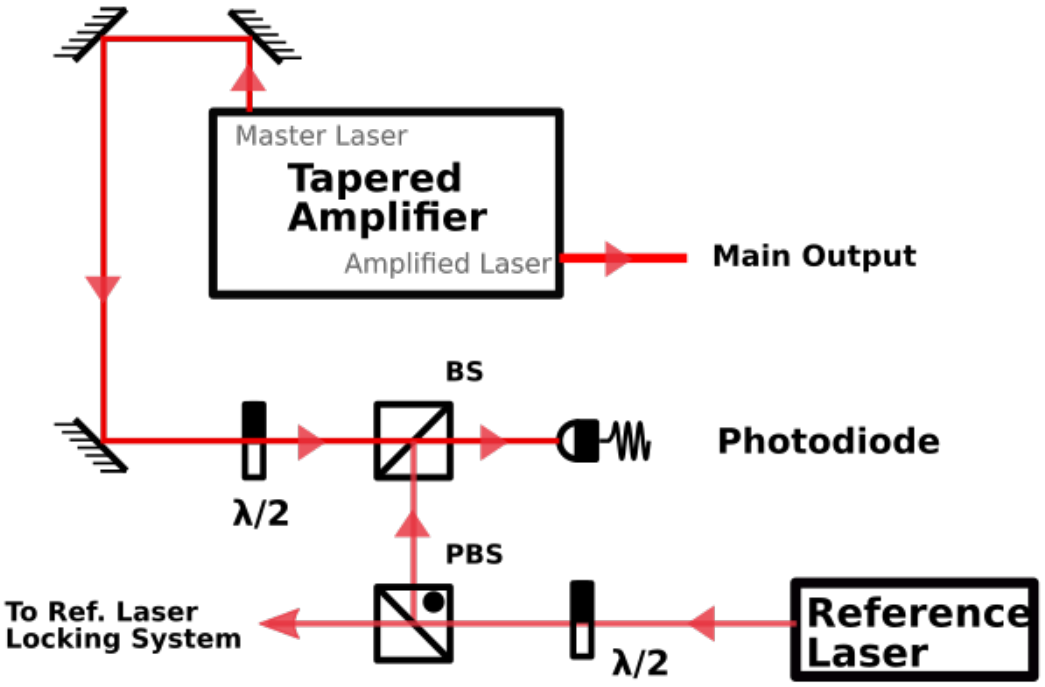


Fig. 3.12: Schematic of the beat lock setup between the reference laser and tapered amplified.

The linearly polarized laser beams from the already locked reference laser and TA seed laser are merged using a non-polarizing beam splitter cube. The half-wave plate (HWP) on one branch is used to adjust the polarization of that laser beam so that it matches the other laser. The photodiode must have a large enough bandwidth to cover the range of the beat frequency. In our case, we are interested in the frequency difference between the two lasers in a range of $20 \sim 150$ MHz, we are using a fast photodiode (Thorlabs PDA 10A) to provide a bandwidth of hundreds of MHz.

Note that, due to the nature of beat locking, one would never get the second laser locked to exactly the same frequency as the reference laser, thus additional frequency shifting devices like acoustic optical modulators (AOM) are needed after the output of the beat locked laser.

The next step is convert the photodiode signal to lockable error signal, with flexibility to tune the frequency difference while both lasers are locked. One important

feature of the beat signal is that there are two frequency components

$$\cos(w_1 t) + \cos(w_2 t) = 2\cos\left(\frac{w_1 + w_2}{2}t\right)\cos\left(\frac{w_1 - w_2}{2}t\right). \tag{3.9}$$

One can extract the component of the frequency difference term by applying a low-pass filter. Based on this property, a series of RF electronic devices can be used to generate the error signal, as shown in Fig. 3.13, where the phase detection is the same as the one used for reference laser locking.

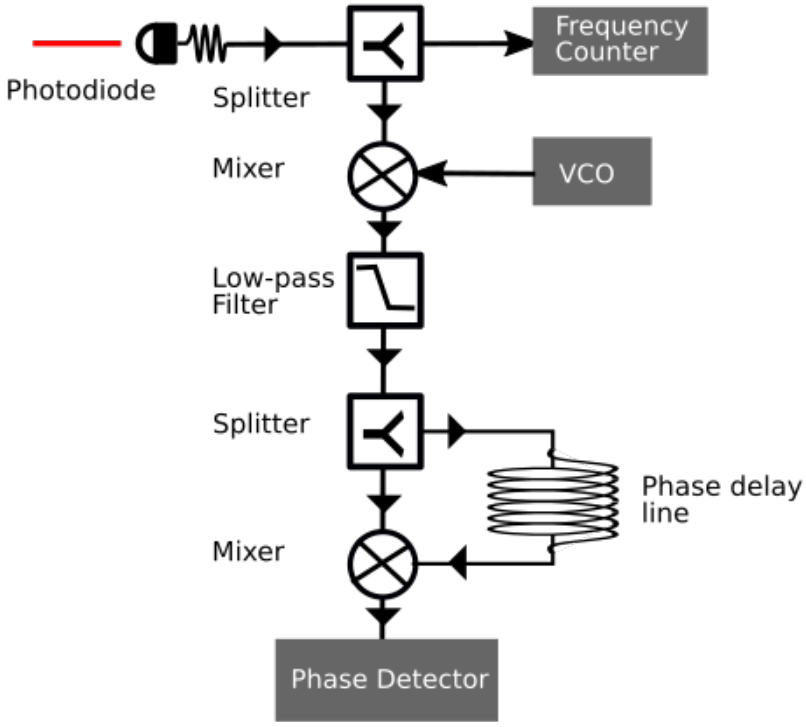


Fig. 3.13: Schematic of the beat lock RF processing setup.

The photodiode acts naturally as a low-pass filter for the beat signal, due to its limited bandwidth of a few hundred MHz. Thus, the result signal from photodiode only has frequency component $\|f_{\text{ref}} - f_{\text{TA}}\|$. The voltage signal is fed to a splitter (Minicircuit ZDC-10-1) to extract a small portion for real time monitoring of the frequency difference between the two lasers using a frequency counter (Universal Frequency Counter 1992). To achieve tunability while the laser is locked, the main part of the signal is then connected to a mixer (Minicircuit ZAD-1+) to multiply it with an external RF signal from a voltage controlled oscillator (VCO, Minicircuit

ZOS-150+, $75 - 150$ MHz). The mixed signal is then passed through a low pass filter to extract the low frequency component. At this point, the signal becomes $\|f_{\text{ref}} - f_{\text{TA}} - f_{\text{VCO}}\|$, which is the value we want to stabilize.

Similar to the way we lock the reference laser, the seed laser frequency is also modulated coarsely by grating piezo voltage and finely by the laser diode current. The error signal generated is shown in Fig. 3.14.

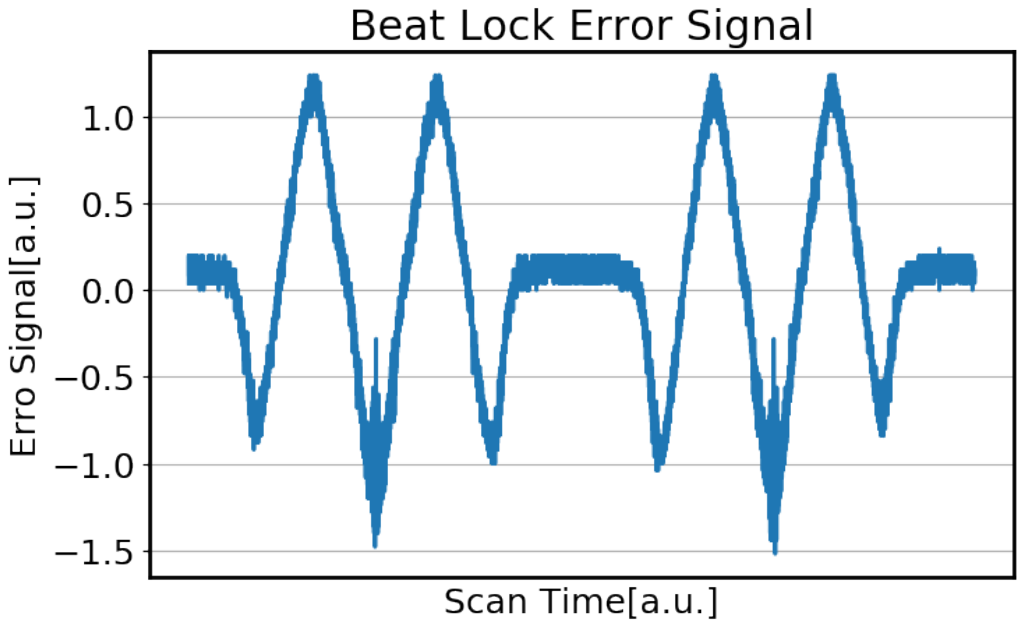


Fig. 3.14: Beat lock error signal.

### 3.2.6 Optics layout

For an overview of our optics setup, there are a total of three lasers: the reference laser, TA-MOP, and TA-MOT. A list of locking method and the light source frequency is shown in Table 3.2.6.

The output light from the two TAs are further modified by a series of optics for frequency adjustment, beam shaping, coupling, and more. A simplified schematic is shown in Fig. 3.15.

Generally, we are using an electo-optic modulator (EOM) to add sidebands to the TA-MOT laser at frequencies for both pump and repump transitions. This branch of the laser system is used for optical molasses, chirped slowing and MOT. TA-MOP

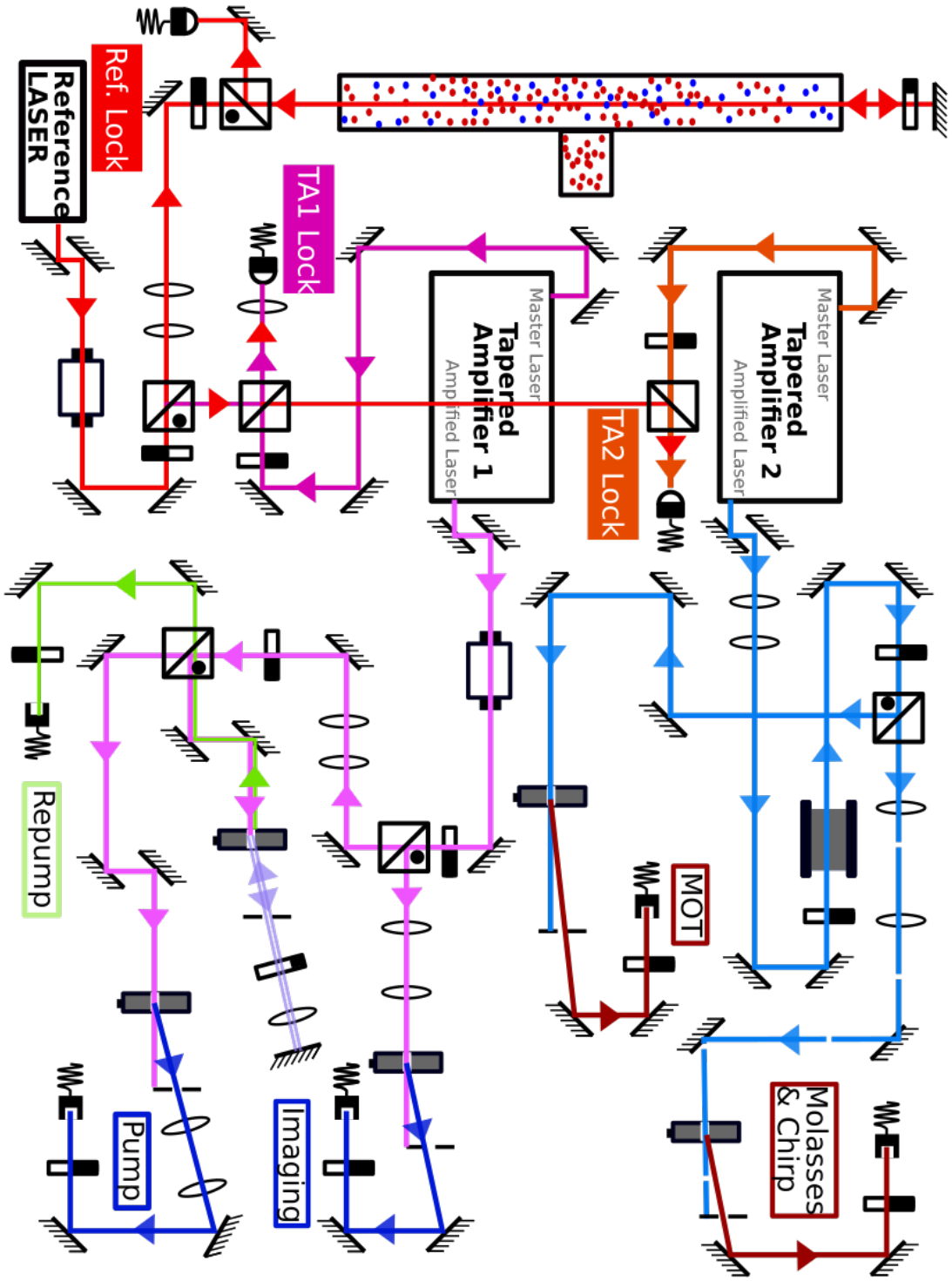


Fig. 3.15: Optics layout.

| Laser | Detune | Locking Method | Reference | Power |
|---|---|---|---|---|
| Reference | 0 MHz | SAS* | Lithium Cell | 15 mW |
| TA-MOT | + 80 MHz | Beat lock | Reference Laser | 400 mW |
| TA-MOP | - 80 MHz | Beat lock | Reference Laser | 400 mW |

Table 3.1: List of laser source properties of the experiment. The detune is referenced to the lithium-7 D2 line $^2S_{1/2} \rightarrow {}^2P_{3/2}$. Note the frequency and the power listed are at the output of the laser, in the experiment extra optics were used to modify the frequency as well as the power. Among all three lasers, the frequency detune of the reference laser is always fixed, while the detunes of the other two TAs are adjustable using a VCO while they are locked.
$*$: Saturated Absorption Spectroscopy.

is used to provide the above pump and repump lasers separately, also with tunable frequency and switchable power. A list of these parameters can be found in Table 3.2.6.

| Laser Source | Detune | Application |
|---|---|---|
| TA-MOT | 0 MHz, -803 MHz | Molasses, Chirp, MOT |
| TA-MOP | 0 MHz, -803 MHz | Optical pumping, imaging |

Table 3.2: Laser frequencies used in the experiment after passing through all the modification optics. Detune is referenced to the pump frequency (Lithium 7 D2 transition $^2S_{1/2} \rightarrow {}^2P_{3/2}$). The two frequency component in the laser from TA-MOT branch is generated by EOM sidebands, thus is in a single laser beam, while the frequencies of the laser from TA-MOP branch correspond to two separate single-frequency laser beam produced by an AOM.

## 3.3 Frequency modulation

### 3.3.1 Laser sideband generation with EOM

For experiments with optical molasses, chirped slowing, and MOP, a single laser beam with both pump and repump frequencies is required. While one can merge two laser beams with different frequencies using a non-polarizing beam splitter (BS), we choose to use a 813 MHz EOM to generate the sideband with the laser beam at pump frequency, as shown in Fig. 3.15.

An EOM is an electro-optical device used for phases modulation, the same method we used to do frequency modulation to get generate an error signal in saturated absorption spectroscopy for laser locking. Basically an RF signal drives a crystal to generate time-dependent birefringence to add a modulated phase term to the light field. In turn this generates frequencies sidebands with the same frequency shift from the carrier frequency as the driving frequency of the EOM. The amplitude of each component is described by a Bessel function, as shown in Eq. 3.6. The EOM we are using is a QUBIG EO-Li7-3M, which provides tunable frequency from 633 MHz to 843 MHz. A list of key parameters of this EOM can be found in Table 3.3.1.

| | |
|---:|---|
| Resonant frequency | 633 - 843 MHz |
| Bandwidth | 2.7 MHz |
| Quality factor | 301 |
| RF power for 1 rad @ 671 nm | 24.6 dBm |
| Max. RF power | 1 W |
| Aperture | 3 x 3 mm |
| AR coating | 630 - 1100 nm |

Table 3.3: List of important EOM properties.

Before we started using EOM, a series careful measurement and calibration were performed with a scanning Fabry-Perot cavity[2]. A schematic of the test setup is shown in Fig. 3.16. A FLUKE 6060B RF signal generator is used as the RF source, which is then amplified by an amplifier (Minicircuits ZHL-42) to provide power up to about 28 dBm ($\approx$ 630 mW). The Fabry-Perot has a piezo to modulate the cavity length, which is driven by a sawtooth-shaped RF signal.

Initially, we calibrated the RF power sent to the EOM to ensure that it does not exceed the power limit of the EOM. This is done with a calibrated RF source and an RF power meter (Minicircuits RF power meter). A plot of the input and output powers for the RF generator and power amplifier is shown in Fig. 3.17.

Once the power is calibrated, a series of measurement using the Fabry-Perot on the light passing through the EOM was performed. First, the light incident on the EOM has to be linearly polarized and its polarization has to be aligned with specific axis to the EOM. This was accomplished by adjusting the HWP in front of EOM while monitoring the signal output from the EOM on an oscilloscope. The optimal

[2]Parameters of the Fabry-Perot Cavity: 671 nm, FSR = 1.5 GHz, cavity length = 5 cm, con-focal

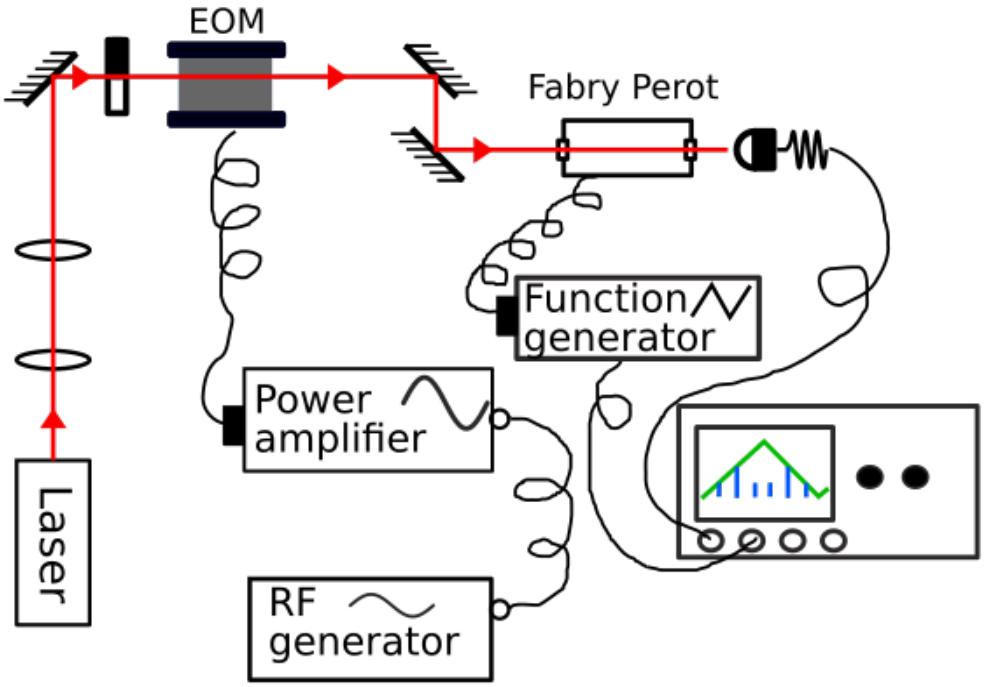


Fig. 3.16: EOM test setup.

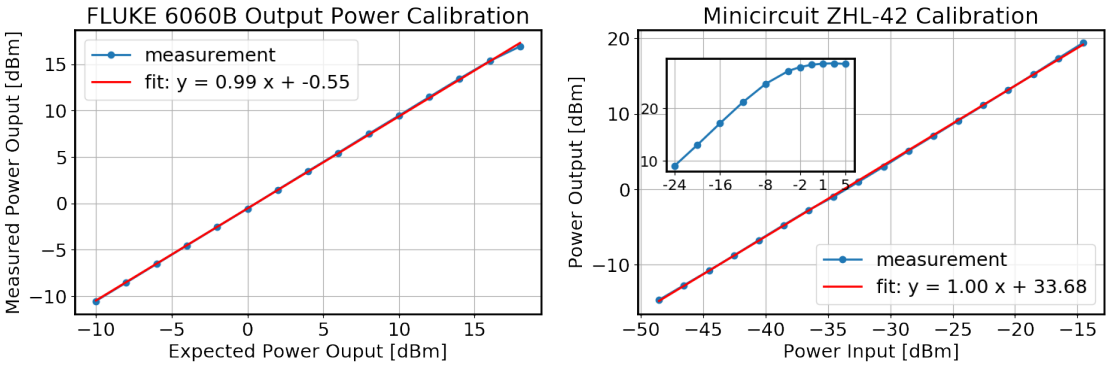


Fig. 3.17: EOM RF System Power Calibration.

.

point is the one maximizes the intensity ratio between 1st order sideband and carrier at low modulation depth ($\beta < 1$ rad).

Second, the modulation depth $\beta$ is optimized by simply scanning the input RF power around theoretical value. The relationship between modulation depth and the carrier-to-sideband ratio is shown in Fig. 3.18.

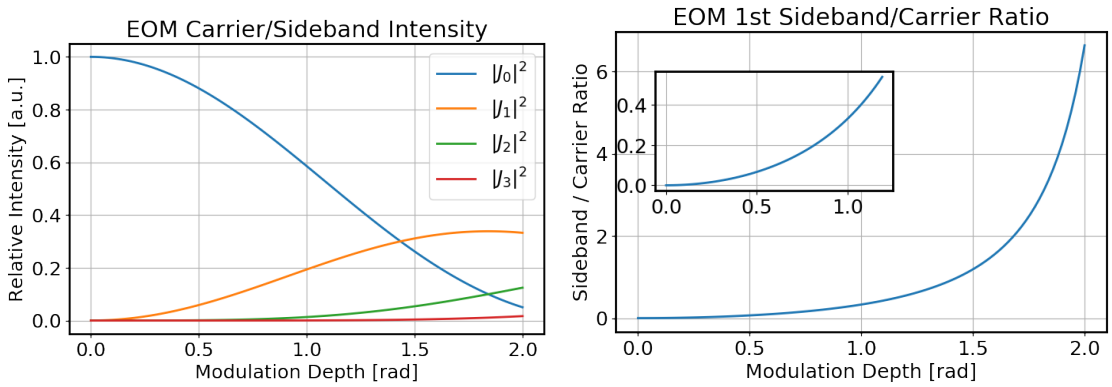


Fig. 3.18: EOM sideband/carrier relative intensity and ratio.

.

In our experiment, we choose the modulation depth to be around $\beta \approx 1$ rad to keep primarily the carrier and 1st order sideband. Under this modulation depth the 1st order to carrier intensity ratio is 0.33. An example of the Fabry-Perot output is shown in Fig. 3.19.

Multiple measurement similar to 3.19 were performed and a Python script was used to automatically detect and extract carrier / sideband peaks. The ratio between 1st order sideband and carrier peak height is then plot along with expected values from the Bessel function, as shown in Fig. 3.20.

### 3.3.2 Laser frequency chirping

Although desirable for cold atom experiments, the relatively slow spontaneous decay rate $\gamma = 5.6$ MHz of the D line transition and the high temperature required to produce a lithium beam make it a relatively difficult atom to slow. In our experiment, we use our magnetic decelerator to reduce most of the kinetic energy of supersonic lithium beam from $\approx 500\ \mathrm{m\,s^{-1}}$ to $50\ \mathrm{m\,s^{-1}}$. Laser frequency chirping is then used to further slow down the atoms to be trapped in a MOT.

For atom with mass $m$ slowed by a resonant laser beam, the maximum scatter rate for a laser far above the saturation intensity is given by $\gamma_p = \gamma/2$. From this one can derive the maximum deceleration from Doppler cooling as

$$a_{\max} = \frac{\hbar\omega\Gamma}{2m} = \frac{\pi\hbar\gamma}{m\lambda}, \tag{3.10}$$

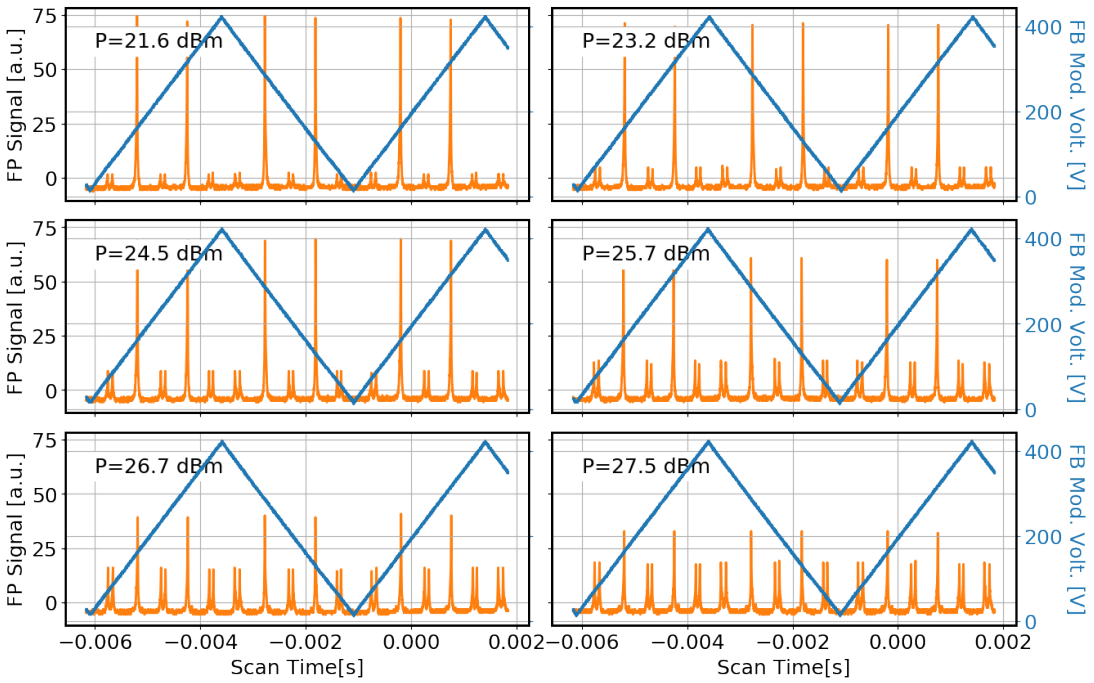


Fig. 3.19: The EOM spectrum measurement with the Fabry-Perot, under different power input to EOM. Blue line: Fabry-Perot output signal, yellow line: modulation signal sent to the Fabry-Perot.

where $\hbar$ is reduced Planck constant, $\omega = 2\pi\nu$ is laser frequency in radians, $\Gamma = 2\pi\gamma$ is the natural linewidth in rad/s and $\lambda$ is the laser wavelength. For lithium, $a_{\max} \approx 1.6 \times 10^6\ \mathrm{m\,s^{-2}}$. With this acceleration, the distance required to stop an atom with initial most probable velocity at $v_0 = \sqrt{2k_bT/m}$ (assume Maxwell-Boltzmann distribution) is given by

$$L_{\min} = \frac{v_0^2}{2a_{\max}} = \frac{k_bT_{||}\lambda}{\pi\hbar\gamma}, \tag{3.11}$$

where $k_b$ is the Boltzmann constant and $T_{||}$ is the atom beam temperature along the propagation direction. The required laser chirping frequency range can be calculated as

$$\delta\nu = \frac{v_0}{\lambda} = \frac{1}{\lambda}\sqrt{\frac{2k_bT}{m}}. \tag{3.12}$$

In combination with the deceleration time $\delta t_{\min} = v_0/a$, the maximum slew rate $R_f$ of the laser frequency is

$$R_{f_{\max}} = \frac{\delta\nu}{\delta t_{\min}} = \frac{a_{\max}}{\lambda} = \frac{\pi\hbar\gamma}{m\lambda^2}. \tag{3.13}$$

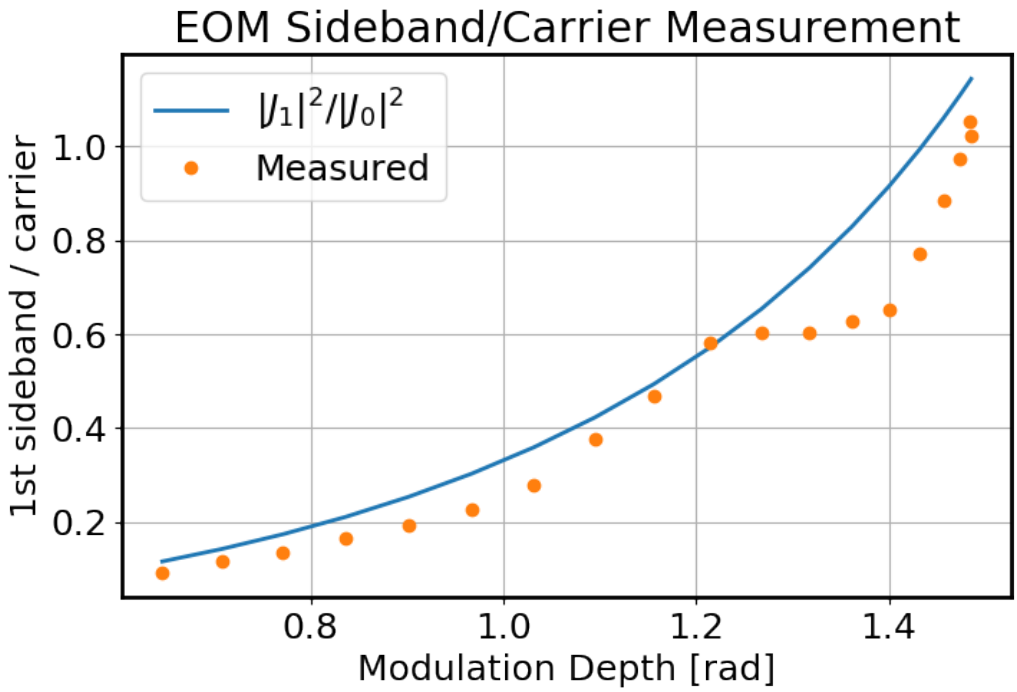


Fig. 3.20: Measured 1st sideband/carrier ratio, along with calculation according to Bessel function.

We achieve chirping of our laser without losing the locking point in two steps: first, a TTL signal is sent to the PID controller to set it on hold; second, the voltage of the TA master laser piezo is quickly modulated with a constant slew rate for the chosen starting and ending values. The TTL for holding the PID has to be larger than the piezo modulation time window, as shown in Fig. 3.21.

## 3.4 Laser transfer and fiber coupling

To gain flexibility in our laser transfer and space usage, we use multiple fibers to guide laser from our optical table to our experiment apparatus. There are two things we took special care of when using single-mode, polarization-maintaining (PM) fibers.

First, the laser power on the input end of fiber should not exceed the intensity limit of the fiber, which can be calculated by using provided power limit and fiber mode field diameter.

Second, and most importantly, in order to have a good power and polarization

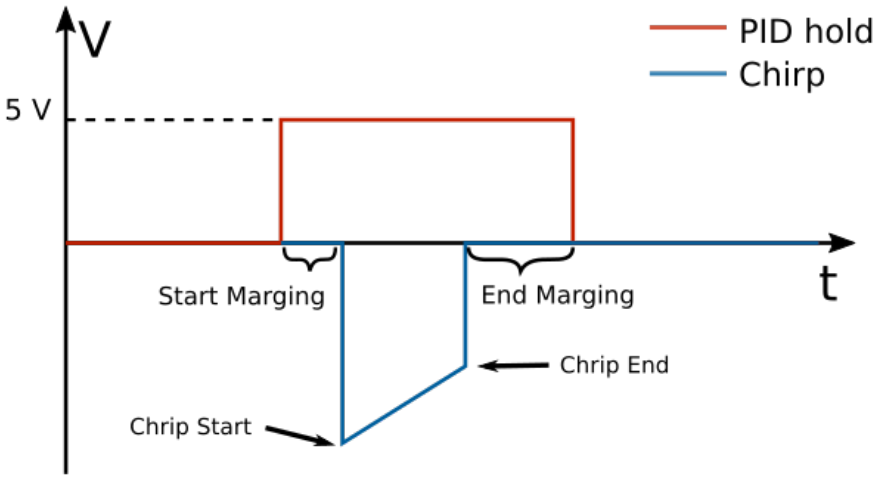


Fig. 3.21: Timing plot for chirping and PID.

.

stability from the output end of the fiber, single mode PM fibers have to be coupled with laser light polarization parallel to either the slow or fast axes. The slow axis of panda type PM fiber is usually marked by an alignment key on the fiber end. At the early stage of our fiber coupling, we noticed that the polarization fluctuated a lot due to small vibrations of the fiber, which is especially obvious if one has a polarizing beam splitter (PBS) after the output end of the fiber.

As a careful alignment of laser polarization to the fiber axis is needed, here I briefly describe the procedure and measurement we went through to gain a good stability. The experiment setup is pictured in Fig. 3.22.

As shown in the Fig. 3.22, a HWP is put in front of the input end of the fiber to allow adjustment of the polarization. The QWP is used to correct ellipticity of the polarization. If one already knows that the input laser is linearly polarized, then the QWP on the schematic is not necessary. On the output end, a PBS and a photodiode is set up acting as a polarization checker. An iterative procedure was taken to find the optimal angle for the HWP at the input end:

- Slight shake the fiber at any position to observe AC signal change on the oscilloscope.

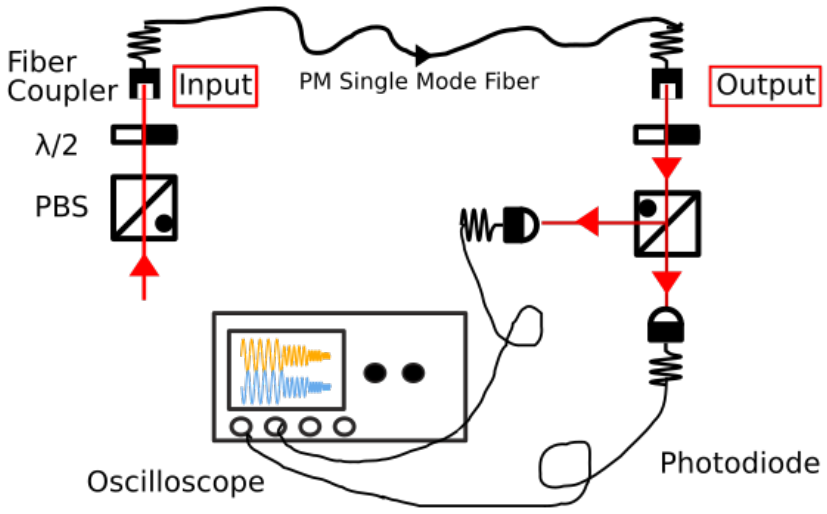


Fig. 3.22: Setup for fiber coupling optimization.

.

- Rotate the HWP by a small angle ($\sim$ 5 deg), then repeat previous step.
- Repeat above two steps until the AC signal doesn't appear to change compared to not shaking of the fiber.

An example of our observations from two photodiodes after PBS are shown in Fig. 3.4.

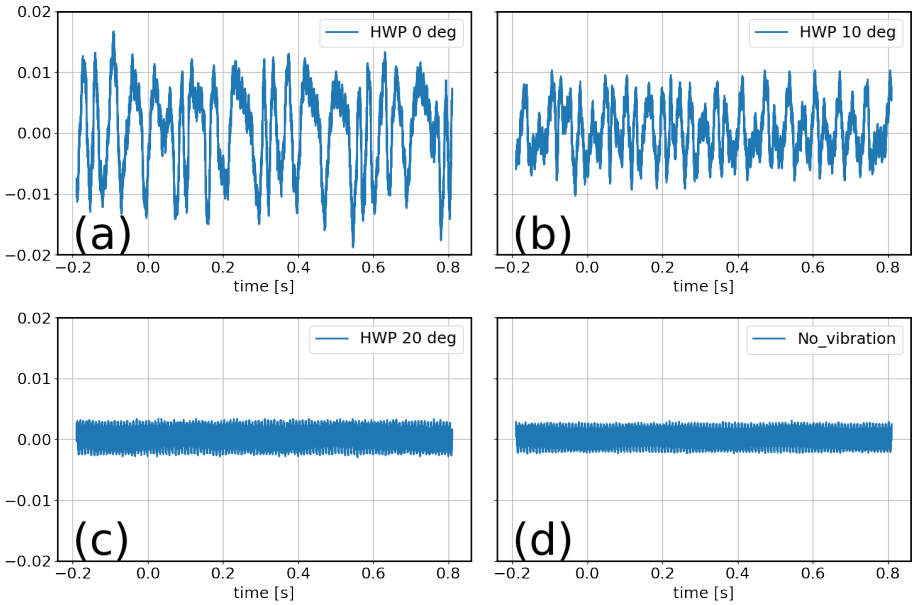


Fig. 3.23: Photodiode signal from fiber output after PBS. One can see (a) a lot of AC noise in the signal, which means when shaking the fiber the polarization changes significantly. By tuning the HWP at the input end of fibe, as seen in (b) and (c), the situation improved and the output light is almost immune to fiber vibrations, just like (d) when fiber is not shaked.

# Chapter Four: Supersonic beam and entrainment

Our journey towards cold atom physics starts with the atom source. Cold atomic and molecular beams have a long history [102] of being used for precision spectroscopy [108], collision studies [47], chemical reactions [111], and many other areas [67]. Generally, the small thermal velocity of a cold atom beam has the benefit of reducing the Doppler broadening in any Doppler sensitive measurement. Two most important characteristics, high-flux and low temperature, make a cold atom beam an ideal source for many studies that require reduced statistical uncertainty as well as narrower linewidth. Additionally, atom beams have been used as successful sources for cold atom studies [70].

The first optical confinement of atoms was realized using a pulsed evaporated atomic beam source produced by irradiation of a pellet of sodium metal with a nanosecond high power Nd-YAG laser, followed by chirped laser deceleration to further reduce the speed of atom beam for trapping [25]. Later the same methods were used to load a magneto-optical trap (MOT) [99]. Low-pressure cesium vapor has also been used as source to directly load a low-field magnetic trap [83]. A widely used method to generate atom vapor is passing current through an atom dispenser [10]. Similar methods of generating atom vapor also include light-induced atomic desorption [7]. Another popular way is using a thermal atomic beam generated by a heated oven and a series of collimation slits, with the Zeeman slower [96]. More recently, room temperature rubidium vapor has been used to directly load a MOT on a chip [97].

Since their development in the 1990s, pulsed supersonic nozzles [50] provide a great source for the cold atom community. Their high beam flux as well as low transverse beam temperature are a big advantage of this method over others. One pulsed nozzle design was developed by Uzi Even in the early 2000s, called 'Even-Lavie valve' [41], which generates beams with tight collimation, high intensity and low temperatures.

While the Even-Lavie valve performs very well with atoms and molecules that stay in gas phase at cryogenic temperatures, the low temperature of the beam is further limited by the condensation or clustering [58]. This limits the use of the Even-Lavie valve to only certain species. Additionally, the velocity of the supersonic beam relative to the lab frame adds another challenge in its application towards trapped

atoms. We try to address these two challenges with new approaches. First, we explored a method to seed interesting species like lithium into a carrier gas generated by Even-Lavie valve. Second, a 3D magnetic decelerator is built to reduce the beam speed from about 500 $\mathrm{m\,s^{-1}}$ to 50 $\mathrm{m\,s^{-1}}$.

Our aim in this part of the experiment is to generate a supersonic lithium beam, with high flux and low temperature. However, lithium by itself is a solid and thus cannot be used to generate supersonic beam by a nozzle, let alone at cryogenic temperatures. Our approach is to use an element that stays gaseous even at extremely low temperatures (<77 K) as a supersonic 'carrier'. We then seed the carrier gas with our 'payload', the lithium atoms. We call the process 'entrainment'. Noble gases are good candidates for the entrainment stage as well as for the decelerator stage since they are not paramagnetic. Through a series of experiments we want to find a set of parameters such that we can generate a bright supersonic lithium beam with relatively low translation speed.

In this chapter, the supersonic beam generated by an Even-Lavie valve is discussed. I describe the experiment we have done to explore the beam proprieties with different elements. With Helium as the carrier gas, we further explored the methods of seeding lithium atoms to form a supersonic lithium beam. The characterization of the resulting lithium beam is also explored.

## 4.1 Beam from Even-Lavie valve

### 4.1.1 Overview

When high pressure gas expands through an aperture into vacuum, usually there are two types of beams that may form: an effusive beam and a supersonic beam, depending on the ratio of the mean free path $\lambda$ of the particles to the nozzle opening diameter $D$.

An effusive beam is formed when $\lambda \gg D$, or the mean free path of the atoms is much larger than the orifice diameter. The resulting beam undergoes an expansion without collisions between the particles, thus it maintains identical velocity distribution as the gas in the reservoir and the temperature do not change from the expansion. This kind of beam follows the well-known Maxwell-Boltzmann velocity distribution.

A supersonic Beam is the counterpart of an effusive beam, when $\lambda \ll D$, or the mean-free-path is much shorter than the opening size of the nozzle, the atoms will undergo several collisions during the expansion. This results in a supersonic beam, usually with longitudinal speed being higher than the speed of sound at the same temperature. Intuitively, more atoms will escape the nozzle from collisions that convert the transverse velocity component to the longitudinal velocity. Thus, the atoms in the beam end up with a high longitudinal velocity but a narrower velocity distribution. This effectively leads to the cooling of the beam.

An illustrative comparison of the velocity distribution between an effusive and a supersonic beam is shown in Fig. 4.1. The velocity distribution is calculated for an effusive and a supersonic nozzle at a temperature of 100 K. The resulting velocity of the effusive beam covers a broad range with the same temperature as the nozzle, while the velocity distribution of the resulting supersonic beam undergoes a narrow peak at a higher mean velocity, which corresponds to a temperature of 100 mK, as also shown from the measurement on Fig. 4.11.

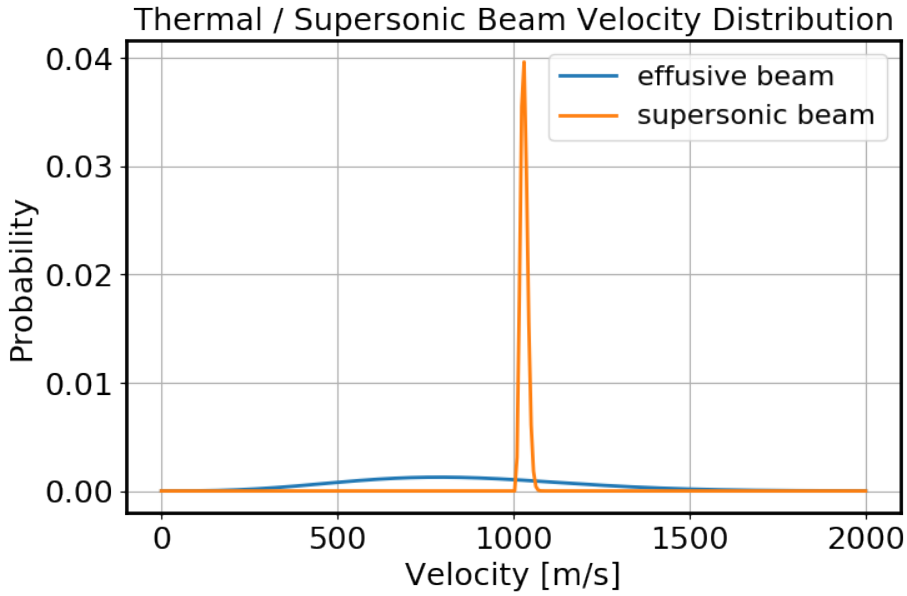


Fig. 4.1: An illustrative comparison of velocity distribution for thermal and supersonic helium beam resulting from a nozzle temperature of 100 K. Calculation based on the Maxwell-Boltzmann beam distribution.

Supersonic nozzles have been applied successfully to generate cold and isolated

molecules since the 1980s, originally with continuously operated nozzles [11,43], later with pulsed operation [8], at ambient or elevated temperatures. The development of pulsed valves enabled a remarkable increase in the achieved beam intensity while not exceeding the required pumping capacity of the vacuum system. More recently, the development of the fast acting valves with a duty cycle less than 20 µs enabled the use of higher pressures, which yields improvement in the beam directionality, cooling, and brightness [42,61]. Further cooling the nozzle with a cryocooler to lower temperatures helps reduce the beam temperature as well as it translation speed [41]. Having a cold and slow beam is crucial for conducting our experiment.

There is a large range of pulsed valves that produce a supersonic beam, such as the Jordan valve [46], the Even-Lavie valve [41], the Nijmegen pulsed valve [126], and the piezo-actuated valves [65]. The properties of the produced molecular beams vary. We chose the Even-Lavie valve because it is compact, works at cryogenic temperatures ($> 10$ K) and produces short pulses (5 µs $\sim$ 100 µs).

The general structure of an Even-Lavie valve is shown in Fig. 4.2. A high-current pulse ($\sim$ 500 A) generates a magnetic field of about 2.5 T at the coil center, which pulls and releases the paramagnetic high speed hammer in as short as 10 µs, with accurate control over the valve opening time. The short opening time of the valve results in a short pulse of atoms through the 100 µm opening. This nozzle can be operated at a repetition rate up to 1 kHz. The body of the valve is made of copper in order to facilitate operations down to 10 K.

Typically, a skimmer located a few hundreds of nozzle diameters downstream is also implemented. The skimmer further reduces the beam transverse temperature and provides collimation by throwing away those hot atoms that are located at the outer part of the beam. The skimmer is 5 mm in diameter, located 17 cm downstream from the nozzle opening and is held at ambient temperature. A recent study from our collaborator Edvardas Narevicius has shown that the beam can be brightened by shock-wave suppression through cooling the skimmer to low temperatures [105].

### 4.1.2 Cooling mechanism and terminal velocity

Let's look into the thermodynamic mechanism behind the low temperature of the supersonic beam. From the aspect of thermal energy, the process of beam expansion of a high pressure nozzle can be approximated as an adiabatic and isotropic process

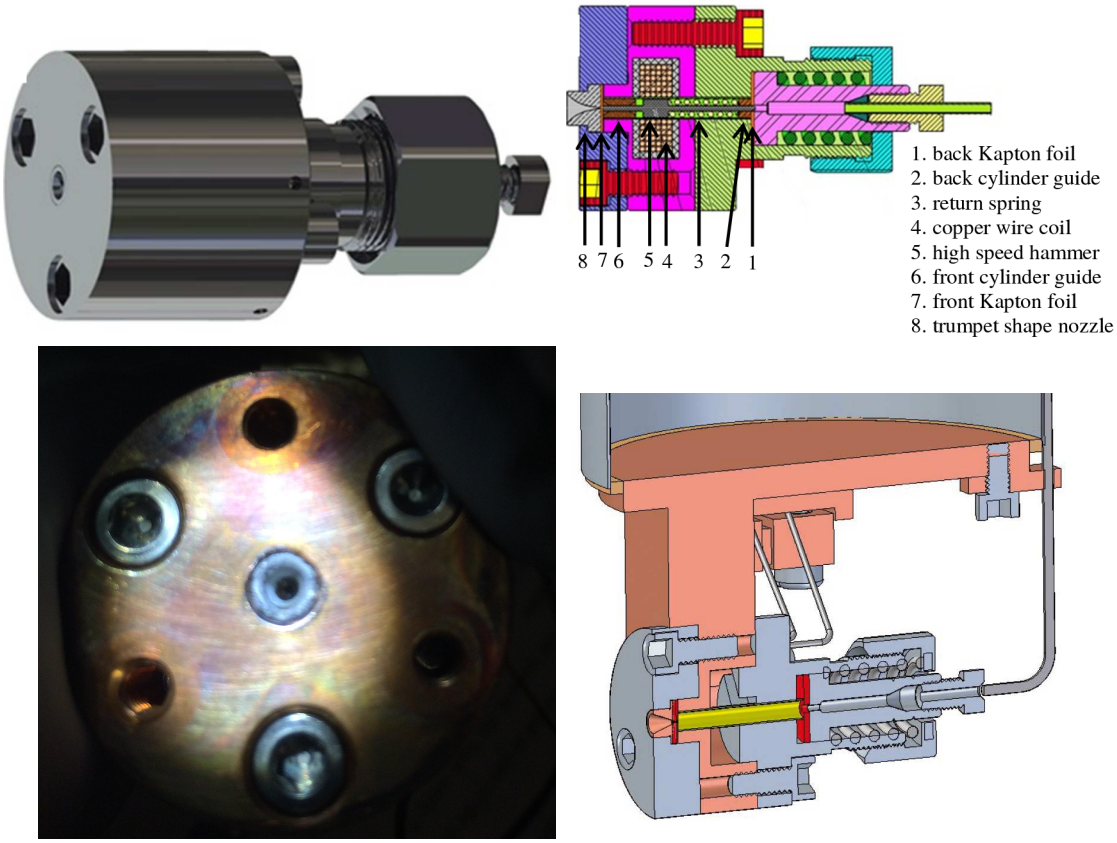


Fig. 4.2: The Even-Lavie valve. Top:Even-Lavie valve CAD drawing and its structure [40]. Bottom: image of the orifice of Even-Lavie valve and cryogenic setup in the experiment.

[72,114]. The sum of enthalpy H and kinetic energy of the gas is conserved, specifically, before and after the adiabatic expansion

$$H(x) + \frac{1}{2}mv(x)^2 = H_0, \tag{4.1}$$

where $H(x)$ is the enthalpy of the gas at position $x$ from the nozzle, and $v(x)$ is the average flow velocity of the beam. Additionally, for an ideal gas, the relationship between temperature and enthalpy is given by

$$\Delta H = H(x) - H_0 = C_p(T - T_0). \tag{4.2}$$

From the above two equations we can see that the reduction of beam temperature stems from the fact that the thermal energy of the beam is converted into the kinetic

energy of the forward motion. The amount of cooling is closely related to the property of the gas species.

Using the above two equations and note that the ratio of the specific heats for ideal gas is

$$\gamma = C_p/C_v. \tag{4.3}$$

The terminal longitudinal velocity is given by:

$$v_t = \sqrt{\frac{\gamma}{\gamma - 1}\frac{2k_B T_0}{m}}. \tag{4.4}$$

However, this equation is not always true, especially at low temperatures, as discussed in Section 4.1.3. For a monatomic gas, $\gamma = 5/3$ and Eq. 4.4 can be further written as:

$$v_t = \sqrt{\frac{5k_B T_0}{m}} \tag{4.5}$$

From Eq. 4.1 $\sim$ 4.4 we can see, that the cooling is achieved by increasing the translation speed. Remember, our goal is to achieve a cold, bright lithium beam with relatively low speed ($\sim 50\ \mathrm{m\,s^{-1}}$). To realize this, we have to find a balance between the speed and the temperature of the beam. A good strategy is to go with low nozzle temperatures ($T_0$), which helps achieve both of the requirements mentioned above. In addition, we can choose the atomic species as well as nozzle parameters (e.g. stagnation pressure, pulse length, etc) for further optimization.

Due to the nature of the supersonic beams, the formula for the atomic flux is not easily derived and remains an interesting topic for researchers [73, 92].Uzi Even et al. performed a series of related experiments measuring the velocity as well as flux of the supersonic beams [24].

### 4.1.3 Cooling limitation

The expected terminal velocity as in Eq. 4.4 does not always decrease with the nozzle temperature as a square root. Similarly, cooling down the nozzle to low temperatures does not always help in reducing the beam temperature [58]. The lowest achievable temperature depends on the properties of the gas as well as the geometry of the experiment, such as the nozzle shape and the skimmer distance. According to the study by Uzi Even et al. [58], the lower boundary of the beam temperature

is set by the condensation in the jet. While two-body collisions are mainly responsible for translational cooling, large clusters are formed due to enhanced many-body collisions at low temperatures through which they release condensation energy into the beam, thus causing the counter effect of heating. The previous assumption of an ideal monatomic gas is not valid when clusters are present in the beam.

From the beam dynamics point of view, there are generally three regimes for a supersonic expansion: First, a high pressure region with viscous flow is located close to the nozzle. In this region collision frequency is extremely high such that thermodynamic equilibrium is guaranteed. Second, there is an intermediate regime where collision is still frequent enough to facilitate the cooling, but the thermodynamic equilibrium is not guaranteed. Finally, there is the regime where very few collisions occur and molecular flow is reached.

A free expansion through supersonic nozzle under continuum conditions is shown in Fig. 4.3. The supersonic beam is formed by a gas expansion from a high pressure source into a lower pressure background. Due to the pressure difference on the two sides of the nozzle, the gas exiting the nozzle opening is accelerated. A critical value [49],

$$G = (\frac{\gamma+1}{2})^{\frac{\gamma}{\gamma-1}} \tag{4.6}$$

is introduced to model the speed of the beam. Here $\gamma$ is the ratio of the specific heats. For all gases $G$ is lower than 2.05 [89]. The ratio between the pressure in the nozzle $p_0$ and the ambient $p_b$ is called flow off-design ratio $n_p = p_0/p_b$ [128], When $n < G$, the flow is subsonic ($M < 1$). Supersonic speed ($M > 1$) is reached when $p_0/p_b \gg G$ at the nozzle exit.

The continuum free expansion in the near field include a Mach disk, barrel shock and free jet boundary [94]. The supersonic cone is bounded by barrel shocks, and the Mach disk separates the subsonic and supersonic flow. The location where the downwind side of the barrel shock intersects the Mach disk is known as the triple point [91]. In the supersonic region, the velocity of the beam increases during the expansion while its temperature decreases. The beam parameter in this zone is independent of boundary conditions (thus also called 'zone of silence'), which is due to the fact that information propagates at the speed of sound. Exciting the Mach disk, the gas undergoes a molecular flow and maintains its temperature thereafter. A simulation using Monte Carlo finite element method of a continuous supersonic nozzle of size

100 µm at room temperature and 300 psi stagnation pressure is also shown on the same figure, where the color indicating the local density of atoms.

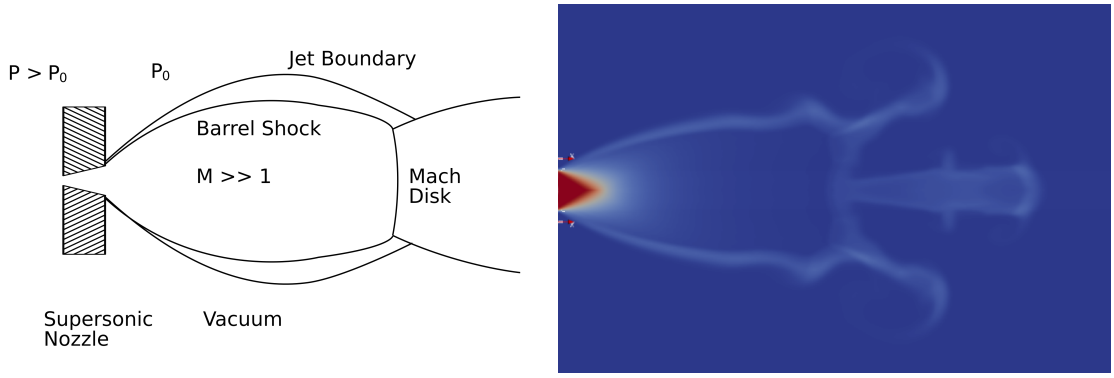


Fig. 4.3: The structure of beam as emitted from a supersonic nozzle and passing a skimmer at the position of mach disk. Left: the regimes of a continuous supersonic flow, which consists of Mach disk, barrel shock and free jet boundary. Different regions are noted with the corresponding Mach numbers and the pressure. Right: simulation of a continuous supersonic beam density distribution, with nozzle size of 100 µm at 300 psi pressure under the room temperature. Color indicates the local density of atoms. One can see that the barrel shock confines the gas under supersonic expansion, the flow regimes are well seperated by the Mach disk.

The study of condensation in a supersonic beam is more based on experiment rather than theory. An intuitive illustration of the clustering procedure is as follows:

As the nozzle temperature is reduced towards lower temperatures, the number of two- and three-body collisions increases. While the normal two-body collisions help to cool and stabilize the beam, the three-body collisions are responsible for the enhanced generation of clusters during the expansion. After the temperature reaches a certain regime, the increase in three-body collisions will dominate and the heating effect will start limiting the beam temperature [42]. The nozzle geometry has a significant influence on the beam collimation as well as the temperature. Detailed research about the nozzle geometry and the skimmer design can be found at [40, 41].

## 4.2 Temperature measurement

### 4.2.1 Single-point measurement

Following the previous discussion of the cooling mechanism, here we derive the formula that describes the temperature of the supersonic beam along the longitudinal direction. Assuming we operate the supersonic nozzle at a region where there are no clusters, we can treat the atoms as an ideal gas, therefore having equations

$$\begin{aligned} \frac{T}{T_0} &= (\frac{p}{p_0})^{\frac{\gamma-1}{\gamma}} \\ C_v &= C_p - R \\ H(x) - H_0 &= C_p(T - T_0), \end{aligned} \tag{4.7}$$

where $R \approx 8.314\ \mathrm{J\,mol^{-1}\,K^{-1}}$ is the ideal gas constant, $\gamma = C_p/C_v$ is the ratio of the specific heats, and $T$ and $T_0$ are the temperatures of beam at position $x$ and the source, respectively.

Now let's incorporate our equations with the Mach number, which is the ratio between the beam velocity and the speed of sound at temperature T,

$$M(T) = \frac{v(x)}{a(T)}, \tag{4.8}$$

where for an ideal gas the speed of sound is given by

$$a(T) = \sqrt{\frac{\gamma RT}{m_{\mathrm{mol}}}}, \tag{4.9}$$

where $m_{\mathrm{mol}}$ is the molar mass of the atom. With a bit of calculation one can write down the expression for the beam temperature as:

$$T = \frac{T_0}{1 + \frac{\gamma-1}{2}M^2}. \tag{4.10}$$

After enough propagation distance, the velocity distribution of the atoms cloud can be described as a Maxwell-Boltzmann distribution at thermal equilibrium,

$$\begin{aligned} f(v) &= Av^3 \exp\left(\frac{mv_\parallel^2}{2k_BT}\right), \\ &= Av^3 \exp(-\frac{v_\parallel}{\Delta v_\parallel}) \end{aligned} \tag{4.11}$$

where $v_{\parallel}$ is the beam velocity along the propagation direction, and $\Delta v = \sqrt{\frac{2k_BT}{m}}$ is the velocity spread measured as twice the standard deviation. Using this result with Eq. 4.7 and 4.9, the Mach number can then be expressed in terms of the velocity spread,

$$M = \frac{2}{\gamma}\frac{v}{\Delta v} = \frac{2}{\gamma}S. \tag{4.12}$$

Here we introduce the definition of speed ratio as $S = \frac{v}{\Delta v}$.

Plugging this result into Eq. 4.10, we finally have the expression for the temperature of supersonic beam along the longitudinal direction as:

$$T = \frac{T_0}{1 + \frac{\gamma-1}{\gamma}S^2} \tag{4.13}$$

Specifically, a monatomic gas like helium and lithium under ideal conditions $\gamma = C_p/C_v = 5/3$, we have the temperature as

$$T_{\parallel} = \frac{T_0}{1 + \frac{2}{5}S^2}. \tag{4.14}$$

Typically in an experiment with a single-point measurement one can not directly get the beam velocity $v$. Consider that the time-of-flight signal is actually what was measured in an experiment, and further assume $\Delta v \ll v$, that the beam is very cold longitudinally, and consider $v = L/t$, we find

$$f(t) = A\frac{l^4}{t^5}\exp\left(-\frac{(t-t_0)^2}{(\Delta t)^2}\right) \tag{4.15}$$

and

$$S = \frac{v}{\Delta v} \approx \frac{t_0}{\Delta t}, \tag{4.16}$$

where $t_0$ is the beam measurement peak arrival time, and $\Delta t$ is the 2-sigma width of the time-of-flight signal.

Thus, we have derived the equation to calculate the beam temperature along the longitudinal direction, by a single point time-of-flight measurement from the arrival time and the 2-sigma time width. This expression works well at relatively warm nozzle temperatures, but as we cool down the nozzle to about 20 K, the equation deviates from our observations, due to the limitation from condensation, as discussed in Section 4.1.3.

### 4.2.2 Two-point measurement

We measured the beam properties at about 1 m after the skimmer, at this distance the beam can be treated at thermal equilibrium. Thus, the velocity distribution can be written as

$$f(v) = Av^3 \exp\left(-\frac{mv^2}{2k_BT}\right), \tag{4.17}$$

where A is normalizing factor.

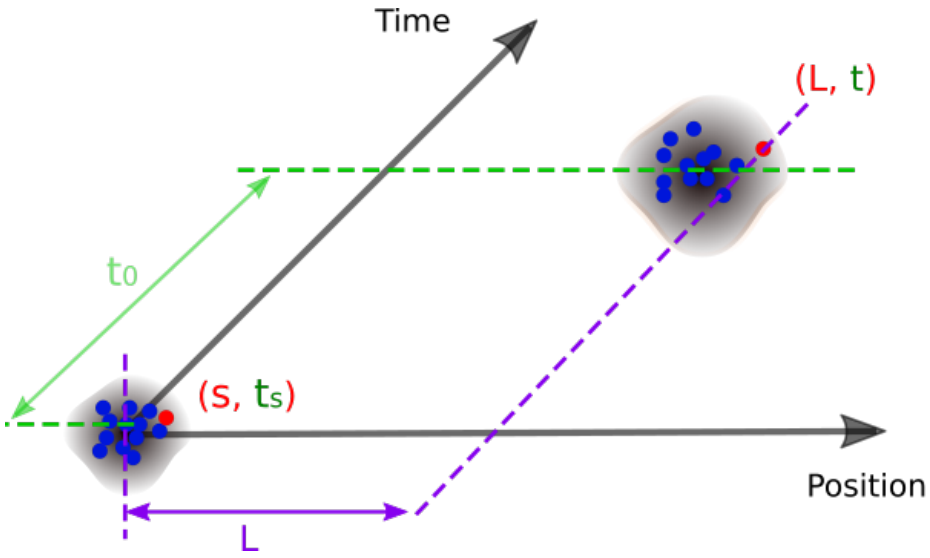


Fig. 4.4: Illustration of atom beam propagation temperature calculation. The clould center of atoms with unknow temperature is located at the origin of the time and position, a random atom in the cloud has coordinates of time $t_s$ and location $S$. At a distance of $L$ from the original cloud center, the same atom is detected at time $t$, while the cloud center arrives at the same location at a time $t_0$. The width of the cloud at this location is described as Eq. 4.19.

Let's now consider atoms in a source cloud at time $t_s$ located at a distance $s$ away from the cloud center. After time $t$ the same atoms are detected at distance $L$ downstream from the original cloud center, as shown in Fig. 4.4. According to the velocity distribution and $v = \frac{L-s}{t-t_s}$, the signal strength can be written in terms of $t$, $s$

and $t_s$ as

$$\begin{aligned} f(t,s,t_s) &= A\frac{(L-s)^4}{(t-t_s)^5}\exp\Big[-\frac{m}{2k_BT}(\frac{L-s}{t-t_s}-v_0)^2\Big] \\ &\overset{t_0=L/v_0}{=} \frac{(L-s)^4}{(t-t_s)^5}\exp\Big[-\frac{m}{2k_BT}(\frac{(t-t_0)v_0-s/v_0}{t-t_s}-v_0)^2\Big] \\ &= \frac{(L-s)^4}{(t-t_s)^5}\exp\Big[-\frac{mv_0^2}{2k_BT}\frac{(t_0-s/v_0-t+t_s)^2}{(t-t_s)^2}\Big] \\ &\approx \frac{L^4}{t_0^5}\exp\Big[-\frac{mv_0^2}{2k_BT}\frac{(t_0-s/v_0-t+t_s)^2}{t_0^2}\Big] \end{aligned}, \tag{4.18}$$

where $t_0 = L/v_0$ is the time need for the cloud center to propagate a distance of $L$. From this equation we can get the beam full-width-half-maximum (FWHM) $w$,

$$w(t_0) = \sqrt{\frac{8\ln 2 k_B T t_0^2}{mv_0^2}}. \tag{4.19}$$

The above distribution $f(t,s,t_s)$ still depends on the spatial ($s$) and temporal ($t_s$) distribution $g(s,t_s)$ at the source location. The measured signal at the second location is the integration over $s$ and $t_s$. However, the measurement at the original location won't tell us the expression of $g(s,t_s)$. Fortunately we could assume $g(s,t_s)$ follows a normal distribution with FWHM $w_{t_s}$ and $w_s$,

$$g(s,t_s) = \frac{4\ln 2}{\pi w_s w_{t_s}}\exp\Big(-\frac{4\ln 2 s^2}{w_s^2}\Big)\exp\Big(-\frac{4\ln 2 t_s^2}{w_{t_s}^2}\Big). \tag{4.20}$$

By integrating the distribution at the first measurement point, we find

$$\begin{aligned} f(t) &= \int_s\int_{t_s} f(t,s,t_s)g(s,t_s)dsdt_s \\ &= A\frac{L^4}{t_0^5}\frac{w}{w'}\exp\Big[-4\ln 2\frac{(t-t_0)^2}{w'^2}\Big] \end{aligned}, \tag{4.21}$$

where the time-of-flight width is $w'(t) = w^2 + w_{t_s}^2 + w_s^2/v_0^2$, which shows the broadening from the finite distribution of the source. However, $w'$ depends on where the measurement is performed. To extract the temperature of the beam, one needs to rely on $w$ as in Eq. 4.19.

We can carry out a two measurement at a well separated distance, which yields two measurement of $w'(t_1)$ and $w'(t_2)$, at peak arrival time $t_1$ and $t_2$, respectively. The measured beam temperature can thus be written as

$$T_\parallel = \frac{mv_0^2}{8\ln 2 k_B}\frac{w'(t_2)^2 - w'(t_1)^2}{t_2^2 - t_1^2}. \tag{4.22}$$

Note that $w'(t_1)$ and $w'(t_2)$ here are the FWHM in seconds at two different locations measured at time $t_1$ and $t_2$ correspondingly.

A similar derivation shows that, if we have the measurement of transverse spatial FWHM at two locations, the standard deviation of the transverse beam velocity is

$$v_\perp = \sqrt{\frac{1}{8\ln 2}\frac{W'(t_2)_2^2 - W'(t_1)_2^2}{t_2^2 - t_1^2}}, \tag{4.23}$$

where $W'(t_1)$ and $W'(t_2)$ are the atomic beam FWHM in meters measured at the two locations at time $t_1$ and $t_2$, respectively. Thus, the beam transverse temperature can be calculated as

$$T_\perp = \frac{m v_\perp^2}{k_B}. \tag{4.24}$$

## 4.3 Entrainment

### 4.3.1 Overview

The Even-Lavie valve provides us with a great source of carrier gas at low temperatures, and a mixture of different gas species in a supersonic nozzle has been done previously by directly adding different molecules in the gas line [1]. Another way to have two species in the supersonic beam is to use merged-beams [121]. However, these existing methods all have in common that the supersonic beam of the used molecular species can be generated directly, however, most atoms that are of interest to cold atom community, such as the alkali atoms, have a high melting point and are in solid at the room temperature. Because of this, one cannot generate a beam from these elements in a nozzle.

A different method has to be used if we want to make a supersonic lithium beam. One good approach is to use the 'seeding' technique, where the beam of gas of interest is mixed with a large group of a light dilute gas. The seeded specie is thereby accelerated to a velocity essentially equal to that of the dilute gas at the source temperature. We have been collaborating with the group of Edvardas Narevicius on exploring ways to achieve a good entrainment of lithium into a supersonic beam. Previously, they were able to seed and trap $10^5$ lithium atoms with a beam of a supersonic mixture of an oxygen and krypton mixture at a nozzle temperature of 165 K [2]. They seeded the lithium by laser ablation of a solid target placed near

the valve. In this method, the temperature of the lithium beam they generated is about 3 K, and they estimated the amount of entrained lithium to be on the order of $10^7$ atoms per pulse[1]. Further reducing the temperature of the lithium beam while having a large atom number seems challenging.

The theoretical study of the beam seeding technique is still an unsolved problem. Most study on the interaction between atoms in a supersonic beam is done through the Monte Carlo simulation with a predefined interaction potential and cross section [75]. Rather than the molecule properties, various influences from parameters of the environment such as boundary condition, background pressure, temperature, etc, make it even harder to study this problem thoroughly. We explore the various parameters experimentally to achieve the highest number of entrained atoms while minimizing the disturbance introduced by the entrainment.

In our experiment, we explored different noble gases at different temperatures for lithium entrainment. We tried laser ablation with a high power pulsed Nd-YAG laser to provide a lithium source in the early stage of our experiment. However, we found that either the number of entrained atoms is limited as in Narevicius' group, or the plasma generated by laser ablation heats up the beam significantly. Rather than pursuing this method, we decided to use an electrically heated oven to provide a semi-collimated lithium source. Additionally, we explored the potential of adding a high current pulsed metal ribbon above the oven opening and located on the other side of supersonic beam, in order to increase the amount of atoms that undergo the entrainment process.

We used a source vacuum chamber to generate the lithium atoms and entrain them into a supersonic carrier. After the entrainment, there is a skimmer for collimation and further reducing the beam transverse temperature, then a detection chamber where we performed measurement using different tools, e.g. laser fluorescence, hot-wire detector, residual gas analyzer (RGA), as shown in Fig. 4.5. The Even-Lavie valve and lithium source are located in the source chamber which has a vacuum of below $1 \times 10^{-8}$ Torr. Experiment details and results are discussed in this section.

[1]private communication through email

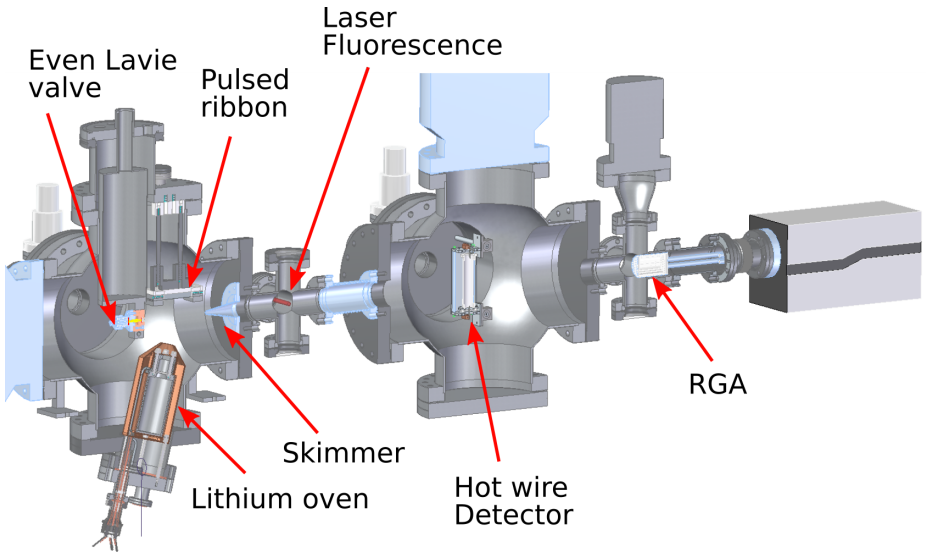


Fig. 4.5: Schematic of entrainment experiment setup. The detection tools together with the vacuum chamber are mounted on a translational stage such that measurements at multiple points can be obtained along the longitudinal direction.

### 4.3.2 Lithium oven

To generate the dilute lithium gas flow in the supersonic beam path, we used an electrically heated oven filled with natural abundance lithium (92.41 % $^7Li$ and 7.59 % $^6Li$). The lithium oven is located in the vacuum at a distance of about 10 cm from Even-Lavie valve, with its opening facing the beam path about 2 cm below. We make use of the lithium vapor pressure to generate the lithium vapor, as shown in Fig. 2.2, which is given by equation [57],

$$P = 10^{4.98821 - \frac{7918.984}{T - 9.52}} \quad \text{with } T \in [298, 1600]K, \tag{4.25}$$

where P is the vapor pressure in bar, and T is the temperature in Kelvin. Note that the melting point of lithium under standard pressure is 180 °C.

We adopt a design of the capillary lithium oven [106][2], as shown in Fig. 4.6. The oven nozzle and oven reservoir are wrapped with electric heater wires and can be heated separately.

There are totally 528 capillaries in the first version of our oven, with each capillary 100 µm in diameter and 5 mm in length. At 550 °C, the lithium vapor pressure is 1.8

[2]In the original paper an aligned micro-capillary array is used for the oven nozzle and $1.2 \times 10^{14}$ atoms per second is obtained at 525 °C by the author.

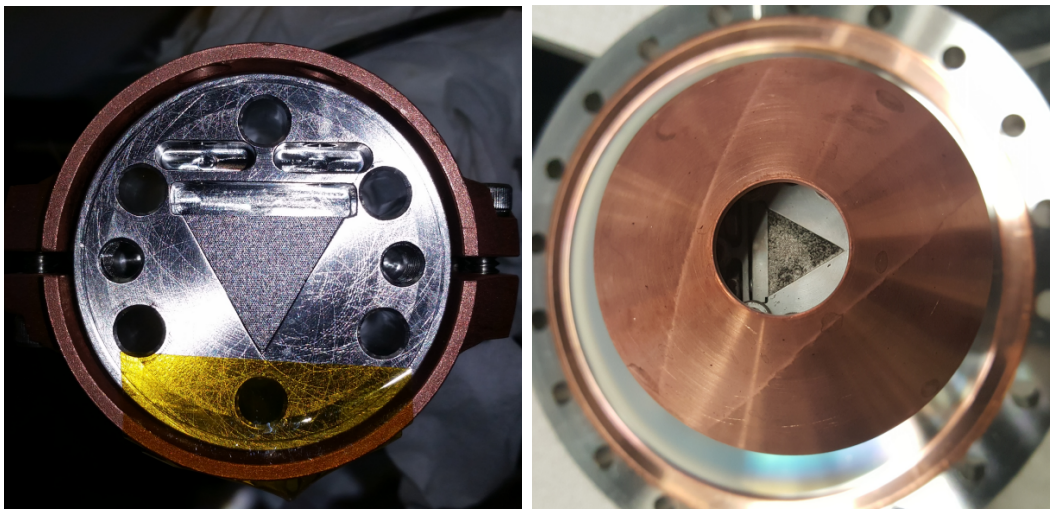

Fig. 4.6: Picture of capillary oven. Left: top view of the capillary oven nozzle; Right: top view of oven with copper shielding.

pa a with mean free path of 14 mm which is much larger than the aperture diameter, thus in the effusive regime. The flux in terms of atom number can be estimated by

$$\Phi = \frac{n_0 v}{4} N A \alpha, \tag{4.26}$$

where the number of gas atoms noted as $\Phi$, the mean velocity of atoms are given by $v = \sqrt{3k_B T}/m$, total number of capillaries are $N = 528$, the opening area of the nozzle can be calculated from $A \approx \pi(100\mu m/2)^2$, and the number density is $n_0 = \frac{p}{k_b T}$ as derived from ideal gas law. The fraction of atoms passing through $\alpha \approx 0.6\%$ can be estimated from the aspect ratio of the capillaries. This estimation yields about $1.8 \times 10^{15}$ atoms per second at 550 °C and $6.3 \times 10^{15}$ atoms per second at 600 °C.

### 4.3.3 Pulsed ribbon

Since the supersonic carrier gas is generated from a pulsed source (pulse length $\sim$ 10 µs) while the lithium oven is producing a constant flux of lithium, more than 99% of lithium atoms coming out of the oven are not directly entrained during the time that the supersonic carrier gas passes by. Collecting those lithium atoms that are not within the proper time window and re-emit them helps improve the entrainment.

Our idea is to place a thin Nichrome ribbon above the oven nozzle but on the other side of the supersonic beam, as shown in Fig. 4.7. The ribbon will act as

a lithium collector when the supersonic nozzle is not activated. By passing a high current pulse through the ribbon that is synchronized to the supersonic nozzle trigger with a proper delay, we heat up the ribbon to around 1000 °C in a short time and remit the collected lithium atoms. As the inactive time of the nozzle (1 $\sim$ 5 s) is much longer compared to its opening time($\sim$ 10 µs), this method could effectively increase the lithium atoms that are entrained.

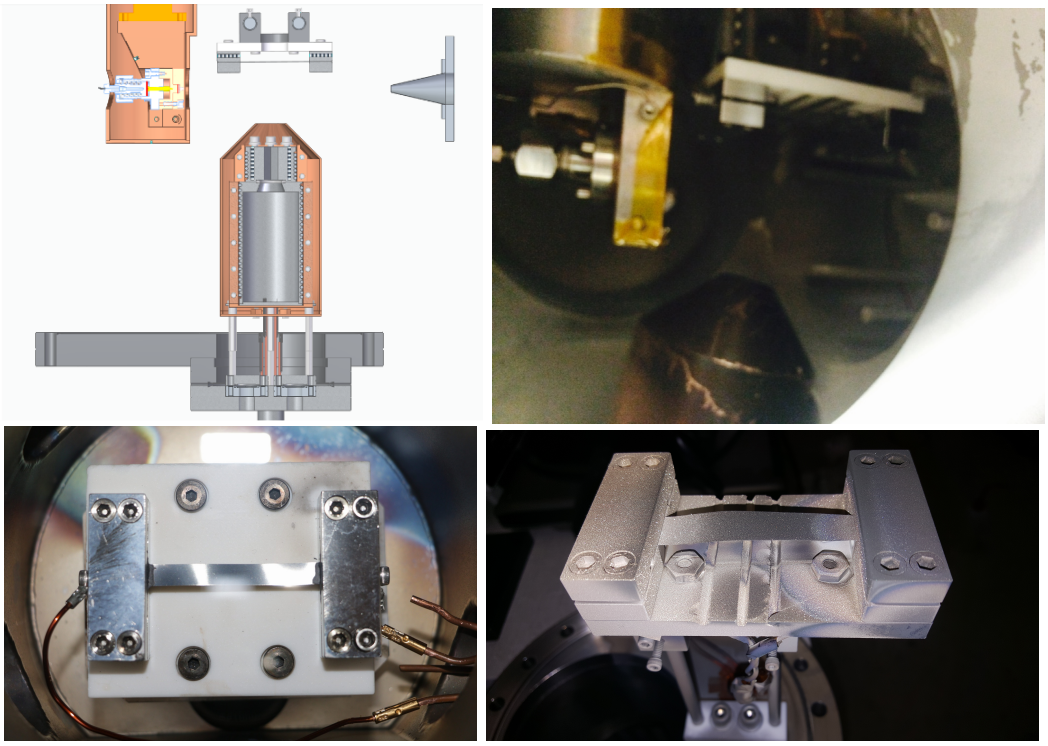

Fig. 4.7: The experiment of entrainment using the oven and ribbon. Top: the schematic of entrainment setup and the real image with the experiment apparatus. Bottom: Ribbon wiring and ribbon with accumulated lithium on the surface after running oven without ribbon for several hours.

The general idea of the high current pulse is based on an LCR circuit. We use a similar circuit as ones in our decelerator CBOX (Fig. 5.15 board) with fixed capacitance of 22 mF. The capacitors are charged up to 300 V and the output current goes through a fixed inductor with inductance of 2 µH. A Nichrome ribbon with resistance 0.2 Ω and dimension of 0.002 x 3 x 0.2 inch is used to carry a 60 µs and 1200 A high current pulse at a rate of every 3 seconds. The calculated ribbon temperature is shown in Fig. 4.8. This result agrees with later measurement from a pyrometer.

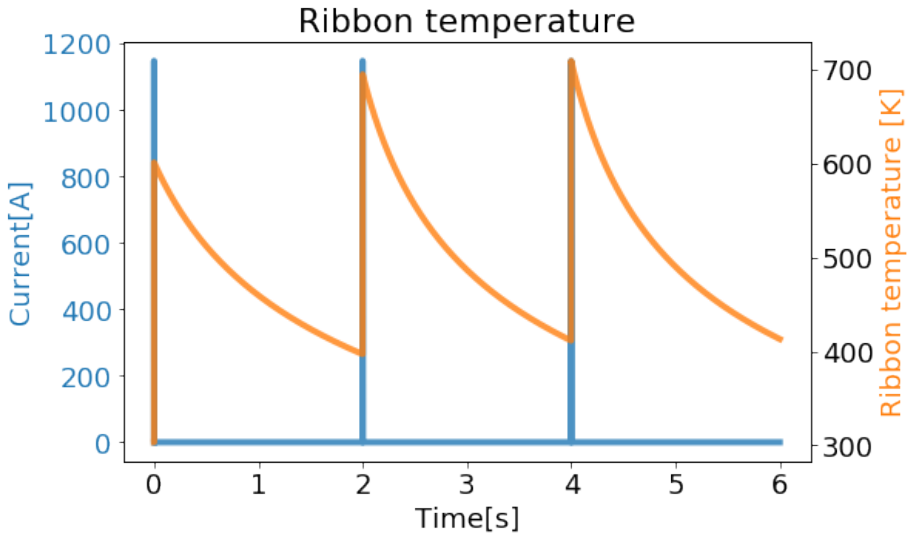


Fig. 4.8: Calculated current (blue) and temperature (orange) of the ribbon over time.

## 4.4 Experiment

### 4.4.1 Overview

The cryogenic temperature in our experiment was created either from liquid nitrogen at 77 K or from a compressed helium cryocooler (SHI Cryogenics CH-204) operated at around 10 $\sim$ 20 K. The cryocooler is further cooled by institutionally provided chilled water, which is kept at a temperature of less than 10 °C and was circulated by a heat exchanger.

We first experimented with the supersonic beam at different parameters, e.g. temperature, pressure, pules length, etc. As helium is the only one from our candidate list (He, Ne, Ar, Kr) that stays in gas phase at 20 K, more experiments have been done with it. We also experimented with Ne, Ar, and Kr at higher temperatures, the result will be summarized later.

Once getting into a proper parameter space for the supersonic beam, entrainment of lithium into Helium is attempted. Both methods, with only the lithium oven and with the ribbon + oven were tested. The goal at this stage is two-fold: first, we'd like to get the lithium beam velocity below 500 $\mathrm{m\,s^{-1}}$, as this is the limit speed up to which our decelerator is capable of capturing atoms. Additionally, we want to optimize the entrained lithium atom number ($> 10^9$ atoms per pulse) while keeping

the beam at a low temperature ($< 250$ mK) such that enough atoms can be efficiently decelerated later.

### 4.4.2 Detection methods

Multiple detection methods were used for measuring the time-of-flight signal of helium and lithium. We use a residual gas analyzer (RGA, Stanford research system RGA-100) to measure the time-of-flight signal of helium and other gases, as shown in Fig. 4.5. Laser fluorescence and a hot wire detector were used to detect the lithium. All these detection instruments are in the detection vacuum chamber ($\sim 10^{-9}$ Torr) which is mounted on a translation stage such that measurements can be achieved at different locations along the beam propagation axis.

#### 4.4.2.1 Residual Gas Analyzer

The residual gas analyzer (RGA) is a mass spectrometer for analyzing gas components inside a vacuum below $10^{-4}$ Torr. A small fraction of gas molecules are ionized, the resulting positive ions are detected and measured according to their molecular masses. The detection and analyzation happens sufficiently fast so that it can be used for detecting time-of-flight of dilute gas as well. We have the ionizer of our RGA located in the path of the atomic beam and directly facing the incoming atoms.

#### 4.4.2.2 Hot wire Detector

The hot wire detector, or Langmuir-Taylor detector, works according to surface ionization process, with detection probability almost independent of atom velocities [33]. The positive ion from the ionization event is collected by an electrode and the signal of the ion current is obtained. Surface ionization of an atom occurs if the ionization potential $I$ of the atom is comparable to the work function $\Phi$ of the metal. The probability of atoms to be emitted as positive ions is given by the Saha-Langmuir law,

$$P_+ = \frac{1}{1 + \frac{g_0}{g_+} \exp[\frac{I-\Phi}{k_B T}]}, \tag{4.27}$$

Where $g_+$ and $g_0$ are the statistical weights of the ion and atom ground states, for alkali atoms $g_0/g_+ = 2$. $I$ is the ionization potential of the atom, for lithium $I = 5.392eV$. The work function for rhenium as the hot wire ribbon is $\Phi = 4.96$ eV.

Usually the wire temperature is kept at 1500 K or larger, in order to reduce the ion residence time on the surface. This residence time is given by $\tau = \tau_0 \exp(E_{\text{ads}}/k_B T)$, where $E_{\text{ads}}$ is the ion adsorption energy ($\sim$ ev). The structure of our wire detector is shown in Fig. 4.9. To extract the ionization probability, we have run our wire

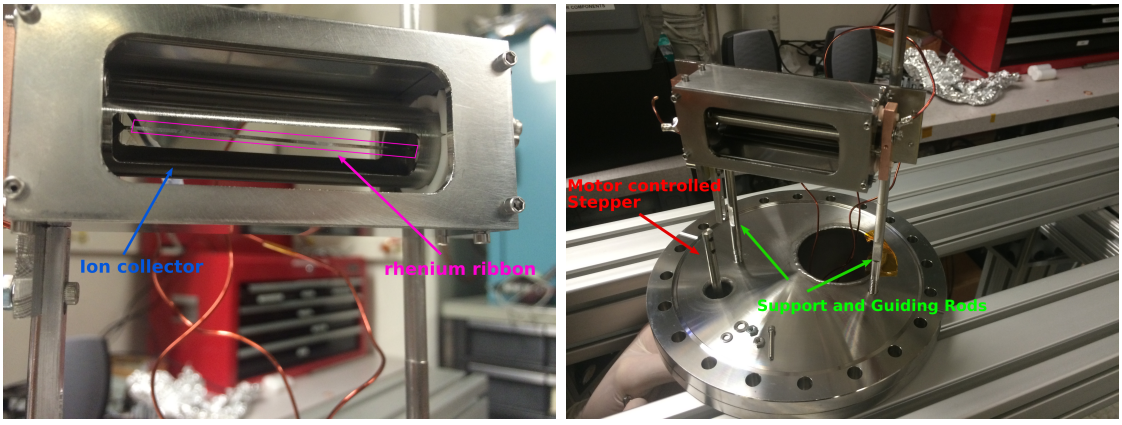


Fig. 4.9: Image of hot wire detector with motor controlled translation stepper

detector at different currents and measured the temperature with a pyrometer. At 3.5A, the temperature is about 1890 K, yields an ionization probability of 3.4 %. The rhenium ribbon has dimension of 0.001 x 0.0315 x 2 inches. The output current signal is converted into a voltage using a Femto current amplifier, an SRS voltage amplifier is used for extra amplification and noise filtering. The conversion between atom number in a short time window to measured voltage $U$ is then given by:

$$N_{\text{atoms}} = \frac{1}{e \cdot P_{\text{ion}} \cdot P_{\text{detect}} \cdot G_{\text{amp}}} \int_{t_0}^{t_1} U(t) \tag{4.28}$$

where $P_{\text{ion}} = 0.034$ is given by Eq. 4.27, $e$ is the electron charge, $G_{\text{amp}}$ is the total amplifier gain during the experiment, and $P_{\text{detect}} = 0.3$ is the detection probability which is calibrated from a laser fluorescence measurement.

Since the hot wire detector is only 800 µm wide, we scan it transversely through the cross section of the atomic beam and then integrate over time to obtain a total atom number value. In the mean time, the wire scan measurement could also give us the atom beam size along the scan direction.

#### 4.4.2.3 Laser fluorescence

The laser fluorescence detection is widely used in atomic physics experiments. A typical setup is to have a laser beam intersect with the atom beam at a right angle, with its frequency tuned on resonance with a certain atomic transition and power above the saturation intensity of the transition. The atom number is calculated from the scattered photons measured by a photo detector. For a three-level transition like the lithium D2 line, when a single probe laser beam is used for probing, atoms go dark after 2 cycles on average with sufficient amount of time interacting with the laser. This assumes the transition has a branching ratio of 0.5 [120]. Additionally, one has to know the solid angle $\Omega$ of the photo detector relative to the atom beam center, the quantum efficiency $Q_{\text{quant}}$, and the current-to-voltage conversion gain $Q_{\text{I-to-V}}$ to calculate the total atom number,

$$N_{\text{atom}} = \frac{2\pi}{\Omega Q_{\text{quant}} G_{\text{I-to-V}}} \int_{t_0}^{t_1} U dt. \tag{4.29}$$

### 4.4.3 Supersonic helium beam

#### 4.4.3.1 General characterization

We first tested the helium beam signal dependency on the Even-Lavie nozzle pressure and nozzle temperature at a fixed pulse length of 20 µs. For this test, we are interested in the influence of the Even-Lavie valve pressure and temperature on the supersonic beam flux and temperature.

The helium signal is detected through time-of-flight measurement by the RGA and is integrated over time to get a total signal. Additionally, Eq. 4.14 was used to extract the helium beam temperature from a single point measurement.

Fig. 4.10 shows the dependency of the helium flux on the supersonic nozzle stagnation pressure and the temperature. From the plot one can see that the flux does not change much with pressure at room temperature, but does obviously decrease when the nozzle is cooled down to lower temperatures. At the extremely low valve pressure the helium flux starts to increase, this could be due to the increased mean-free-path which reduces collision and increases throughput, as approaching effusive flow.

The dependency of temperature of the supersonic beam on the nozzle pressure and temperature is shown in Fig. 4.11. One can see that by decreasing the Even-Lavie valve pressure the temperature of the atom beam first decreases and then increases.

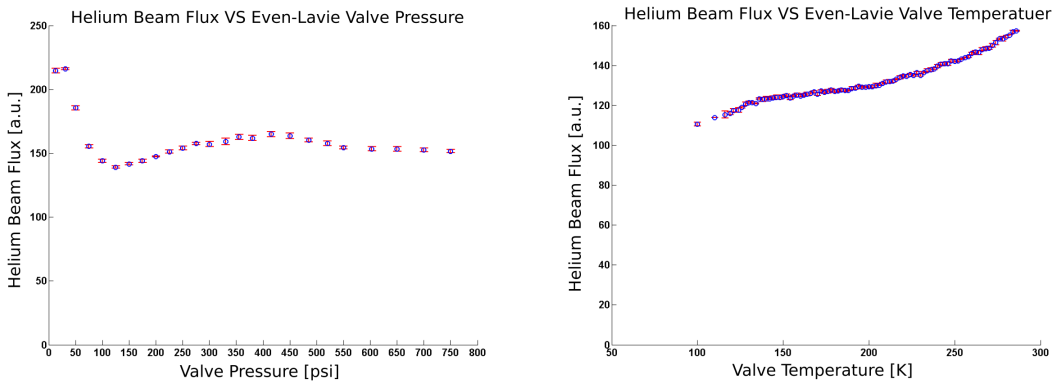


Fig. 4.10: The helium supersonic beam flux dependency on Even-Lavie valve parameters. Left: flux dependency on nozzle stagnation pressure at room temperature. Right: flux dependency on nozzle temperature at 300 psi nozzle stagnation pressure. Both measured at 20 µs nozzle pulse length.

The way to understand this intuitively is to consider the collision rate of atoms at the nozzle opening. Lower pressure results in a smaller atom number density in the Even-Lavie nozzle, which, similar to its influence to atom flux, reduces the collision rate. As discussed before, the two-body collision contributes to the cooling effect in a supersonic nozzle. Thus, the resulting temperature increases at low pressure. The decrease of the beam temperature with lower nozzle temperature is obvious, according to Eq. 4.14.

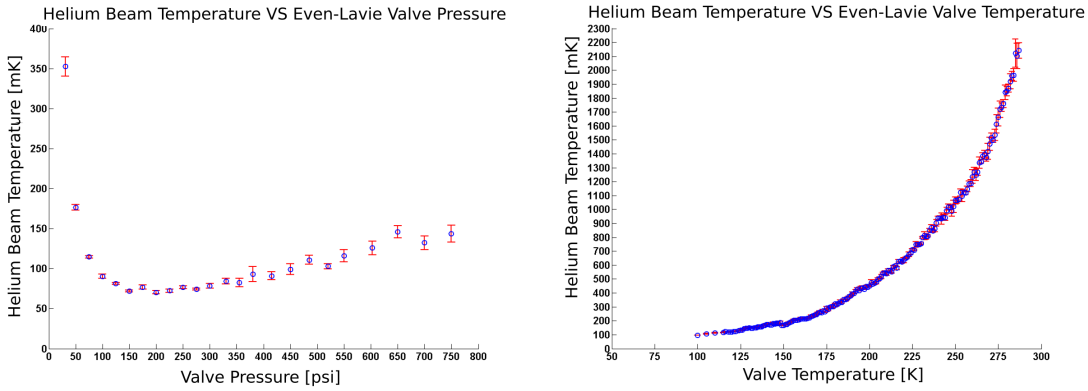


Fig. 4.11: The helium supersonic beam temperature dependency on Even-Lavie valve parameters. Left: temperature dependency on nozzle stagnation pressure at nozzle 100 K. Right: temperature dependency on nozzle temperature at 300 psi nozzle stagnation pressure. Both measured at 20 µs nozzle pulse length.

Additionally, we obtain the helium beam velocity through an RGA two-point measurement, where we got the speed of $\sim$ 2000 $\mathrm{m\,s^{-1}}$ at room temperature and $\sim$ 1000 $\mathrm{m\,s^{-1}}$ at around 100 K. This beam velocity is too fast for the decelerator to capture, thus parameters at even lower temperatures using the cryocooler are explored. An example of a time-of-flight beam speed measurement is shown in Fig. 4.12, together with velocity results from linear fitting at different Even-Lavie valve temperatures.

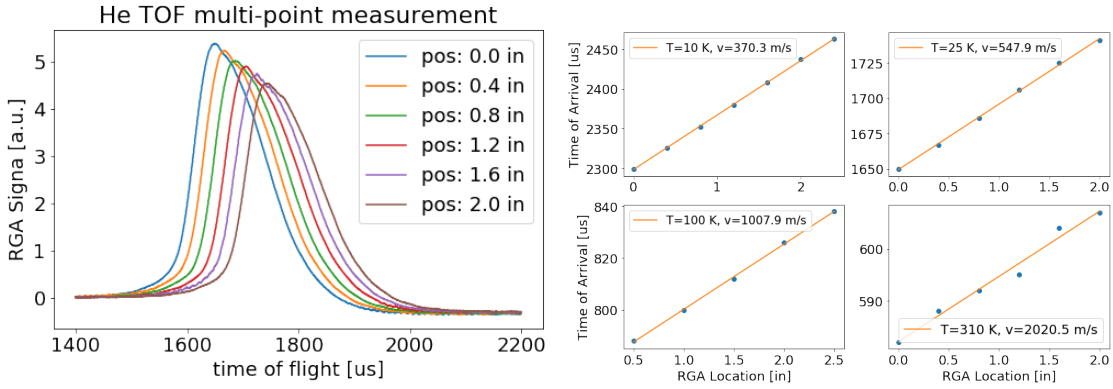


Fig. 4.12: The time-of-flight measurement of helium beam velocity. Left: example of a time-of-flight measurement at valve temperature 25K, TOF signal is obtained at multiple RGA locations, the time of arrival is then extracted to get beam velocity. Right: linear fit of multi-point TOF measurement at different valve temperatures, velocities are extracted from line fitting. Nozzle pulse length: 7.6 µs, stagnation pressure: 300 psi.

#### 4.4.3.2 Beam Properties at 10K Nozzle Temperature

As we have seen that the helium beam temperature gets colder with lower translation speed when the supersonic nozzle is cooled to lower temperatures, we directed our experiment with the supersonic beam to even lower temperatures. With the help of a cryocooler we were able to get the nozzle temperature down to 10 K with good stability ($\Delta T < 0.5$ K). Additionally, we wrapped a thin heater wire on the 2nd cooling stage of the cryocooler in order to gain a bit of temperature controllability, as the cryocooler can only operate at its lowest temperature. By doing this we can tune the nozzle temperature in the range of 10 K $\sim$ 30 K, which yields beam velocities

ranging from 450 $\mathrm{m\,s^{-1}}$ to 550 $\mathrm{m\,s^{-1}}$. We then performed a full characterization of the beam in this region.

First, shown in Fig. 4.13 is the helium beam time-of-flight signal detected by an RGA, as a measurement of the change of the beam flux when cooling down towards 10K. Nozzle pulse length is fixed at 20 µs with a stagnation pressure of 300 psi for this test. One may notice that the total signal goes down when getting to colder temperatures.

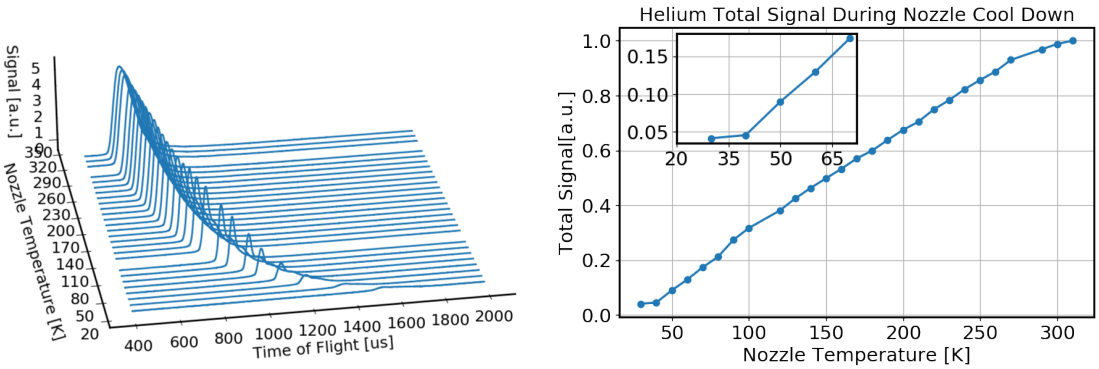


Fig. 4.13: Helium supersonic beam time-of-flight measurement during the cool down process of the nozzle from the room temperature to 10 K, as measured by a RGA.

Additionally, we found that the nozzle pulse length and stagnation pressure also influence the beam shape and total signal. Various tests have been performed on these parameters, the change of beam shape at a parameter set that is close to the optimal point is shown in Fig. 4.14.

### 4.4.4 Other carrier gases

In addition to helium, we also explored other elements as carrier gas: Neon, Argon and Krypton. Their translation velocities at different nozzle temperatures were measured, using either liquid nitrogen(boiling point 77 K) or dry ice(sublimates at 194.65 K) as the cooling source. A list of result is shown in Table 4.1.

### 4.4.5 Entrainment with oven

We started testing entrainment of lithium into helium at a nozzle temperature of 100 K. For this test we were using the hot wire detector as the measuring tool. By

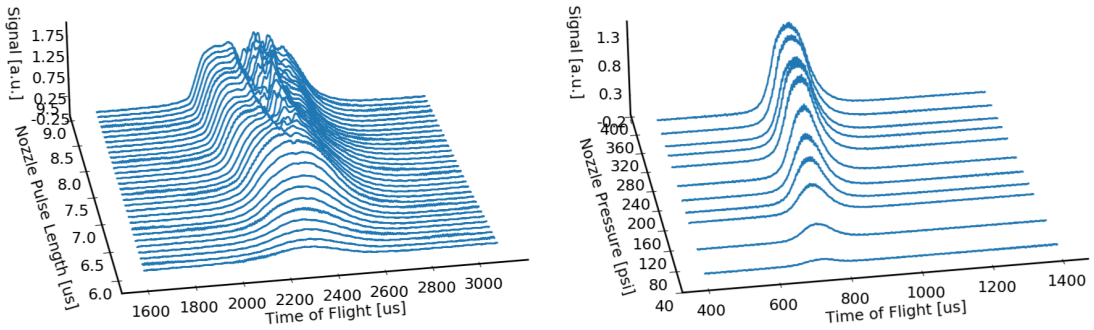


Fig. 4.14: Helium supersonic beam shape variation due to the nozzle pulse length change (left) and pressure change (right). Data shown are near the optimal region at the nozzle temperature 10 K.

| Element | Speed | Melting Point | Clustering Point |
|---|---|---|---|
| Helium | 2000 $\mathrm{m\,s^{-1}}$@293 K<br>1000 $\mathrm{m\,s^{-1}}$@100 K<br>550 $\mathrm{m\,s^{-1}}$@30 K<br>450 $\mathrm{m\,s^{-1}}$@10 K | 4.2 K | 30 K |
| Neon | 940 $\mathrm{m\,s^{-1}}$@310 K<br>550 $\mathrm{m\,s^{-1}}$@102 K | 25 K | 80 K |
| Argon | 503 $\mathrm{m\,s^{-1}}$@293 K<br>440 $\mathrm{m\,s^{-1}}$@141 K | 83 K | 240 K |
| Krypton | 284 $\mathrm{m\,s^{-1}}$@185 K | 116 K | N/A |

Table 4.1: A list of measured supersonic beam final speed with various element at different nozzle temperatures. Data measurement using RGA at multiple point along beam propagation direction. Also shown is their melting temperature as well as temperature below which cluster starts form [40].

scanning the hot wire transversely across the atomic beam with a step size the same as its width (0.0315 inch), we could get a 2D map of the lithium atoms along two directions: the beam propagation axis and the hot wire detector moving direction (as in position of hot wire).

We first optimized the Even-Lavie nozzle parameters (e.g. pressure, pulse length) for oven entrainment, then the ribbon pulse is added with optimization of its pulse length, delay, voltage, etc. A comparison of lithium flux from these two methods is shown in Fig. 4.15.

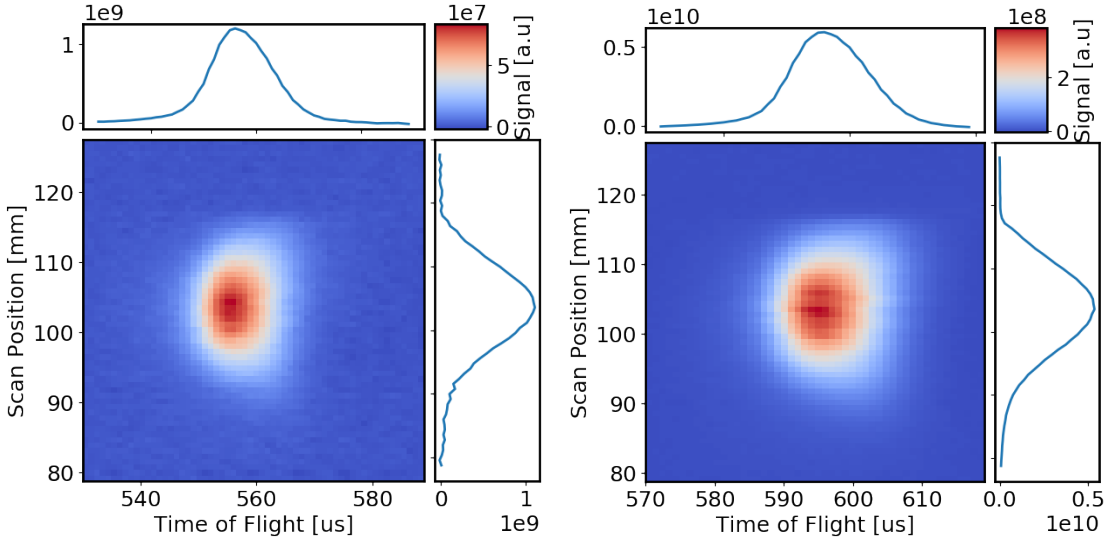


Fig. 4.15: 2D map of lithium beam using scanning hot wire detector, using entrainment method of oven only (left) and oven + pulsed ribbon (right). The line plots on the side show the summed result along the corresponding axis.

Additionally, we extracted the number of lithium atoms, based on a few parameters of the hot wire: an ionization probability 0.0365, an ion current capture probability of 0.3, and an amplifier gain of $10^6$. The time-of-flight signal corresponding to each of the hot wire measurement positions is integrated through a proper time window, yields the results shown in Fig. 4.16. A gaussian function is then fit to the result in order to extract the area under the curve, which corresponds to the total number of lithium atoms detected. Then Eq. 4.28 is applied to extract the total atom number, resulting in $2.2 \times 10^{10}$ atoms per shot for oven entrainment, and $1.1 \times 10^{11}$ atoms per shot for oven+ribbon entrainment. The latter gives a total entrained lithium atom number with a factor of 5 compared to the former one.

Getting this amount of lithium seeded in the supersonic helium beam, we were then confident to move forward to temperatures below 30K, where the helium beam is much colder, we expect the same temperature for the lithium beam. At an Even-Lavie nozzle temperature around 20 K[3], a few hot wire scan measurements were performed with only the oven as the entrainment method to simplify the process. The 2D atom cloud map as well as total atom number is shown in Fig. 4.17.

[3]Nozzle pulse length 7.4 µs and stagnation pressure at 300 psi

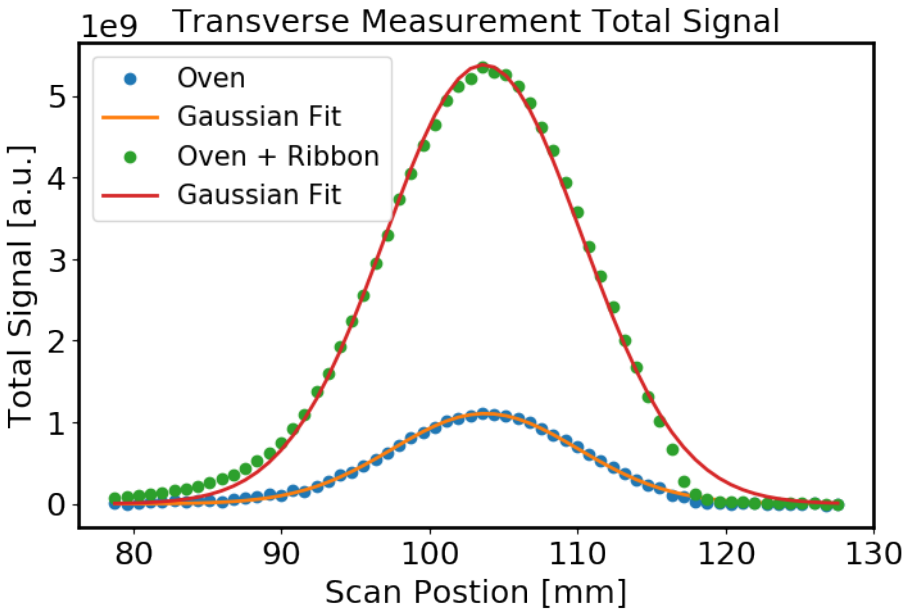


Fig. 4.16: Integrated lithium ion signal from the hot wire for each wire scan position. The signal is integrated current over a window of time-of-flight.

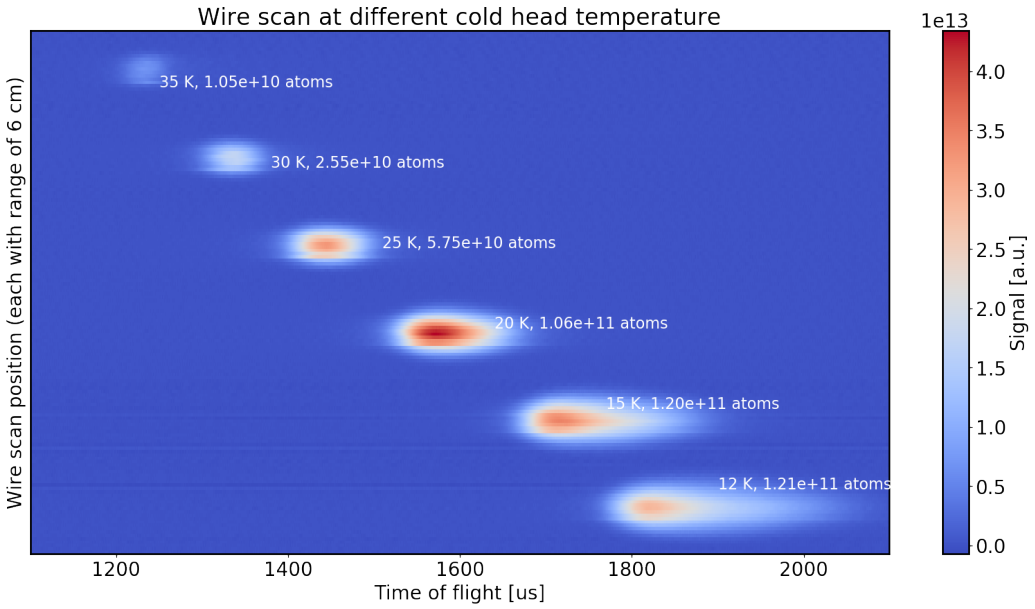


Fig. 4.17: Lithium 2D map from hot wire scan at low temperatures, with entrainment method of oven at 550 °C.

.

There are several observations from Fig. 4.17: First, the lithium beam becomes slower when the carrier gas is cooled to lower temperatures, which agrees with our previous observation on the helium beam. Second, more lithium atoms get entrained at lower carrier temperatures as compared to the similar result at nozzle temperature of 100K (Fig. 4.16), even though the total flux of the carrier helium gas goes down (Fig. 4.13). Third, given specific Even-Lavie nozzle parameters, such as the pulse length and the pressure, there exists an optimal nozzle temperature such that a cloud of lithium atoms with high density and high total atom number is formed.

We further explored the third point from above, with a large amount of nozzle parameter scans and finally settled on a nozzle temperature of 15 K $\sim$ 20 K. We estimated the transverse temperature of the lithium beam to be about 60 mK, at a distance of about 1.5 meters from the skimmer. We then moved forward to add the ribbon in addition to the hot oven as the entrainment method.

### 4.4.6 Entrainment with pulsed ribbon

The parameter space for entrainment with the ribbon is much larger than just using the oven, as there are additional parameters involved, such as ribbon voltage, ribbon pulse length, ribbon delay, ribbon size, ribbon geometry, etc. A lot of effort has been spent on searching for a set of optimal parameters with the ribbon to get the highest gain over just the oven. Here only a few results close to optimal point are shown. I will discuss them briefly.

For a better signal-to-noise ratio and faster data acquisition, we used laser fluorescence instead of the hot wire as the detection method. Similarly, the laser spot size is collimated down to about 1 mm diameter and scanned transversely perpendicular to the atom beam. In such a way the same 2D map of the lithium cloud can be achieved as in the hot wire detector.

From the exploration of ribbon parameters, we found that with a ribbon pulse length of 100 µs and a ribbon relative delay to nozzle of -50 µs $\sim$ 0 µs provide a good beam shape and flux. The total entrained atom number is sensitive to the ribbon voltage, which determines the surface temperature of the ribbon. Additionally, the pulse length of the carrier gas also influences the entrainment property. A set of measurement data from the scanning laser is shown in Fig. 4.18.

From plots in Fig. 4.18, one may see that with pulsed ribbon we could get up to

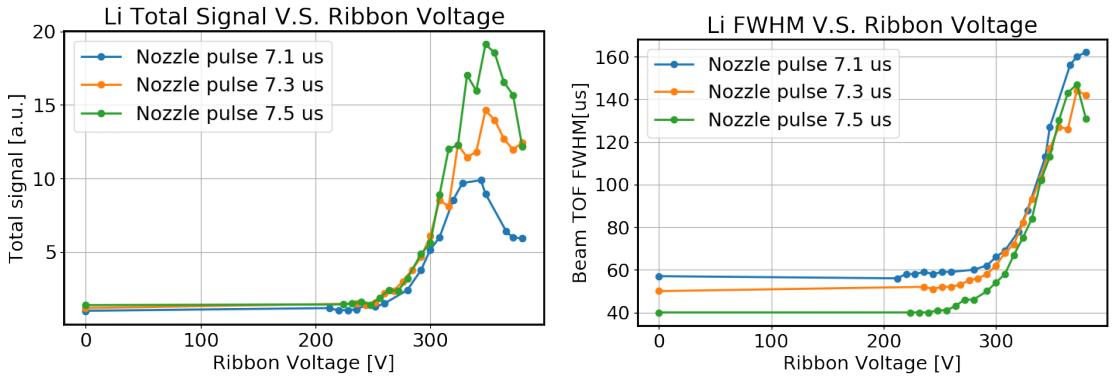


Fig. 4.18: Ribbon + Oven entrainment with ribbon voltage scan at different nozzle pulse length, shown are lithium cloud total signal (left), normalized to data point corresponding to oven entrainment only (when ribbon voltage is 0), and time-of-flight FWHM (right).

almost 20 times the amount of lithium as compared to only using the oven. The gain over the oven entrainment first increases with increasing ribbon voltage, then starts decreasing after reaching a maximum with even higher ribbon voltages. It is possible that the increasing current in the pulsed ribbon starts influencing the carrier gas. An additional observation during the experiment is that the electric arcs between the two ribbon clamps starts to appear at these high voltages.

One may also notice that, with increased amount of lithium atoms entrained due to ribbon pulsing, the resulting lithium beam properties also change. Shown on the right of Fig. 4.18 is the increasing FWHM of the time of light measurement with the increased ribbon voltage. We further confirmed with addition two-point measurement that this is from the increasing temperature of the lithium beam. Unfortunately, this beam heating effect from pulsed ribbon is unexpected. As we are getting decent amount of lithium atoms with only oven as entrainment method, we decide to move on with it and leave the ribbon method as potential future improvements that can be done in our system.

A full characterization of the lithium beam is done with a two point scanning laser measurement, as shown in Fig. 4.19. The laser separation is 0.2 m, and the data was measured under nozzle temperature at 18 K and other optimized parameters.

A lot of useful information can be extracted from this measurement. First, let's look into the longitudinal speed of the beam. The time of arrival is extracted from the

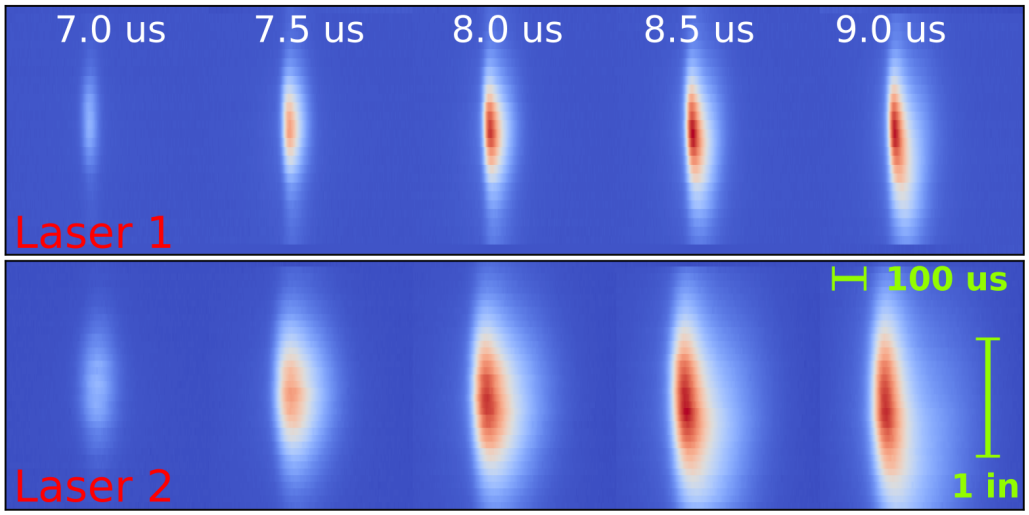


Fig. 4.19: Laser two-point measurement 2D map of lithium beam with oven entrainment, at various nozzle pulse length from 7 µs to 9 µs. The two lasers are set apart by 0.2 m.

peaks for both lasers, knowing the separation of the two measurement points allows us to find the speed of the beam, as shown in Fig. 4.20.

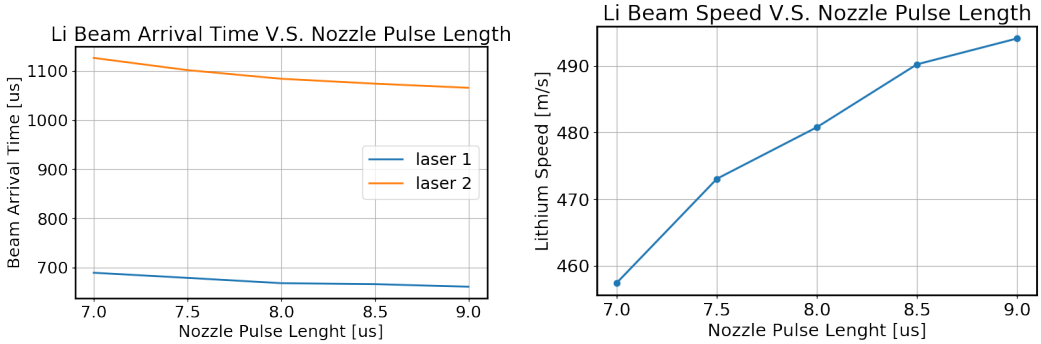


Fig. 4.20: Lithium beam longitudinal velocity from laser two-point measurement, using oven as entrainment method. Laser separation 0.2 m.

As our laser is scanned in perpendicular to the atom beam, the width can thus be extracted and using Eq. 4.23 and 4.24, shown in Fig. 4.21.

Additionally, we also used laser spectroscopy at low intensity to extract the transverse temperature of beam, as shown in Fig. 4.22.The laser frequency is detuned from the resonant frequency using a VCO the measured lithium signal is plotted in relation

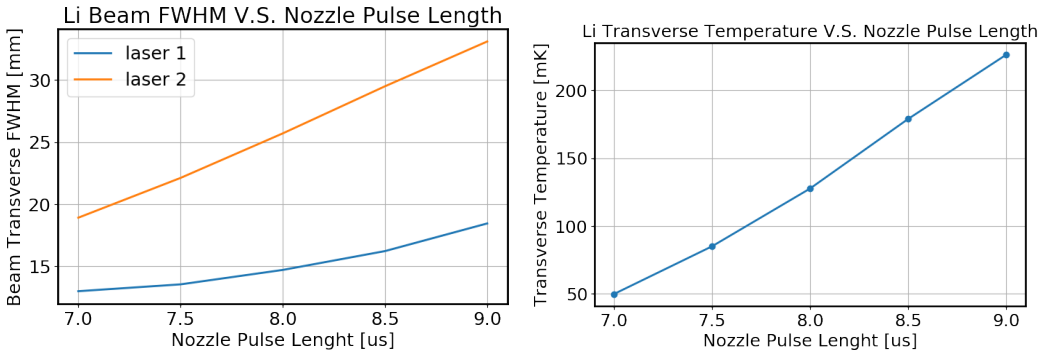


Fig. 4.21: Lithium beam transverse temperature from laser two-point measurement, using oven as entrainment method. Laser separation 0.2 m.

to the frequency detuning. The standard deviation is extracted from a Gaussian fit, which is then used to extract the beam temperature. The resulting temperature is 160 mK at a nozzle pulse length of 8.0 µs, which is close to the result from two-point measurement.

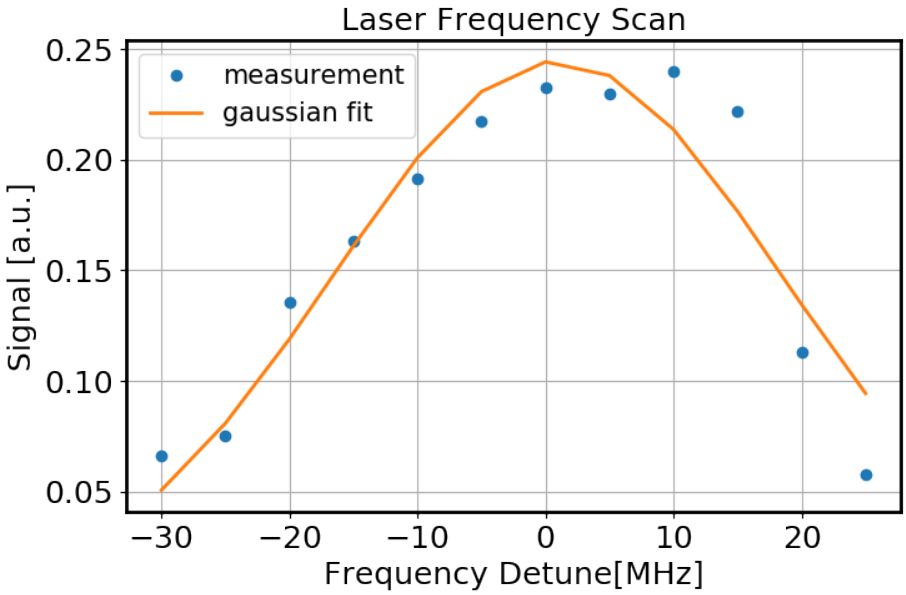


Fig. 4.22: Lithium beam transverse temperature measurement from laser spectroscopy. Oven is used as entrainment method at 18K. Gaussian fit result equation: $0.24 * exp[(x - 0.94)^2/(2 * (17.44)^2)]$.

Similarly, the longitudinal temperature can be extracted by studying the time-of-

flight FWHM, and using Eq. 4.22. The result is shown in Fig. 4.23.

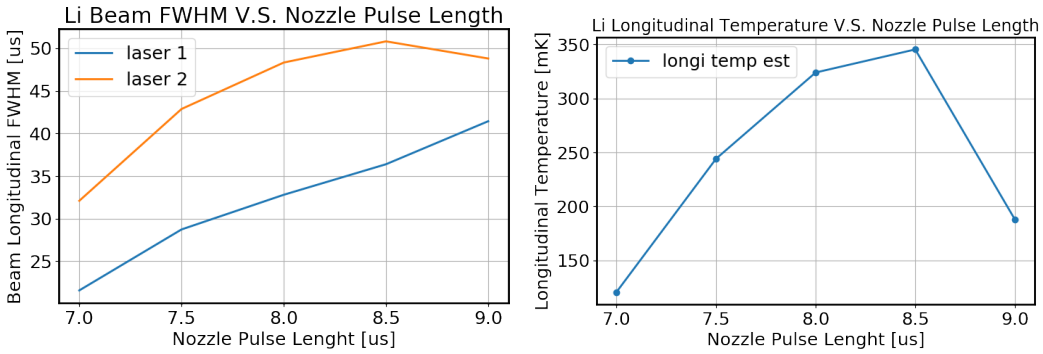


Fig. 4.23: Lithium beam longitudinal temperature from laser two-point measurement, using oven as entrainment method. Laser separation 0.2 m.

### 4.4.7 Summary

From above discussions, we come up with a set of parameters for operating the decelerator. The Even-Lavie nozzle is chosen to be operated at a temperature of 18 K with 7.5 µs pulse length, using helium as the carrier gas. This condition combined with a hot lithium oven at 550 °C gives us a lithium beam containing about $10^{11}$ atoms with a longitudinal speed of 480 $\mathrm{m\,s^{-1}}$, which is within the capture range of the decelerator. Additionally, the lithium cloud under this condition has a translation temperature of under 100 mK and a longitudinal temperature of under 250 mK, which is suitable for the moving trap in the decelerator.

We found these parameters with a measurement at about 1.5 m downstream from the skimmer, however, the actual entrance of decelerator is preferred to be located as close as possible to the skimmer exit. These obtained parameters are good as a starting point for operating the decelerator, fine-tuning might be needed later for optimizing its performance.

# Chapter Five: Magnetic decelerator

In the previous chapter we discussed the properties of the supersonic lithium beam exiting the Even-Lavie valve. As has been pointed out, although the low transverse temperature of the beam ($< 100$ K) is a good starting point, the longitudinal velocity of the beam is way too high to trap or perform any measurement that needs longer than a few microseconds. The 2.5-meter-long magnetic decelerator, which is discussed in this chapter, is built to slow the atoms to trappable velocities, without raising the transverse temperature.

Another novel property of our magnetic decelerator is that it only relies on the magnetic momentum of atoms or molecules for deceleration. Thus, it is a general method that is applicable to almost all neutral elements in the periodic table with magnetic momentum. This is a tremendous advantage over the traditional Zeeman decelerator which relies on the scattering force from a resonant photon and is hence largely limited by availability of a resonant transition and a laser. As an example application of interest, our magnetic could potentially provide flux of cold hydrogen atoms, or even anti-hydrogen.

In this chapter, I present the ideas behind our magnetic decelerator assembly with theoretical analysis and experiment measurement. Numerous details of the decelerator design, assembly, electronics, control sequences, and configurations are provided. Due to its complexity, a series of methods have been developed to test the control and electronic functionality. These test measurements are also discussed. Finally, I show the performance of the magnetic decelerator in the experiment, including the optimization procedure and potential improvements.

## 5.1 Deceleration methods

Deceleration, or slowing, is necessary when loading atoms into a confinement region from a directed source. A Zeeman slower, which relies on the magnetic Zeeman effect to keep decelerating atoms on resonant with a counter propagating laser, is the most commonly used technique for alkali atoms. The technique was first realized by William D. Phillips [96] and became a common step for realization of the

Bose-Einstein Condensation (BEC). Together with Steven Chu and Claude Cohen-Tannoudji, the Nobel Prize in 1997 is rewarded for their contributions on development of methods to cool and trap atoms with laser light [26]. The electric counter part of the Zeeman slower, the Stark decelerator [13], which relies on electric dipole moment of molecules, was first realized in 1999. There are also many other deceleration methods that have been developed since then. The Optical Stark Decelerator [45] uses an optical dipole force at high laser power, the Rydberg Stark decelerator has been applied on hydrogen [125], the time-varying electric-field gradient slowing makes use of a large electric dipole polarizability [76], and a high intensity pulsed optical lattice has also been used to slow supersonic molecules [9].

### 5.1.1 The Zeeman slower

The commonly used Zeeman slower consists of a series of solenoids wrapped around a vacuum cylinder, together with a cooling laser that is counter propagating towards the atomic beam. The coils are arranged in a way such that atoms experience larger magnetic fields at high velocities, thereby compensating the large Doppler shift of the laser frequency. This guarantees that the atoms always remain resonant with the laser. As the atoms slow down, smaller magnetic field strength is needed, which is provided by fewer solenoid windings, as shown in Fig. 5.1. The required spatially inhomogeneous magnetic field is given by [79]

$$B = B_0 + B_z\sqrt{1 - z/z_0}, \tag{5.1}$$

where $B_0$ is the bias field which defines the angular momentum axis for atoms, $B_z$ is the maximum field along z axis (atom propagation direction), $z$ is the position along the same direction and $z_0$ is the total length of the Zeeman slower.

Zeeman slower has the advantage of maintaining a high atom-photon scattering rate. However, since it relies on the force from the photon scattering along one dimension, the Zeeman slower only works for atoms with a closed optical dipole transition to avoid atoms going dark to the laser, hence it is limited to just a few atoms. Most molecules can not be decelerated by this method. Another shortcoming is that the deceleration is only along the z-axis. As atoms get slowed down, the expansion along transverse direction could lead to loss. To reduce the transverse expansion, on often add an extra stage of optical molasses for transverse cooling.

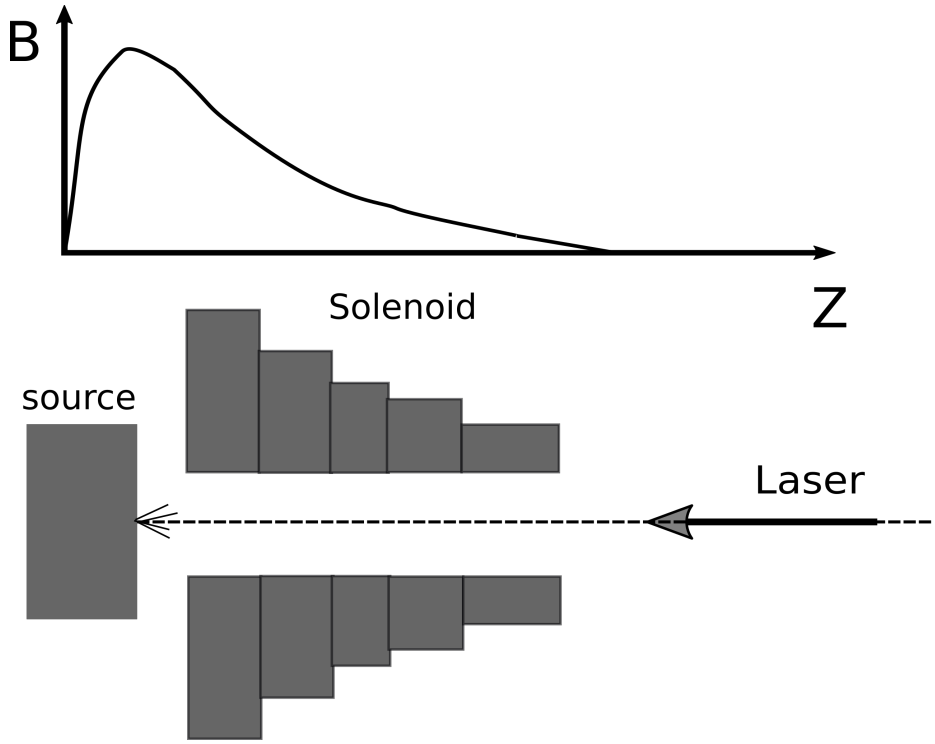


Fig. 5.1: A typical setup of Zeeman slower.

Some groups use spectrally broadened laser to perform the cooling over a large range of Doppler shifts [22].

### 5.1.2 The Stark decelerator

The Stark decelerator leverages the attraction of bipolar molecules in an external electric field. Molecules in an appropriate quantum state with electric dipole moment will gain Stark energy in an electric field, which is compensated by a loss in kinetic energy. With a constant electric field, atom will regain the loss in kinetic energy when leaving the field region. In the sense of energy, it is just like the molecules are climbing a potential wall of electrical dipole energy. If the electric field is switched off before the molecules start experiencing a decreasing field strength, the molecules will not regain their lost kinetic energy. By repeating this procedure through multiple stages of pulsed electric fields, molecules can be slowed to a standstill. A typical setup of a Stark decelerator is shown in Fig. 5.2, where a sequence of high voltage dipoles are switch on and off alternatively, creating effectively moving potential hills

that always keep up right in front of the molecule cloud. Usually there are additional sets of hexapole fields to perform focusing transversely, as the potential wall is only one-dimensional and doesn't provide any confinement.

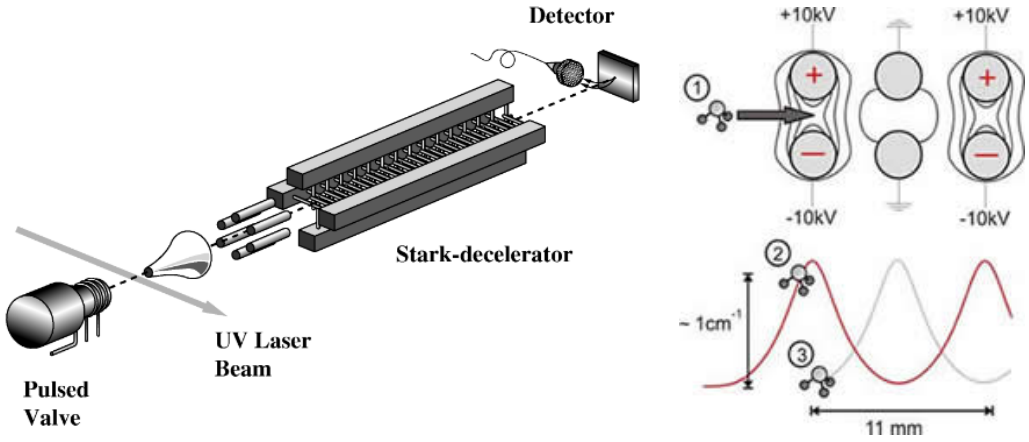


Fig. 5.2: A typical setup of the Stark decelerator, figure from [13].

### 5.1.3 The magnetic Coilgun

The magnetic coil gun, or sometimes called the Zeeman decelerator (as distinguished from the Zeeman slower), is the magnetic counter part of the Stark decelerator. It is based on the same idea as the Stark decelerator, but uses magnetic dipole moment instead of electric dipole moment.

The magnetic coilgun was first demonstrated by our group and Merkt's group at ETH Zürich. The magnetic coil gun initially consists of 18 coils in 2007 [88], and later upgraded to 64 coils in 2008 [86]. Metastable neon atoms were used for deceleration. This magnetic coil gun was later applied to molecules. In 2008, our group and co-worker reported the deceleration of oxygen molecules [87]. The general setup of the coilgun is shown in Fig. 5.3. Merkt and co-workers also demonstrated the deceleration based on the same idea to slow down a beam of Hydrogen [116] and Deuterium atoms [59], initially using six and later 12 pulsed magnetic field stages [60].

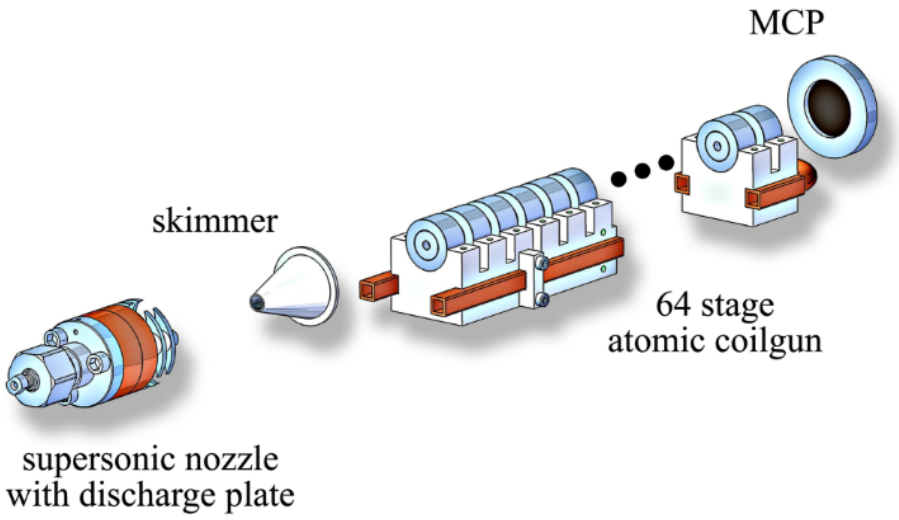


Fig. 5.3: A typical setup of magnetic coilgun, figure from [86].

### 5.1.4 Summary

As can be seen from the above discussion, there are generally three categories of deceleration methods for atoms or molecules: the photon scattering, the electrical dipole potential, and the magnetic dipole potential. They all have their advantages and limitations, as summarized in Table 5.1.

| Method | Pros. | Cons |
|---|---|---|
| The Zeeman slower | simple, fast | Only applicable to a few atoms, due to availability of cycling transition and laser. No transverse confinement. |
| The Stark decelerator | strong force; compact; low current; easy to control. | Only applicable to molecules with large electric dipole. No transverse confinement. |
| The Magnetic Coilgun | General for atoms and molecules with magnetic dipole | Weak force; needs high current in coils; weak transverse confinement. |

Table 5.1: Comparison of deceleration methods for atoms and molecules.

## 5.2 The adiabatic decelerator

### 5.2.1 Operation principle

The adiabatic decelerator is similar to the magnetic coilgun in that it makes use of the magnetic dipole moment of atoms or molecules, but it is still a different method of deceleration. Instead of making use of the potential hill experienced by atoms along one dimension in a magnetic field, the idea of adiabatic decelerator is to wrap the atom or molecule cloud with a three-dimensional, "effectively" moving trap. By reducing the moving speed of the trap along the propagation axis of atoms while keeping them confined in the other two directions, atoms or molecules are decelerated adiabatically without spreading in transverse directions.

To optimize the deceleration, there are a few questions to answer: How to create a trap unit? What is the trap profile? How to make the trap "effectively" moving? And how to control each of the moving trap unit accurately in terms of their field strength and activation time? All these questions will be discussed individually in the following subsections.

### 5.2.2 Trapping force

There are many ways one can exert controlled force on neutral atoms and molecules. We prefer a general method that can be applied to most of neutral atoms as well as molecules. Since almost all neutral atoms in their ground state or metastable states are paramagnetic, as shown in Fig. 5.4, we elect to use magnetic forces. Additionally, most molecules also have paramagnetism property.

Atoms and molecules are said to be paramagnetic when they have a net magnetic dipole moment. The dipole moment in atoms and molecules originates from the motion of the unpaired electrons around the atomic core or the molecule center. This magnetic dipole moment can be used as a handle to control the motion.

### 5.2.3 The quadrupole trap

Having selected the magnetic dipole moment as the general handle to control the motion of atoms or molecules, the next step is to make a trap from it. A magnetic trap should exert conservative force pointing towards a specific point, e.g. trap cen-

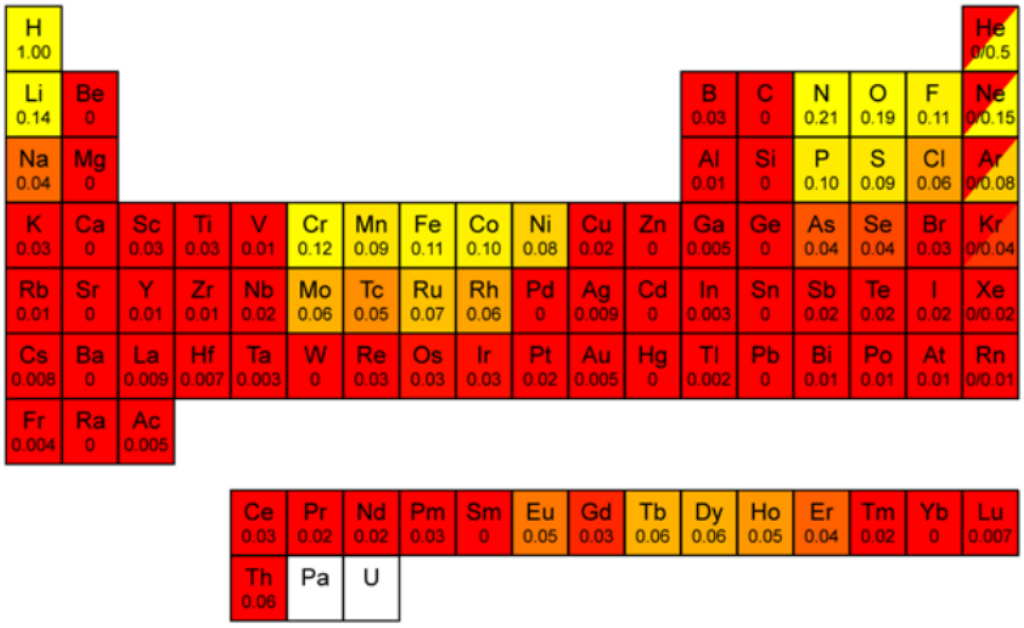


Fig. 5.4: Periodic table of elements with the maximum effective magnetic dipole of ground-state atoms (in Bohr magneton) [38] divided by their mass (in AMU). Nobel gas has their metastable state included. Yellow color shows relative high magnetic dipole to mass ratio, red shows low and white shows no magnetic dipole. Figure srouce: [14].

ter, in all three dimensions. The force experienced by a magnetic dipole and the corresponding potential energy is given by

$$\vec{F} = \nabla(\vec{\mu} \cdot \vec{B}) \tag{5.2}$$

and

$$U = -\vec{\mu} \cdot \vec{B} = m_j g_j \mu_B B, \tag{5.3}$$

where magnetic moment is given by $\vec{\mu} = -m_j g_j \mu_B \hat{z}$, with Bohr magneton $\mu_B$, $m_j$. Here $m_j$ is the fine structure total angular momentum projected along its axis $\hat{z}$, and $g_j$ as the Landé g-factor. The magnetic moment $\vec{\mu}$ originates from the electron motion described by the Amperian loop model. $\vec{B}$ is the magnetic field. In most cases, where the changing rate of the external magnetic field is smaller than the Larmor frequency, the magnetic dipole moment $\vec{\mu}$ of an atom is always aligned parallel with the direction of field $\vec{B}$.

Atoms with states $m_j > 0$ are trend to move towards the magnetic field minimum, called "low-field-seekers" (LFS). Similarly, those atoms with states $m_j < 0$ are inclined to stay at the field maximum, they are called "high-field-seekers" (HFS). Thus, LFS is suitable to be trapped at the field minimum.

Such a trap can be realized by using a pair of coils oriented along the same axis but with current flow in the opposite direction, called the 'anti-Helmholtz' configuration, or magnetic quadrupole, as shown in Fig. 5.5.

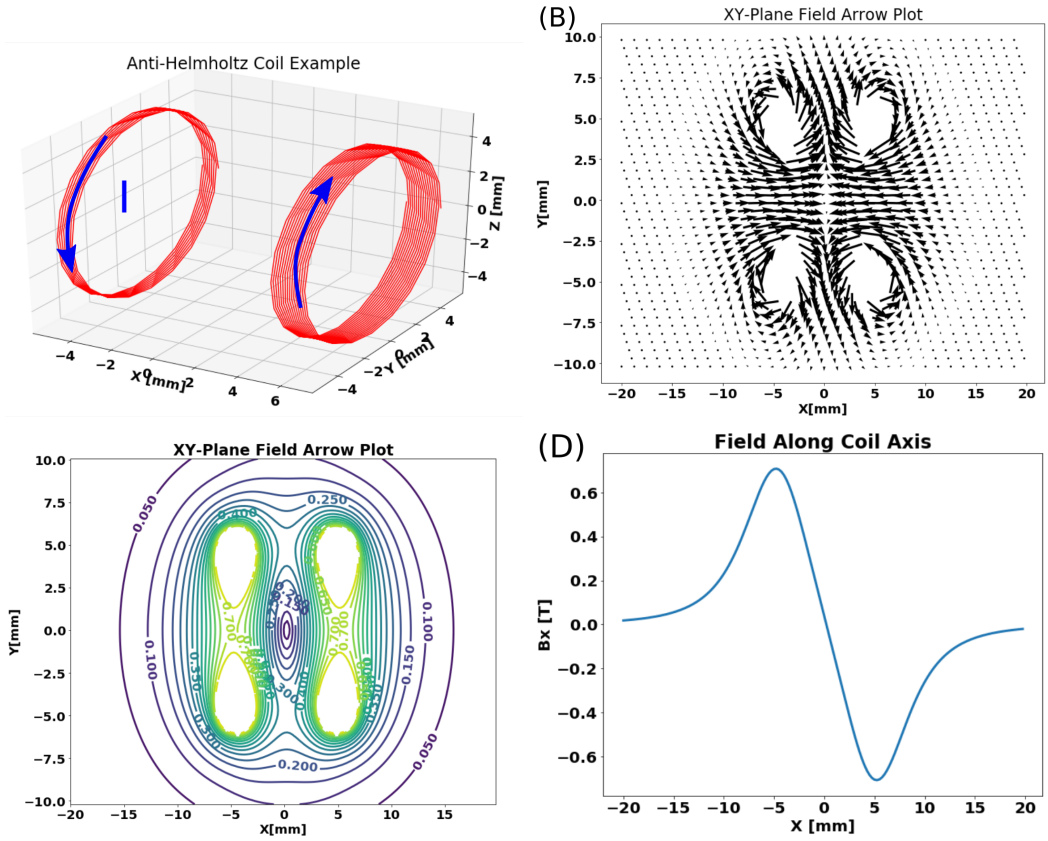


Fig. 5.5: An example of the anti-Helmholtz setup with balanced coil winding. (A) shows the geometry of the coil pair; (B) shows an arrow plot of magnetic field; (C) is the contour plot of the field strenght and (D) shows the field strength along the symmetry axis. Coil radius: 5mm, coil space: 10 mm, current: 400 A, coil winding: 16.

The magnetic field along the coil axis is given by:

$$\begin{aligned} \vec{B_z}(z) &= \frac{\mu_0 R^2}{2}\left[\frac{I_1 N_1}{((d/2-z)^2+R^2)^{3/2}}\hat{z} + \frac{I_2 N_2}{((d/2+z)^2+R^2)^{3/2}}\hat{z}\right] \\ &\overset{I1=-I2=I}{=} \frac{\mu_0 I R^2}{2}\left[\frac{N_1}{((d/2-z)^2+R^2)^{3/2}}\hat{z} + \frac{N_2}{((d/2+z)^2+R^2)^{3/2}}\hat{z}\right] \end{aligned}, \tag{5.4}$$

where $\mu_0 = 1.257 \times 10^{-6}$ N A is the vacuum permeability, $R$ is the coil radius (assume both coils have the same radius), and $I_1$, $I_2$ are the currents in each of the coils with their sign indicates the direction of current. The coils are separated by a distance of $d$ and the field is given at a displacement of $z$ from the geometric center of the coil pair.

If we set the winding for the two coils in the anti-Helmholtz to be the same, the magnetic field minimum $\|B\|_{\min}$ will be located at the center of the coils. More generally, if given the two coils with different winding $N_1 \neq N_2$, the field minimum corresponding to $B_x(x) = 0$ is given by

$$\begin{cases} z = \frac{2\sqrt{d^2Q-(Q-1)^2R^2}+(Q+1)d}{2(Q-1)} & Q \neq 1 \\ z = 0 & Q = 1 \end{cases}. \tag{5.5}$$
$$\text{with} \quad Q = (\frac{N_2}{N_1})^{\frac{2}{3}}$$

When $d = 2R$, and $N_2/N_1$, we have the displacement of field minimum from the geometry center of the coils $z \approx 0.2R$. For our magnetic decelerator, $R = 5$ mm, resulting in a displacement of about 1 mm, as can be seen from Fig. 5.6. Similarly, The potential energy of a magnetic dipole in such a field yields a minimum at the near the center of the trap, as shown in Fig. 5.5 and Fig. 5.6.

Remember that our ultimate goal is to decelerate the atoms. If atoms are moving with a constant speed, the trap profile seeing by atoms will appear to be the same as in the lab frame, shown in Fig. 5.6. However, when the atoms undergo a deceleration, the trap potential experienced by them will have to be modified, as the co-moving frame is not an inertial frame. The modified potential energy of a magnetic dipole in a decelerating trap is given by

$$U_{\text{co-moving}} = m_j g_j \mu_B B + ma\Delta z, \tag{5.6}$$

where $a < 0$ is the constant acceleration of the moving trap, $\Delta z$ is the displacement of the atoms relative to the zero-field center of the trap, and $m$ is the mass of atom.

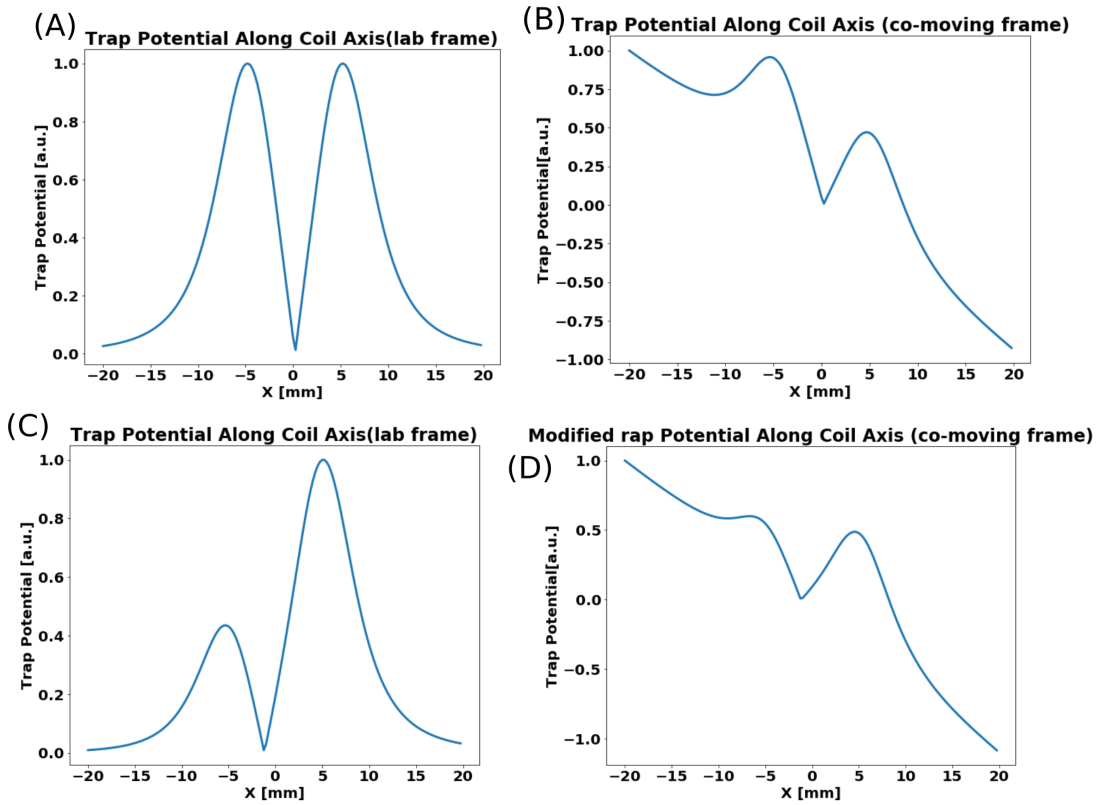


Fig. 5.6: Calculation of trap potential along symmetry axis with anti-Helmholtz configuration. Showing in the figure is the trap potential with the same windings (16) for both coils, in lab frame (A) and co-moving frame (B), as wll as modified trap potential with from coil winding of 16 and back coil winding 8, in lab frame (C) and co-moving frame (D). Coil radius: 5mm, coil space: 10 mm, current: 400 A, acceleration: 45580 $\mathrm{m\,s^{-2}}$.

From Eq. 5.6 we learn that, due the to deceleration ($a < 0$), the front trap peak in Fig. 5.6 (A) will be reduced while the trap back peak will be lowered, resulting a modified potential seeing by atoms as in 5.6 (B).

When the same winding are applied for the front and back coils, one notice that the actual trap depth is limited to the lower peak of the potential energy (Fig. 5.6 (B)). This indicates that the balanced winding setup is not fully making use of the generated potential. As an improvement, we can apply different winding to the front and back coils in the anti-Helmholtz configuration, e.g. 16 winding for the front coil, and 8 winding for the back coil. This modification yields an imbalanced potential in the lab frame but gives better balancing in the co-moving frame, as can be seen in

Fig. 5.6 (D). The calculation of imbalanced coil setup of anti-Helmholtz configuration is shown in Fig. 5.7.

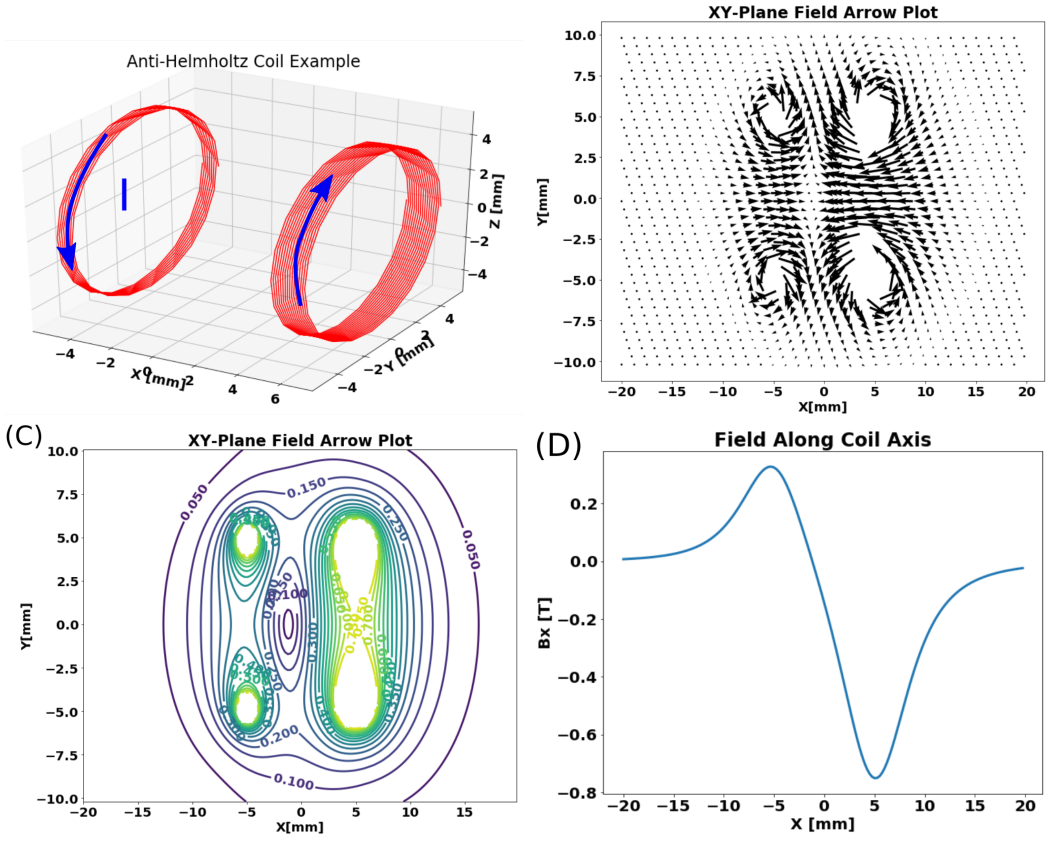


Fig. 5.7: Imbalanced anti-Helmholtz coils setup with front coil 16 winding and back coil 8 winding. Shown in the figure are the geometry of the coil pair (A), the arrow plot of magnetic field (B), the contour plot of field strength (C) and the field strength along the symmetry axis (D). Coil radius: 5mm, coil space: 10 mm, current: 400 A.

Study of the trap potential in the co-moving frame helps to decide the trap depth along the longitudinal direction. From Eq. 5.6, a rough estimation of the front and back potential in co-moving frame is

$$\begin{aligned} U_{\text{front-co-moving}} &= \max\{0, m_j g_j \mu_B B_{\text{front}} + mad/2\} \\ U_{\text{back-co-moving}} &= m_j g_j \mu_B B_{\text{back}} - mad/2 \end{aligned} . \tag{5.7}$$

Then the trap depth in kelvin is given by

$$T_{\text{trap}} = \frac{\min\{U_{\text{front-co-moving}}, U_{\text{back-co-moving}}\}}{k_B}, \tag{5.8}$$

where $k_B = 1.38 \times 10^{-23}$ $\mathrm{m^2\,kg\,s^{-2}\,K^{-1}}$ is the Boltzmann constant. The trap depth in term of temperature $T_{\mathrm{trap}}$ has to be at least as large as the atom cloud temperature.

### 5.2.4 Moving trap time sequence

In the previous section we discussed the unit trap configuration for deceleration. The next problem to answer is how to make the trap move together with the atoms. Physically moving the coil in a controlled manner at hundreds of meters per second is not viable. An alternative is to fix a series of coils along the atom beam path while switch on the corresponding trap only when at in the trap center. This way, we switch a 480 traps in a timely controlled manner to create an "effectively" moving trap.

Importantly, simply a moving trap itself won't guarantee that the atoms are decelerated properly, one also need to handle the transferring of atomic cloud from one trap to the next, which we want to be as smooth as possible. The smooth transferring of atoms between the traps is realized by overlapping neighboring traps in both space and time. In the time domain, we used a sine shaped current pulse to generate these fields in the decelerator, as shown in Fig. 5.8.

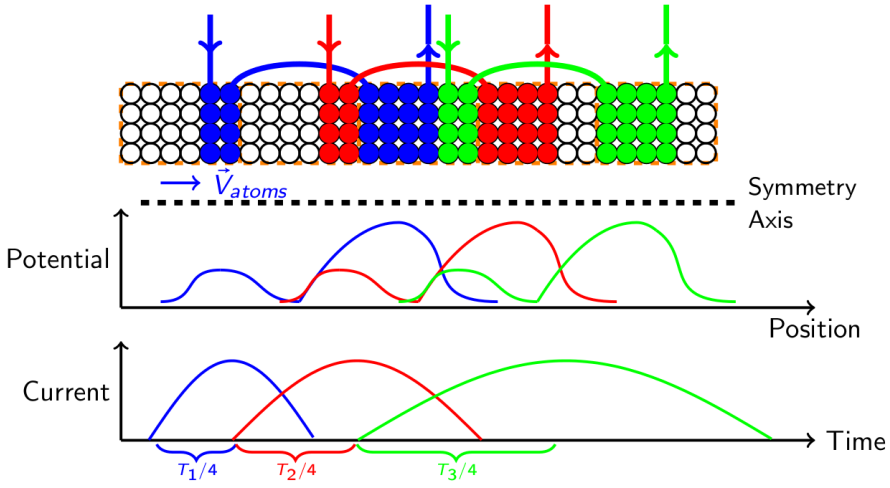


Fig. 5.8: Illustration of moving trap setup. Top: three traps forming unbalanced anti-Helmholtz coils are arranged in an overlapped manner, only half are shown according to symmetry. Middle: the trap potential distribution in the lab frame. Bottom: current in coils as a function of time, showing the overlap between neighboring pulses.

Fig. 5.8 shows imbalanced anti-Helmholtz coil configurations, with front coil having 16 winding (4 x 4) and back coil having 8 winding (2 x 4). This arrangement also yields the result that the maximum potential of the previous trap is spatially overlapping with the next trap minimum. If we use a fixed coil distance $d$ for each trap, the overlapping part of two neighboring traps becomes $d/2$. This distance can be set by using a plastic spacer. In our settings, the wire diameter is 405 µm, corresponding to American Wire Gauge (AWG) of 26. Precise control of coil spacing was realized by careful design of coil mount structure. The coils are activated using half-sine shaped current pulse.

The trap turn on time determines the relative position of an atom cloud in a trap when the corresponding trap is activated. In order to achieve the maximum deceleration from each individual trap, we only switch off the trap when the atoms reach the top of the corresponding potential hill. In the mean time, the next trap is activated, at which point the atoms are at the field minimum the next trap, as shown in Fig. 5.8. This operating manner is similar to the one for the Stark decelerator and the coilgun, as discussed in Section 5.1.2 and Section 5.1.3.

Once we have a moving trap, we would like to write the trap turn on time $t_j$ and the trap pulse length $T_j$ as a function of trap number $j$, total number of traps $N$, initial velocity $v_0$, and the final velocity $v_t$.

First, assuming an overall constant deceleration, the distance of j-th trap center from the center of first trap is

$$L_j = d(j-1), \tag{5.9}$$

where $d$ is the trap center to center distant as well as coil separation in a trap. Thus, the total distance for the constant deceleration is $L_N = d(N-1)$. Knowing the initial and targeted velocities, the acceleration a can be derived according to the Newtonian dynamics:

$$a = \frac{v_t^2 - v_0^2}{2L} = \frac{v_t^2 - v_0^2}{2d(N-1)} \quad j = 1, 2, ..., N. \tag{5.10}$$

Second, using the global acceleration derived above, and note that a trap is turned on when atoms arrive at the field minimum, we have the atom speed for the j-th trap as:

$$\begin{aligned} v_j &= \sqrt{v_0^2 + 2aL_j} \\ &= \sqrt{\frac{j-1}{N-1}v_t^2 + \frac{N-j}{N-1}v_0^2} \end{aligned} \tag{5.11}$$

with $v_1 = v_0$, $v_N = v_t$, and $j = 1, 2, ..., N$. The turn on time for the $j^{th}$ trap is given by

$$\begin{aligned} t_j &= t_1 + \frac{v_j - v_1}{a} \\ &= t_0 + \frac{2d(N-1)(\sqrt{\frac{j-1}{N-1}v_t^2 + \frac{N-j}{N-1}v_0^2} - v_0)}{v_t^2 - v_0^2}, \end{aligned} \tag{5.12}$$

where $t_1 = t_0$. Thus the total deceleration time is $T_{\text{tot}} = t_N - t_1 = \frac{2d(N-1)}{v_t + v_0}$.

The pule length of the j-th trap, $T_j$, is just twice $t_{\text{j+1}} - t_{\text{j}}$, or

$$\begin{aligned} T_j &= 2(t_{\text{j+1}} - t_{\text{j}}) \\ &= \frac{4d(N-1)}{v_t^2 - v_0^2}\Big[\sqrt{\frac{j}{N-1}v_t^2 + \frac{N-j-1}{N-1}v_0^2} - \sqrt{\frac{j-1}{N-1}v_t^2 + \frac{N-j}{N-1}v_0^2}\Big]. \end{aligned} \tag{5.13}$$

Finally, to get some feeling of the actual values used, we apply the above equations to our experiment. We decelerate the atoms from $v_0 = 480\ \text{m}\,\text{s}^{-1}$ to $v_f = 50\ \text{m}\,\text{s}^{-1}$ with $N = 480$ coils. The calculated acceleration is $a = 46484\ \text{m}\,\text{s}^{-2}$, the pulse length of traps ranges from $T_1 \approx 80$ µs to $T_{480} \approx 400$ µs, and the total deceleration time is $T_{\text{tot}} \approx 10$ ms.

## 5.3 Assembly

### 5.3.1 Trap coils

According to the characterization of the atom beam (see Section 4.4), an atom cloud with transverse dimension of less than 8 mm (FWHM) is obtained after the skimmer. We decide to make the diameter of the decelerator coils to be about 10 mm. The design is targeted for an initial speed of 480 $\text{m}\,\text{s}^{-1}$ and a final speed of 50 $\text{m}\,\text{s}^{-1}$. Combined with other considerations from the aspect of electronics and structure, a set of trap coil parameters was decided, as shown in Table 5.2. The total length of the decelerator is about 2.5 m.

Considering the realization of the spatial overlapping of neighboring traps, the front and back coils of each anti-Helmholtz coil pairs are structurally packed separately. Shown in Fig. 5.9, a coil pack is sandwiched in between two others, and two consecutive odd or even packs contribute to a pair of anti-Helmholtz coils than forms a trap. Such arrangement makes use of the space efficiently while avoiding entanglement of wires.

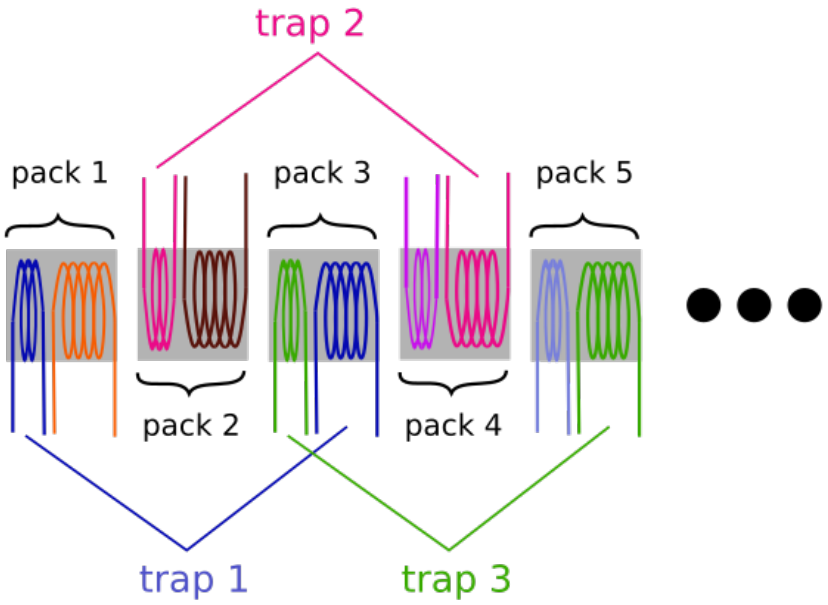


Fig. 5.9: The schematic of coil packing. Each coil of the same anti-Helmholtz pair is packed with the one in the skipped neighborhood.

To dissipate heat generated by the high current pulses, every 10 coil packs are further assembled into an aluminum heat sink block with plastic spacers to set the correct separation distance. Heat conducting epoxy (EPOXIES CAT.30TB13) was applied and baked for 4 hrs to make the unit solid, as shown in Fig. 5.10, in total there are 48 these blocks. A vacuum tube made of Inconel goes through the opening and all

| | |
|---|---|
| Coil bore diameter | 10.2 mm |
| Coil wire diameter | 405 µm (AWG 26) |
| Coil winding front | 4 (layers) x 4 (turns) |
| Coil winding back | 4 (layers) x 2 (turns) |
| Anti-Helmholtz coils inductance | 4.8 µH |
| Anti-Helmholtz coils resistance | 0.15 Ω |
| Total resistance for single coil circuit | 0.20 Ω |
| Front-back coil separation | 10.8 mm |
| Coils overlapping | 5 mm |
| Coils current | $0 \sim 500$ A |
| Total number of coils | 480 |

Table 5.2: Adiabatic decelerator coil design parameters.

aluminum heat sinks are aligned. There is extra supporting electric interface attached to each of the heat sink holders, to convert wires to through hole pin interfaces, so that the 10 coils as a whole in the heat sink unit can be plug in and our easily to current supplying circuits, as shown in Fig. 5.10.

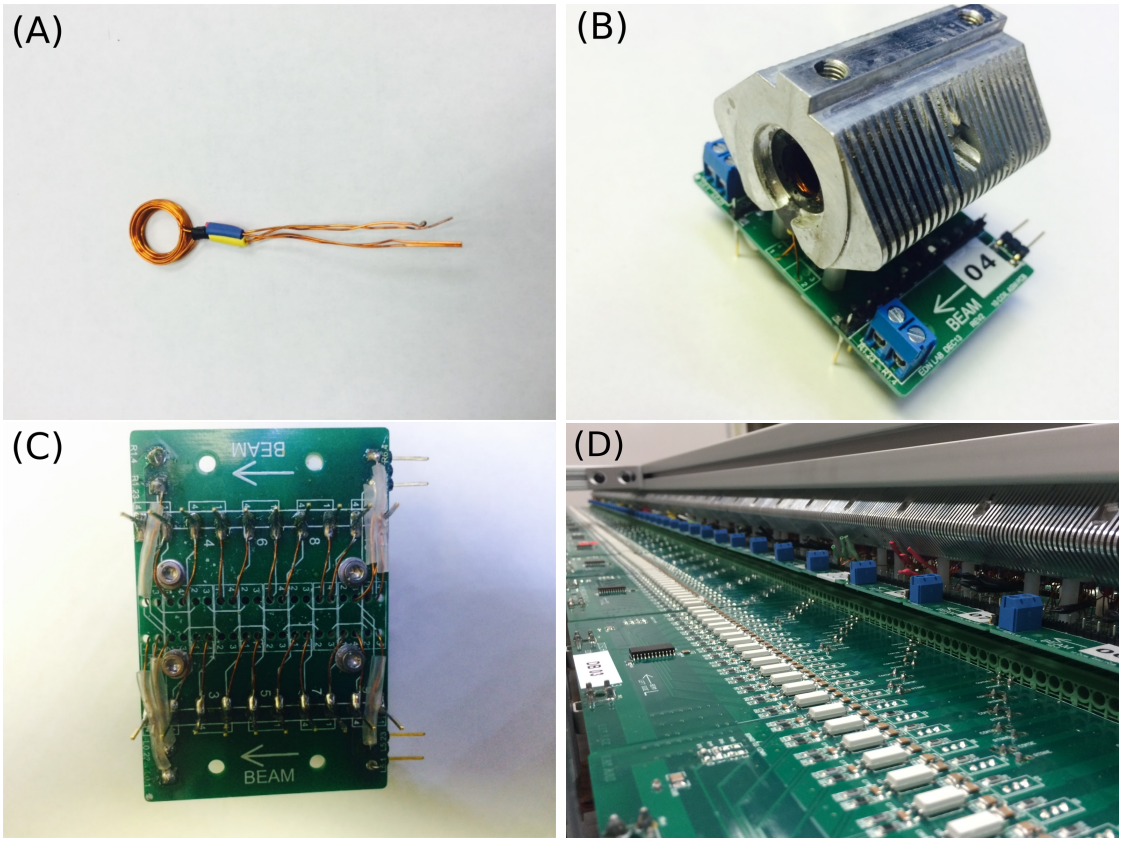


Fig. 5.10: Assembly of trap coils. Shown figures are: a single coil pack unit (A), an aluminum heat sink unit with 10 coils pairs (B), the support board for a heat sink unit (C) and a top view of 480 coils assembled on discharge board (D).

For a single trap with this setup and 400 $\sim$ 500 A current, the trap field along longitudinal and transverse direction is calculated, as shown in Fig. 5.11, the corresponding longitudinal and trap depth is also shown on the save figure with acceleration value $a = -46484\ \mathrm{m\,s^{-2}}$.

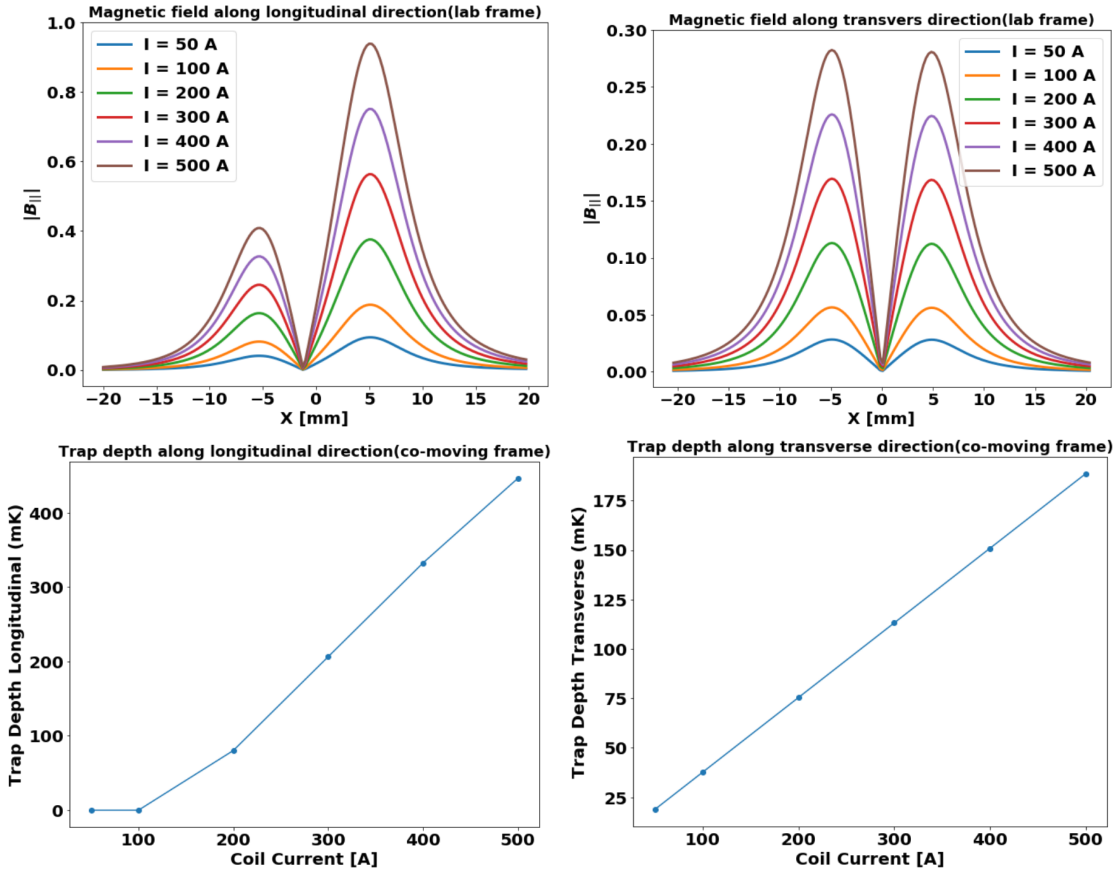


Fig. 5.11: Calculated magnetic field in a single Anti-Helmholtz pair with real parameters. Shown figures are: the magnetic field along the longitudinal direction (A), the magnetic field along the transverse direction (B), the trap depth along the longitudinal direction (C), and the trap depth along transverse direction (D).

### 5.3.2 Electronics

The electronic design of the adiabatic decelerator was quite a challenge. Some design requirements are:

- High current $\sim$ 500 A pulse is challenging for PCB.
- Precisely controlled current pulse width and start tiem of 480 individual coils.
- Consecutive pulse separation is small (10 ms $\sim$ 90 ms), recharge capacitor in time is necessary.

- Keep the sequence configurable to give pulse length ranges from 20 µs to 200 µs.

The general approach of achieving high current pulses is to use charged capacitor banks. In order to provide various current pulse times, combinations of binary valued (1, 2, 4, 8, ...) capacitors and inductors are used in the circuits, with an insulated-gate bipolar transistor (IGBT) associated to each of them as a configurable switch. By triggering a selected subset of these IGBTs we can configure the actual inductance $L$ and capacitance $C$ for each individual trap, thus control the pulse length.

Let's look at how to choose the values for L, C and R. Each of the 480 anti-Helmholtz coils can be modeled as an inductor with certain resistance $R$. For an RLC circuit, we have the current $i(t)$ as a function of time given by

$$\begin{aligned} & \frac{d^2i(t)}{dt^2} + \frac{R}{L}\frac{di(t)}{dt} + \frac{1}{LC}i(t) = 0 \\ or \quad & \frac{d^2i(t)}{dt^2} + 2\alpha\frac{di(t)}{dt} + \omega_0^2 i(t) = 0 \end{aligned}, \tag{5.14}$$

where $R$, $L$, $C$ are the total resistance, inductance and capacitance in the circuit, respectively. The RLC circuit undergoes oscillation with the attenuation factor $\alpha = R/2L$, the resonance frequency $\omega_0 = 1/\sqrt{LC}$ and the damping factor $\zeta = \alpha/\omega_0 = \frac{R}{2}\sqrt{\frac{C}{L}}$.

In our setup, each anti-Helmholtz coil circuit has a resistance of about $R_{\text{coil}} = 0.15\ \Omega$, inductance $L_{\text{coil}} = 4.8$ µH, with additional inductance from circuit, we have $\alpha = \frac{R}{2L} \leq \frac{R_{\text{coil}}}{2L_{\text{coil}}} = 20833$, which corresponding to damping time $1/\alpha$ of at least 48 µs. To ensure the damping time is long enough during the various pulse lengths, we want:

$$\text{Condition 1} : L_{\text{tot}} \geq \frac{T_{1/2}R}{2} = 0.1T_{1/2} \tag{5.15}$$

where $T_{1/2}$ is the pulse length of current in the coil in units of seconds.

Depending on the value of damping factor $\zeta$, the equation can be solved in different ways according to the under-damped ($\zeta < 1$), the over-damped ($\zeta > 1$) and the critically-damped ($\zeta = 1$) conditions. In our case, since a half-sine pulse is preferred, under-damped circuit is used, which requires

$$\begin{aligned} \text{Condition 2} : \zeta > 1 \Rightarrow & \frac{R}{2}\sqrt{\frac{C}{L}} > 1 \\ \Rightarrow & \frac{C}{L} > 100 \end{aligned}. \tag{5.16}$$

Additionally, we use thyristors to only obtain the positive part of the sine current. In the under damped situation, the solution of the current is

$$i(t) = C_1 e^{-\alpha t}\sin(\omega_d t) + C_2 e^{-\alpha t}\cos(\omega_d t), \tag{5.17}$$

where $\omega_b = \sqrt{\omega_0^2 - \alpha^2} = \omega_0\sqrt{1-\zeta^2}$ is the oscillation frequency, $C_1$ and $C_2$ are constants. We also have the time domain boundary condition: $i(0) = 0, V_{\rm coil}(0) = L_{\rm coil}\frac{di}{dt}|_{\rm t\,=\,0} = V_0$, which requires current of the anti-Helmholtz coil at initial discharge time to be 0 while the voltage to be the voltage on the capacitor banks. We have the solution of current as

$$i(t) = \frac{U_0}{L_{\rm coil}\sqrt{\frac{1}{LC} - \frac{R^2}{4L^2}}} e^{-\alpha t}\sin(\omega_b t). \tag{5.18}$$

Another quick but rough way to estimate the current in the circuit is using energy conservation in the circuit, ignoring the 0.15 $\Omega$ resistance and time dependencies, the energy in capacitors should be converted to inductors, $\frac{1}{2}L_{\rm tot}i^2 = \frac{1}{2}CU^2$ yields

$$i \approx V_0\sqrt{\frac{C}{L_{\rm tot}}}. \tag{5.19}$$

Also the half-sine pulse length can be approximated when $\alpha \ll \omega_0$, as

$$T_{1/2} \approx \pi\sqrt{LC}. \tag{5.20}$$

The above discussion provides a guideline for design of the circuit which satisfies all the requirements.

Considering the charging time for the capacitor bank, 10 sets of the same circuit were used to provide the current to the decelerator coils in a circulated way, called "tune boxes" ($TB1 \sim TB10$), e.g. tune box $TB1$ is responsible for coil number 1, 11, 21, ..., 471. Each tune box consist three circuit boards: the Boost Convert Charger (BCC), the Capacitor Box (CBOX) and the Inductance Box (LBOX). The output of each tune box is then connected to the upper level copper distribution lines which guide the current to the circuit boards interfacing with decelerator coils, called discharge board. The whole structure is shown in Fig. 5.12. We now discuss each circuit in turn.

**The Boost Convert Charger (BCC)** In order to get about 500 A current pulse, one needs voltages on the capacitors around 500 V. Simultaneously charging

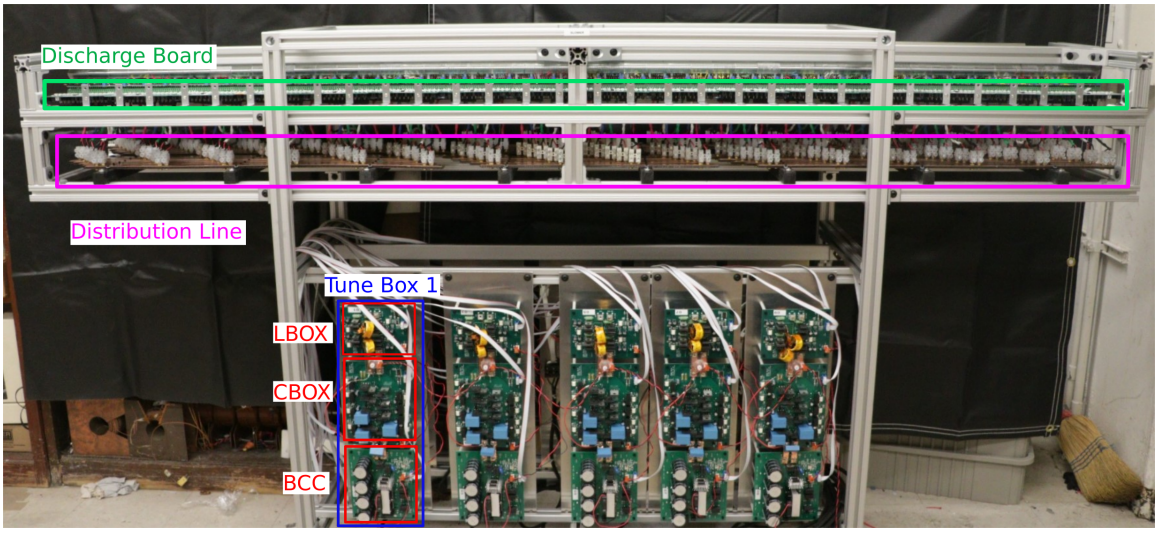


Fig. 5.12: Overview of decelerator electronics: Tune Box (TBX), BCC, LBOX, Discharge Board.

multiple parallel circuits to high voltages in a short time ($\sim$ 100 µs) is challenging. Charging a 10 µF capacitor with 2 A constant current takes $\Delta t = \frac{UC}{I} \approx 2.5$ ms, which is much longer than the total time that atoms spend in 10 consecutive coils (10 tune boxes are activated in a circulated way, total time atoms spend in 480 coils is about 10 ms). To shorten this time, one can either increase the charging current or use a boost circuit. Since large current increases the requirement of the power supply as well as PCB traces. A boost circuit is used for this purpose. The basic design of the BCC is shown in Fig. 5.13

We apply 100 V from an external DC power supply to the input terminal of the BCC. In step one, 10 capacitors each with 3900 µF capacitance get charged to $V_{\text{in}} = 100V$ with a current up to 2 A. IGBT1 and IGBT2 (model IXYX120N120C3), which act as fast and high power switches, are kept off at this point. Then, at step two, IGBT1 is activated while IGBT2 is still off. Charges from the capacitor bank flow through the 16 µH inductor yields a current of $I_{\text{step2}} = I_0 \sin(\omega_0 t)$, where $I_0 = V_{\text{in}}\sqrt{\frac{C}{L}} \approx 4937$ A and $\omega_0 = \frac{1}{\sqrt{LC}}$. If we let this process go by itself, after $\Delta t = \pi\sqrt{LC}/2 \approx 78$ µs the voltage on the capacitor bank drops to 0 V and the current in the inductor reaches a maximum of $I_0$. All the energy on the capacitor bank is thus transferred to the inductor. However, the current is too high and the time length is too long for practice considerations, so we interrupt step 2 before it

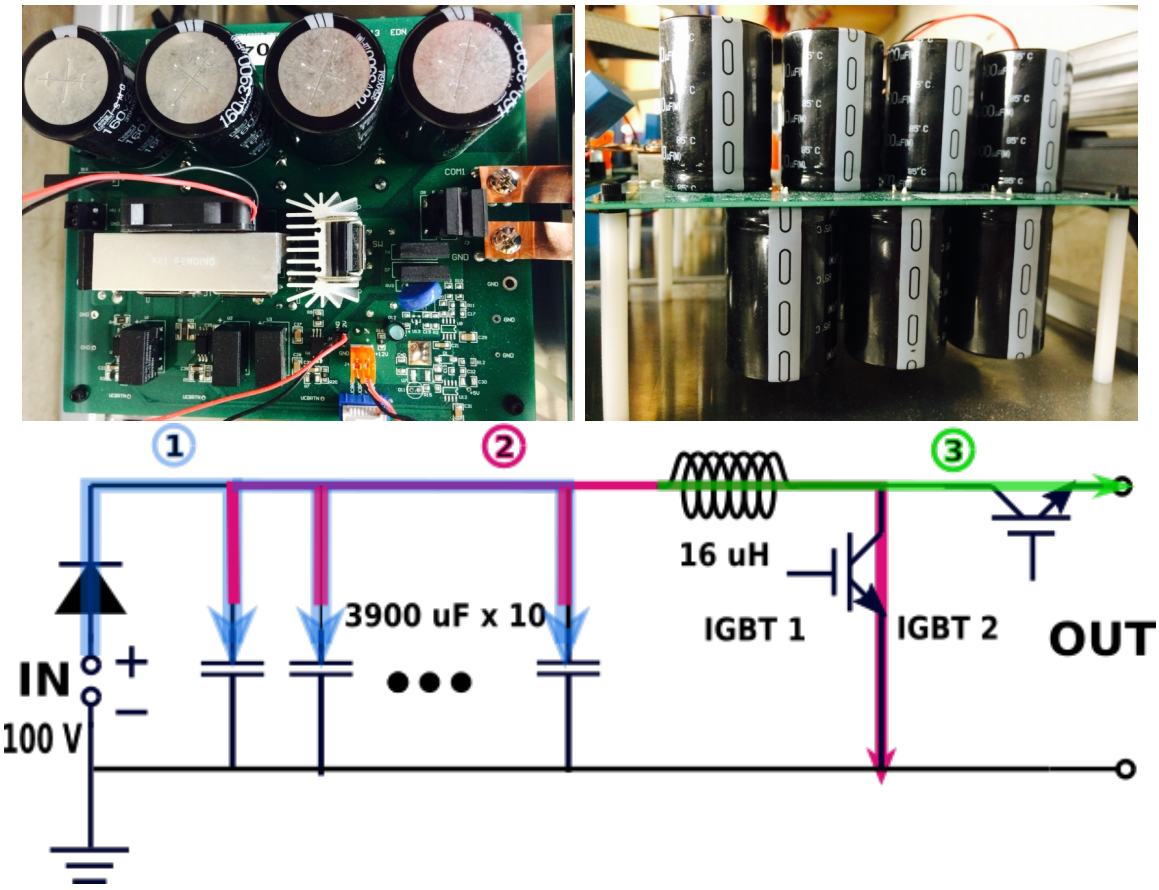


Fig. 5.13: Image of a BCC unit(top) and simplified schematic of Boost Convert Charger (BCC, bottom). Colored arrows show the operation sequence.

goes too far. In step 3, far before the current on the inductor reaches its maximum, switch off IGBT1 and activate IGBT2, where energy stored in the inductor is then transferred to the output in the form of current. At this moment, there is still energy left on capacitor bank, so steps 2 $\sim$ 3 are repeated a few times to keep dumping current to the output. The whole BCC acts as a DC voltage to pulsed-high-current converter whose output is then used to charge the CBOX. The voltage conversion from the BCC to the CBOX is measured to be about 1:4, as shown in Fig. 5.14

**The Capacitor BOX (CBOX)** Together with LBOX, the CBOX provides the tunability of the pulse time length. There are multiple binary-valued capacitors (1, 2, 4, 8, 16, 32, 32+32, in µF) that are connected in parallel on the CBOX. Each of the capacitors is connected to an IGBT in series which acts as a selector. The selection

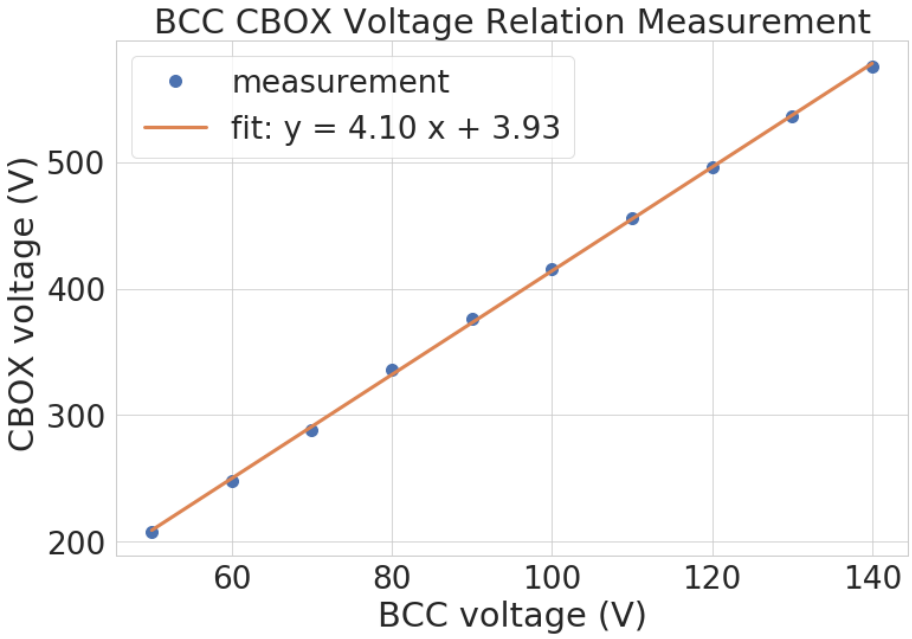


Fig. 5.14: Measurement of voltage relation between the BCC input voltage (from external DC power supply) and the voltage on the CBOX capacitor bank.

of capacitor is provided by an external TTL signal which triggers an optocoupler to output control voltage on the gate of the IGBT. The real image and simplified schematic is shown in Fig. 5.15.

**The Inductor Box (LBOX)** Similar to the CBOX, there are 4 binary-valued, home-made inductors (2, 4, 8, 16 µH) on the LBOX, connected in series. To realize the selectability, each inductor has an IGBT connected in parallel for form a bypass circuit. The inductors are made from copper ribbon wires, with kapton tape as insulation medium in between each layer and were held together by epoxy. The resistance and inductance of these home-made inductors were calibrated using an LCR meter (LCR816). The image and schematic of the LBOX is shown in Fig. 5.16

**The Discharge Board** The discharge board enables individual control of the discharge timing for each individual traps, as well as rectifying the current pulse shape to be a half-sine. The first task is realized by using two 16-channel analog multiplexers (74HC4067) with totally 8-bit inputs and 30 outputs to control 30 individual traps on each of the discharge boards. The decelerator consists of totally 16 of these discharge boards to support the 480 traps. The circuit layout implements a symmetric pattern

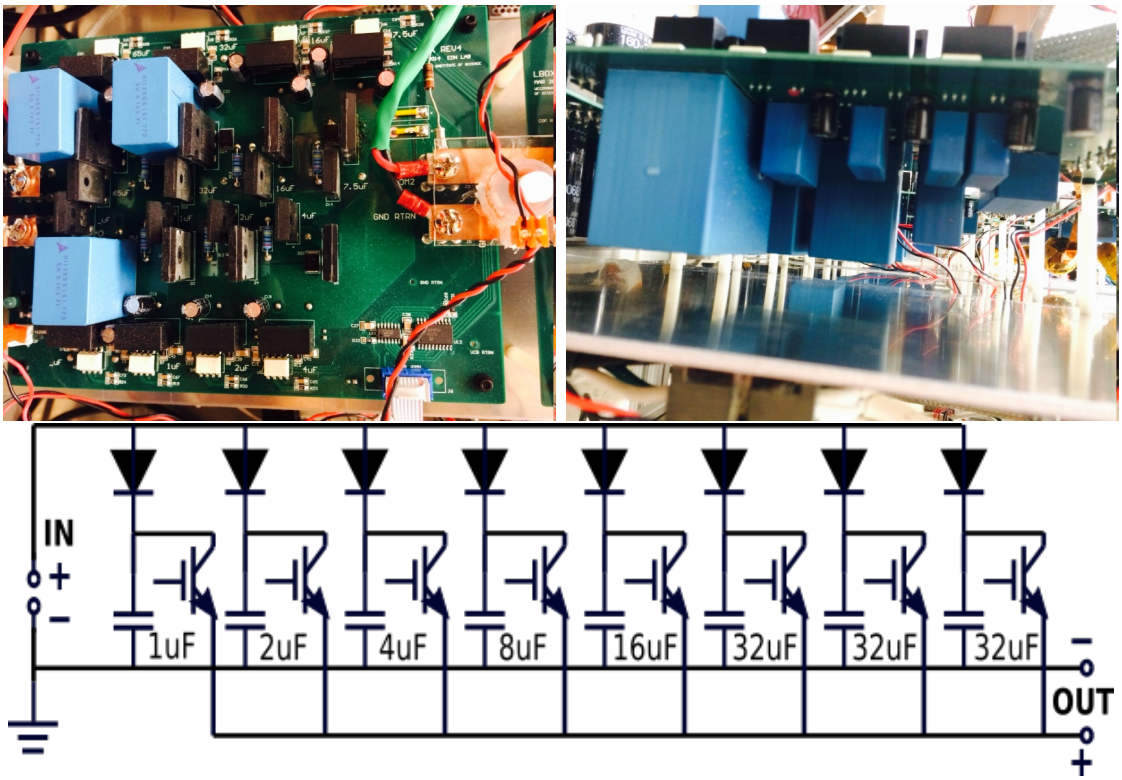


Fig. 5.15: Image of a CBOX unit(top) and simplified schematic.

with controls for even and odd numbered traps separated to different circuits. In total there are 10 distribution lines (5 lines each of for the odd and even sides) corresponding to 10 tune boxes As seen in Fig. 5.17.

The second task of realizing the half-sine current pulse from an under damped source is done by a thyristor, or silicon-controlled rectifier (SCR), which is a solid-state semiconductor device that only conducts when the gate receives a current trigger and continues to conduct until the current drops below a (near zero) threshold value. There are three different modes of the operation status of a thyristor: forwarding conducting, forward blocking and reverse blocking, as illustrated in Fig. 5.18.

### 5.3.3 FPGA

For each of the 480 traps, there are more than 20 TTL pulses which need to be generated and sent in a short time interval ($<$ 100 µs). A large amount of logic operations has to be processed in parallel at a high speed and a time resolution of

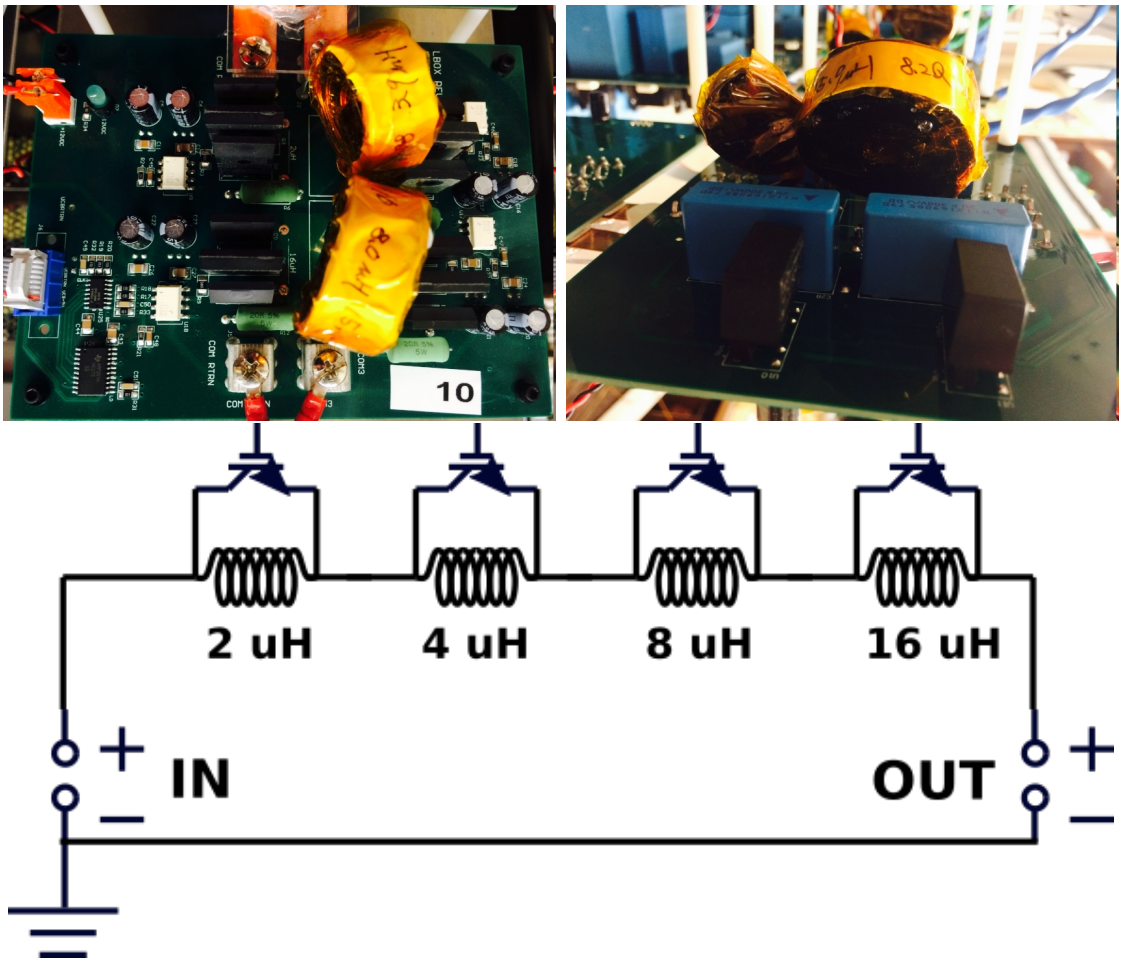


Fig. 5.16: Image of a LBOX unit(top) and simplified schematic.

microseconds level. Additionally, configurability is also preferred so that the decelerator could work in a controlled way. In consideration of all above requirements, two field programmable gate array (FPGA) devices were used for this task.

An FPGA has a matrix of re-configurable logic units connected to realize a hardware implementation of a software application. As compared to processors, FPGAs use dedicated hardware for processing logic and do not have an operating system. Since the processing paths are parallel, different operations do not have to compete for resources, thus guarantees a fast speed and parallelization of multiple control loops at different rates.

The Xilinx SPARTAN 3E FPGAs are embedded on two separate interfacing boards to control the odd and even numbered coils. The firmware is written in

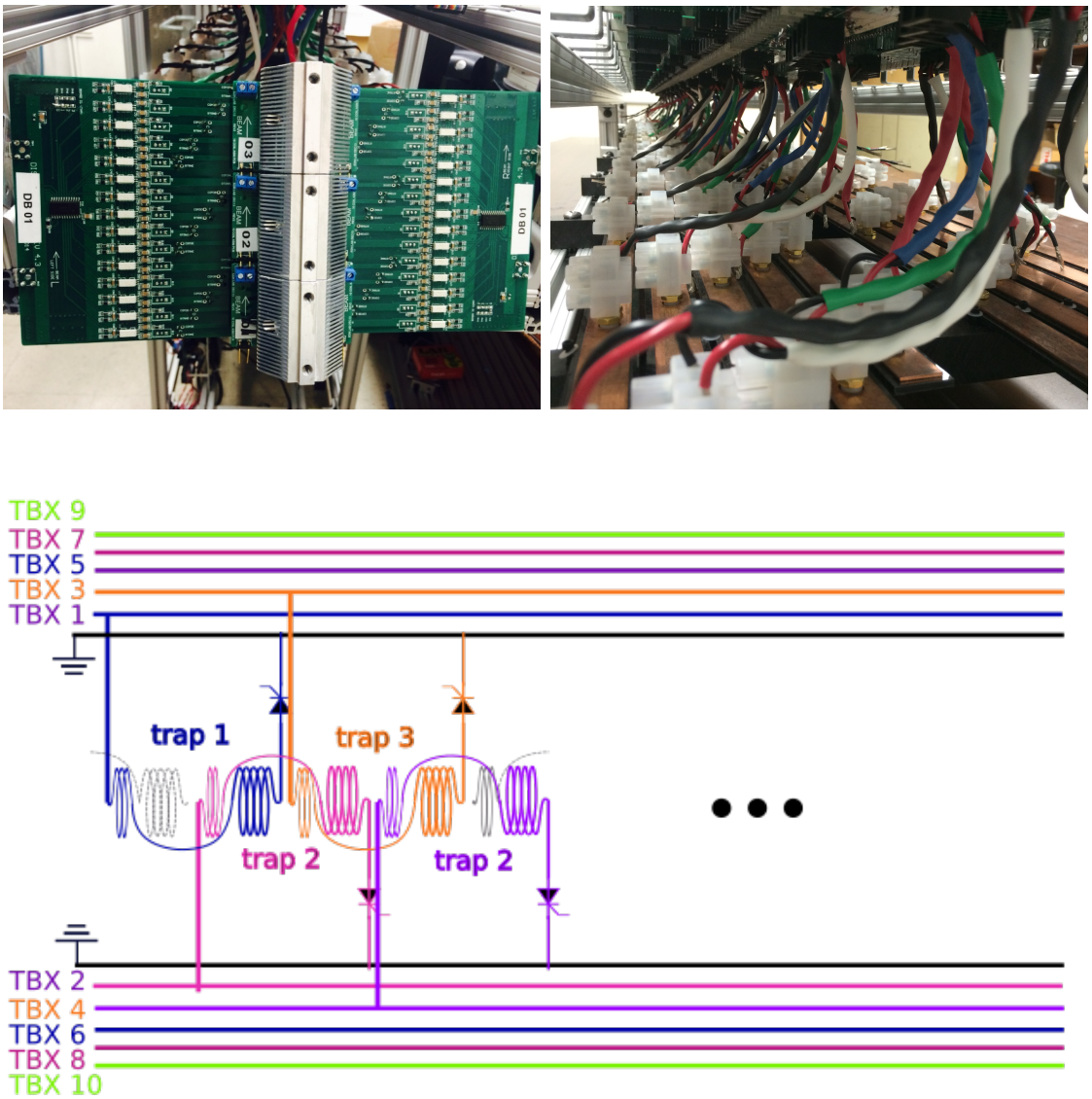


Fig. 5.17: Image of a discharge board unit(top) and simplified schematic(bottom).

hardware description language (VHDL) by our collaborator Julia Narevicius. For each trap we need have control of many parameters: the charging sequence from a BCC board, the circuit capacitance configuration from a CBOX board, the circuit inductance configuration from a LBOX board, and the discharge time from a discharge board. Ribbon wires are used for the communication between the two FPGAs as well as each of the BCC, the CBOX, the LBOX and discharge boards. An extra breakout

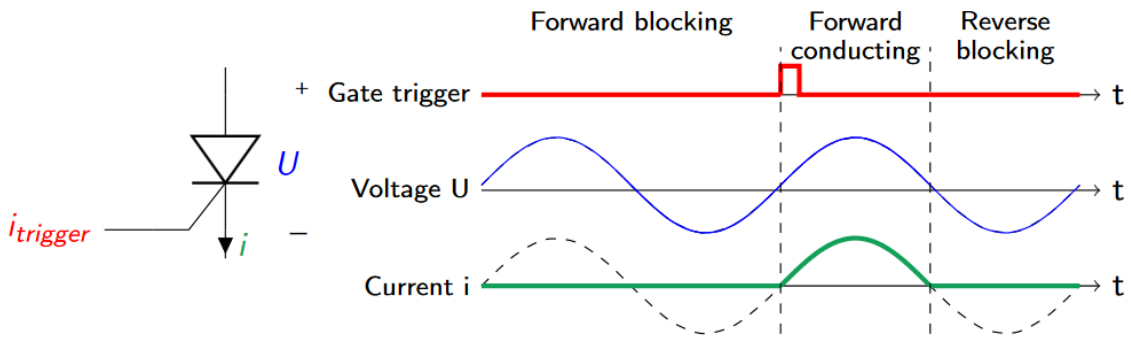


Fig. 5.18: Thyristor and its working mode depend on gate current and bias voltage.

board is used to group the pins from FPGA output in an organized way, as shown in Fig. 5.19. Next, the control sequence for the discharge board will be discussed briefly.

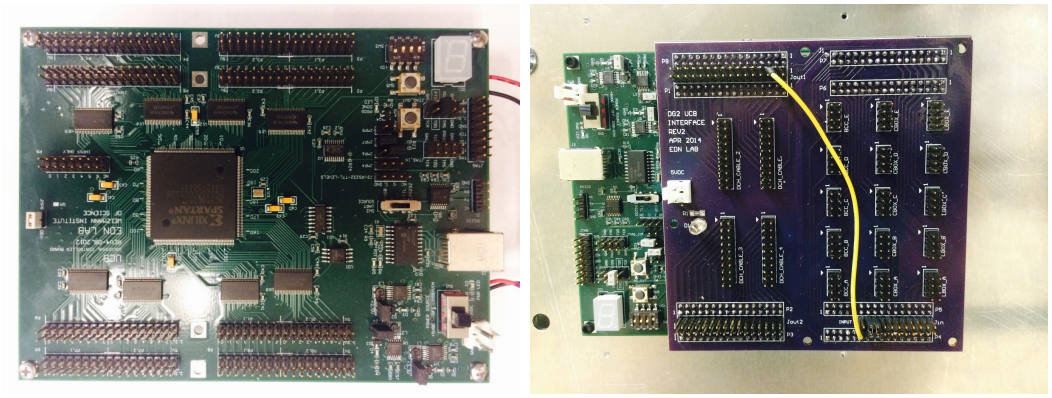

Fig. 5.19: Image of FPGA used for control the decelerator. Left: bottom layer layout. Right: top layer connections.

The information we need to inform a discharge board about a single discharge event includes "which"(which trap) and "when"(discharge trigger). To tell which one of the 480 traps needs to be discharged, totally 9 bits ($9^2 = 512$) are necessary. These 9 bits are further divided to different logic groups to locate the specific trap, shown in Fig. 5.20. In addition, an extra pin is need to transfer TTL signal to time the triggering of the thyristor.

The basic operation procedures of our decelerator are described as following: First, the control sequence is generated by a MATLAB/Python script according to the dis-

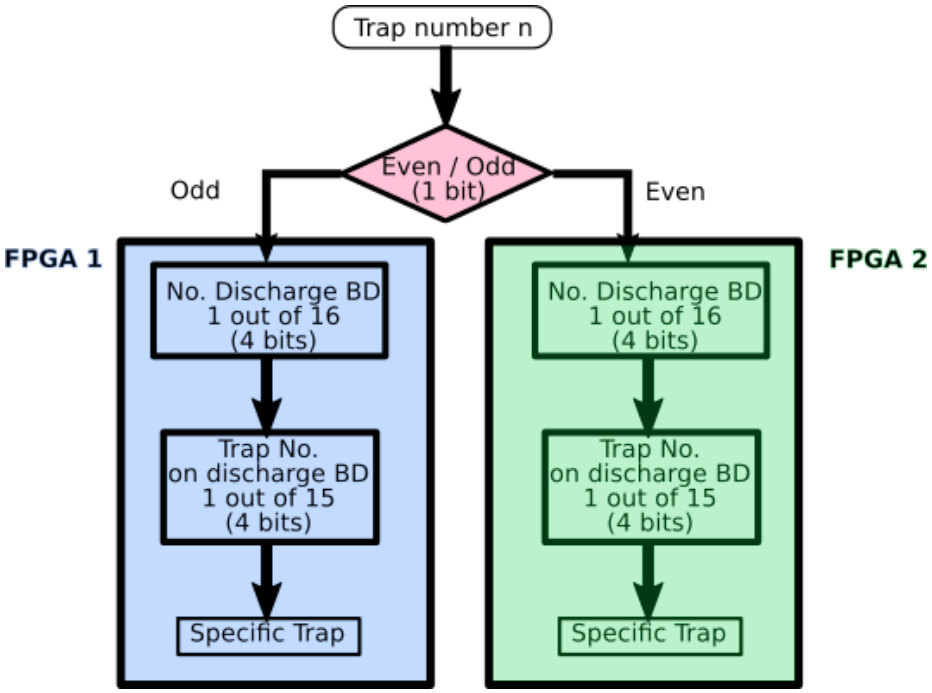


Fig. 5.20: Schematic of bits information in determination of 1 out of 480 traps. 9 total bits needed with 2 FPGAs.

cussion in Section 5.2.4. The output information from the script includes a table of trap number, tune box number, the BCC charge time, coil discharge time, total capacitance, total inductance, charge margin time (gap between charge and discharge). Second, the generated sequence is converted to binary code and loaded to the two FPGAs. Finally, a triggering pulse synchronized with other parts of experiment is sent to both FPGAs, which triggers the function of the FPGAs and a series of sequence is sent to the tune boxes.

A complete working flow for generating a configured current pulse is: The result of the FPGA outputs first trigger a BCC from specific tune box, which charges the corresponding the CBOX to a high voltage level ($\sim$ 400 V). At this point all the capacitors on the same CBOX are at the same voltage. Then a few capacitors with their capacitance summed to a certain value will be discharged. The output current from the discharge then goes through the LBOX. Similarly, only a few certain inductors on the LBOX that fulfill the inductance configuration will carry the current. By this step, we have made an LC circuit that involves customized values of $C$ and $L$. The output current is then directed to the distribution line under discharge board.

In the mean time, the thyristor for the corresponding trap is activated and the same current is thus directed through. When the current in the trap coil ends its first half-sine period, the thyristor will shut it off and thus end the pulsing. The same procedure is repeated with corresponding configured sequences for all other traps. An example of the voltage on the CBOX during the charging stage is shown in Fig. 5.25.

### 5.3.4 Vacuum tube

Since all the electronics and coils are located outside of the vacuum, a 2.5 m long Inconel tube is used as the 'tunnel' that guides the atoms through all the decelerator coils. This tube interfaces with the source and detection chambers through an ultra-torr connector (Swagelok) and an 2.75 inch flange. We choose inconel as the material for the vacuum tube, for its relatively high resistivity ($\rho \sim 1 \times 10^{-6}\ \Omega\,\mathrm{m}$, as compared to the stainless steel ($5 \sim 7 \times 10^{-7}\ \Omega\,\mathrm{m}$). The outer surface of the tube is additionally covered by a thin heat sink layer to insulate itself from the decelerator coils. The whole tube was baked at 160 °C under a vacuum of $10^{-7}$ Torr for a few days before we connect it to other chambers in the experiment.

## 5.4 Verification

### 5.4.1 Pulsed magnetic field measurement

In the previous section we've discussed the design of an imbalanced anti-Helmholtz coil as a single unit of the decelerator. The calculation performed earlier (see Fig. 5.11) has shown an anticipated trap depth of 350mK longitudinally and 150 mK transversely. In this section, we discuss the measurement of the magnetic field profile in the trap.

In order to measure the magnetic field inside the anti-Helmholtz trap, a short AC current pulse of 400 A was applied. we used one of the tune boxes to generate the current with a pulse length in the 10 µs $\sim$ 200 µs range.

We did not use the gauss meter for the magnetic field measurement, as its time resolution is not high enough[1]. Instead, we rely on the Faraday effect, which provides

[1]The gauss meter we have only gives up to kHz response resolution.

us a fast and accurate way to perform the measurement. The Frarday effect, or Frarday rotation, is an effect that the polarization plane of a linearly polarized light will be rotated by a certain angle when interacting with the medium that is placed in a magnetic field. The rotation angle of the polarization plane is proportional to the magnetic field strength along the laser propagation direction. This proportionality is governed by the Verdet constant, $V$, as a property of the medium. The medium which provides a large Verdet constant is called a Faraday rotator. The rotation angle $\beta$ of the polarization plane of laser along the direction of the magnetic field is given by relation

$$\beta = V \int_0^d B(x)dx \approx VBd, \tag{5.21}$$

where $d$ is the propagation distance of light in the medium, and $B$ is the magnetic field component along that direction. An approximately localized measurement is valid when the change of the magnetic field is small over $d$.

In this measurement, a terbium gallium garnet (TGG) crystal was used with a high Verdet constant of -134 rad $\mathrm{m}^{-1}$ $\mathrm{T}^{-1}$. The experiment setup is shown in Fig. 5.21. A 633 nm light from a Helium-Neon laser is shaped by a telescope, passing through a polarizing beam splitter(PBS)[2], and then the TGG crystal rod (3mm diameter, 2.5 mm length). The TGG crystal is held by a hollow Teflon rod with inner diameter slight larger than the crystal. The rod is carefully aligned to the axis of the anti-Helmholtz coil and translated along the same direction using a translation stage with a resolution of 0.02 mm. The transmitted light from the TGG crystal passes through another PBS and detected by a fast photodiode (Thorlabs PDA10A, rise time $< 10$ ns).

We use a setup shown in Fig. 5.21 to perform the measurement. To calibrate the measurement, first, the laser power as in voltage $V_0$ was measured without present of the trap coil. Then the trap coil under the measurement was pulsed with a 400 A current, a decrease of the measured laser signal $\Delta V$ is detected by the photodiode. An example scope trace is shown in Fig. 5.22. The rotation angle of the laser polarization plane can be derived from this measurement as

$$\beta = \arccos\left(\sqrt{\frac{V_0 - \Delta V}{V_0}}\right). \tag{5.22}$$

[2]extinction ration larger than 100 : 1

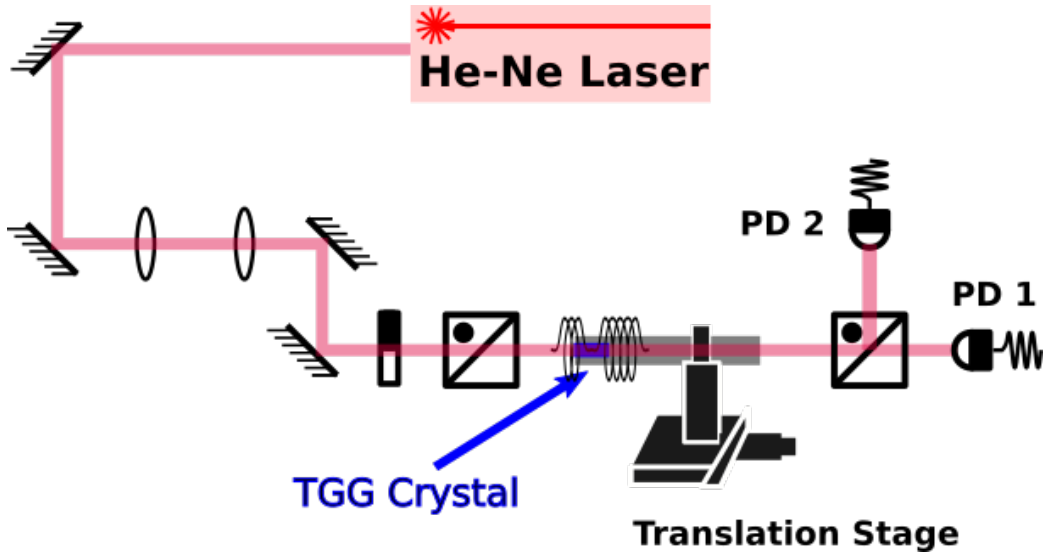


Fig. 5.21: Optics set up for measuring pulse magnetic field with TGG crystal.

Combining above equation with Eq. 5.21, the average magnetic field over the length of TGG crystal can thus be calculated.

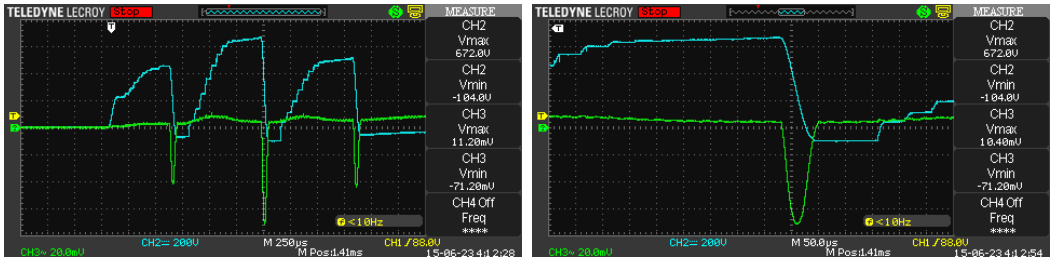


Fig. 5.22: Example of pulsed magnetic field measurement using TGG crystal and photodiode. Blue trace(channel 2, DC mode): voltage on the CBOX, 3 charging(stepwise increasing voltage) and discharging(sharp drop of voltage) are shown, measure value shows real voltage value. Yellow trace(channel 1, AC mode): the intensity change of detected signal from photodiode, indicates the change of polarization after laser going through the TGG crystal in the pulsed magnetic field.

Same measurement were performed with different positions of TGG crystal inside the coil. In this way, we could map out the magnetic profile inside the pulsed coil, as shown in Fig. 5.23. This measurement help us find out some malfunctioning coils at an early stage.

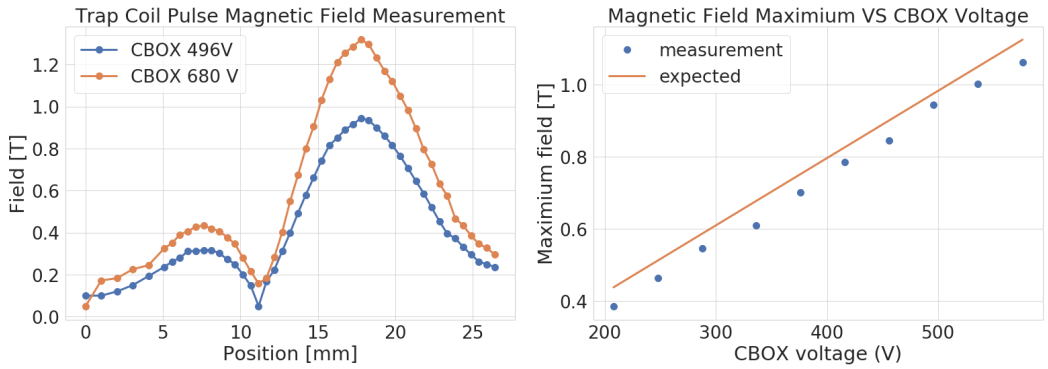


Fig. 5.23: Axial measurement of magnetic field in anti-Helmholtz coil trap. Left: Magnetic field profile along coil axis with different the CBOX voltages. Right: the relation between the CBOX voltages and maximum magnetic field long coil axis, also shown is the calculated peak field strength from in Eq. 5.19.

### 5.4.2 Current pulse length monitoring

The trap turn-on time and period has also been measured, as a way to check any potential malfunction of our circuits. Since there are effectively 480 different circuits in total, probing each of the current pulse is necessary.

In order to realize a simple independent test of each current pulse, a relative measurement relying on Faraday's low was developed. One characterization of the decelerator circuit is that all the 480 current pulses can be traced from the output end of the 10 tune boxes. We thus installed a pick up coil sensor at the output end of the CBOX on each of the tune boxes. The pick up coils are oriented in such a way that magnetic flux induced by the current at the CBOX output is maximized, as shown in Fig. 5.24.

The output of all the pickup coils are then chained together and low pass filtered ($>$ 100 kHz) and monitored by an oscilloscope. The noise filtering is necessary in order to isolate the wanted signal from the IGBT switching noise. An example is shown in Fig. 5.25, together with the corresponding the CBOX voltage.

The pickup coil signal for a single current pulse is shaped like a skewed sine wave. The starting time of this signal corresponds to the discharge time of each trap. The skewness is from the inductance of the pickup coil itself which influences the starting of the pickup signal. This signal is further processed using a python script to first find the 1st-order derivative to extract a rough range of the discharge event, then a

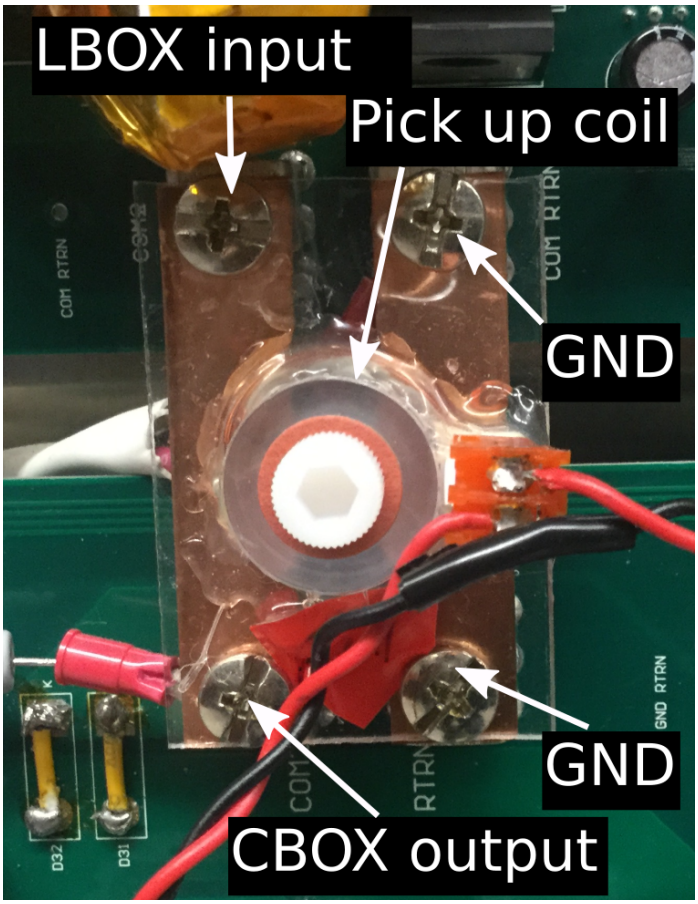


Fig. 5.24: Image of the pickup coil. The pickup coil is located in between the bridging copper traces between the CBOX output and the LBOX input.

sine function is fitted to find the pulse length, as shown in Fig. 5.26.

The pickup coil output trace for all pulses are recorded and analyzed. A python script was written to automatically locate and extract the information for each pulse, specifically the discharge time and pulse length. The result from this measurement is compared to the expected values, as shown in Fig. 5.27.

From Fig. 5.27 one can see that the discharge pulse length agrees reasonably well with the configured FPGA sequence, the percent error is generally below 15% through different runs. Note that the pickup coil signal contains a lot noise which adds some uncertainty to this measurement. This pick-up coil method can be done in the real time during the operation of the deceleration, thus serves as a convenient monitoring tool.

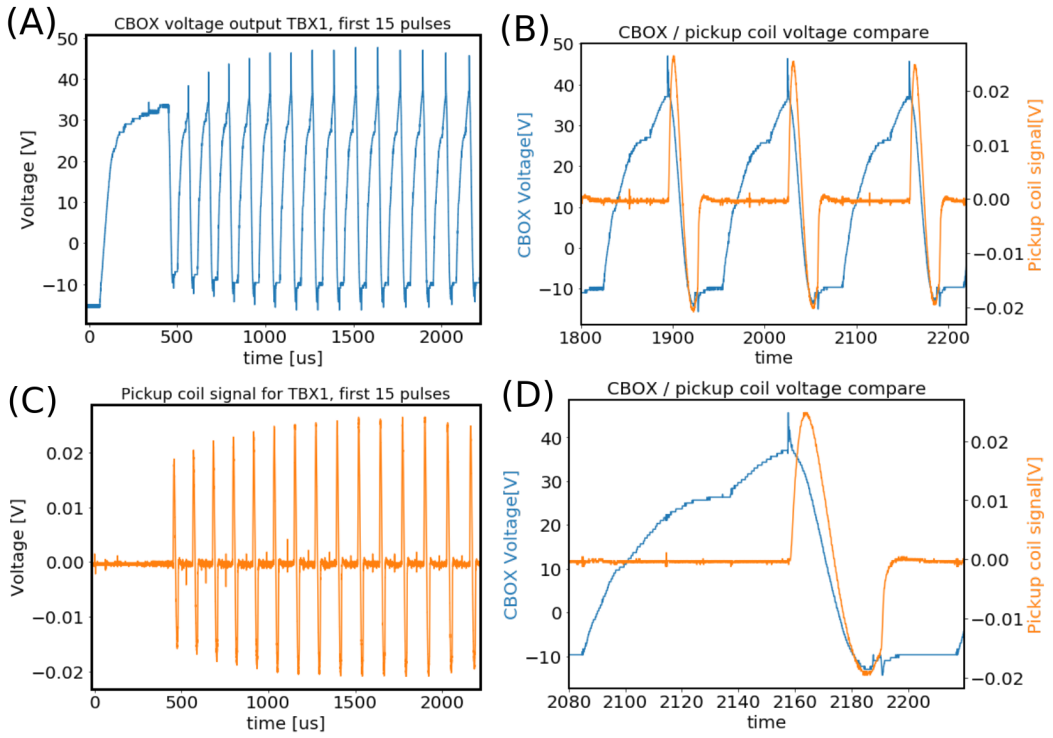


Fig. 5.25: A demonstration of oscilloscope measurement on the CBOX voltage output (A) and corresponding pickup coil signal (C). Additional zoomed in plots at different scale is also shown(B, D). Only the first 15 pulses are shown from tune box 1.

## 5.5 Decelerator test

### 5.5.1 Decelerator testing setup

The testing setup for the decelerator can be seen in Fig. 5.29 and 5.28. The entrance of the decelerator vacuum tube is connected through an ultra-torr Swagelok to the 10-inch flange from the source chamber (where the skimmer is mounted). Due to the limited space for supporting structures, there is about 10 cm distance between the skimmer and the first trap of the decelerator. The output of the decelerator is connected to an 2.75 inch 4-way cross with AR coated viewports, then a 10 in detection chamber which provides optical access as well as space for detection tools like the hot wire detector and the RGA. In the early stage of testing, we also had an extra 2.75 inch 4-way cross between the skimmer and the decelerator entrance, for additional laser-based measurement.

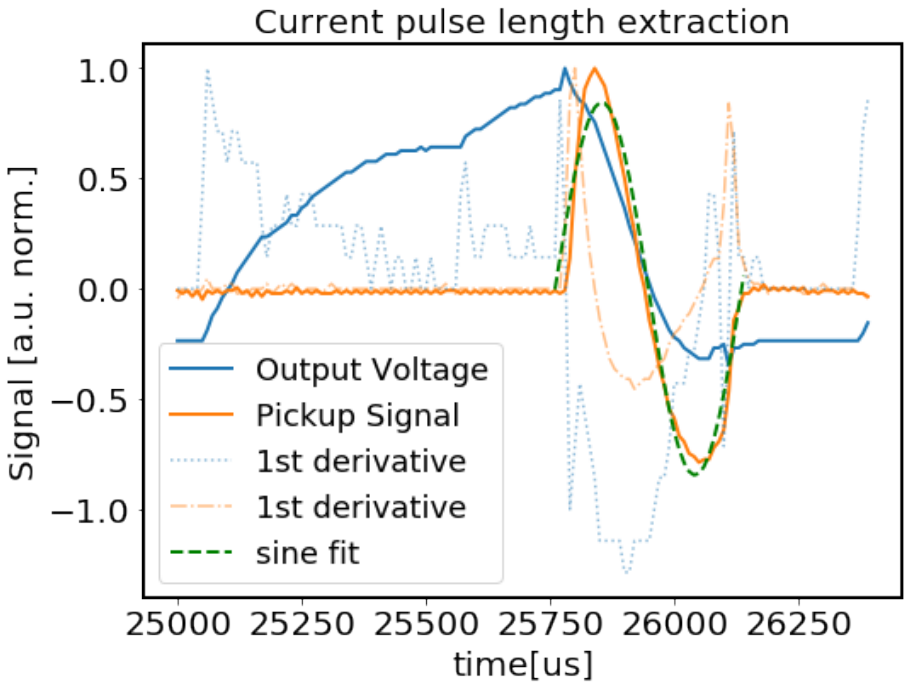


Fig. 5.26: A demonstration of process method used to extract current pulse length from pickup coil signal.

The vacuum tube inside the decelerator was aligned carefully with laser. During the experiment, with oven at 550 °C and nozzle pulsing at 0.3 Hz, the source chamber can be maintained at around $10^{-8}$ Torr while the detection chamber at around $10^{-9}$ Torr.

We mainly used the laser fluorescence to detect lithium atoms, assisted with hot wire detection and laser absorption measurement. Additionally, a residual gas analyzer (RGA, model SRS 200) was used to measure the helium carrier gas. The RGA also provides a weak lithium signal under the setting of a high channel electron multiplier (CEM) voltage.

### 5.5.2 Searching for a signal after slowing

Like many experiments with a sophisticated setup, we didn't see any signal in the first few trials. Careful analysis and a step-by-step parameter search finally lead to the observation of slowed atoms after the decelerator.

First, a laser position scan along the transverse direction of the atom beam before

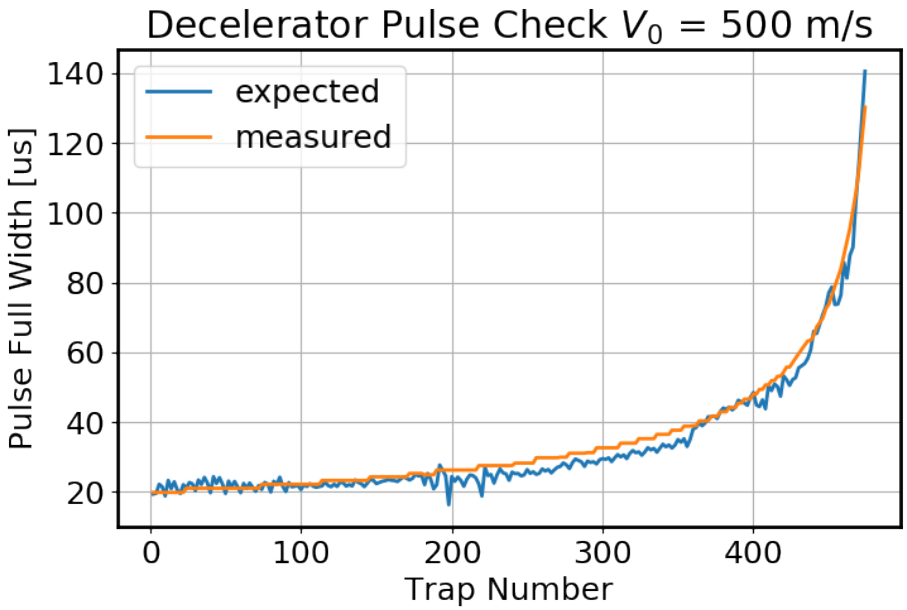


Fig. 5.27: Estimated decelerator pulse width. The result is compared to the expected value from the FPGA configuration sequence.

the decelerator was performed. This measurement is to make sure that the entrance of the decelerator is located at a position where the size of the lithium beam is small. The integrated time-of-flight signal at each of the laser position is shown in Fig. 5.30, from which we obtained a measurement of beam FWHM of 8.2 mm, which is smaller than the trap transverse size (10 cm) but is quite close. We believe future improvement can be made by shortening this distance.

Second, we made sure that there is a straight pass of beam line through our apparatus. Without the decelerator in operation, we observed the carrier Helium atoms using the RGA, which is located at the very end of the beam line, about 3 m from the supersonic nozzle. The observed helium time-of-flight signal is shown in Fig. 5.31. Unfortunately, initially we did not observe any lithium signal that passes through the 2.5 m decelerator. Later we realized that the extra length introduced by the measurement chamber (2.75 in cross) located in between the skimmer and the decelerator reduced the amount of atoms coupled into decelerator a lot. After removing this detection chamber we did observe the fluorescence of lithium atoms that directly propagated through the decelerator when it's not in operation.

Third, we notice that trappable lithium atoms are only those 'low-field-seekers'

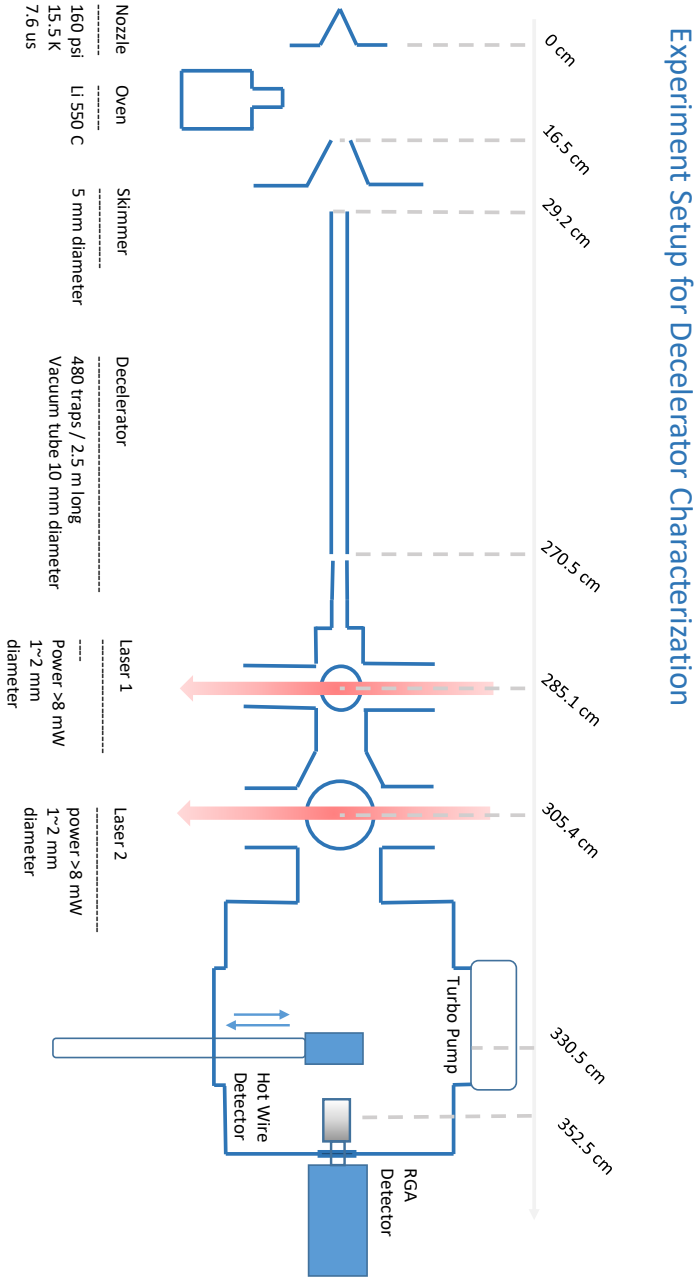


Fig. 5.28: Testing setup schematic for the decelerator and some key dimensions.

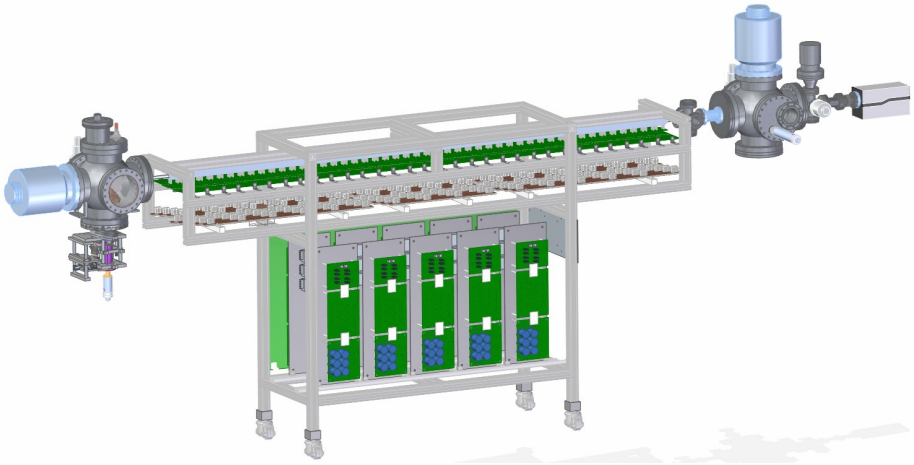

Fig. 5.29: Testing setup for the decelerator. From left to right are: source chamber, decelerator, detection chamber.

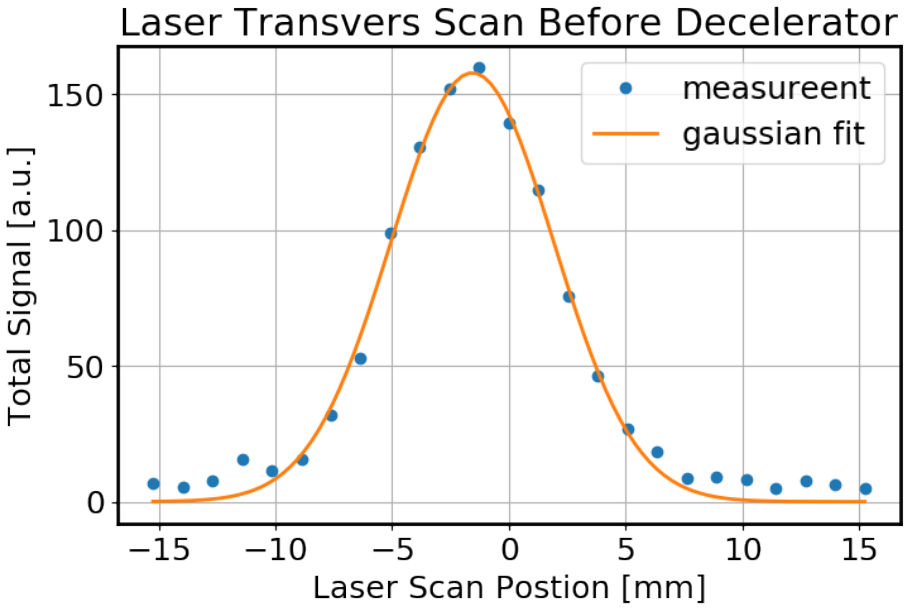


Fig. 5.30: Lithium laser transverse scan fluorescence signal before decelerator.

at ground level hyperfine states $F = 2$ of $^2S_{1/2}$. These atoms take about half of the original amount of lithium coming out from the skimmer. For this reason, the probe laser used for fluorescence detection after the decelerator was locked to D2 transition $^2S_{1/2}, F = 2 \Rightarrow {}^2P_{3/2}$.

Additionally, in order to increase signal strength of potentially decelerated lithium atoms after the decelerator, we started our test with a decelerator setting of large final velocity, close to a guiding mode. This idea is based on the consideration of the beam expansion at the output of the decelerator. The laser detection point is located at a distance of 15 cm from the last trap in the decelerator. Thus, we configured the decelerator to operate with a final velocity of 300 $\mathrm{m\,s^{-1}}$.

Finally, there are many other parameters that are crucial for the deceleration: the time delay of the decelerator trigger relative to the nozzle pulse, the decelerator initial velocity. These parameters are scanned in a small range at their estimated value. The started with scanning the decelerator delay at a fixed decelerator initial velocity of $v_0 = 480\mathrm{m\,s^{-1}}$. Once obtained a signal, $v_0$ is scanned to further improve the signal level. All these test were done at an Even-Lavie nozzle temperature of 18 K and pressure of 300 psi.

With above procedures and some patience, we have detected the decelerated lithium signal, as shown in Fig. 5.31. On the same figure we also include the comparison of the signal regarding different decelerator configurations, e.g. the initial and final speed. A few observations from the figure include: (1) Lithium signal arrives at a time of 7.5 ms, which agrees with a simple calculation based on the constant deceleration. (2) The decelerator noise in the detected signal is a nice time marker from which we extract the free expansion time of the slowed atom cloud is about 500 µs. (3) The initial and final speed of the decelerator configuration influence the detected signal strength, a rough range of 20 $\mathrm{m\,s^{-1}}$ around the optimal initial speed can give us the lithium signal.

We also checked the internal state of the decelerated atoms. We performed the same measurement with two different laser frequencies, the pump laser transition ($^2S_{1/2}, F = 2 \Rightarrow 2^P_{3/2}$) and the repump laser transition ($^2S_{1/2}, F = 1 \Rightarrow 2^P_{3/2}$). Through this measurement, as shown in Fig. 5.32, we confirmed that the decelerated atoms are all in their low-field-seeking states.

From the bottom plots of Fig. 5.31 one may notice that the lithium signal at the output end decreases quickly once configured to slower final velocities. This requires further optimization, which will be discussed in following sections. Once having all optimization finished, the beam properties are then characterized.

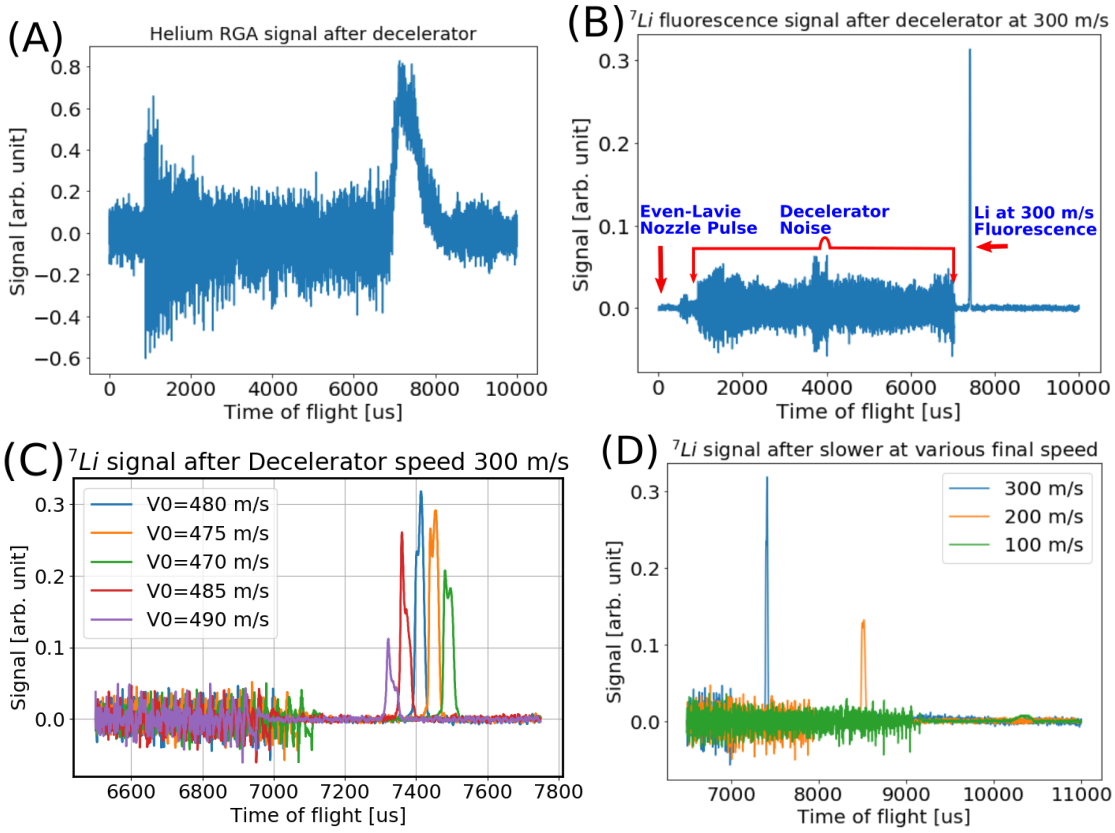


Fig. 5.31: Signal that first observed after our decelerator and its variances with scan parameter. Figures includ the helium signal (not slowed) after the decelerator measured from the RGA (A), the slowed Li signal after the decelerator with speed $v_f = 300\ \mathrm{m\,s^{-1}}$ (B), with important experiment annotated on the figure, the lithium signal with different decelerator initial speed configurations (C), and the lithium signal with different decelerator final speed configurations (D).

## 5.6 Optimization

### 5.6.1 Overview

The optimization of the decelerator for a maximum throughput is a complicated procedure. Relevant parameters that can help improve the detected lithium signal include: the probing laser parameters, the decelerator speed parameters, the decelerator time sequences, and the Even-Lavie nozzle parameters, etc. I describe our strategy to efficiently go through the optimization procedure as the following:

First, we optimize the laser detection. This is to make sure that the detected

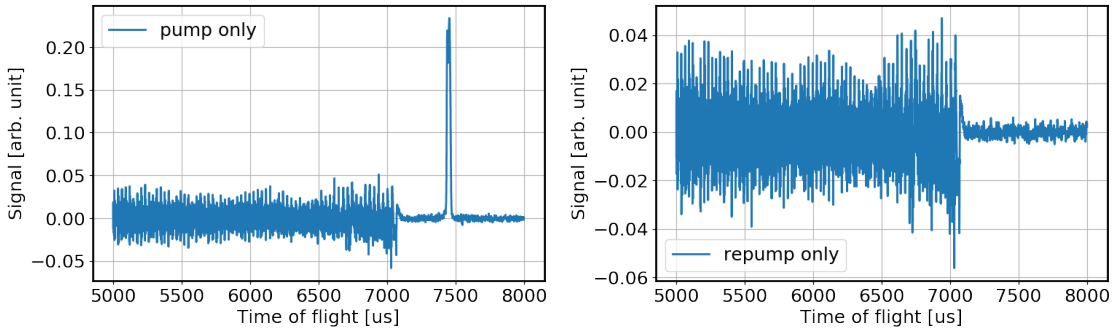


Fig. 5.32: Detected signal by laser fluorescence using only pump (left) and repump(right). The measurement confirms that decelerated atoms are all at ${}^2S_{1/2}, F = 2$ ground state.

signal correctly reflects the number of decelerated atoms. Second, with fixed laser parameters, we optimize the timing related to different parts of the experiment, e.g. nozzle pulse length, decelerator delay. Third, we optimize the decelerator speed configurations. This step combined with the previous step helps to get us in a region where we see a good amount of lithium; Fourth, fine tune Even-Lavie nozzle parameters around previous obtained values without decelerator. This step was performed in case the previously obtained optimal parameters for a free propagation beam is not valid for the decelerator. Finally, we fine tune the decelerator control sequence. This was assisted by the pickup coil measurement, as in Section 5.4.2, in order to further optimize the decelerator configurations in a finer manner.

### 5.6.2 Laser saturation

We used laser fluorescence for detecting the lithium atoms. As the first step, we made sure that the laser frequency is above saturation. Doing this will confirm that the total atom signal does not depend on its speed. In our experiment we used a single frequency pump laser (${}^2S_{1/2}, F = 2 \Rightarrow {}^2P_{3/2}$) with power tunability to an upper bound of more than 10 mW. A laser power scan result is shown in Fig. 5.33, where we see that saturation is guaranteed with laser power above 2 mW given its size of $\sim$ 1.5 mm diameter.

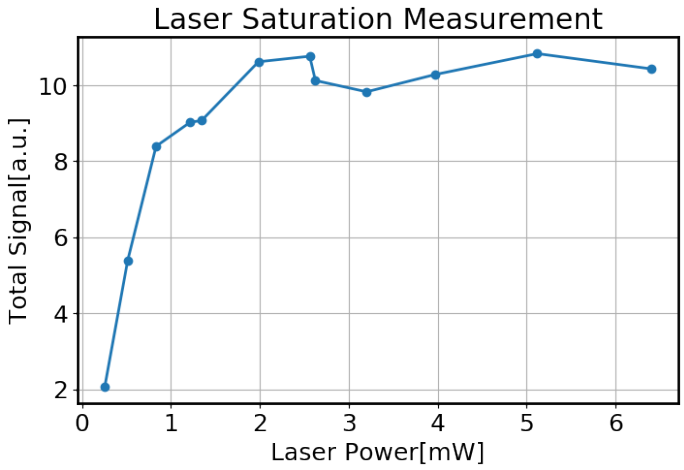


Fig. 5.33: Probe Laser saturation power measurement with $\sim$ 1mm diameter size.

### 5.6.3 Decelerator delay

To optimize the measured total lithium signal after the decelerator, the atom cloud has to be captured at a right time. We would measure the influence of delay on the output lithium signal and see how sensitive it is to the experiment. The decelerator trigger delay effectively decides the relative position of the atom cloud in the first trap when deceleration begins.

Here we scanned the decelerator trigger delay over a range of 40 µs, which corresponds to the relative position change of atom cloud of about 19 mm, given the initial speed $v_0 = 480\ \mathrm{m\,s^{-1}}$ and the final speed $v_t = 200\ \mathrm{m\,s^{-1}}$, as shown in Fig. 5.34

### 5.6.4 Decelerator initial speed

Previously we did a full characterization of the lithium beam speed under different nozzle parameters when decelerator is not connected (Section 4.4). Now we scan the initial trap velocity of the decelerator to match that of the lithium beam. The decelerator initial speed was scanned with a step size of 5 $\mathrm{m\,s^{-1}}$, around 470 $\mathrm{m\,s^{-1}}$, as shown in Fig. 5.35.

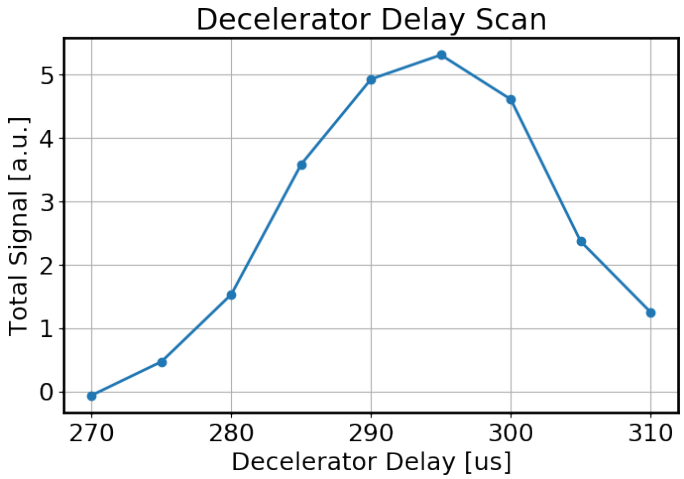


Fig. 5.34: Decelerator delay scan relative to Even-Lavie nozzle pulse. The decelerator is configured with initial velocity of 480 $\mathrm{m\,s^{-1}}$ and final velocity of 200 $\mathrm{m\,s^{-1}}$.

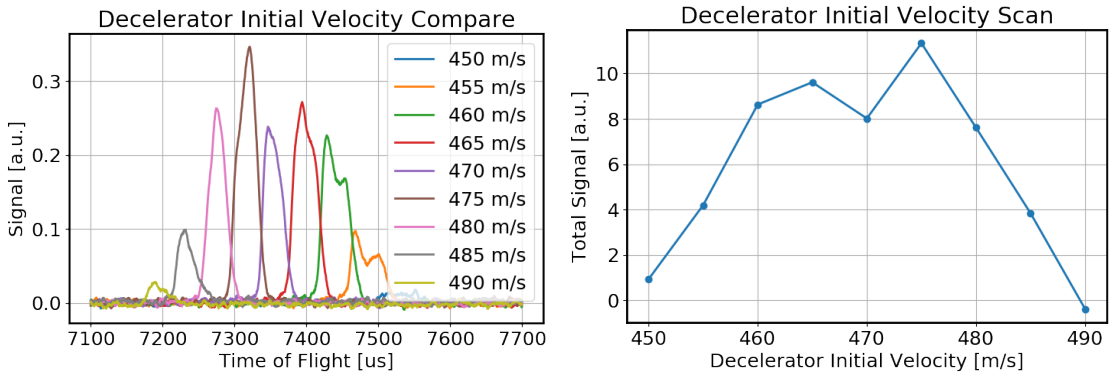


Fig. 5.35: Compare different decelerator initial velocities, with final velocity of 200 $\mathrm{m\,s^{-1}}$.

### 5.6.5 Decelerator acceleration ratio

Another parameter that must be optimized is the acceleration ratio, which adjusts the acceleration set for the mannually divided two sections of the decelerator. The 480 traps are divided intentionally divided into two sections with 180 in first and 300 in the second section. The coils in the first sections bypass the LBOX to generate the shortest possible pulses when atoms are moving the fastest. The acceleration ratio $a_1/a_2$ between the two sections is thus used as a way to compensate this difference in electronic design. Although this difference is already taken into account when

generating decelerator sequence, fine-tuning may still be needed with this parameter. A scan over this parameter is shown in Fig. 5.36, from which we set the optimal deceleration ratio to be 0.9.

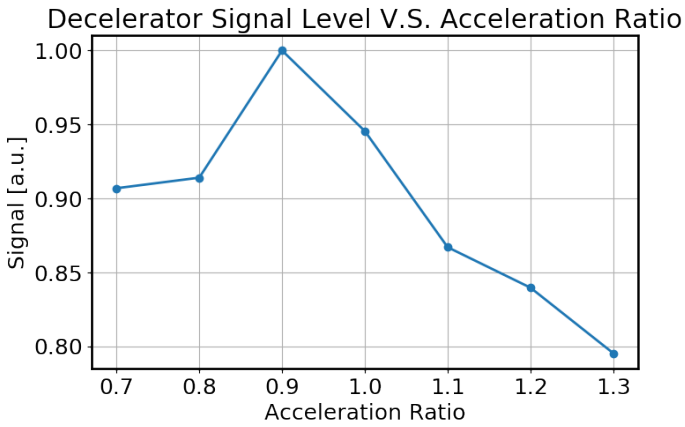


Fig. 5.36: Decelerator acceleration ratio fine tuning.

### 5.6.6 Optical pumping

As only atoms in LFS states are being decelerated, additional slow atoms can be gained by optically pumping all atoms into the LFS states before slowing. This is done using a repump laser ($^2S_{1/2}, F = 1 \Rightarrow {}^2P_{3/2}$). From measurement shown in Fig. 5.37, a factor of 1.5 is obtained with the optical pumping, as compared to without it. A theoretical estimation can be done as following: assume the atoms coming out from the oven are evenly distributed among all 8 ground hyperfine states, 4 of which are in LFS states(F=2, $m_F = -1, 0, 1, 2$) and the other 4 are in the HFS (F=1, $m_F = -1, 0, 1$, F=2, $m_F = -2$) states, as seen from Fig. 2.1. If we assume the repump light pumps all the three F=1 states uniformly to the five F=2 magnetic sub levels, the population of paramagnetic states now becomes a factor of $(3 * 4/5 + 4)/4 = 1.6$ times that of before optical pumping. This factor is close to the measured result of 1.5 from Fig. 5.37.

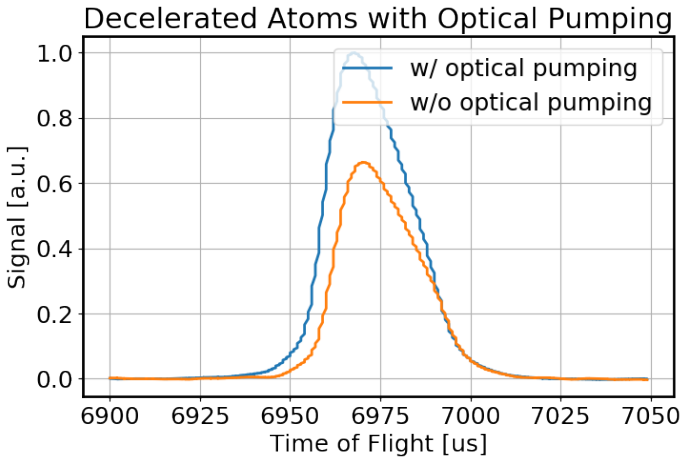


Fig. 5.37: Compare decelerated atom signal with/without optical pumping before the decelerator. Data obtained at decelerator final velocity of 200m s$^{-1}$, nozzle temperature 18K.

## 5.7 Characterization

### 5.7.1 Decelerated atoms at various velocities

Laser measurement was performed on the decelerated atoms at different final velocities. The two lasers (denote as 'laser1' and 'laser2') are from the same imaging beam as in Fig. 3.15, separated by distance of 19.5 cm. Each of these two lasers are above the saturation power with spot sizes of 2 mm diameter and are carefully aligned such that they intersect with atomic at a right angle. During the measurement, only the decelerator final velocity was changed. The 2D map of time-of-flight measurement from 'laser1' is shown in Fig. 5.38. The measurement from 'laser2' shows similar feature with expanded beam size.

Based on these two-point laser scan, various aspect of the output atom beam can be characterized, as discussed in follow sections.

#### 5.7.1.1 Beam Velocity

The very first characteristic we would like to know is whether the atoms exiting the decelerator are at the correct final speed. From the two-point measurement data, we could extract the information of beam speed through the peak arrival time and the laser separation distance. The measured and expected output speed of atoms by

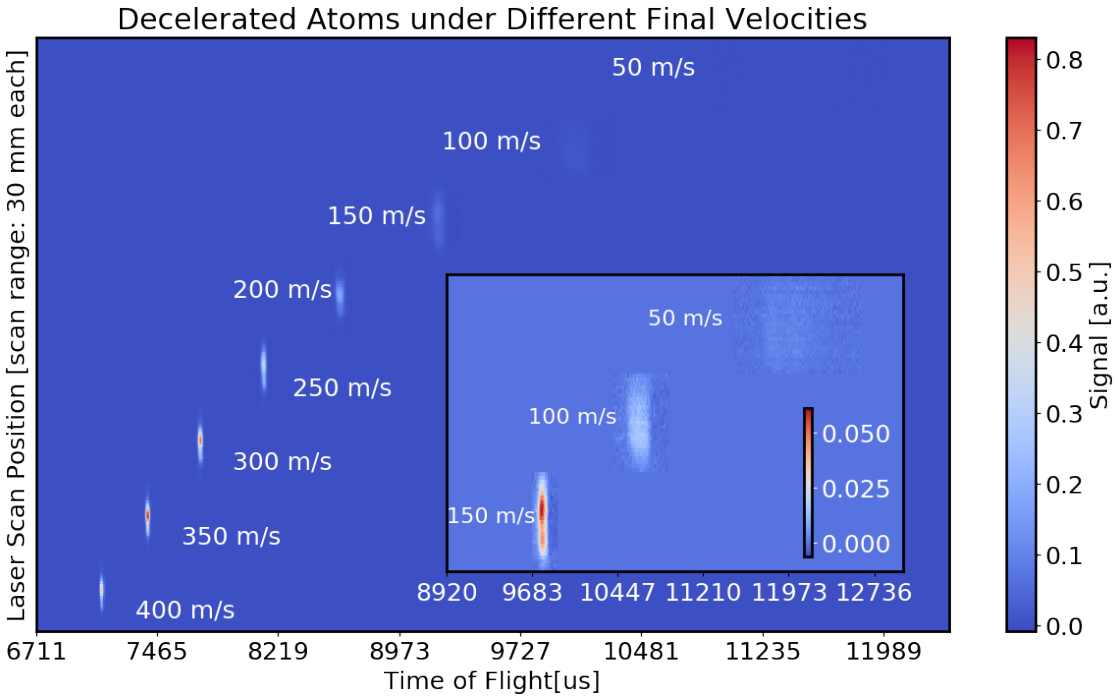


Fig. 5.38: Combined 2D map of decelerated atoms at various final velocities. Deceleration initial velocity: 475 $\mathrm{m\,s^{-1}}$.

the decelerator is shown in Fig. 5.39. As can be seen that the measured velocities agree with expectation very well, with the largest deviations of 7.5 $\mathrm{m\,s^{-1}}$.

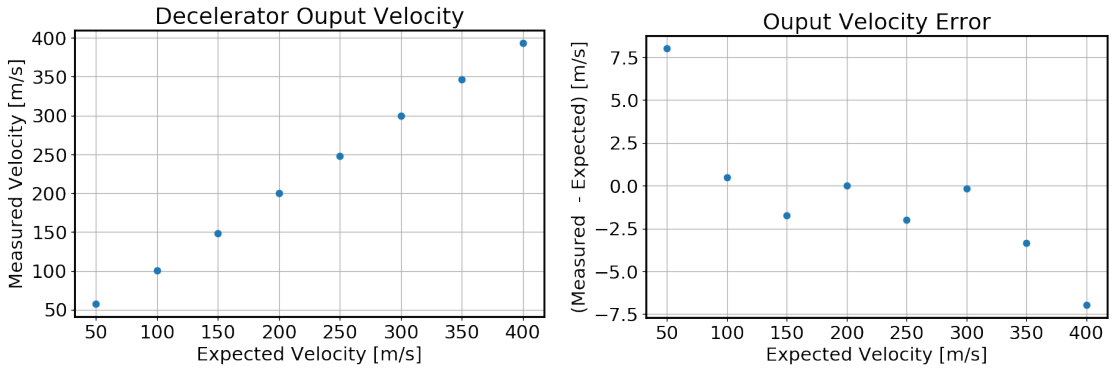


Fig. 5.39: Compare measured and expected velocity of atoms exiting the decelerator.

#### 5.7.1.2 Total Atom Number

The total number of atoms is estimated from the integrated time-of-flight fluorescence and interpolated it by the laser scan positions. Shown in Fig. 5.40 is the plot of total atom number under different decelerator final velocities at the location of 'laser1'. A comparison between measurements from 'laser1' and 'laser2' is also shown with their values normalized to maximum.

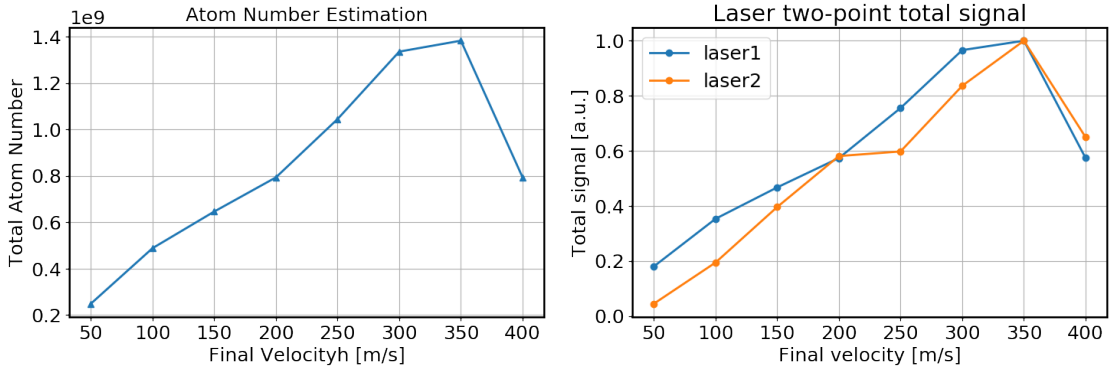


Fig. 5.40: Estimated total atoms number(left) and compare of total signal change between two lasers. Laser separation 19.5 cm.

During the measurement we also noticed that output atomic beam was clipped by the vacuum tube connecting the decelerator and the measurement chamber, especially when low decelerator final velocities were configured. This clear clipping is obvious on Fig. 5.38. However, the above atom number estimation doesn't count for this lose, which means the actual output atom number right after the decelerator could be higher.

#### 5.7.1.3 Atom Beam Size

The atom beam size can also be obtained from the laser scan and time-of-flight measurement. We performed this measurement at various decelerator final velocities and extract the beam size from a Gaussian fit. The results are shown in Fig. 5.41. Since the closest laser measurement point is about 15 cm down stream from the decelerator exit, direct measurement of beam size output from decelerator could not be measured. Fortunately, a fast beam the undergoes less transverse spread can give us a value of the beam width that is close to the true size at the decelerator end. From

'laser1' measurement at a final velocity of 400 $\mathrm{m\,s^{-1}}$, as shown in Fig. 5.42, we can tell that the output atom beam size is about 7mm, smaller than 10 mm(decelerator trap size).

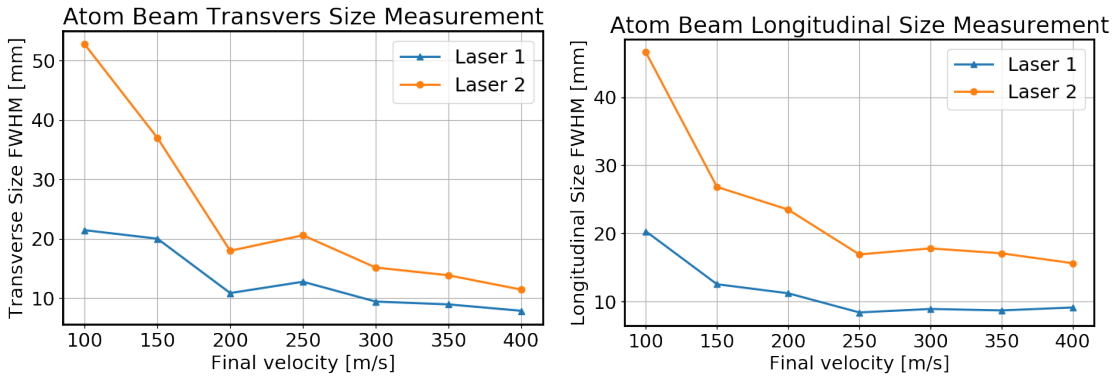


Fig. 5.41: Measured atom beam size along transverse and longitudinal direction, after propagating 15 cm(laser 1) and 35 cm(laser 2) from decelerator exit.

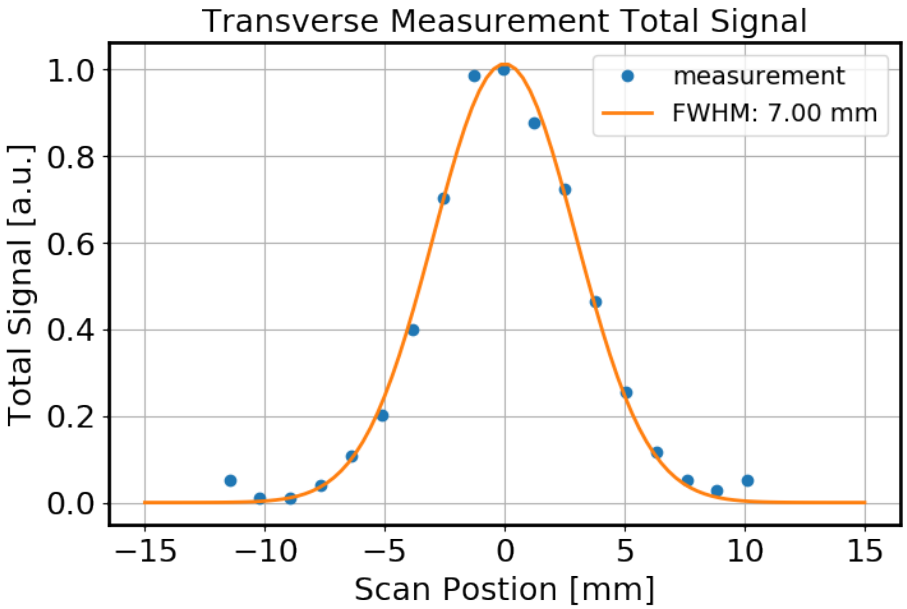


Fig. 5.42: Decelerated atom signal at 200 $\mathrm{m\,s^{-1}}$ with two different.

#### 5.7.1.4 Atom Beam Temperature

The atom beam temperature can also be extracted from our two-point laser measurement. According to the previous discussion in Section 4.2.2, the extracted beam transverse and longitudinal temperatures are shown in Fig. 5.43. Despite some noise in the measurement, the output atom cloud has generally around 20 mK $\sim$ 30 mK temperature, corresponding to a velocity standard deviation of 5 $\mathrm{m\,s^{-1}}$ $\sim$ 6.5 $\mathrm{m\,s^{-1}}$ in its center-of-mass frame.

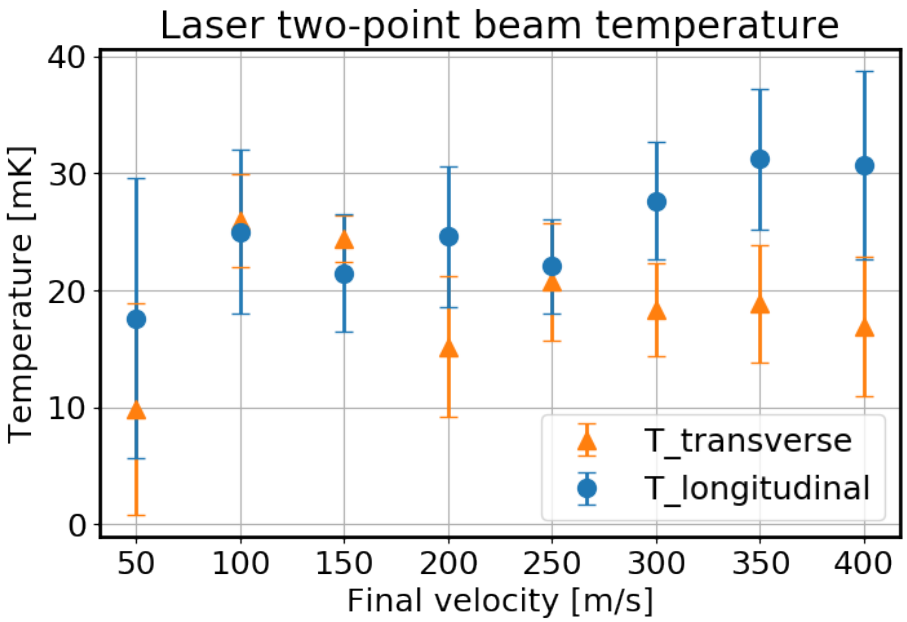


Fig. 5.43: Atom beam temperature along longitudinal and transverse direction, extracted from two-point laser scan measurement.

### 5.7.2 Compare with the ribbon entrainment

The pulsed ribbon is added in addition to further boost the signal at the output end of the decelerator. We did careful measurement of the decelerated lithium atoms using the hot wire detector in order to get a total atom number. A comparison of the two entrainment methods at decelerator final speed of 200 $\mathrm{m\,s^{-1}}$ is shown in Fig. 5.44.

From the measurements in Fig. 5.44, the total atom number obtained with only oven entrainment is extracted to be $1.8 \times 10^9$ per shot, and $3.9 \times 10^9$ atoms per

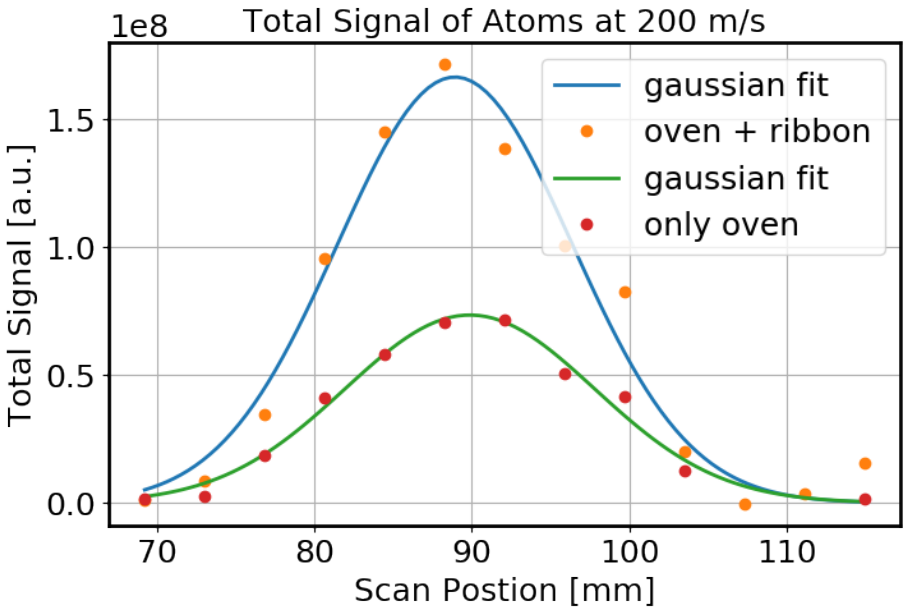


Fig. 5.44: Decelerated atom signal at 200 $\mathrm{m\,s^{-1}}$ with two different entrainment methods.

shot with ribbon entrainment combined with oven. One may notice that the ribbon entrainment does not bring us as much of improvement as compared to the measurement without decelerator. This is due to the heating effect from ribbon entrainment, as shown in Fig. 4.18, where one may notice that the lithium beam temperature went up together with increased entrained atom number by the ribbon. In order to reduce the complexity of our experiment, the ribbon is not on for the rest of the experiment.

# Chapter Six: Optical molasses and chirped cooling

Atoms exiting the decelerator can be trapped directly with a permanent magnetic trap, as shown by our collaborator Edvardas Narevicius [2]. In the future, we plan to experimentally demonstrate a novel magneto-optical (MOP) cooling [101] (see Section 7.3), which requires a controllable trap, i.e. a MOT that can be switched on/off quickly. However, atoms leaving the decelerator will have an average velocity of 50 $\mathrm{m\,s^{-1}}$, which is too fast for loading a MOT. Although the decelerator can be modified (with some electronic and structural engineering) so that atoms moving with even lower final velocities can be achieved, we decided not to move along this path mainly in consideration of the budget. Instead, we added extra laser cooling stages in order to load the MOT with the minimum change of appratus.

Transverse cooling through optical molasses is needed to minimize the transverse expansion of the decelerated atoms before they are loaded to the MOT. Chirped cooling is necessary to reduce the speed of atoms down to about 40 $\mathrm{m\,s^{-1}}$ or lower for trapping. In this chapter, I discuss the basic theory of the optical molasses and chirped cooling, and show our experiment results from implementing these two techniques on the decelerated atoms.

## 6.1 Optical molasses

The interactions between atoms and light in a 2-level model is described by optical Bloch equations (see Section 2.2.2). Under this simple model, the force exerted by a near-resonant light on atoms can be derived from the photon scattering rate (Eq. 2.26) and Newton's second law $F = \frac{dp}{dt}$, where $p$ is the momentum of a single photon. This gives

$$\begin{aligned} F_{\mathrm{spon}} &= \hbar k R_{\mathrm{scatt}} \\ &= \frac{\Gamma \hbar k}{2} \frac{s_0}{1 + s_0 + 4\delta^2/\Gamma^2}. \end{aligned} \tag{6.1}$$

We call $F_{\mathrm{spon}}$ the spontaneous force for its dependency on photon absorption and spontaneous emission, and $k = 2\pi/\lambda$ is the wave number of laser.

The largest scattering rate that can be achieved in this setting is when $s_0 \gg 1$, yields $F_{\text{spon\_max}} = \hbar k\Gamma/2$. Using the lithium-7 D2 line transition as an example, $F_{\text{spon\_max}} \approx 1.8 \times 10^{-20}$ N. This force will exert acceleration of $1.6 \times 10^6$ m s$^{-2}$ when acting on atoms.

In order to make use of this scattering force for cooling an atom cloud, i.e. reducing the velocity spread modeled by the Maxwell-Boltzmann distribution, the spontaneous force must be velocity-selective. A good analog of this idea is a damped oscillator. One may notice that the frequency detune $\delta = \omega - \omega_0$ of the photon (Eq. 6.1) seen by atoms can be engineered as a function of the velocity using the Doppler shift,

$$\Delta\omega = \vec{k} \cdot \vec{v}, \tag{6.2}$$

where $\Delta\omega$ is the frequency shift in rad s$^{-1}$, $k = 2\pi/\lambda$ is the wave number, and $v$ is the atom velocity. Including this into our calculation, the total frequency detune of the laser seeing by the atoms is then given by

$$\delta_{\text{tot}} = \omega - \omega_0 + \vec{k} \cdot \vec{v}. \tag{6.3}$$

The direction of photon momentum flow $\vec{k}$ determines the direction of the force on atoms, while the total detune $\delta_{\text{tot}}$ decides which velocity group of the atoms that will experience the force. In the one dimensional case, two counter propagating lasers are used with a same frequency of $\omega < \omega_0$ ('red' detuned). For a three level system like the lithium-7 D2 line, an additional repump laser is ncessary close the scattering cycle, as shown in Fig. 6.1.

Thus, the total force for any atoms in the cloud in the 1D-molasses becomes

$$\begin{aligned}
\vec{F}_{\text{molasses1D}} &= \vec{F}_{\text{laser1}} + \vec{F}_{\text{laser2}} \\
&= \vec{F}_{\text{spon}}(\delta_{\text{tot}} = \omega - \omega_0 - \vec{k}_1 \cdot \vec{v}) + \vec{F}_{\text{spon}}(\delta_{\text{tot}} = \omega - \omega_0 + \vec{k}_2 \cdot \vec{v}) \\
&= \frac{\Gamma\hbar k}{2}\left[\frac{s_0}{1 + s_0 + 4(\omega - \omega_0 - kv)^2/\Gamma^2} - \frac{s_0}{1 + s_0 + 4(\omega - \omega_0 + kv)^2/\Gamma^2}\right]\hat{v}
\end{aligned}, \tag{6.4}$$

where $\hat{k}$ indicates that the direction of the force is along the atom velocity direction.

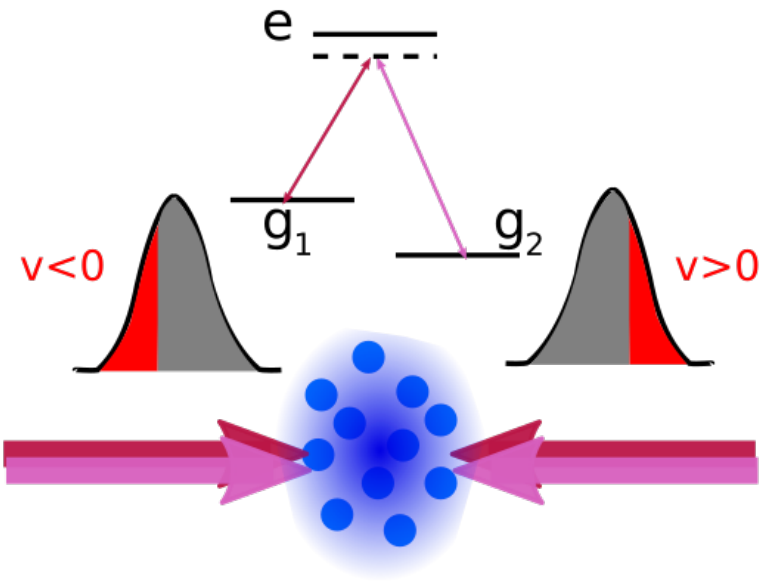


Fig. 6.1: Illustration of optical molasses along one dimension.

At small Doppler shifts, $\|kv\| \ll \omega - \omega_0$, the molasses force can be approximated as

$$\begin{aligned}\vec{F}_{\text{molasses}} &\approx \left[F_{\text{spon}}(\delta = \omega - \omega_0) - kv\frac{\partial F_{\text{spon}}}{\partial \delta}\bigg|_{\omega-\omega_0}\right]\hat{v} - \left[F_{\text{spon}}(\delta = \omega - \omega_0) + kv\frac{\partial F_{\text{spon}}}{\partial \delta}\bigg|_{\omega-\omega_0}\right]\hat{v} \\ &= -2kv\frac{\partial F_{\text{spon}}}{\partial \delta}\bigg|_{\omega-\omega_0}\hat{v} \\ &= \frac{8\hbar\delta k^2}{\Gamma}\frac{s_0}{(1+s_0+4\delta^2/\Gamma^2)^2}\vec{v}\end{aligned} , \tag{6.5}$$

where $\delta = \omega - \omega_0$ is the laser frequency detune in $\text{rad}\,\text{s}^{-1}$ relative to resonant transition of that atom.

The relation between the molasses force and the laser detune is shown in Fig. 6.2, at a fixed detune of $2\Gamma$ and saturation parameter $s_0 = 1$. From the same figure one can see that in the linear region at the middle of the plot, atoms experience negative forces proportional to their velocities. The capture velocity of the molasses is thus given by the boundary of this linear dependency, which is $v_c = \sigma/k = (\omega - \omega_0)/k$. The corresponding capturing beam temperature is $\frac{m\sigma^2}{k_B k^2}$.

The same discussion applies to 2D or 3D cases.

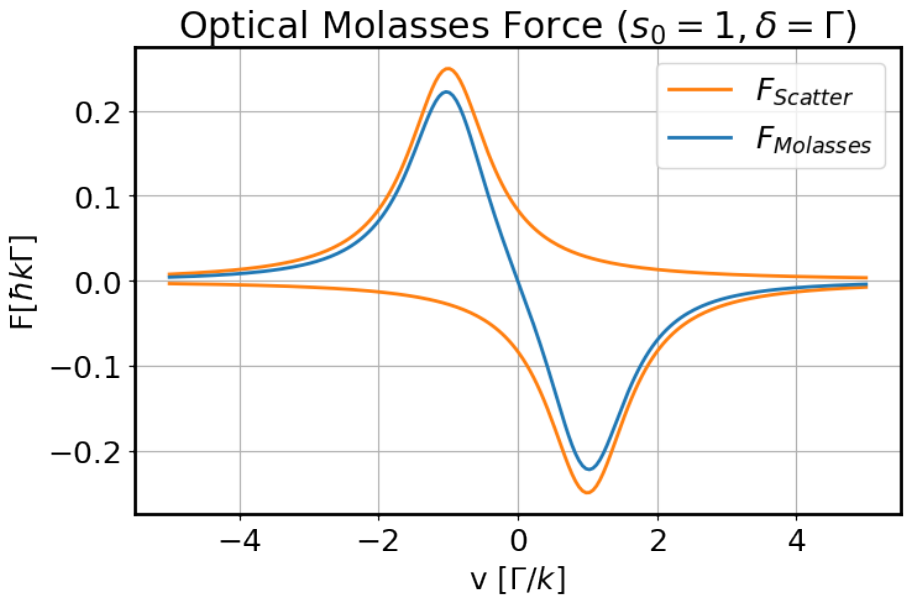


Fig. 6.2: 1D optical molasses force under different velocities. Laser detune 1 natural linewidth, saturation parameter 1.

## 6.2 Chirped cooling

The spontaneous force discussed in Section 6.1 may vanish when atoms go out of resonance due to the reduced velocity and thus the Doppler shift, especially when atoms are moving with large velocities. Two techniques have been developed to compensate the out-of-resonance issue: (1) Shift atom energy levels through external magnetic fields, i.e. the Zeeman slower [96]; (2) Actively adapt the laser frequency according to the velocity change. We chose the second method for its simplicity.

The application of the scattering force along one dimension brings us to the chirped cooling. Unlike optical molasses, chirped cooling uses a single counter-propagated laser beam with a constantly changing ('chirped') frequency. The total detune of photons to the atoms in Eq. 6.3 is still valid, where $\vec{v}$ becomes the overall translation velocity of the atom cloud.

There exists an upper bound of the laser chirping rate. The maximum deceleration is given when the velocity change of atoms can just 'catch up' with the change of laser frequency, or simply keep the maximum spontaneous force as in Eq. 6.1. Which

yields $\delta_{\text{tot}} = 0$ and

$$\begin{aligned} \omega &= \omega_0 + \vec{k} \cdot v \\ \Rightarrow \left(\frac{d\omega}{dt}\right)_{\max} &= \frac{\vec{k} \cdot \vec{v}}{t} \\ \Rightarrow \left(\frac{d\omega}{dt}\right)_{\max} &= -k\frac{dv}{dt} \quad (\text{assume } \hat{k} \cdot \hat{v} = 1) \end{aligned} \quad . \tag{6.6}$$

The maximum deceleration corresponds to the maximum deceleration is given by

$$\begin{aligned} a_{\max} = \frac{dv}{dt} &= -\frac{F_{\text{spon}}}{m} \\ &= \frac{\hbar k \Gamma}{2} \frac{s_0}{1 + s_0 + 4\delta_{\text{tot}}^2/\Gamma^2} \\ &= \frac{\hbar k \Gamma}{2} \frac{s_0}{1 + s_0} \quad (\text{when } \delta_{\text{tot}} = 0) \end{aligned} \quad . \tag{6.7}$$

Combine above two equations we can get an expression of the maximum chirping rate,

$$\left(\frac{d\omega}{dt}\right)_{\max} = -\frac{\hbar \Gamma k^2}{2} \frac{s_0}{1 + s_0}. \tag{6.8}$$

A large saturation parameter $s_0 \gg 1$ is preferred in order to achieve large spontaneous force. In the case of lithium-7 D2 line, the maximum deceleration is $a_{\max} = -1.6 \times 10^6 \text{ m s}^{-2}$ and maximum laser chirping rate is about 2.5 MHz µs$^{-1}$.

## 6.3 Experiment

The final experiment setup of optical molasses and chirped cooling for loading the MOT is shown in Fig. 6.9. A 1.33 inch cross chamber with viewports is connected after the decelerator and is used for 2D optical molases. After the molasses chamber, the atoms propagate over a distance of 40 cm where the chirped cooling is applied during a small time window. The MOT chamber is also connected for future work.

### 6.3.1 Optical molasses on decelerated atoms

In our beamline, the atom cloud output velocity from the decelerator is tunable from range 50 m s$^{-1}$ to 350 m s$^{-1}$, with both transverse and longitudinal temperature of about 30 mK ($\approx$ 6 m s$^{-1}$). Considering the degrading of the signal due to the

expansion of the slow atom beam, we chose a velocity of 200 $\mathrm{m\,s^{-1}}$ for testing. A simplified setup schematic is shown in Fig. 6.3

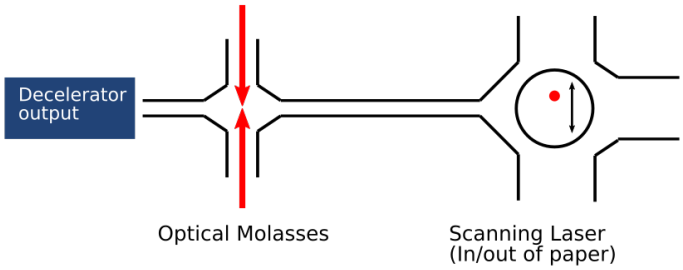


Fig. 6.3: The experiment setup for 2D map laser measurement of optical molasses. The detection laser in oriented in/out of the image plane and scaned along the direction that optical molasses is applied.

First, special care was taken to make sure that our molasses laser and detection laser beams are perpendicular to the atom beam. This was done by performing laser spectroscopy under different atom beam velocities. The laser frequency of the molasses is scanned by a VCO and its intensity was kept at about 0.01 $\mathrm{mW\,cm^{-2}}$, far below the saturation intensity. An optimal right angle between lasers and the atom beam is achieved when the spectroscopy plot for different atom beam velocities overlap, as shown in Fig. 6.4. According to Doppler shift(Eq. 6.2) a small angle offset will result in shifting of the frequency profile by amount of

$$\Delta\omega = kv\cos\left(\frac{\pi}{2}+\theta\right) \approx kv\theta, \tag{6.9}$$

where $k$ is the wave vector for pump or repump beam and $v$ is the atomic beam velocity along the longitudinal direction. Using an atomic beam velocity of 200 $\mathrm{m\,s^{-1}}$ as an example, we expect to see a 5 MHz shift on the frequency scan plot for an angle deviation of 1 degree.

Once the lasers are well aligned, a 2D time-of-flight and detecting laser position map is obtained, as shown in Fig. 6.5. Compared to the case without molasses, one can see obviously that the cloud size is squeezed due to the applied optical molasses. The integrated signal along detecting laser transverse position is shown in Fig. 6.6.

Interestingly, a 1D molasses with heavily imbalanced weak laser power between the incoming and retroflected laser is shown in Fig. 6.7, where the 2D map data shows

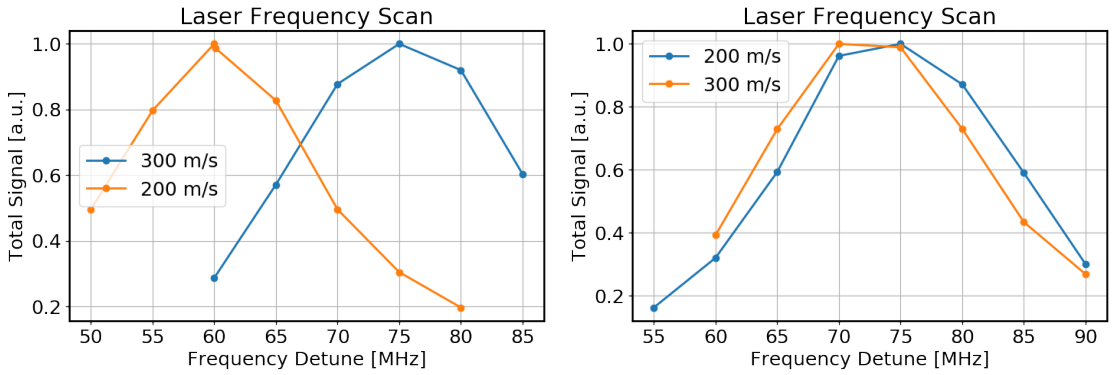


Fig. 6.4: Experimental measurement of 1D molasses with unbalanced(left) and balanced(right) power.

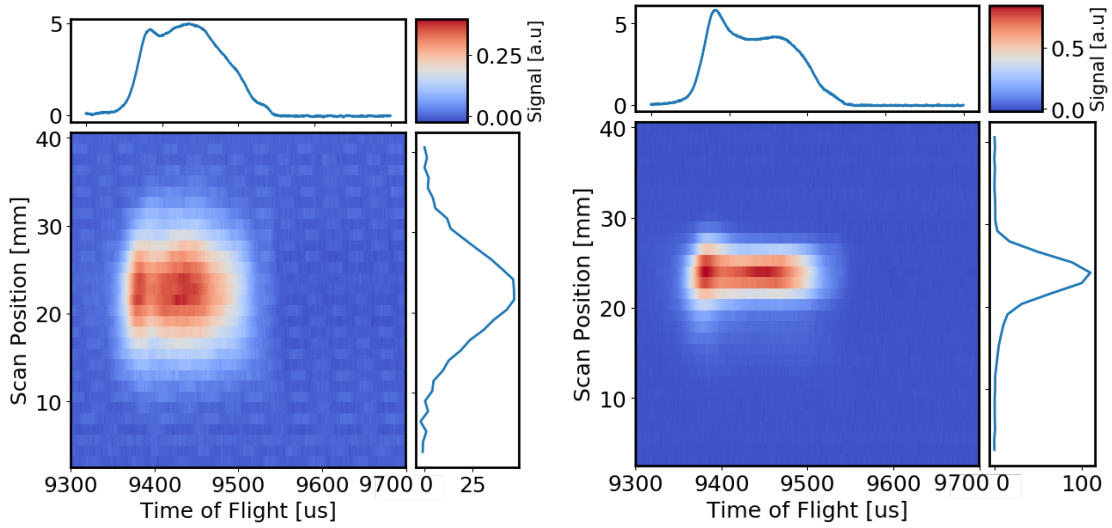


Fig. 6.5: A 2D map comparison between no molasses (left) and with molasses(right). The 2d map is obtain from scanning laser along the direction that molasses is applied.

a shifted atom cloud position in time. This is due to the fact that slower atoms arrive later and are subjected to this imbalanced force for a longer amount of time, resulting in a larger transverse shift.

The frequency detune of the molasses laser was scanned for optimization. An obtained plot of total signal measured at a very narrow slice ($\sim$ 1 mm) at the center of the atom beam downstream is shown in Fig. 6.8. The fluorescence signal reflects the cooling effects from the optical molasses. A higher signal level indicates a colder beam that has more atoms spatially passes through the laser slice. From the plot, one

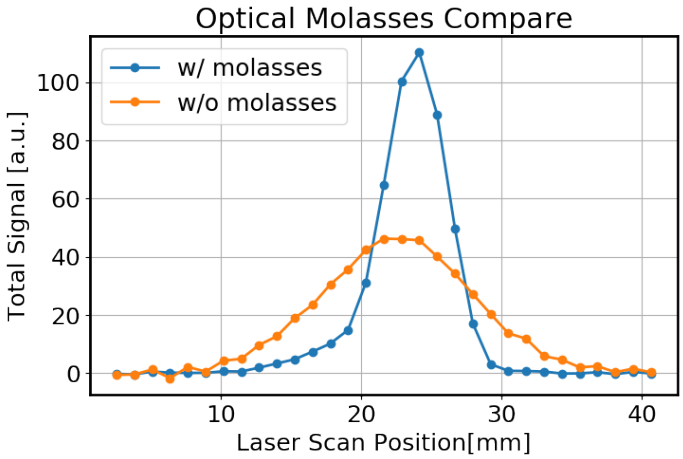


Fig. 6.6: Integrated laser scan signal comparison for no molasses and with molasses case

can learn that when the molasses lasers are far red or far blue detuned the molasses exert no effects. As the laser frequency gets closer to resonant frequency, the molasses induces compression on the neighborhood of small red detune and de-compression on the neighborhood blue detune. An optimal frequency of the optical molasses is thus can be obtained from this measurement, which is about -10 MHz.

### 6.3.2 Chirped cooling with modulated laser

We apply chirped cooling along beam propagation direction to further reduce the translation speed of the atoms down to below 40 $\mathrm{m\,s^{-1}}$ which our MOT is capable of capturing. A schematic of this setup is shown in Fig. 6.9.

We started testing chirped cooling on a beam with velocity 200 $\mathrm{m\,s^{-1}}$ after the decelerator. Then the same procedure was applied to lower translation velocities.

The laser for chirping is taken from the molasses beam, through a power-sharing setup using AOM, as shown in Fig. 6.10. The chirping laser is aligned such that it can propagates from the very end of the MOT chamber through the 2.5 m long decelerator tube all the way to the center of the Even-Lavie valve, thus guaranteeing a good overlap ofthe laser and atomic beam.

If using an atomic beam a velocity of 200 $\mathrm{m\,s^{-1}}$ and target the final velocity to 30 $\mathrm{m\,s^{-1}}$, the scanning range of chirp laser has to be $k\|v_f - v_i\| = \frac{2\pi}{\lambda}\|v_f - v_i\| \approx 255$ MHz. We implement this by holding the PID in the laser locking system and modulating the

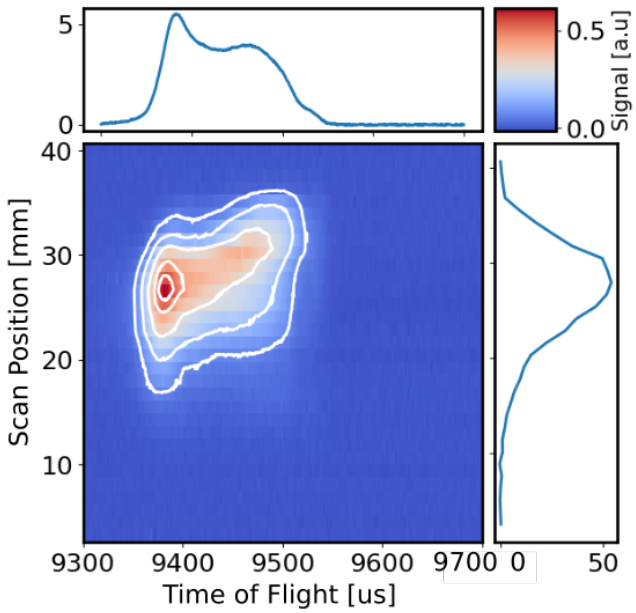


Fig. 6.7: 2D map of atom cloud after optical molasses with intentionally unbalanced laser power between incoming laser and retroflected laser

grating piezo voltage, where there is a linear dependency between the laser frequency and the grating piezo voltage. An example of the PID holding TTL signal and piezo modulation voltage signal is shown in Fig. 3.21.

Before starting the chirped cooling, we calibrated the laser frequency change in terms of the piezo voltage, by measuring laser frequency-piezo voltage plot. The slope of this plot gives us the rate of frequency change per piezo voltage change. The measurement was done in three different ways to get a good calibration: (a) By laser locking error signal; (b) By locking loop RF frequency counter; (c) Direct measurement by a wave meter.

**Calibration using error signal** The error signal generated by the laser beat locking is symmetric with respect to a frequency difference of zero. In our locking system, we know that locking to the point as noted on Fig. 6.11 will get 80 MHz from the reference laser. Thus, we know the corresponding locking point in symmetric gives -80 MHz. Considering that these two points are separated by 0.290 V, the laser frequency change relative to the TA piezo voltage change is 551 MHz per volt.

**Calibration using frequency counter** This requires the laser to be unlocked

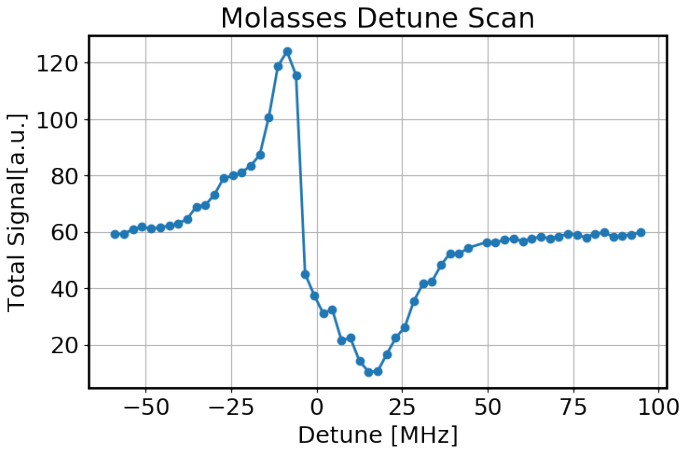


Fig. 6.8: Total signal of atoms after optical molasses under different laser detune.

and the grating piezo modulation amplitude to be 0, effectively only changing the piezo DC offset voltage. In the mean time one can read out the difference between the TA frequency and the reference laser frequencyunder a particular piezo voltage. Roughly about 10 data points were taken around our locking point and a liner fitting is performed, as shown in Fig. 6.12, which yields 554 MHz/V.

**Calibration using wavemeter** The calibration using frequency seems simple but is not quite accurate due to the lack of resolution. We also use direct measurement of the laser frequency using our wavemeter (HighFinesse WS-7), which gives 2 MHz resolution. We followed the same procedure as with the frequency counter and the result is shown in Fig. 6.12, which indicates a laser frequency to piezo voltage relation of 566 MHz $\mathrm{V}^{-1}$.

From above calibration one notice that there are deviations between calibration methods. The methods using the frequency counter and the wavemeter are prone to frequency drifting as the laser is not locked. We chose the calibrated TA frequency to piezo voltage ratio to be 554 MHz/s, while in the experiment we keep in mind there could be a 10 MHz calibration error.

We start testing with varying chirp start frequency by setting the targeted frequency to be 0 MHz detuned from the resonance. Since for this test our atom beam has a velocity of 200 $\mathrm{m\,s}^{-1}$, we choose to start from a higher bound (350 $\mathrm{m\,s}^{-1}$) and gradually reduce the frequency. The time-of-flight signal from laser fluorescence downstream is shown in Fig. 6.13.

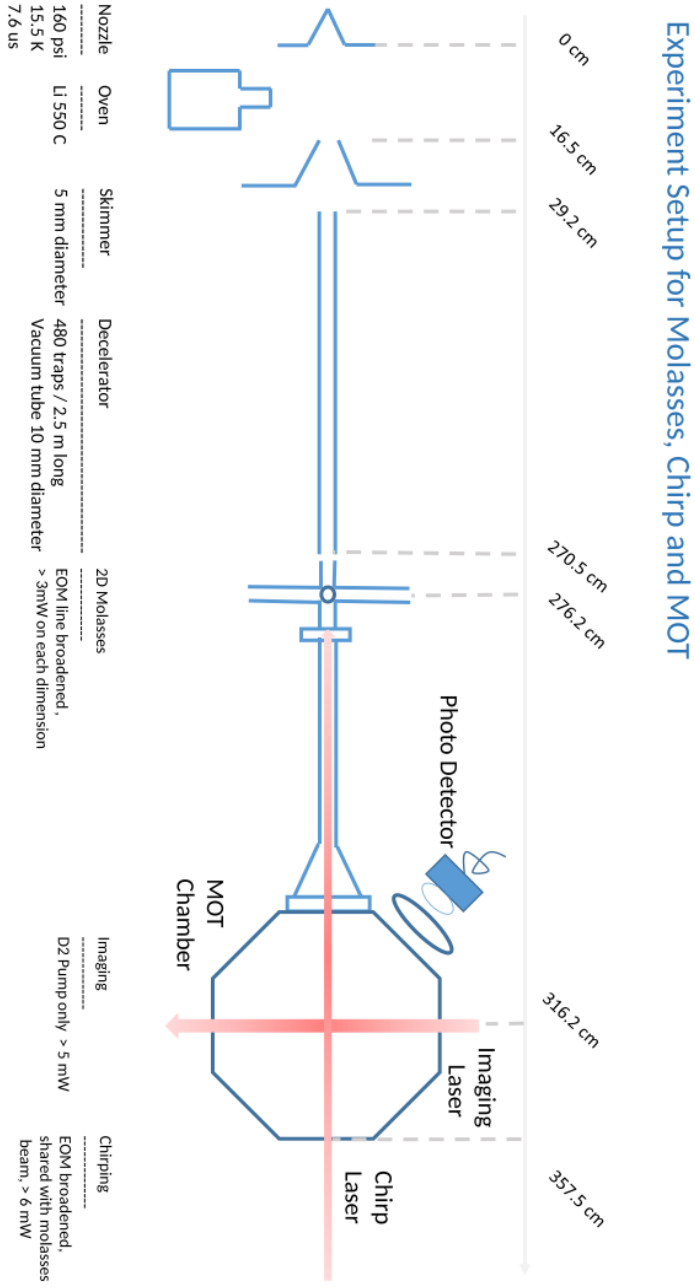


Fig. 6.9: Experiment setup for chirped cooling test.

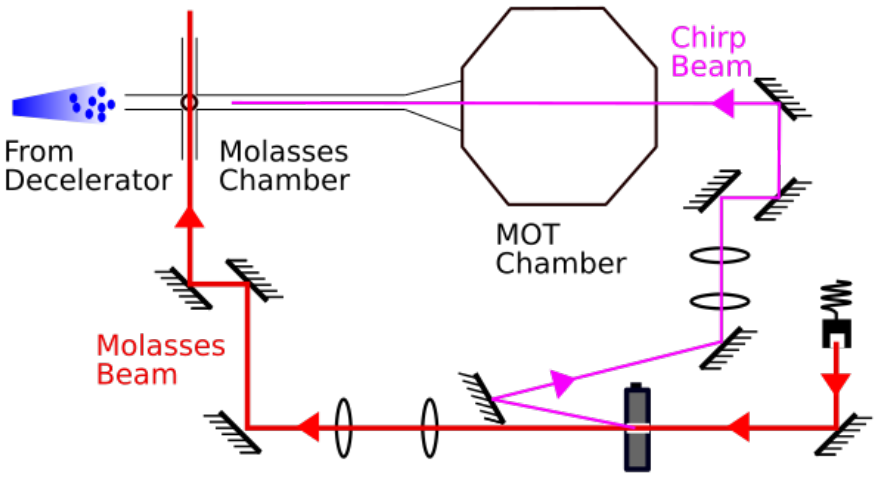


Fig. 6.10: Laser setup for power sharing between the molasses laser beam and the chirping laser beam.

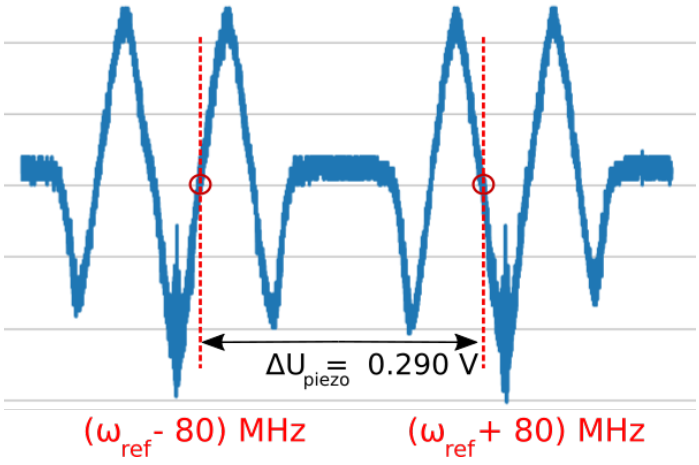


Fig. 6.11: Piezo voltage to frequency change calibration using TA beat lock error signal.

From the figure one can see that when the chirp starting frequency corresponds to a much higher Doppler velocity (280 $\mathrm{m\,s^{-1}} \sim 350\ \mathrm{m\,s^{-1}}$) compared to atom beam velocity (200 $\mathrm{m\,s^{-1}}$), a small part of the atom cloud is decelerated, but it is not sufficient to stop the atoms. The atoms seem get more decelerated when subjected

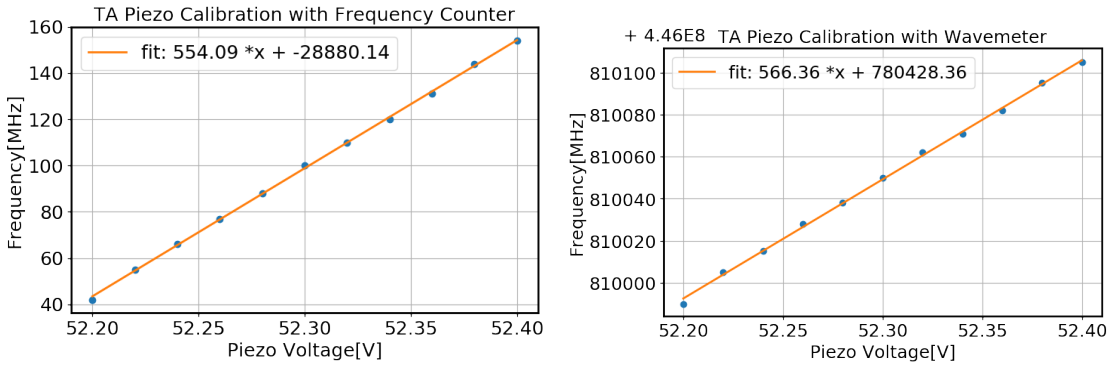


Fig. 6.12: Piezo voltage to frequency change calibration using a frequency counter(left) and wavemeter(right)

to a lower starting frequency. This is due to the reduced chirping rate as we have a fixed total chirping duration. As the chirp start frequency gets close to resonance with the atoms, we observe a time-of-flight signal with two peaks with different speed, which indicates that the chirping becomes more efficient for part of the atoms in the cloud, but due to high chirping rate not all atoms are decelerated together. Further reducing the chirp start frequency below the corresponding atoms' velocity gets us to no slowed atoms, at this region all atoms arrive before the measurement window (9400 us) with their original velocities.

From this study we decide to set the chirp start frequency higher than the corresponding Doppler shift, such that laser interaction with atoms is guaranteed when its frequency is lowered. We further studied the chirping duration as well as different chirp end velocities.

The chirp end frequency corresponds to the expected final velocity of atoms. From the previous test we notice that not all atoms are getting decelerated. Here various of data taking under different chirp final velocities are shown in 6.14, with fixed long chirp time. We observe that the total fluorescence signal of decelerated atoms stays about the same at high final velocities ($123\ \mathrm{m\,s^{-1}} \sim 188\ \mathrm{m\,s^{-1}}$), and starts going down when even lower velocities ($< 113\ \mathrm{m\,s^{-1}}$) were approached. This is due to the increasing time of atom cloud transverse expansion which we confirmed with a scanning laser measurements.

Next, the total chirp time was studied at fixed starting and ending frequency. As shown from the 2D map data in Fig. 6.15, there are two 'strips' of detected signal,

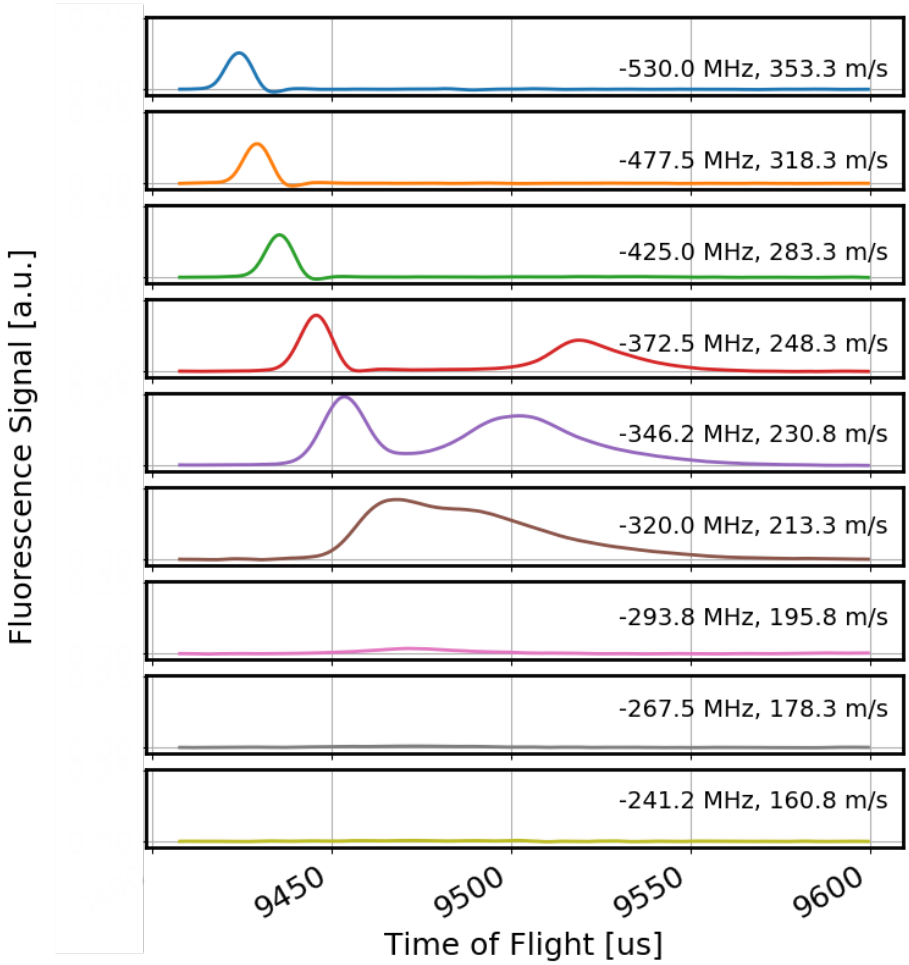


Fig. 6.13: Time-of-flight measurement of chirped atoms with different chirp start frequency corresponding to labeled velocities. Shared Y-axis with the same scale for signal in a arbitrary unit.

the ones that arrive earlier are atoms that were not interacting with the laser, wjereas the ones come later in time are from the atoms that got slowed by the laser. As the chirp time increases, more atoms are transferred to the slower part because of the increased interaction time.

The same chirp time scan was performed for a different laser chirping range, shown in Fig. 6.16.

One important parameter for us is the final velocity of the atom cloud after chirping, ideally one would take a two-point measurement of the atom beam to decide its velocity; however, in our setup only one laser measurement point is accessible.

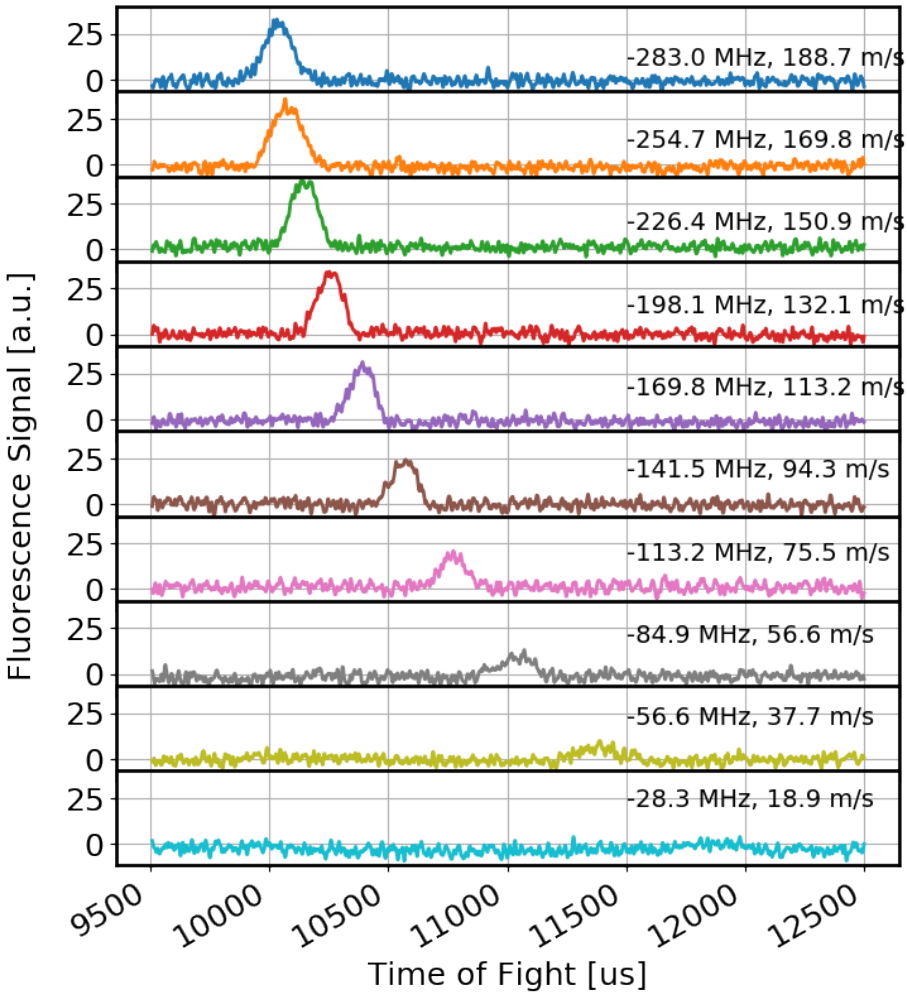


Fig. 6.14: Time-of-flight measurements of chirped atoms with different chirp end frequency corresponding to labeled velocities.

Nevertheless, we came up with a method that would allow us to estimate the beam speed from its arrival time at the detection point.

We have a fixed distance of $L = 0.40$ m between molasses chamber (where we know the beam arrival time $t_0$) and the detection point in the MOT chamber. Assuming that the atom beam has an initial velocity $v_0$ and an actual final velocity of $v_t$ after chirped cooling, denoting the start chirping time is $t_D$ (chirp delay), then the arrival time of atoms at the detection point after chirp is given by:

$$t = t_D + \frac{L - v_0(t_D - t_0) + C}{v_t} \tag{6.10}$$

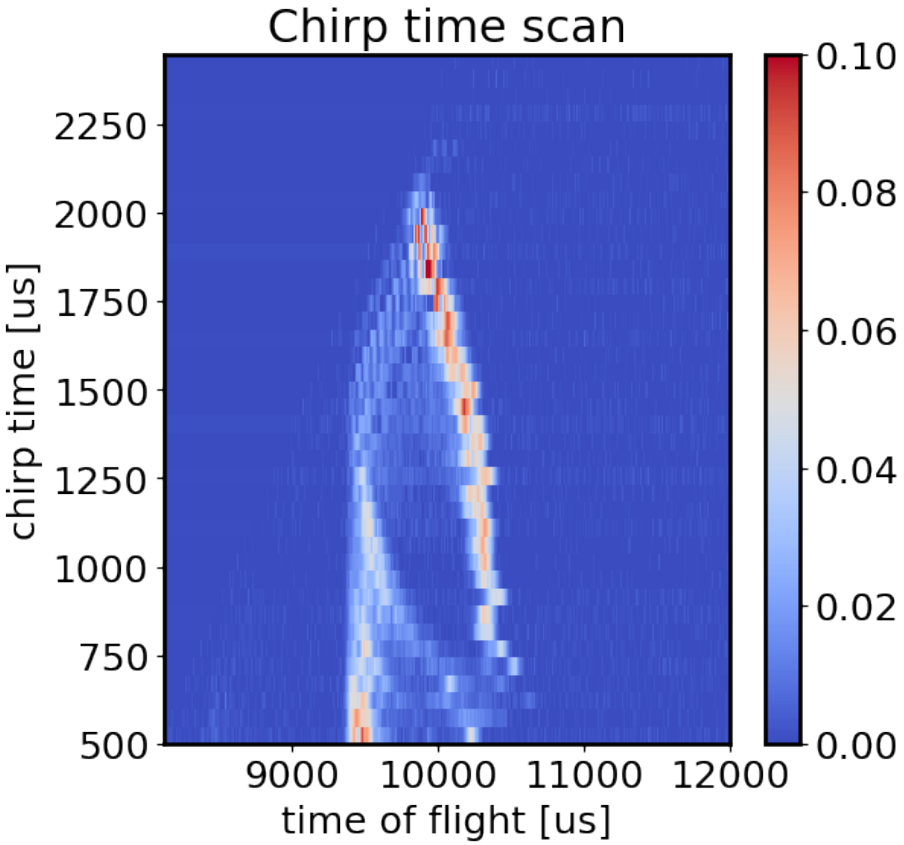


Fig. 6.15: Time-of-flight measurement of chirped atoms with different chirping duration(y-axis).

Where C is a constant that counts time during the deceleration and some fixed margin time between the chirping start and the actual deceleration. From the above equation, if we scan the chirp delay $t_D$ over a range of values, the slop of the $t - t_D$ plot yields a value of $-v_0/v_f$, which is the ratio between the initial and the final velocities of the atom beam. An example of such chirp delay scan is shown in Fig. 6.17.

Using this method as an estimation, we could figure out the final velocity of the atom beam. We explored the parameters needed for slowing atoms from various velocities to below 40 $\mathrm{m\,s^{-1}}$, with which we can then move on to the future experiment of trapping atoms in a MOT.

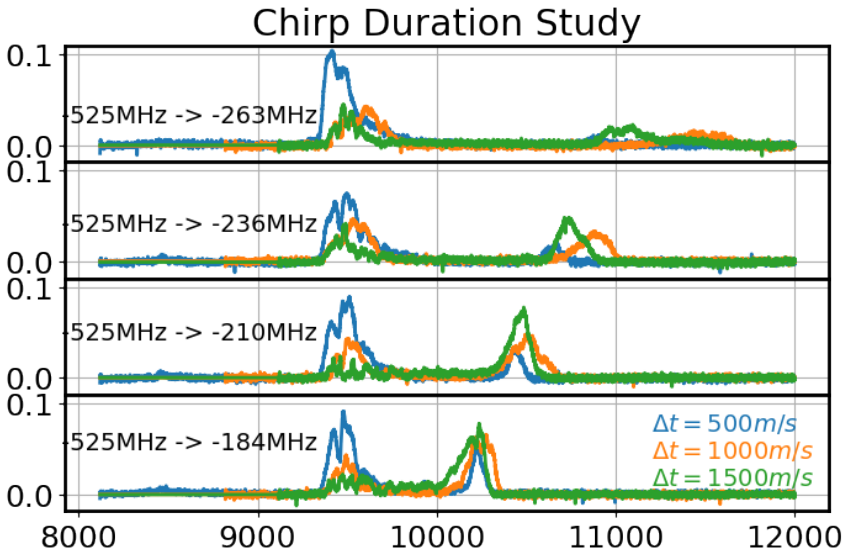


Fig. 6.16: Time-of-flight measurement of chirped atoms with different chirping duration for different chirp frequencies.

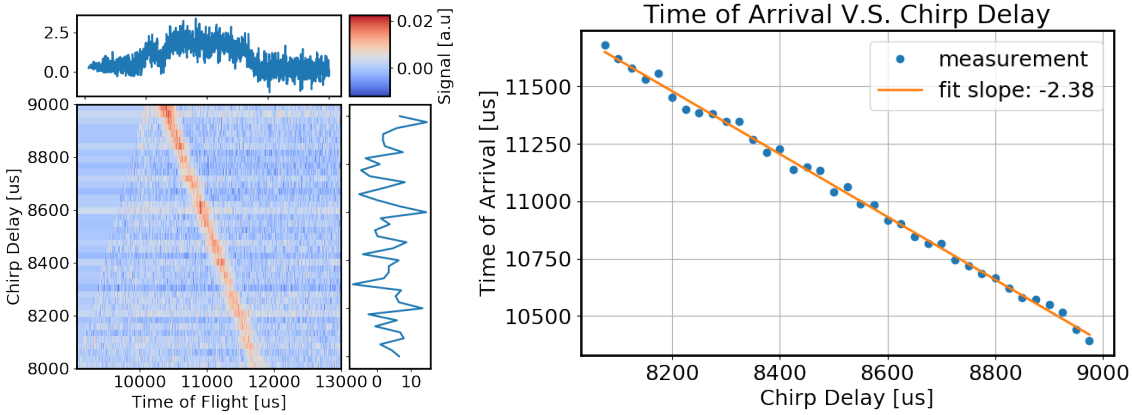


Fig. 6.17: An example of extracting beam velocity from chirp delay scan. Left: a 2D map of time-of-flight measurement under different delay scan. Right: extracted atom cloud arrival time versus chirp delay, where the slope of the linear fit gives the ratio of velocities before/after chirp.

# Chapter Seven: Conclusion

In the cold atom physics community, significant progresses have bee made since the realization of a BEC [3, 21, 32]. It has opened the possibility of a truly coherent matter wave. A few of the many related areas include an atom interferometry [28,37], atom laser [51, 68], atom lithography [107], and ultra-sensitive magnetometry [117]. A key limiting factor in the performance of all these devices is the spectral brightness and therefore the flux of the atoms. Moreover, the applicable atom species are limited to alkali atoms and a few others (Section 1.2.1). The work outlined in this dissertation explored a solution to the above two limitations. Improvement in these factors and thus above mentioned areas will lead to a wealth of progress in atomic physics.

This chapter provides a summary of this dissertation. I also disscuss the current bottlenecks of the experiment as well as the improvements that can be made to further enhancing its performance. The described methods, combined with our future work on Magneto-Optic Cooling (MOP), is potentially able to provide a versatile alternative to the state-of-the-art laser cooling method.

## 7.1 Summary of work

We have proposed a general method for generating cold atom sources with high flux. Due to the nature of our method, any atoms in the periodic table that are paramagnetic or can be made paramagnetic are candidates for a cold atom source. We demonstrated our approach using lithium atoms and reported that $10^8$ atoms at temperature of 30 mK can be achieved every 10 ms, at nearly zero velocity in the laboratory frame. Improved performance of our experimental setup can be easily achieved with some additional engineering, as described in Section 7.3.

We based our atom source on a combination of an Even-Lavie supersonic nozzle and an effusive hot oven. The supersonic nozzle, when operated at high stagnation pressure of 300 psi and low temperature of 15 K, generates a supersonic beam of about $10^{13}$ helium atoms at 100 mK. We then entrained lithihum atoms from a hot oven that is electrically heated to 550 °C, by which we achieved $10^{10}$ lithium atoms per pulse after the skimmer. This lithium beam has the same temperature as the carrier

at equilibrium and a longitudinal speed of $\sim 500\ \mathrm{m\,s^{-1}}$. A magnetic decelerator with 480 anti-Helmholtz coil pairs was then built to decelerate these lithium atoms to 50 $\mathrm{m\,s^{-1}}$, while preserving their low temperatures. A lithium beam with $10^8$ atoms at the end of the decelerator was achieved, at a temperature of 30 mK.

We explored the supersonic beam and entrainment under various settings. Specifically, we characterized the helium beam from the Even-Lavie nozzle under different sets of parameters, making sure that we could have a decently slow beam with a low temperature. Then we studied the entrainment of lithium atoms into the helium beam, by a hot oven and a pulsed ribbon. The resulting lithium beam was characterized and optimized with the current experiment settings. Lasers and a hot wire detector were used for detection and characterization.

The magnetic decelerator was constructed and tested in multiple phases. The magnetic field in the decelerator traps were measured and characterized. A series of electronics were built and their output voltage and stability were tested. While assembling various parts, we incorporated diagnostic circuits to provide system level testing and debugging. Time control sequences were realized through FPGA boards and the program interface was implemented. We explored a large parameter space to optimize the decelerator sequence. The output beam from the decelerator at different velocities and other conditions were characterized.

Before extra engineering are implemented to further improve the performance of the decelerator so that no lasers are needed for cooling, we prepare our current working system for trapped atoms, using optical molasses and chirped cooling. By the time of this dissertation was written, we achieved trapped atoms in a MOT with 2 s lifetime and an estimated atom number of $10^8$ per pulse.

## 7.2 Limitations and improvement

There are a few problems that limit the performance of our entrainment and decelerator. As for the entrainment part, the lithium atoms coming out from the hot oven occupies almost an angle of 180°, which limits the efficiency of the entrainment. This additional limits the highest temperature we can operate the oven, as the vacuum can only be maintained at $10^{-7}$ Torr, which corresponds to a maximal oven temperature of 600 °C. Moreover, operating the oven at higher temperatures accelerates the

depletion of the lithium. We tried to limit the angle spread by an oven with capillary tube filled nozzle as was done in previous work by David M. Weld et al. [106], but at temperatures above 550 °C, the performance of the oven is poor as it no longer operates as an effusive source of lithium.

An improvement could be to increase the aspect ratio of the capillary tubes. Though this may limit the total output flux of lithium, the narrower emission angle spread would improve the entrainment efficiency. Another potential solution could be a circulating heat pipe, a 'T' shaped oven to limit the output of the lithium while increasing the interaction between the lithium and the carrier gas.

The idea of using a pulsed ribbon in addition to a hot oven is a great method to increase the effective entrainment duty cycle. However, as shown in Fig. 4.18, the gain factor of 20 is accompanied by an increasing temperature of resulting beam, by a factor of 3, which is not desired. Additional experiment trials and simulation of the ribbon-to-beam distance may enable us to find a better configuration where entrainment by a pulsed ribbon would improve the atom number without substantially increasing the temperature of the beam.

There is still a lot of room to improve the performance of our decelerator. First, a compact design of connection between our source chamber and decelerator would improve the coupling of atoms into the decelerator tube. Previously we achieved about factor of 10 improvement by replacing a 2.75 inch chamber with a shorter guiding tube. Second, more robust electronics could help increasing the trap depth of the decelerator, which in turn would enable us to operate the supersonic beam at a higher temperature and effectively achieve a higher flux, as shown in Fig 4.11 and Fig. 4.13. Recently the group of our collaborator Prof. Edvardas Narevicius has implemented superconducting coils to enable higher current in their coils. Third, the output coupling of the decelerator could be improved. As shown in Fig. 5.38, the output atom beam is clipped by the narrow inner diameter of connecting vacuum parts, due to the expansion of atom cloud at a low velocity. Shortening this distance could improve the output coupling the decelerator and achieving more atoms. Additionally, the lowest terminal velocity of the decelerator is 50 $\mathrm{m\,s^{-1}}$ under the current design. This is due to the fact that a longer high current pulse is needed at lower decelerator velocities. It is not hard to solve this problem by utilizing larger capacitor banks and improved electronics. Once this is done, a slower velocity can be achieved and atoms exiting the decelerator could be directly loaded to a MOT without the assistance of optical

molasses and chirped cooling.

## 7.3 Future goals

The most exciting future direction of this project is to experimentally realize the MOP cooling on trapped atoms. MOP cooling is a newly proposed cooling method by our group in 2014 [101], which is a conceptually new method which relies on magnetic forces to realize the phase space compression of atoms cloud. An ensemble of lithum-7 atoms can be prepared as a mixture of LFS and HFS, which will change its phase space density if a quick magnetic pulse is applied.

Specifically, if all atoms moving along a given direction (e.g. +z) are transferred to an LFS state and all atoms moving in the opposite direction (-z) placed in a HFS, magnetic field with a gradient along z will push both groups to have lower velocities. This in turn lead to a phase space compression along the velocity direction. An illustrative schematic is shown in Fig. 7.1

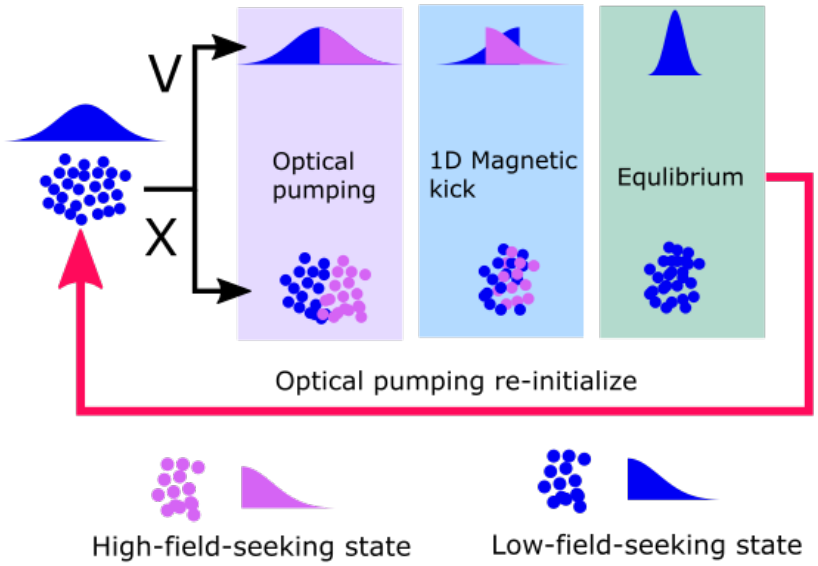


Fig. 7.1: A demonstration of MOP cooling.

There are three distance preparation steps are needed. First, optical pumping is used to transfer all atoms in the same magnetic state. Second, the selective optical pumping, which can be done either in a real space or in velocity space. In real space

one needs to shape the laser to only cover half of the trapped atom cloud, while in velocity space, one could use the well-established technique called stimulated rapid adiabatic passage [119]. Third, one-dimensional magnetic kicking, has been demonstrated in our accepted paper "Observation of a quasi-one-dimensional variation of the Stern-Gerlach effect"(accepted on March 19, 2019). This 3-step cycle can be repeated for a new velocity distribution until a required compression along the chosen velocity axis is achieved. Alternatively, a combination of coils and lasers oriented along other axes can be used to realize the 3D phase space compression.

The above methods of entrainment, deceleration, and MOP cooling, together with well-established methods of optical pumping, magnetic trapping and perhaps evaporative cooling, will enable the creation of an ultra-bright atoms laser [101]. Such a cooling method may be used to produce a very large BEC, which would benefit areas such as atom interferometry [28, 37], atom laser [51, 68], atom lithography [107], and ultra-sensitive magnetometry [117].

# Bibliography


[1] N. Akerman, M. Karpov, L. David, E. Lavert-Ofir, J. Narevicius, and E. Narevicius. Simultaneous deceleration of atoms and molecules in a supersonic beam. *New Journal of Physics*, 17(6):065015, June 2015. 60

[2] N. Akerman, M. Karpov, Y. Segev, N. Bibelnik, J. Narevicius, and E. Narevicius. Trapping of Molecular Oxygen together with Lithium Atoms. *Phys. Rev. Lett.*, 119, 11 2016. 60, 129

[3] M. H. Anderson, J. R. Ensher, M. R. Matthews, C. E. Wieman, and E. A. Cornell. Observation of Bose-Einstein Condensation in a Dilute Atomic Vapor. *Science*, 269(5221):198 – 201, 1995. 2, 4, 5, 146

[4] E. Arimondo, M. Inguscio, and P. Violino. Experimental determinations of the hyperfine structure in the alkali atoms. *Rev. Mod. Phys.*, 49:31 – 75, January 1977. 19

[5] A. Ashkin. Trapping of Atoms by Resonance Radiation Pressure. *Phys. Rev. Lett.*, 40:729 – 732, March 1978. 4

[6] A. Aspect, E. Arimondo, R. Kaiser, N. Vansteenkiste, and C. Cohen-Tannoudji. Laser Cooling below the One-Photon Recoil Energy by Velocity-Selective Coherent Population Trapping. *Phys. Rev. Lett.*, 61:826 – 829, August 1988. 4

[7] S. N. Atutov, R. Calabrese, V. Guidi, B. Mai, A. G. Rudavets, E. Scansani, L. Tomassetti, V. Biancalana, A. Burchianti, C. Marinelli, E. Mariotti, L. Moi, and S. Veronesi. Fast and efficient loading of a Rb magneto-optical trap using light-induced atomic desorption. *Phys. Rev. A*, 67:053401, May 2003. 48

[8] D. Bahat, O. Cheshnovsky, U. Even, N. Lavie, and Y. Magen. Generation and detection of intense cluster beams. *The Journal of Physical Chemistry*, 91(10):2460 – 2462, 1987. 51

[9] P. F. Barker and M. N. Shneider. Slowing molecules by optical microlinear deceleration. *Phys. Rev. A*, 66:065402, December 2002. 81

[10] S. Bartalini, I. Herrera, L. Consolino, L. Pappalardo, N. Marino, G. D'Arrigo, and F. S. Cataliotti. Full characterization of the loading of a magneto–optical trap from an alkali metal dispenser. *The European Physical Journal D - Atomic, Molecular, Optical and Plasma Physics*, 36(1):101 – 104, October 2005. 48

[11] S. M. Beck, D. L. Monts, M. G. Liverman, and R. E. Smalley. Intramolecular vibrational redistribution in electronically excited naphthalene. *J. Chem. Phys.*, 70(2):1062 – 1063, 1979. 51

[12] T. Bergeman, G. Erez, and H. J. Metcalf. Magnetostatic trapping fields for neutral atoms. *Phys. Rev. A*, 35:1535 – 1546, February 1987. 5

[13] H. L. Bethlem, G. Berden, and G. Meijer. Decelerating Neutral Dipolar Molecules. *Phys. Rev. Lett.*, 83:1558 – 1561, August 1999. 81, 83

[14] Hendrick L. Bethlem. Getting a handle on difficult atoms. *Physics*, 1, September 2008. 86

[15] D. Bhattacharyya, B. K. Dutta, B. Ray, and P. N. Ghosh. Line shape simulation and saturated absorption spectroscopic measurement of Rb–D2 transition. *Chem. Phys. Lett.*, 389(1):113 – 118, 2004. 25

[16] Black and E. D. An introduction to Pound-Drever-Hall laser frequency stabilization. *American Journal of Physics*, 69:79 – 87, January 2001. 24

[17] V. Bolpasi, N. K. Efremidis, M. J. Morrissey, P. C. Condylis, D. Sahagun, M. Baker, and W. von Klitzing. An ultra-bright atom laser. *New Journal of Physics*, 16(3):033036, March 2014. 1

[18] P. T. Bolwijn and C. Th. J. Alkemade. Power broadening and collision broadening of gas laser transitions. *Phys. Lett. A*, 25(8):632 – 634, 1967. 13

[19] Bose. Plancks Gesetz und Lichtquantenhypothese. *Zeitschrift für Physik*, 26(1):178 – 181, December 1924. 2

[20] C. C. Bradley, C. A. Sackett, and R. G. Hulet. Bose-Einstein Condensation of Lithium: Observation of Limited Condensate Number. *Phys. Rev. Lett.*, 78:985 – 989, February 1997. 2

[21] C. C. Bradley, C. A. Sackett, J. J. Tollett, and R. G. Hulet. Evidence of Bose-Einstein Condensation in an Atomic Gas with Attractive Interactions. *Phys. Rev. Lett.*, 75:1687 – 1690, August 1995. 2, 146

[22] Y. Chan and N. D. Bhaskar. Cooling of cesium atomic beam with light from spectrally broadened diode lasers. *J. Opt. Soc. Am. B*, 12(12):2347 – 2351, December 1995. 82

[23] S. Chaudhuri, S. Roy, and C. S. Unnikrishnan. Evaporative Cooling of Atoms to Quantum Degeneracy in an Optical Dipole Trap. *Journal of Physics: Conference Series*, 80:012036, September 2007. 4, 6

[24] W. Christen, K. Rademann, and U. Even. Supersonic Beams at High Particle Densities: Model Description beyond the Ideal Gas Approximation. *J. Phys. Chem. A*, 114(42):11189 – 11201, 2010. Pmid: 20961156. 53

[25] S. Chu, L. Hollberg, J. E. Bjorkholm, A. Cable, and A. Ashkin. Three-dimensional viscous confinement and cooling of atoms by resonance radiation pressure. *Phys. Rev. Lett.*, 55:48 – 51, July 1985. 4, 48

[26] Steven Chu, Claude Cohen-Tannoudji, and William D. Phillips. The Nobel Prize in Physics 1997, 1997. 81

[27] J. S. Coursey, D. J. Schwab, J. J. Tsai, and R. A. Dragoset. Atomic Weights and Isotopic Compositions (version 4.1), 2015. 18

[28] A. D. Cronin, J. o. Schmiedmayer, and D. E. Pritchard. Optics and interferometry with atoms and molecules. *Rev. Mod. Phys.*, 81:1051 – 1129, July 2009. 146, 150

[29] H. D. Curtis. A Brief Review of Recent Progress in Solar Physics. *Publications of the Astronomical Society of the Pacific*, 16:133, June 1904. 1

[30] J. Dalibard and C. Cohen-Tannoudji. Dressed-atom approach to atomic motion in laser light: The dipole force revisited. *J. Opt. Soc. Am. B*, 2(11):1707 – 1720, November 1985. 4

[31] D. Das and V. Natarajan. Absolute frequency measurement of the lithium $D$ lines: Precise determination of isotope shifts and fine-structure intervals. *Phys. Rev. A*, 75:052508, May 2007. 19, 20

[32] K. B. Davis, M.-O. Mewes, M. R. Andrews, N. J. van Druten, D. S. Durfee, D. M. Kurn, and W. Ketterle. Bose-Einstein Condensation in a Gas of Sodium Atoms. *Phys. Rev. Lett.*, 75:3969 – 3973, November 1995. 2, 4, 5, 146

[33] R. Delhuille, A. Miffre, E. Lavallette, M. Büchner, C. Rizzo, G. Trénec, J. Vigué, H. J. Loesch, and J. P. Gauyacq. Optimization of a Langmuir–Taylor detector for lithium. *Rev. Sci. Instrum.*, 73(6):2249 – 2258, 2002. 66

[34] B. DeMarco and D. S. Jin. Onset of Fermi Degeneracy in a Trapped Atomic Gas. *Science*, 285(5434):1703 – 1706, 1999. 2, 3

[35] P. H. Diamond, U. Frisch, and Y. Pomeau. Editorial introduction to the special issue "Plasma physics in the 20th century as told by players". *The European Physical Journal H*, 43(4):337 – 353, December 2018. 1

[36] S. A. Diddams, J. C. Bergquist, S. R. Jefferts, and C. W. Oates. Standards of Time and Frequency at the Outset of the 21st Century. *Science*, 306(5700):1318 – 1324, 2004. 1

[37] J. P. Dowling. Correlated input-port, matter-wave interferometer: Quantum-noise limits to the atom-laser gyroscope. *Phys. Rev. A*, 57:4736 – 4746, June 1998. 146, 150

[38] J. M. Doyle, B. Friedrich, J. Kim, and D. Patterson. Buffer-gas loading of atoms and molecules into a magnetic trap. *Phys. Rev. A*, 52:R2515 – R2518, October 1995. 86

[39] T. Esslinger, I. Bloch, and T. W. H. ansch. Bose-Einstein condensation in a quadrupole-Ioffe-configuration trap. *Phys. Rev. A*, 58:R2664 – R2667, October 1998. 5

[40] U. Even. Pulsed Supersonic Beams from High Pressure Source: Simulation Results and Experimental Measurements. *Advances in Chemistry*, 2014:1 – 11, 08 2014. 52, 55, 72

[41] U. Even. "The Even-Lavie valve as a source for high intensity supersonic beam". *EPJ Techniques and Instrumentation*, 2(1):17, December 2015. 48, 51, 55

[42] U. Even, I. Al-Hroub, and J. Jortner. Small He clusters with aromatic molecules. *Chemical Physics - CHEM PHYS*, 115, 08 2001. 51, 55

[43] U. Even, Y. Magen, J. Jortner, and H. Levanon. Electronic excitations of magnesium tetraphenylporphyrin in supersonic expansions. *J. Chem. Phys.*, 76(12):5684 – 5692, 1982. 51

[44] R. P. Feynman. Superfluidity and Superconductivity. *Rev. Mod. Phys.*, 29:205 – 212, April 1957. 2

[45] R. Fulton, A. I. Bishop, and P. F. Barker. Optical Stark Decelerator for Molecules. *Phys. Rev. Lett.*, 93:243004, December 2004. 81

[46] W. R. Gentry and C. F. Giese. Ten-microsecond pulsed molecular beam source and a fast ionization detector. *Rev. Sci. Instrum.*, 49(5):595 – 600, 1978. 51

[47] J. J. Gilijamse, S. Hoekstra, S. Y. T. van de Meerakker, G. C. Groenenboom, and G. Meijer. Near-Threshold Inelastic Collisions Using Molecular Beams with a Tunable Velocity. *Science*, 313(5793):1617 – 1620, 2006. 48

[48] N. Gisin, G. '. Ribordy, W. Tittel, and H. Zbinden. Quantum cryptography. *Rev. Mod. Phys.*, 74:145 – 195, March 2002. 1

[49] T. E. Gough, J. S. Muenter, A. Dymanus, D. Lainé, R. E. Miller, W. Demtröder, J. Hepburn, A. Legon, J. J. Sloan, U. Valbusa, G. Boato, L. Mattera, R. B. Doak, D. Auerbach, G. Coma, B. Poelsema, M. Asscher, and G. A. Somorjai. *Atomic and Molecular Beam Methods: Vol. 1*, volume 1. Oxford University Press, 01 1992. 54

[50] O. F. Hagena. Pulsed valve for supersonic nozzle experiments at cryogenic temperatures. *Rev. Sci. Instrum.*, 62(8):2038 – 2039, 1991. 48

[51] S. A. Haine and J. J. Hope. Outcoupling from a Bose-Einstein condensate with squeezed light to produce entangled-atom laser beams. *Phys. Rev. A*, 72:033601, September 2005. 146, 150

[52] T. W. Hänsch and A. L. Schawlow. Cooling of gases by laser radiation. *Optics Communications*, 13(1):68 – 69, 1975. 3

[53] D. M. Harber, J. M. McGuirk, J. M. Obrecht, and E. A. Cornell. Thermally Induced Losses in Ultra-Cold Atoms Magnetically Trapped Near Room-Temperature Surfaces. *J. Low Temp. Phys.*, 133(3):229 – 238, November 2003. 5

[54] C. Henkel, S. Pötting, and M. Wilkens. Loss and heating of particles in small and noisy traps. *Appl. Phys. B*, 69(5):379 – 387, December 1999. 5

[55] E. A. L. Henn, J. A. Seman, G. Roati, K. M. F. M. aes, and V. S. Bagnato. Emergence of Turbulence in an Oscillating Bose-Einstein Condensate. *Phys. Rev. Lett.*, 103:045301, July 2009. 1

[56] H. F. Hess. Evaporative cooling of magnetically trapped and compressed spin-polarized hydrogen. *Phys. Rev. B*, 34:3476 – 3479, September 1986. 4

[57] W. T. Hicks. Evaluation of Vapor-Pressure Data for Mercury, Lithium, Sodium, and Potassium. *J. Chem. Phys.*, 38(8):1873 – 1880, 1963. 18, 62

[58] M. Hillenkamp, S. Keinan, and U. Even. Condensation limited cooling in supersonic expansions. *J. Chem. Phys.*, 118(19):8699 – 8705, 2003. 48, 53

[59] S. D. Hogan, D. Sprecher, M. Andrist, N. Vanhaecke, and F. Merkt. Zeeman deceleration of H and D. *Phys. Rev. A*, 76:023412, August 2007. 83

[60] S. D. Hogan, A. W. Wiederkehr, M. Andrist, H. Schmutz, and F. Merkt. Slow beams of atomic hydrogen by multistage Zeeman deceleration. *J. Phys. B: At. Mol. Opt. Phys.*, 41(8):081005, April 2008. 83

[61] L. Holmegaard, J. H. Nielsen, I. Nevo, H. Stapelfeldt, F. Filsinger, J. K. upper, and G. Meijer. Laser-Induced Alignment and Orientation of Quantum-State-Selected Large Molecules. *Phys. Rev. Lett.*, 102:023001, January 2009. 51

[62] L. Van Hove. Review of recent advances in high energy physics. *Comput. Phys. Commun.*, 22(2):187 – 197, 1981. 1

[63] K. Hueck, N. Luick, L. Sobirey, J. Siegl, T. Lompe, H. Moritz, L. W. Clark, and C. Chin. Calibrating high intensity absorption imaging of ultracold atoms. *Opt. Express*, 25(8):8670 – 8679, April 2017. 15

[64] S. Imanishi, U. Tanaka, and S. Urabe. Frequency Stabilization of Diode Laser Using Dichroic-Atomic-Vapor Laser Lock Signals and Thin Rb Vapor Cell. *Japanese Journal of Applied Physics*, 44(9A):6767 – 6771, September 2005. 25

[65] D. Irimia, D. Dobrikov, R. Kortekaas, H. Voet, D. A. van den Ende, W. A. Groen, and M. H. M. Janssen. A short pulse (7 $\mu$s FWHM) and high repetition rate (dc-5kHz) cantilever piezovalve for pulsed atomic and molecular beams. *Rev. Sci. Instrum.*, 80(11):113303, 2009. 51

[66] D. Jaksch. Optical lattices, ultracold atoms and quantum information processing. *Contemporary Physics*, 45(5):367 – 381, 2004. 1

[67] J. Jankunas and A. Osterwalder. Cold and Controlled Molecular Beams: Production and Applications. *Annu. Rev. Phys. Chem.*, 66(1):241 – 262, 2015. Pmid: 25532950. 48

[68] M. T. Johnsson and S. A. Haine. Generating Quadrature Squeezing in an Atom Laser through Self-Interaction. *Phys. Rev. Lett.*, 99:010401, July 2007. 146, 150

[69] W. Ketterle and N. J. Van Druten. Evaporative cooling of trapped atoms. *Adv. At. Mol. Opt. Phys.*, 37, 12 1996. 4

[70] A. Kohlhase and S. Kita. Pulsed metastable atomic beam source for time-of-flight applications. *Rev. Sci. Instrum.*, 57(12):2925 – 2928, 1986. 48

[71] A. Lambrecht, J. M. Courty, S. Reynaud, and E. Giacobino. Cold atoms: A new medium for quantum optics. *Appl. Phys. B*, 60(2):129 – 134, February 1995. 1

[72] R. A. Larsen, S. K. Neoh, and D. R. Herschbach. Seeded supersonic alkali atom beams. *Rev. Sci. Instrum.*, 45(12):1511 – 1516, 1974. 52

[73] R. L. LeRoy, T. R. Govers, and J. M. Deckers. Supersonic molecular beam intensities. *Can. J. Chem.*, 48(6):927 – 933, 1970. 53

[74] P. D. Lett, R. N. Watts, C. I. Westbrook, W. D. Phillips, P. L. Gould, and H. J. Metcalf. Observation of Atoms Laser Cooled below the Doppler Limit. *Phys. Rev. Lett.*, 61:169 – 172, July 1988. 4

[75] S. Longo, P. Diomede, A. Laricchiuta, G. Colonna, M. Capitelli, D. Ascenzi, M. Scotoni, P. Tosi, and F. Pirani. From Microscopic to Macroscopic Modeling of Supersonic Seeded Atomic Beam. In O. Gervasi, B. Murgante, A. Laganà, D. Taniar, Y. Mun, and M. L. Gavrilova, editors, *Computational Science and Its Applications – ICCSA 2008*, pages 1131 – 1140, Berlin, Heidelberg, 2008. Springer Berlin Heidelberg. 61

[76] J. A. Maddi, T. P. Dinneen, and H. Gould. Slowing and cooling molecules and neutral atoms by time-varying electric-field gradients. *Phys. Rev. A*, 60:3882 – 3891, November 1999. 81

[77] W. I. McAlexander, E. R. I. Abraham, and R. G. Hulet. Radiative lifetime of the $2P$ state of lithium. *Phys. Rev. A*, 54:R5 – R8, July 1996. 19

[78] A. D. McNaught and A. Wilkinson. *Compendium of Chemical Terminology, 2nd ed. (The "Gold Book").* Blackwell Scientific Publications, 1997. 17

[79] H. J. Metcalf and P. van der Straten. *Laser Cooling and Trapping.* Graduate Texts in Contemporary Physics. Springer New York, 2001. 81

[80] M.-O. Mewes, M. R. Andrews, N. J. van Druten, D. M. Kurn, D. S. Durfee, and W. Ketterle. Bose-Einstein Condensation in a Tightly Confining dc Magnetic Trap. *Phys. Rev. Lett.*, 77:416 – 419, July 1996. 2

[81] M.-O. Mewes, M. R. Andrews, N. J. van Druten, D. M. Kurn, D. S. Durfee, C. G. Townsend, and W. Ketterle. Collective Excitations of a Bose-Einstein Condensate in a Magnetic Trap. *Phys. Rev. Lett.*, 77:988 – 991, August 1996. 5

[82] A. L. Migdall, J. V. Prodan, W. D. Phillips, T. H. Bergeman, and H. J. Metcalf. First Observation of Magnetically Trapped Neutral Atoms. *Phys. Rev. Lett.*, 54:2596 – 2599, June 1985. 5

[83] C. Monroe, W. Swann, H. Robinson, and C. Wieman. Very cold trapped atoms in a vapor cell. *Phys. Rev. Lett.*, 65:1571 – 1574, September 1990. 48

[84] S. A. Moses, J. Covey, M. T. Miecnikowski, D. S. Jin, and J. Ye. New frontiers with quantum gases of polar molecules. *Nature Physics*, 13, 10 2016. 6

[85] R. Nagar, D. Abraham, N. Tessler, A. Fraenkel, G. Eisenstein, E. P. Ippen, U. Koren, and G. Raybon. Frequency-modulation mode locking of a semiconductor laser. *Opt. Lett.*, 16(22):1750 – 1752, November 1991. 24

[86] E. Narevicius, A. Libson, C. G. Parthey, I. Chavez, J. Narevicius, U. Even, and M. G. Raizen. Stopping Supersonic Beams with a Series of Pulsed Electromagnetic Coils: An Atomic Coilgun. *Phys. Rev. Lett.*, 100:093003, March 2008. 7, 83, 84

[87] E. Narevicius, A. Libson, C. G. Parthey, I. Chavez, J. Narevicius, U. Even, and M. G. Raizen. Stopping supersonic oxygen with a series of pulsed electromagnetic coils: A molecular coilgun. *Phys. Rev. A*, 77:051401, May 2008. 83

[88] E. Narevicius, C. G. Parthey, A. Libson, J. Narevicius, I. Chavez, U. Even, and M. G. Raizen. An atomic coilgun: Using pulsed magnetic fields to slow a supersonic beam. *New Journal of Physics*, 9(10):358 – 358, October 2007. 83

[89] A. Naß and E. Steffens. Direct simulation of low-pressure supersonic gas expansions and its experimental verification. *Nuclear Instruments and Methods in Physics Research Section A: Accelerators, Spectrometers, Detectors and Associated Equipment*, 598(3):653 – 666, 2009. 54

[90] K. M. O'Hara, S. R. Granade, M. E. Gehm, T. A. Savard, S. Bali, C. Freed, and J. E. Thomas. Ultrastable $CO_2$ Laser Trapping of Lithium Fermions. *Phys. Rev. Lett.*, 82:4204 – 4207, May 1999. 2, 3

[91] M. M. Orescanin, D. Prisco, J. M. Austin, and S. W. Kieffer. Flow of supersonic jets across flat plates: Implications for ground-level flow from volcanic blasts. *Journal of Geophysical Research: Solid Earth*, 119(4):2976 – 2987, 2014. 54

[92] A. S. Palau, S. D. Eder, T. Andersen, A. K. '. Ravn, G. Bracco, and B. Holst. Center-line intensity of a supersonic helium beam. *Phys. Rev. A*, 98:063611, December 2018. 53

[93] W. Petrich, M. H. Anderson, J. R. Ensher, and E. A. Cornell. Stable, Tightly Confining Magnetic Trap for Evaporative Cooling of Neutral Atoms. *Phys. Rev. Lett.*, 74:3352 – 3355, April 1995. 5

[94] K. A. Phalnikar, F. Alvi, and C. Shih. Behavior of Free and Impinging Supersonic Microjets. *15th AIAA Computational Fluid Dynamics Conference*, 06 2001. 54

[95] W. D. Phillips. Nobel Lecture: Laser cooling and trapping of neutral atoms. *Rev. Mod. Phys.*, 70:721 – 741, July 1998. 3

[96] W. D. Phillips and H. Metcalf. Laser Deceleration of an Atomic Beam. *Phys. Rev. Lett.*, 48:596 – 599, March 1982. 4, 48, 80, 132

[97] S. Pollock, J. P. Cotter, A. Laliotis, and E. A. Hinds. Integrated magneto-optical traps on a chip using silicon pyramid structures. *Opt. Express*, 17(16):14109 – 14114, August 2009. 48

[98] D. E. Pritchard. Cooling Neutral Atoms in a Magnetic Trap for Precision Spectroscopy. *Phys. Rev. Lett.*, 51:1336 – 1339, October 1983. 5

[99] E. L. Raab, M. Prentiss, A. Cable, S. Chu, and D. E. Pritchard. Trapping of Neutral Sodium Atoms with Radiation Pressure. *Phys. Rev. Lett.*, 59:2631 – 2634, December 1987. 5, 48

[100] W. Radloff, V. Stert, and H.-H. Ritze. New Spectral Information by Lamb-Dip Spectroscopy. In J. L. Hall and J. L. Carlsten, editors, *Laser Spectroscopy III*, pages 454 – 454, Berlin, Heidelberg, 1977. Springer Berlin Heidelberg. 27

[101] M. G. Raizen, D. Budker, S. M. Rochester, J. Narevicius, and E. Narevicius. Magneto-optical cooling of atoms. *Opt. Lett.*, 39(15):4502 – 4505, August 2014. 129, 149, 150

[102] N. Ramsey and O. U. Press. *Molecular Beams*. International series of monographs on physics. OUP Oxford, 1956. 48

[103] A. Ruschhaupt, J. G. Muga, and M. G. Raizen. One-photon atomic cooling with an optical Maxwell demon valve. *J. Phys. B: At. Mol. Opt. Phys.*, 39(18):3833 – 3838, September 2006. 1

[104] L. Salasnich. Fermionic condensation in ultracold atoms, nuclear matter and neutron stars. *Journal of Physics: Conference Series*, 497:012026, April 2014. 2

[105] Y. Segev, N. Bibelnik, N. Akerman, Y. Shagam, A. Luski, M. Karpov, J. Narevicius, and E. Narevicius. Molecular beam brightening by shock-wave suppression. *Science Advances*, 3(3), 2017. 51

[106] R. Senaratne, S. V. Rajagopal, Z. A. Geiger, K. M. Fujiwara, V. Lebedev, and D. M. Weld. Effusive atomic oven nozzle design using an aligned microcapillary array. *Rev. Sci. Instrum.*, 86(2):023105, 2015. 62, 148

[107] I. Shvarchuck, Ch. Buggle, D. S. Petrov, K. Dieckmann, M. Zielonkowski, M. Kemmann, T. G. Tiecke, W. von Klitzing, G. V. Shlyapnikov, and J. T. M. Walraven. Bose-Einstein Condensation into Nonequilibrium States Studied by Condensate Focusing. *Phys. Rev. Lett.*, 89:270404, December 2002. 146, 150

[108] K. F. Smith and P. J. Unsworth. Molecular beam spectroscopy. *Science Progress (1933- )*, 53(209):45 – 59, 1965. 48

[109] A. Steane. Quantum computing. *Rep. Prog. Phys.*, 61(2):117 – 173, February 1998. 1

[110] M. R. Tarbutt. Laser cooling of molecules. *Contemporary Physics*, 59(4):356 – 376, 2018. 6

[111] E. H. Taylor and S. Datz. Study of Chemical Reaction Mechanisms with Molecular Beams. The Reaction of K with HBr. *J. Chem. Phys.*, 23(9):1711 – 1718, 1955. 48

[112] J. Thévenin, M. Vallet, M. Brunel, H. Gilles, and S. Girard. Beat-note locking in dual-polarization lasers submitted to frequency-shifted optical feedback. *J. Opt. Soc. Am. B*, 28(5):1104 – 1110, May 2011. 25

[113] A. G. Truscott, K. E. Strecker, W. I. McAlexander, G. B. Partridge, and R. G. Hulet. Observation of Fermi Pressure in a Gas of Trapped Atoms. *Science*, 291(5513):2570 – 2572, 2001. 3

[114] J. P. Valleau and J. M. Deckers. Supersonic molecular beams: Ii. Theory of the formation of supersonic molecular beams. *Can. J. Chem.*, 43(1):6 – 17, 1965. 52

[115] S. Y. T. van de Meerakker, H. L. Bethlem, N. Vanhaecke, and G. Meijer. Manipulation and Control of Molecular Beams. *Chem. Rev.*, 112(9):4828 – 4878, 2012. Pmid: 22449067. 6

[116] N. Vanhaecke, U. Meier, M. Andrist, B. H. Meier, and F. '. '. Merkt. Multistage Zeeman deceleration of hydrogen atoms. *Phys. Rev. A*, 75:031402, March 2007. 83

[117] M. Vengalattore, J. M. Higbie, S. R. Leslie, J. Guzman, L. E. Sadler, and D. M. Stamper-Kurn. High-Resolution Magnetometry with a Spinor Bose-Einstein Condensate. *Phys. Rev. Lett.*, 98:200801, May 2007. 146, 150

[118] E. V. Vilshanskaya, S. A. Saakyan, V. A. Sautenkov, D. A. Murashkin, B. B. Zelener, and B. V. Zelener. Saturation spectroscopy of calcium atomic vapor in hot quartz cells with cold windows. *Journal of Physics: Conference Series*, 946:012130, January 2018. 25

[119] N. V. Vitanov, A. A. Rangelov, B. W. Shore, and K. Bergmann. Stimulated Raman adiabatic passage in physics, chemistry, and beyond. *Rev. Mod. Phys.*, 89:015006, March 2017. 150

[120] T. E. Wall. Preparation of cold molecules for high-precision measurements. *J. Phys. B: At. Mol. Opt. Phys.*, 49(24):243001, November 2016. 68

[121] Q. Wei, I. Lyuksyutov, and D. Herschbach. Merged-beams for slow molecular collision experiments. *J. Chem. Phys.*, 137(5):054202, 2012. 60

[122] J. Weiner, V. S. Bagnato, S. Zilio, and P. S. Julienne. Experiments and theory in cold and ultracold collisions. *Rev. Mod. Phys.*, 71:1 – 85, January 1999. 1

[123] J. D. Weinstein, R. Decarvalho, T. Guillet, B. Friedrich, and J. Doyle. Magnetic trapping of calcium monohydride molecules at millikelvin temperature. *Nature*, 395:148 – 150, 09 1998. 4

[124] D. J. Wineland and H. Dehmelt. Laser Fluorescence Spectroscopy on Tl + Mono-Ion Oscillator. *Bulletin of the American Physical Society*, 20, 1975. 4

[125] Y. Yamakita, S. R. Procter, A. L. Goodgame, T. P. Softley, and F. Merkt. Deflection and deceleration of hydrogen Rydberg molecules in inhomogeneous electric fields. *J. Chem. Phys.*, 121(3):1419 – 1431, 2004. 81

[126] B. Yan, P. F. H. Claus, B. G. M. van Oorschot, L. Gerritsen, A. T. J. B. Eppink, S. Y. T. van de Meerakker, and D. H. Parker. A new high intensity and short-pulse molecular beam valve. *Rev. Sci. Instrum.*, 84(2):023102, 2013. 51

[127] A. Zanzi and B. Ricci. Chameleon fields and solar physics. *Mod. Phys. Lett. A*, 30(10):1550053, 2015. 1

[128] V. I. Zapryagaev, D. A. Gubanov, I. N. Kavun, N. P. Kiselev, S. G. Kundasev, and A. A. Pivovarov. Investigation of supersonic jets shock-wave structure. *AIP Conference Proceedings*, 1893(1):030058, 2017. 54

[129] X. Zhang, Y. Chen, G. Liu, W. Wu, L. Wen, and W. Liu. Quantum information and many body physics with cold atoms. *Chin. Sci. Bull.*, 57(16):1910 – 1918, June 2012. 3